

SEARCHING FOR LONG-LIVED DARK PHOTONS WITH THE HEAVY PHOTON SEARCH EXPERIMENT

A DISSERTATION
SUBMITTED TO THE DEPARTMENT OF PHYSICS
AND THE COMMITTEE ON GRADUATE STUDIES
OF STANFORD UNIVERSITY
IN PARTIAL FULFILLMENT OF THE REQUIREMENTS
FOR THE DEGREE OF
DOCTOR OF PHILOSOPHY

Matthew Reagan Solt

July 2020

¹²

© Copyright by Matthew Reagan Solt 2020
All Rights Reserved

¹³

I certify that I have read this dissertation and that, in my opinion, it is fully adequate in scope and quality as a dissertation for the degree of Doctor of Philosophy.

¹⁴

(Philip Schuster) Principal Adviser

I certify that I have read this dissertation and that, in my opinion, it is fully adequate in scope and quality as a dissertation for the degree of Doctor of Philosophy.

¹⁵

(John Jaros)

I certify that I have read this dissertation and that, in my opinion, it is fully adequate in scope and quality as a dissertation for the degree of Doctor of Philosophy.

¹⁶

(Dan Ackerib)

I certify that I have read this dissertation and that, in my opinion, it is fully adequate in scope and quality as a dissertation for the degree of Doctor of Philosophy.

¹⁷

(Pat Burchat)

Approved for the Stanford University Committee on Graduate Studies

¹⁸

¹⁹ **Abstract**

²⁰ A heavy photon (also called a dark photon or A') is a hypothetical vector boson that arises from a
²¹ massive $U(1)$ abelian gauge symmetry. Because of the ability of heavy photons to kinetically mix
²² with the Standard Model photon, they are connected to many of hidden sector models and are
²³ favored for a variety of dark sector scenarios, particularly for dark matter at the sub-GeV mass scale.
²⁴ The Heavy Photon Search Experiment (HPS) is a fixed target experiment at Jefferson Laboratory
²⁵ dedicated to searching for heavy photons in the MeV - GeV mass range and kinetic mixing strength
²⁶ $\epsilon^2 \sim 10^{-5} - 10^{-10}$. It does so through two distinct searches - a search for a narrow mass resonance
²⁷ and, for sufficiently small couplings, a search for secondary vertices beyond a large prompt QED
²⁸ background.

²⁹ In order to perform such searches, the HPS apparatus is a compact forward acceptance spectrometer
³⁰ that must be able to reconstruct particle masses and vertices with extreme precision. Heavy
³¹ photons are electro-produced from a continuous electron beam incident on a thin tungsten foil, and
³² HPS is able to reconstruct momentum of the subsequent decays to e^+e^- pairs through a silicon
³³ vertex tracker (SVT). HPS currently has three datasets - an Engineering Run in 2015 and 2016 as
³⁴ well as a physics run with an upgraded detector in 2019 - all at different energies and beam currents.
³⁵ Presented in this dissertation are heavy photon physics and motivations, introduction to the HPS
³⁶ detector and reconstruction, upgrades and other models of interest, and the results from displaced
³⁷ vertex search from the HPS 2016 Engineering Run which was taken with a 2.3 GeV, 200 nA con-
³⁸ tinuous electron beam and collected a total of 10753 nb^{-1} (equivalent to 5.4 days of continuous
³⁹ beam).

⁴⁰ The new results from the 2016 Engineering Run displaced vertex search, performed in the mass
⁴¹ range $60 - 150 \text{ MeV}$ and a range of $\epsilon^2 \sim 10^{-10} - 10^{-8}$, show that HPS was unable achieve the
⁴² required luminosity to set a meaningful physical limit on the canonical A' model. However, the
⁴³ background required to perform a displaced A' search (0.5 background events per mass search bin)
⁴⁴ was achieved with 90% of the dataset blinded. In addition, a search for further downstream decays
⁴⁵ that miss part of the acceptance of the tracker is performed. Finally, the sensitivity to other models
⁴⁶ that contain displaced vertices are explored and preliminary projections show that HPS will have
⁴⁷ sensitivity to new territory with this dataset. This combined work on the displaced vertex search



Figure 1: This is my current placeholder figure.

⁴⁸ is informative for future datasets that will search for A 's in the same way but include simple, yet
⁴⁹ critical, upgrades to the detector. The expected sensitivity to future datasets with these upgrades
⁵⁰ is shown.

⁵¹ Acknowledgments

⁵² I would like to thank a very long list of people...

⁵³ Contents

⁵⁴ Abstract	iv
⁵⁵ Acknowledgments	vi
⁵⁶ 1 Introduction	2
⁵⁷ 2 Motivation	6
⁵⁸ 2.1 Observations	6
⁵⁹ 2.1.1 Galactic Rotation Curves	6
⁶⁰ 2.1.2 Weak Gravitational Lensing	8
⁶¹ 2.1.3 Cosmic Microwave Background	9
⁶² 2.1.4 Big Bang Nucleosynthesis and Type 1a Supernovae	10
⁶³ 2.1.5 Some Properties of Dark Matter	10
⁶⁴ 2.2 Theory Summary	13
⁶⁵ 2.3 Historical Motivations for A' 's	15
⁶⁶ 2.4 Light Dark Matter	17
⁶⁷ 2.5 Signatures of A' 's	21
⁶⁸ 2.6 Overview of Searches	23
⁶⁹ 2.6.1 Colliders	24
⁷⁰ 2.6.2 Beam Dumps	24
⁷¹ 2.6.3 Thin Fixed Target	25
⁷² 2.7 Heavy Photon Fixed Target Kinematics	28
⁷³ 2.8 Fixed Target Backgrounds	30
⁷⁴ 2.9 Overview of HPS	32
⁷⁵ 3 The HPS Detector	33
⁷⁶ 3.1 The Continuous Electron Beam Accelerator Facility (CEBAF)	35
⁷⁷ 3.2 Hall B and HPS Beamline	37
⁷⁸ 3.3 Silicon Vertex Tracker	42

79	3.3.1 Sensors and Readout	44
80	3.3.2 SVT Mechanics	47
81	3.3.3 SVT Data Acquisition, Power, and Services	50
82	3.4 Electromagnetic Calorimeter and Trigger	53
83	3.5 Datasets	57
84	4 Event Reconstruction & Selection	58
85	4.1 HPS Coordinate Systems	58
86	4.2 Ecal Reconstruction	60
87	4.3 SVT Reconstruction	62
88	4.3.1 SVT Hit Reconstruction	62
89	4.3.2 SVT Cluster and 3D Hit Reconstruction	64
90	4.3.3 Track Reconstruction	65
91	4.4 Track Cluster Matching	67
92	4.5 Vertexing	68
93	4.6 Hit Efficiency	71
94	4.7 Tracker Alignment	73
95	4.8 Track-Truth Matching	75
96	4.9 Monte Carlo Samples	77
97	4.10 e^+e^- Preselection	81
98	4.11 Composition of the e^+e^- Sample & Normalization	90
99	4.11.1 MC Normalization	90
100	4.11.2 HPS e^+e^- Rates	90
101	4.11.3 Radiative Fraction	93
102	5 Search for A' Displaced Vertices	97
103	5.1 Previous Results from 2015 Engineering Run	98
104	5.2 Mass Resolution	101
105	5.2.1 Møller Event Selection	101
106	5.2.2 Mass Resolution	104
107	5.3 Displaced A' Rates	108
108	5.3.1 A' Acceptance Effects	108
109	5.3.2 Hit Killing	110
110	5.4 Vertex Cuts	114
111	5.4.1 L1L1	116
112	5.4.2 L1L2	137
113	5.4.3 L2L2	146
114	5.5 Characterizing the Background & Defining the Signal Region	147

115	5.6 Results	151
116	5.6.1 Expected Signal Yield	151
117	5.6.2 Finding Signal Significance	153
118	5.6.3 Setting Limits	154
119	5.6.4 Combining Datasets	156
120	5.7 Systematic Uncertainties	157
121	5.8 Discussion of High z Backgrounds	160
122	5.9 A Machine Learning Approach	164
123	6 Upgrades & the Future of HPS	165
124	6.1 Upgrade Simulations and Installation	166
125	6.2 Preliminary Upgrade Performance & Reach Estimates	174
126	6.3 Generalized Displaced Vertices	178
127	6.3.1 Strongly Interacting Massive Particles (SIMPs)	178
128	6.3.2 SIMP Projections	183
129	7 Conclusions	184
130	Bibliography	185

¹³¹ List of Tables

¹³² 3.1	A summary of the basic parameters for different layers in the SVT.	43
¹³³ 3.2	Summary of the pairs1 Trigger Selection from the 2016 Engineering Run.	56
¹³⁴ 4.1	Basis for several different coordinate systems used in the HPS reconstruction and analysis.	58
¹³⁵ 4.2	Requirements applied to V_0 particles during the reconstruction stage for data (i.e. preprocessing selection).	68
¹³⁶ 4.3	Requirements applied to V_0 particles during the reconstruction stage for MC (i.e. preprocessing selection).	68
¹³⁷ 4.4	Event generators and statistics for MC samples.	77
¹³⁸ 4.5	Basic generator level physics requirements for different physics processes. A 's have no generator level cuts since knowledge of the geometrical acceptance is required to compute the expected number of A 's for different mass and ϵ values.	79
¹³⁹ 4.6	Requirements applied to V_0 after reconstruction as an initial set to study. The time offset for data is 56 ns and the time offset for MC is 43 ns. These requirements are referred to as preselection.	81
¹⁴⁰ 4.7	Table showing the efficiency of each cut on 10% of the 2016 data sample and on MC simulation for tridents, WABs and 80 MeV A' displaced samples. The trident sample contains both Bethe-Heitler and radiative events.	86
¹⁴¹ 4.8	Normalization parameters for the RAD, Tritrig, and WAB samples. The mean μ and the σ are obtained from the distribution of integrated cross-sections (ICS) from the individual generated samples.	90
¹⁴² 4.9	A list of cuts that are used to determine the radiative fraction and the number of e^+e^- events within a mass bin. The cuts are composed of the preselection cuts from Sec. 4.10 with the addition of a few extra cuts including the radiative cut (the cut on e^+e^- momentum sum).	94

157	5.1	Møller event selection for data on e^-e^- pairs. Since electron tracks are not required to match to Ecal clusters, the time difference is between track times and position differences are based on track extrapolations to the Ecal.	102
158	5.2	Møller event selection for MC on e^-e^- pairs. Since electron tracks are not required to match to Ecal clusters, the time difference is between track times and position differences are based on track extrapolations to the Ecal.	102
159			
160	5.3	A summary of the tight cuts for the L1L1 category.	116
161	5.4	Table showing the efficiency of each cut on 10% of the 2016 data sample and on MC simulation for tridents, WABs and 80 MeV A' displaced samples for the L1L1 category. TODO: Update the cuts and numbers	133
162	5.5	A summary of the tight cuts for the L1L2 category.	137
163	5.6	A summary of systematic uncertainties that impact the final result of the displaced vertex search.	157
164	5.7	Normalization parameters for the RAD, Trident-Trig and WAB samples	158
165	5.8	A table of relevant variables for events past z_{cut} for 100% of the data in the L1L1 category.	162
166	5.9	A table of relevant variables for events past z_{cut} for the full tritrig-wab-beam sample in the L1L1 category.	163
167			
168			
169			
170			
171			
172			
173			
174			

¹⁷⁵ List of Figures

¹⁷⁶	1	This is my current placeholder figure.	v
¹⁷⁷	1.1	The Standard Model of Particle Physics is a group of the known elementary particles which is composed of six quarks, six leptons, four gauge bosons (which are responsible for the three fundamental forces), and the Higgs Boson (which is the origin of mass of many of the fundamental particles). Find a picture without a watermark	5
¹⁸¹	2.1	Galactic rotation curves show stars far from the galactic center are orbiting the galactic center far faster than they should gives evidence for invisible matter.	7
¹⁸³	2.2	The Bullet Cluster shows visible matter from X-rays (highlighted in blue) and total matter from gravitational lensing (highlighted in pink).	8
¹⁸⁵	2.3	The Cosmic Microwave Background has temperature fluctuations consistent with extra invisible matter in the early universe.	9
¹⁸⁷	2.4	Left: Big Bang Nucleosynthesis puts an upper bound on the Standard Model matter density in the universe at about 15% of the total energy budget [81]. Right: Measurements from Type 1a supernovae (shaded in blue) together with the CMB and BAO measurements put the total mass in the universe at 30% of the total energy budget along with dark energy at 70% (from the intersection in gray) [18]. A combination of these measurements show that the Standard Model cannot account for most of the matter in the universe.	11
¹⁹⁴	2.5	A one-loop kinetic mixing process where an A' mixes with the SM photon through an interaction of massive fields that couple to both photons.	13
¹⁹⁶	2.6	Left: The results from PAMELA, AMS, and Fermi-LAT showing the positron fraction excess (above the expected calculation from cosmic rays in grey) at above ~ 10 GeV [45]. Right: The Feynman diagram for the dark matter annihilation into two A' s which subsequently decay into e^+e^- pairs. This provides an explanation for positron fraction excess. This explanation has since been disfavored.	15

201	2.7	The mechanism of thermal freeze-out in which dark matter and SM matter are in 202 thermal equilibrium in the early universe. As the universe cools (x -axis), the relic 203 abundance of dark matter (y -axis) is depleted by self-annihilation until enough cooling 204 occurs and the dark matter relic abundance is set.	17
205	2.8	The branching ratio for heavy photon decays to SM particles as a function of mass. 206 This assumes no decays into dark sector particles.	21
207	2.9	Existing constraints of heavy photons on the whole parameter space [64]. The con- 208 straints come from a variety of sources including astrophysical measurements, preci- 209 sion QED, and particle accelerator-based experiments. The regional labeled “unified 210 DM” is of particular interest to dark matter for reasons described in Sec. 2.4 and Sec. 211 2.3 and will be the focus. Note that the notation on this plot is such that $\epsilon \rightarrow \chi$ and 212 A' is denoted as γ'	23
213	2.10	A schematic of beam dump experiments SLAC E137 and E141 which searched for 214 long-lived particles that decay in a region several hundred meters from the target. . .	25
215	2.11	The Light Dark Matter eXperiment (LDMX) searches for heavy photon decays to 216 invisibles by measuring the recoil electron momentum and searching for missing mo- 217 mentum. The apparatus includes a tagging tracker, recoil tracker, an Ecal, and an 218 Hcal.	26
219	2.12	Existing constraints for heavy photons from experiments described in Sec. 2.6. The 220 green contours show the projected sensitivity for HPS assuming the allotted 180 days 221 of running time.	27
222	2.13	The kinematics for heavy photon (A') produced from an electron on a fixed target. In 223 general, A' 's retain most of the incident beam energy, remain close to the beam axis 224 due to a small recoil angle, and have a small opening angle.	28
225	2.14	Left pictures show Feynman diagrams for A' (top), RAD (middle) and BH (bottom) 226 events. Right picture shows WAB process.	30
227	2.15	Positron momentum vs electron momentum comparing Bethe-Heitler tridents and 228 A' 's (and hence radiative tridents). A' 's generally have a large x in comparison to 229 Bethe-Heitler. This is for a beam energy of 1.06 GeV.	31
230	3.1	A 3D rendering of the HPS detector complete with the silicon vertex tracker (SVT), 231 electromagnetic calorimeter (Ecal), and chicane.	33
232	3.2	The rate of electrons in at the first layer of the SVT from the so-called “wall of flame” 233 - beam electrons that lose energy due to bremmstrahlung in the target and bend in 234 the magnetic field. To avoid the radiation damage from the wall of flame, the detector 235 is split into top and bottom halves.	34

236	3.3 A schematic of the upgraded Continuous Electron Beam Accelerator Facility (CE- 237 BAF) at Jefferson Laboratory. The machine is a recirculating linear accelerator de- 238 signed to send a beam of electrons of different currents and energies to four different 239 experimental halls (Halls A - D).	35
240	3.4 A schematic of Hall B including the CLAS-12 spectrometer and the HPS detector in 241 the Hall B alcove. The electron beam enters the hall from the left in this picture. . . .	37
242	3.5 An example of a scan from the 2H02 wire harp from the 2016 Engineering Run. This 243 provides a measurement of the beam profile that is useful as input to tuning the 244 beam to its optimal profile at the target. The profile shows a width of 92 μm in x 245 and 14 μm in y with minimal beam tails.	39
246	3.6 A schematic of the HPS beamline inside the Hall B alcove.	40
247	3.7 An example of an SVT wire scan measurement from the 2016 Engineering Run. This 248 provides a measurement of the beam profile as close to the target as possible. This 249 scan shows a beam with a 14 μm width in the y -direction with minimal tails and 35 250 μm from the nominal beam plane. This is an excellent beam profile for HPS.	41
251	3.8 A measurement of the beam halo from 2015 Engineering Run using the occupancy of 252 the first layer of the SVT in a no target run. The beam halo shows a width of 960 μm 253 and 5 orders of magnitude less than the peak of the beam.	41
254	3.9 A schematic of the HPS silicon vertex tracker (SVT) which includes 6 layers of silicon 255 microstrip sensors inside a vacuum and a uniform magnetic field. <i>Maybe find a better 256 picture.</i>	42
257	3.10 A schematic of the APV25 deep submicron readout chip that was originally designed 258 for CMS detectors but is used for the HPS SVT.	44
259	3.11 A picture of the two SVT sensors (end to end) with each sensor. The sensors are 260 readout by APV25 chips which are housed on a hybrid circuit.	45
261	3.12 The APV25 Shaper schematic. The parameters VFS (related to the input voltage) 262 and isha (related to the input current) were optimized for improved time resolution 263 and reduced pileup.	46
264	3.13 A single SVT module which comprises of two silicon microstrip sensors which are axial 265 (front) and stereo (back) to the beam plane. Each sensor is supported by a carbon 266 fiber support structure can be seen protruding from the right of the axial sensor. . . .	47
267	3.14 Layers 1 - 3 modules of the SVT (from left to right) are placed in one of the U-channels. 268 Copper cooling lines and electrical lines can be seen. The wire frames and scan wires 269 can also be seen on the left.	48

270	3.15 A picture inside the SVT vacuum chamber with everything installed except for the target. The frontend boards (FEBs) and FEB cooling plate are on the left. The SVT cooling lines protrude outward in the picture. The first layer of the SVT can be seen in the back behind the wire frames. The SVT is in its closed position and the beam must go through the 1 mm gap between the top and bottom sensors.	49
271		
272		
273		
274		
275	3.16 A schematic of the SVT DAQ system described in Sec. 3.3.3.	50
276		
277	3.17 The FEB cooling plate complete with 10 FEBs fastened to the front and back of the plate.	52
278		
279	3.18 A rendering of the beam's eye view of the HPS Ecal. Each segment is one of the 442 lead tungstate crystals and the Ecal is split in half to avoid radiation damage from the most intense parts of the beam.	53
280		
281	3.19 A schematic of a PbWO ₄ crystal in the Ecal.	54
282		
283	3.20 A schematic of the trigger for the Ecal. Top and bottom halves of the Ecal are each are readout by FADC readout boards, and then sent to the SSP where a trigger decision is made.	55
284		
285	3.21 A summary for the integrated charge over time for the Top: 2015 Engineering Run and Bottom: 2016 Engineering Run. Replace these figures	57
286		
287	4.1 A schematic of the linear collider tracking parameters 4.1 [69].	59
288		
289	4.2 A plot of the digitized waveform that is stored from the DAQ and the fit using Eq. 4.3. The 6 samples used for the fit are in 24 ns intervals (between the red lines). . .	63
290		
291	4.3 The hit efficiency for each top/bottom layer of the SVT for Left: electrons and Right: positrons. The decrease in efficiency in layer 1 and layer 6 can be attributed to increased occupancy and a large number of dead channels, respectively. The difference between electrons and positrons in layer 1 hit efficiency is a result of WABs, where a conversion occurs in layer 1 and fails to produce a hit in both axial and stereo sensors, which is measured as a hit inefficiency.	66
292		
293		
294		
295		
296	4.4 The run-dependent average position in z for unconstrained vertices fit represented by solid points and a solid line for data and MC simulation, respectively.	69
297		
298	4.5 The run-dependent mean (left) and width (right) in x and y for the unconstrained vertex position in data. The MC is represented as a solid line.	70
299		
300	4.6 The measured SVT layer 1 efficiency for electrons in layer 1 bottom stereo sensor. The MC does not have the correct hit efficiencies.	71
301		
302	4.7 The target position is found to be -4.3 mm. I actually need to get these plots. Some placeholders are there for now.	73
303		

304	4.8 Left: The purity for e^+e^- tracks with preselection and layer 1 requirements for tritrig-wab-beam MC. Purity is a measure of how hit on track are associated with the truth matched particle. Right: Tracking layers (ordered in sensor number from upstream to downstream) that contain a hit on track not associated with the truth particle matched to the track (i.e. a bad hit).	75
305		
306		
307		
308		
309	4.9 Left pictures show Feynman diagrams for A' (top), RAD (middle) and BH (bottom) events. Right picture shows WAB process.	78
310		
311		
312		
313	4.10 Track-cluster match number of σ for electrons (left) and positrons (right). A loose cut is placed at $N\sigma < 10$ for both electrons and positrons to eliminate poor track-cluster matches.	82
314		
315		
316	4.11 A cluster time difference cut between electrons and positrons is placed at 1.45 ns to eliminate accidentals from other beam bunches (Hall B bunches are spaced at 2 ns).	83
317		
318		
319	4.12 Cluster-track time difference (with the time offset from Table 4.6) for electrons (left) and positrons (right). A cut is placed at a time difference of 4 ns for both electrons and positrons to eliminate out of time tracks. There is significant mismodeling for the track time resolution; however, this is a data-driven cut.	83
320		
321	4.13 Electron momentum has a minimum momentum cuts at 0.4 GeV in order to reduce low momentum particles that have larger multiple scattering. A maximum momentum cut is placed at 1.75 GeV to eliminate V0s that reconstruct with elastically-scatter electrons in the target. Left: The plot of electron momentum after preprocessing. Right: A plot of the electron momentum used to study full-energy electrons (since most elastically-scatter electrons are cut away during preprocessing). There is some mismodeling for individual particle momenta particularly at low momentum. Replace figure on the right with electron momentum that include an FEE peak.	84
322		
323		
324		
325		
326		
327		
328	4.14 Left: Positron momentum has a minimum momentum cut at 0.4 GeV in order to reduce low momentum particles that have larger multiple scattering. Right: A maximum V0 momentum cut is placed at 2.4 GeV since signal is not expected far above the beam energy at 2.3 GeV.	85
329		
330		
331		
332	4.15 Track χ^2 per degrees of freedom (dof) for electrons (left) and positrons (right). A cut is placed at $\chi^2 < 6$ for both electrons and positrons to eliminate poor tracks that can falsely reconstruct downstream of the target.	85
333		
334		
335	4.16 A loose cut on the unconstrained vertex fit χ_{unc} is placed at 10 to eliminate poorly reconstructed V0s that can incorrectly reconstruct downstream of the target. There is some mismodeling for the cluster time resolution, and there is some mismodeling in the vertex quality.	85
336		
337		
338		
339	4.17 Comparison of 10% Data and tritrig-wab-beam for preselected events.	86

340	4.18 Preselection cutflow for as a function of reconstructed z . Top Right: Run 7800 in		
341	data. Top Left: a fraction of the tritrig-wab-beam sample. Bottom Left: 80 MeV		
342	displaced A' s. Bottom Right: 100 MeV displaced A' s.	87	
343	4.19 Preselection cutflow for reconstructed mass. Top Right: Run 7800 in data. Top		
344	Left: a fraction of the tritrig-wab-beam sample. Bottom Left: 80 MeV displaced A' s.		
345	Bottom Right: 100 MeV displaced A' s.	88	
346	4.20 Preselection cutflow for as a function of reconstructed V0 momentum. Top Right:		
347	Run 7800 in data. Top Left: a fraction of the tritrig-wab-beam sample. Bottom Left:		
348	80 MeV displaced A' s. Bottom Right: 100 MeV displaced A' s.	89	
349	4.21 Distributions of e^+e^- events with scaling all MC cross-sections by 0.8. Upper Left:		
350	e^+e^- momentum sum. Upper Right: e^+e^- invariant mass. Middle Left: Positron		
351	momentum. Middle Right: Positron track slope. Bottom Left: Electron momentum.		
352	Bottom Right: Electron track slope.	92	
353	4.22 Left: The differential cross sections ($d\sigma/dm$) of wab, trident, and radiative trident		
354	components from MC as well as the measured cross section from 10% of the data.		
355	In principle, one would expect the tridents + wabs (turquoise) to agree with data		
356	(blue). The discrepancy is explained in Sec. 4.11.2. Right: The radiative fractions as		
357	a function of mass. It is fit to a 5th order polynomial and is used to determine the		
358	expected radiative trident rate from the number of e^+e^- pairs in a mass bin.	93	
359	4.23 The invariant mass for Left: 10% of the data and Right: 100% of the data with the		
360	radiative cut selection. It is fitted to the an exponential to a 5th order polynomial.		
361	This is the number of e^+e^- pairs in a 1 MeV bin used to normalize the expected		
362	radiative trident rate, and hence the expected A' rate.	94	
363	4.24 Left: The number of A' 's produced for each mass and ϵ^2 in prompt acceptance in-		
364	cluding all efficiencies for 10% of the data. In other words, the term in front of the		
365	integral in Eq. 5.18. Right: The number of A' 's produced for each mass and ϵ^2 in		
366	prompt acceptance including all efficiencies for 100% of the data.	96	
367	5.1 Final event selection for the displaced vertex search in the 2015 Engineering Run for		
368	Left: Data and Right: a luminosity-equivalent tritrig-wab-beam MC sample. The		
369	z_{cut} is shown in red.	99	
370	5.2 Final results for the displaced vertex search for the 2015 Engineering Run. Left: The		
371	number of expected A' events after all analysis cuts and z_{cut} as a function of mass		
372	and ϵ^2 . The maximum number of expected A' events is 0.097 events at an A' mass of		
373	43.6 MeV and $\epsilon^2 = 2.4 \times 10^{-9}$. Right: The limit on the A' cross section as a function		
374	of mass and ϵ^2 where the best limit set is at an A' of 51.4 MeV and $\epsilon^2 = 1.7 \times 10^{-9}$		
375	in which an A' -like model with 35.7 times the cross-section is excluded with 90%		
376	confidence.	99	

377	5.3 From detailed MC studies, it was shown that the backgrounds are due to two main processes. We seek to further mitigate these backgrounds in the 2016 Engineering Run. Left: A vertex is falsely reconstructed downstream of the target due to two large scatters of the e^+e^- pairs away from the beam plane. Right: A vertex is falsely reconstructed downstream of the target due to a track picking up the incorrect layer 1 hit (mis-tracking). These events are usually accompanied by a large scatter in the other particle that is tracked correctly.	100
384	5.4 Fitted e^-e^- spectrum using the Møller selection for Upper Left: Data, Upper Right: Møller MC with track momentum smearing, and Bottom: Møller MC.	103
386	5.5 Upper Left: Fitted reconstructed mass spectrum for a 100 MeV displaced A' . Upper Right: Fitted reconstructed mass spectrum for a 100 MeV displaced A' with track momentum smearing. Lower Left: Reconstructed mass vs truth z decay for a 100 MeV displaced A' . Lower Right: The fitted mass resolution for 100 MeV displaced A' 's as in slices of truth z . Mass resolution is approximately independent of decay length. These plots are for the L1L1 category.	106
392	5.6 Upper Left: Fitted reconstructed mass spectrum for a 100 MeV displaced A' . Upper Right: Fitted reconstructed mass spectrum for a 100 MeV displaced A' with track momentum smearing. Lower Left: Reconstructed mass vs truth z decay for a 100 MeV displaced A' . Lower Right: The fitted mass resolution for 100 MeV displaced A' 's as in slices of truth z . Mass resolution is approximately independent of decay length. These plots are for the L1L2 category.	107
398	5.7 A' mass resolution as a function of mass comparing A' MC, A' MC scaled using the ratio of the Møller mass resolution in data to MC, and A' MC with smearing for the Left: L1L1 category and the Right: L1L2 category. The mass resolution is fitted to a straight line to the MC with track momenta smearing and is used as an input to the size of the mass bins in the final results.	107
403	5.8 Left: Schematic of a relatively short A' decay length in which both daughter particles have a layer 1 hit. This is referred to as L1L1. Right: Schematic of a relatively long A' decay length in which one of the daughter particles misses layer 1 (but hits layer 2) and the other daughter particle hits layer 1. This is referred to as L1L2.	108
407	5.9 The layer 1 efficiency used for the hit killing algorithm as a function of track slope ($\tan\lambda$).	110
409	5.10 The product of geometrical acceptance and efficiency for displaced A' 's for the L1L1, L1L2, and L2L2 categories as well as their sums. 80 MeV displaced A' 's are on the left and 100 MeV displaced A' 's are on the right. The top is before hit killing and the bottom is with hit killing and a fit function fit to the sum of the categories. The top plots I still have to make, I have the same plots there as the bottom as a placeholder.	112

414	5.11 The product of geometrical acceptance and efficiency for displaced A' s for the L1L1, 415 L1L2, and L2L2 categories as well as there sums. These plot are normalized to unity 416 at the target, where the sum is normalized before hit killing and further analysis cuts. 417 80 MeV displaced A' s are on the left and 100 MeV displaced A' s are on the right. 418 The top is without the z_{cut} and the bottom is with the z_{cut} from 10% of the data.	113
419	5.12 Left: A schematic of a prompt background process that has a hit inefficiency in layer 420 1 and is placed in the L1L2 category. Right: A schematic of a prompt background 421 process in which one of the daughter particles scatters away from the beam in the 422 inactive silicon of layer 1 and into the acceptance of the tracker. This process is placed 423 in the L1L2 category and also reconstructs a false vertex downstream of the target.	115
424	5.13 The V0 projection back to the target for Preselection in the L1L1 category. Upper 425 Left: 10% Data with a linear fit to the x - y correlation Lower Left: 10% tritrig-wab- 426 beam with a linear fit to the x - y correlation. The V0 projection back to the target 427 for L1L1 Preselection with rotated x - y coordinates for Upper Right: 10% Data and 428 Lower Right: 10% tritrig-wab-beam. The angle of rotation is $\theta_{data} = 0.0387$ rad in 429 data and $\theta_{MC} = 0.1110$ rad in MC.	117
430	5.14 The run-dependent mean (left) and width (right) for x and y target projection for 431 the unconstrained vertex in data.	118
432	5.15 The V0 projection back to the target significance ($(x(y) - x_{mean}(y))/x_{\sigma}(y)$) using the 433 rotated coordinates for L1L1 Preselection for Upper Left: 10% data Upper Right: 1% 434 tritrig-wab-beam Lower Left: Displaced 80 MeV A' Lower Right: Displaced 100 MeV 435 A' . The elliptical cut at 2σ is shown in red.	119
436	5.16 Plots showing the effect of with and without the V0 projection to the target cut for 437 the L1L1 category. Upper Left: Comparison of VZ distributions for 10% Data and 438 100% tritrig-wab-beam MC for all tight cuts except for the V0 projection to the target 439 cut. Upper Right: Comparison of preselection, tight cuts, and tight cuts without the 440 V0 projection to the target cut for 10% Data. Middle Left: Comparison of the V0 441 projection to the target in units of $n\sigma$. for 10% Data and tritrig-wab-beam MC using 442 all tight cuts except the V0 projection to the target cut. Middle Right: Comparison 443 of preselection, tight cuts, and tight cuts without the V0 projection to the target cut 444 for displaced 80 MeV A' 's. Bottom: Comparison of preselection, tight cuts, and tight 445 cuts without the V0 projection to the target cut for displaced 100 MeV A' 's.	120
446	5.17 Left: Example of mistracking from a layer 1 bad hit that falsely reconstructs down- 447 stream of the target. Right: Geometric picture of the isolation cut comparing the 448 distance between the nearest hit away from the beam δ and the track longitudinal 449 impact parameter of the track z_0 where the correct track is in green and the incorrect 450 track found by the tracking algorithm is in red.	121

451	5.18 Plots showing the effect of with and without the isolation cut for the L1L1 category. Upper Left: Comparison of VZ distributions for 10% Data and 100% tritrig-wab-beam MC for all tight cuts except for the isolation cut. Upper Right: Comparison of preselection, tight cuts, and tight cuts without the isolation cut for 10% Data. Middle Left: Electron isolation cut value for 10% Data and tritrig-wab-beam MC using all tight cuts except the isolation cut. Middle Right: Positron isolation cut value for 10% Data and tritrig-wab-beam MC using all tight cuts except the isolation cut. Bottom Left: Comparison of preselection, tight cuts, and tight cuts without the isolation cut for displaced 80 MeV A's. Bottom Right: Comparison of preselection, tight cuts, and tight cuts without the isolation cut for displaced 100 MeV A's.	123
461	5.19 Reconstructed z vs. the isolation cut value in eq. 5.9 for 10% of the data with preselection and layer 1 requirements. This isolation cut value combines positrons and electrons for both top and bottom, but only uses the minimum positive isolation value for the axial and stereo pair in layer 1.	124
465	5.20 Reconstructed z vs. the isolation cut value in eq. 5.9 for 100% of the tritrig-wab-beam MC sample with preselection and layer 1 requirements. This isolation cut value combines positrons and electrons for both top and bottom, but only plots the minimum positive isolation value for the axial and stereo pair in layer 1. The left plot only selects tracks that match to the same MCParticle, while the plot on the right only selects V0 particles that contain either an e^+ or e^- track that have an incorrect layer 1 hit.	125
472	5.21 Reconstructed z vs. the isolation cut value in eq. 5.9 for an 80 MeV (left) and 100 MeV (right) displaced A' with preselection and layer 1 requirements. This isolation cut value combines positrons and electrons for both top and bottom, but only plots the minimum positive isolation value for the axial and stereo pair in layer 1.	126
476	5.22 A comparison of the reconstructed z distribution for V0 particles with 2 tracks that have all the hits matched to an MC particle (blue) and those with either an e^+ or e^- track with a bad layer 1 hit.	126
479	5.23 Left: Prompt background that falsely reconstructs at a large z due to an e^- particle with a large scatter away from the beam plane in layer 1 of the SVT. The corresponding e^+ does not have a large scatter and the track point back near the primary. A cut on the impact parameter can eliminate such background. Right: A true displaced vertex will have a large impact parameter for both e^+e^- pairs that is correlated with reconstructed z	127

485	5.24 Impact parameter vs. reconstructed z for different mass values of 10% data and A' s 486 in the L1L1 category. The red lines indicate the impact parameter cut at the specified 487 mass value. Upper Left: 10% data in mass range 75-85 MeV. Upper Right: 10% data 488 in the mass range 95-105 MeV. Lower Left: 80 MeV Displaced A' 's. Lower Left: 100 489 MeV Displaced A' 's.	128
490	5.25 Plots showing the effect of with and without the impact parameter cut for the L1L1 491 category. Upper Left: Comparison of VZ distributions for 10% Data and 100% tritrig- 492 wab-beam MC for all tight cuts except for the impact parameter cut. Top Right: 493 Comparison of preselection, tight cuts, and tight cuts without the impact parameter 494 cut for 10% Data. Middle Left: Electron track z_0 for 10% Data and tritrig-wab- 495 beam MC using all tight cuts except the impact parameter cuts. Middle Right: 496 Positron track z_0 for 10% Data and tritrig-wab-beam MC using all tight cuts except 497 the impact parameter cuts. Bottom Left: Comparison of preselection, tight cuts, and 498 tight cuts without the impact parameter cut for displaced 80 MeV A' 's. Bottom Right: 499 Comparison of preselection, tight cuts, and tight cuts without the impact parameter 500 cut for displaced 100 MeV A' 's.	130
501	5.26 Plots showing the effect of with and without the V0 momentum cut for the L1L1 502 category. Upper Left: Comparison of VZ distributions for 10% Data and 100% tritrig- 503 wab-beam MC for all tight cuts except for the V0 momentum cut. Upper Right: 504 Comparison of preselection, tight cuts, and tight cuts without the V0 momentum 505 cut for 10% Data. Middle Left: Comparison of the V0 momentum for 10% Data and 506 tritrig-wab-beam MC using all tight cuts except the V0 momentum cut. Middle Right: 507 Comparison of preselection, tight cuts, and tight cuts without the V0 momentum cut 508 for displaced 80 MeV A' 's. Bottom: Comparison of preselection, tight cuts, and tight 509 cuts without the V0 momentum cut for displaced 100 MeV A' 's.	132
510	5.27 Upper Left: Comparison of 10% Data and tritrig-wab-beam MC for the final event 511 selection in the L1L1 category. Upper Right: Comparison of 10% of the Data for 512 before and after multiple V0 events are removed. Lower Left: Comparison of 80 MeV 513 displaced A' 's for before and after multiple V0 events are removed. Lower Right: 514 Comparison of 100 MeV displaced A' 's for before and after multiple V0 events are 515 removed.	134
516	5.28 Comparisons of tight cuts for the L1L1 category. Upper Left: Comparison of the 517 tight cutflow for 10% Data and tritrig-wab-beam. Upper Right: Comparison of 10% 518 Data and tritrig-wab-beam for events with tight cuts. Lower Left: Tight cutflow for 519 80 MeV displaced A' 's. Lower Right: Tight cutflow for 100 MeV displaced A' 's. . . .	135

520	5.29 Upper Left: Comparison of 10% Data and tritrig-wab-beam MC for the final event 521 selection in the L1L1 category. Upper Right: Comparison of 10% of the Data for 522 before and after multiple V0 events are removed. Lower Left: Comparison of 80 MeV 523 displaced A's for before and after multiple V0 events are removed. Lower Right: 524 Comparison of 100 MeV displaced A's for before and after multiple V0 events are 525 removed.	136
526	5.30 Upper Left: Comparison of 10% Data and tritrig-wab-beam MC for the final event 527 selection in the L1L1 category. Upper Right: Comparison of 10% of the Data for 528 before and after multiple V0 events are removed. Lower Left: Comparison of 80 MeV 529 displaced A's for before and after multiple V0 events are removed. Lower Right: 530 Comparison of 100 MeV displaced A's for before and after multiple V0 events are 531 removed.	136
532	5.31 Upper Left: Comparison of 10% Data and tritrig-wab-beam MC for the final event 533 selection in the L1L1 category. Upper Right: Comparison of 10% of the Data for 534 before and after multiple V0 events are removed. Lower Left: Comparison of 80 MeV 535 displaced A's for before and after multiple V0 events are removed. Lower Right: 536 Comparison of 100 MeV displaced A's for before and after multiple V0 events are 537 removed.	138
538	5.32 Plots showing the effect of with and without the isolation cut for the L1L2 category. 539 Upper Left: Comparison of VZ distributions for 10% Data and 100% tritrig-wab- 540 beam MC for all tight cuts except for the isolation cut. Upper Right: Comparison of 541 preselection, tight cuts, and tight cuts without the isolation cut for 10% Data. Middle 542 Left: Electron isolation cut value for 10% Data and tritrig-wab-beam MC using all 543 tight cuts except the isolation cut. Middle Right: Positron isolation cut value for 10% 544 Data and tritrig-wab-beam MC using all tight cuts except the isolation cut. Bottom 545 Left: Comparison of preselection, tight cuts, and tight cuts without the isolation cut 546 for displaced 80 MeV A's. Bottom Right: Comparison of preselection, tight cuts, and 547 tight cuts without the isolation cut for displaced 100 MeV A's.	140
548	5.33 Impact parameter vs. reconstructed z for different mass values of 10% data and A' 's 549 in the L1L2 category. The red lines indicate the impact parameter cut at the specified 550 mass value. Upper Left: 10% data in mass range 75-85 MeV. Upper Right: 10% data 551 in the mass range 95-105 MeV. Lower Left: 80 MeV Displaced A' 's. Lower Left: 100 552 MeV Displaced A' 's.	142
553	5.34 Comparisons of tight cuts for the L1L2 category. Upper Left: Comparison of the 554 tight cutflow for 10% Data and tritrig-wab-beam. Upper Right: Comparison of 10% 555 Data and tritrig-wab-beam for events with tight cuts. Lower Left: Tight cutflow for 556 80 MeV displaced A's. Lower Right: Tight cutflow for 100 MeV displaced A's. . . .	143

557	5.35 Upper Left: Comparison of 10% Data and tritrig-wab-beam MC for the final event 558 selection in the L1L2 category. Upper Right: Comparison of 10% of the Data for 559 before and after multiple V0 events are removed. Lower Left: Comparison of 80 MeV 560 displaced A's for before and after multiple V0 events are removed. Lower Right: 561 Comparison of 100 MeV displaced A's for before and after multiple V0 events are 562 removed.	144
563	5.36 Upper Left: Comparison of 10% Data and tritrig-wab-beam MC for the final event 564 selection in the L1L1 category. Upper Right: Comparison of 10% of the Data for 565 before and after multiple V0 events are removed. Lower Left: Comparison of 80 MeV 566 displaced A's for before and after multiple V0 events are removed. Lower Right: 567 Comparison of 100 MeV displaced A's for before and after multiple V0 events are 568 removed.	145
569	5.37 Upper Left: 10% Data and full MC comparison in reconstructed z for a slice in mass 570 for L1L1. For both distributions, the fitted mean is shifted to 0. Upper Right: 10% 571 Data and full MC comparison in reconstructed z for a slice in mass for L1L2. For 572 both distributions, the fitted mean is shifted to 0. Lower Left: An example fit of a 573 mass slice in 10% of the data using Eq. 5.15 for the L1L1 category. Lower Right: An 574 example fit of a mass slice in 10% of the data using Eq. 5.15 for the L1L2 category. 575 Update these with 100% data.	147
576	5.38 Top Left: Fitted mean as a function of mass comparing 10% of the data to the full 577 tritrig-wab-beam sample for the L1L1 category. Top Right: Fitted mean as a function 578 of mass comparing 10% of the data to the full tritrig-wab-beam sample for the L1L2 579 category. Middle Left: Fitted σ as a function of mass comparing 10% of the data to 580 the full tritrig-wab-beam sample for the L1L1 category. Middle Right: Fitted σ as a 581 function of mass comparing 10% of the data to the full tritrig-wab-beam sample for 582 the L1L2 category. Bottom Left: Fitted “tail z ” parameter (the number of σ from the 583 mean the function transitions from Gaussian core to exponential tail) as a function 584 of mass comparing 10% of the data to the full tritrig-wab-beam sample for the L1L1 585 category. Bottom Right: Fitted “tail z ” parameter (the number of σ from the mean 586 the function transitions from Gaussian core to exponential tail) as a function of mass 587 comparing 10% of the data to the full tritrig-wab-beam sample for the L1L2 category.	149
588	5.39 The final event selection with overlaid z_{cut} from 100% data, the full tritrig-wab- 589 beam sample, and projected to the full dataset for Top Left: 100% data for the L1L1 590 category, Top Right: full tritrig-wab-beam sample for the L1L1 category, Bottom Left: 591 10% data for the L1L2 category, and Bottom Right: full tritrig-wab-beam sample for 592 the L1L2 category.	150

593	5.40 Left: A comparison of z_{cut} between 10% data and scaled to the full dataset to the maximum z value in a mass bin for the L1L1 category. Right: A comparison of z_{cut} between 10% data and scaled to the full dataset to the maximum z value in a mass bin for the L1L2 category. Update with full dataset	150
594		
595		
596		
597	5.41 Left: The expected number of A' events past z_{cut} including all efficiencies for the L1L1 category for 10% of the data. Right: The expected number of A' events past z_{cut} including all efficiencies for the L1L1 category projected for the full dataset.	151
598		
599		
600	5.42 Left: The expected number of A' events past z_{cut} including all efficiencies for the L1L2 category for 10% of the data. Right: The expected number of A' events past z_{cut} including all efficiencies for the L1L2 category projected for the full dataset.	152
601		
602		
603	5.43 Left: The number of background events past z_{cut} based on the background model and the candidate events past z_{cut} for the L1L1 category. Right: The p-value for the L1L1 category	153
604		
605		
606	5.44 The effects of a single event on the Optimum Interval Method limit for several decay lengths for an 80 MeV mass bin (left) and a 100 MeV mass bin (right). The relative limit (relative to the background-free limit) is plotted as a function of reconstructed z of a single dummy background event. A single background event can result in up to about a 70% worse limit.	154
607		
608		
609		
610		
611	5.45 Left: The limit from Optimum Interval Method for the L1L1 category. Right: The limit from Optimum Interval Method for the L1L2 category.	155
612		
613		
614		
615	5.46 Left: The combined expected number of A' events past z_{cut} including all efficiencies for the L1L1 and L1L2 categories for 10% of the data. Right: The combined expected number of A' events past z_{cut} including all efficiencies for the L1L1 and L1L2 categories for the full dataset. Report minimum value	156
616		
617	5.47 The combined limit from Optimum Interval Method for the L1L1 and L1L2 categories. Report minimum value	156
618		
619	5.48 The ratio of the limit for the L1L1 category from the target 0.5 mm upstream of the nominal position to the target at the nominal position using the Optimum Interval Method. This ratio is used to estimate the systematic uncertainty associated with the error in the target position. This uncertainty is a function of mass and ϵ (because of the variable decay lengths), but a conservative estimate of 5% covers the entire parameter space of interest.	159
620		
621		
622		
623		
624		
625	5.49 Upper Left: The final selection for the L1L1 category on the full dataset. The reconstructed z vs mass for the full dataset that includes all cuts with the exception of the (i.e. $n - 1$ plots) Upper Right: V0 projection to the target cut. Lower Left: Isolation cut. Lower Right: Impact parameter cut. The cuts are described in Sec. 5.4.	160
626		
627		
628		

629	6.1 Left: A schematic comparing the upgraded L0 sensor dimensions to the nominal 630 sensors used in the other layers. L0 sensors are thinner with far less dead material. 631 Right: A picture of an L0 thin sensor full module (stereo side) and hybrid circuit.	165
632	6.2 Left: A comparison of the acceptance for prompt trident events for the nominal 633 detector and the upgraded L0 detector. The acceptance is remarkably close despite 634 the smaller L0 sensor dimensions (the acceptance is concentrated on the center of the 635 sensor near the beam edge). Right: A comparison of the vertex resolution with the 636 nominal detector and upgraded L0 detector. The improvement in vertex resolution is 637 about a factor of 2.	166
638	6.3 The efficiency of a displaced 40 MeV A' separated into different mutually exclusive 639 categories based on the first layer hit by the positrons and electrons for both the 640 nominal and L0 upgraded detector. Left: The nominal detector separated in to L1L1, 641 L1L2, and L2L2. Right: The upgraded L0 detector separated into L0L0, L0L1, L1L1, 642 L0L2, L1L2, and L2L2.	168
643	6.4 A comparison for a 40 MeV displaced A' of the total efficiency (including acceptance 644 effects) between the nominal detector and the upgraded detector by adding the mu- 645 tually exclusive categories in Fig. 6.3. The L0 has increased acceptance for large z 646 due to layers 2 and 3 in the tracker being moved closer to the beam.	168
647	6.5 Left: A schematic of the Ecal showing the side in which positrons trigger. The 648 positron trigger will recover events in which the electron falls in the gap. Right: A 649 picture of the hodoscope which is located in the vacuum chamber behind layer 6 of 650 the SVT and in front of the Ecal, but only on the positron side. Ecal-hodoscope 651 matching enables a positron-only trigger with rates that are manageable for the DAQ. 169	
652	6.6 A comparison of the z_{cut} for several different luminosities (1.7 days, 4 weeks, 10 weeks, 653 and 180 days) for Left: the nominal detector and Right: the upgraded L0 detector. 654 The improvement in z_{cut} by a factor of ~ 2 for the L0 detector is a measure of the 655 the improvement in the signal yield.	170
656	6.7 The estimated projection from early simulations for the upgraded L0 detector assum- 657 ing 4 weeks of a continuous 1.06 GeV beam. The contour is drawn at 2.3 expected 658 events and assumes layer 0 hits for both e^+e^- particles (L0L0).	171
659	6.8 Left: A picture of an L0-3 U-channel on top of the mechanical survey table. Right: 660 A graduate student peers over an L0-3 U-channel inside a test box at SLAC that was 661 used for DAQ testing.	172

662	6.9 The upgraded U-channels were each placed in a test box at SLAC for DAQ testing. Since each box must be cooled and fed dry air, humidity monitoring is needed. Each box contained a humidity sensor which was readout via an Arduino and connected to a Twitter-based alert system. This picture shows an example of a sudden increase in humidity in both test boxes which was immediately followed by an alert tweet. In other words, someone opened the test boxes.	173
663		
664		
665		
666		
667		
668	6.10 Left: A beam’s-eye view of the installed L0 sensors inside the vacuum chamber. This is in the “open” configuration in which the sensors are far from the beam plane (~ 10 mm) so that the beam can be tuned without damaging sensors. Right: A zoomed in version in the “closed” (or operating) configuration where the L0 axial sensors are $500 \mu\text{m}$ from the beam plane.	173
669		
670		
671		
672		
673	6.11 The approximate timeline for the major events that occurred over the course of the 2019 Physics Run. The first beam was delivered to the Hall B in the middle of June. Due to issues over the course of the run, the run was extended from the end of August to the middle of September.	174
674		
675		
676		
677	6.12 A measurement of the beam profile using the SVT scan wires with measures a beam profile of $22 \mu\text{m}$ in y within $50 \mu\text{m}$ of the center of the detector. This is a high-quality beam was the first successful beam for HPS with simultaneous operations of Hall A, Hall B, and Hall C in the 12 GeV era (upgraded CEBAF as described in Sec. 3.1). .	175
678		
679		
680		
681	6.13 Accumulated charge over the course of the 2019 Physics Run. The red line is re-scaled to the luminosity-equivalent total charge from an $8 \mu\text{m}$ thick target since the target configuration was changed several times over the course of the run.	175
682		
683		
684	6.14 Left: A comparison of the vertex resolution for data and MC for with a 4.55 GeV beam. Data is within $\sim 25\%$ of MC and will improve as the tracker alignment is updated. Right: A comparison of data and MC measured cross-sections as a function of e^+e^- momentum sum. The blue line represents events in which the electron track does not match to a cluster in the Ecal. This is a measure of the effectiveness of the hodoscope which shows an increase in the rate of e^+e^- pairs by $\sim 30\%$ in the signal region (large momentum sum).	176
685		
686		
687		
688		
689		
690		
691	6.15 Left: Initial projections for the displaced vertex search from the 2019 Physics Runs with a 4.55 GeV beam. Right: Projections utilizing the full HPS run time of 180 days at both 4.55 GeV and 2.3 GeV. Both of these projections assume layer 0 hits for both e^+e^- particles (L0L0).	177
692		
693		
694		
695	6.16 A hidden $SU(3)$ symmetry in a dark sector can contain hidden hadrons which include dark pions and dark vector mesons. One way for these particles to interact with SM matter is through an indirect interaction via kinetic mixing between an A' and the SM photon as describe in Sec. 2.2.	178
696		
697		
698		

699	6.17 A mechanism in the early universe in which dark pions undergo a $3 \rightarrow 2$ annihilation mechanism followed by heat being dumped into SM sector to produce the cold dark matter observed today. This mechanism can be tuned to achieve the correct dark pion relic abundance of dark matter and is known as the “SIMP Miracle.” This motivates a dark matter mass in the range $\sim 10 - 100$ MeV. HPS can probe the production the mechanism $e^-Z \rightarrow e^-ZA'$ and then $A' \rightarrow \pi_D V_D$ and then $V_D \rightarrow e^+e^-$ where the V_D is long-lived.	179
700		
701		
702		
703		
704		
705		
706	6.18 Left: The reconstructed V0 momentum that shows roughly the different parameter space for canonical A 's and SIMPs. The lower momentum sum of the SIMP parameter space is due to missing energy from the dark pion. Replace this figure Right: The livetime ($c\tau$) of two dark mesons (ρ_D and ϕ_D) for a given set of parameters. The livetime $c\tau \sim 0.1 - 10$ mm is within HPS range.	182
707		
708		
709		
710		
711	6.19 Contours in the $m_{\pi_D} - (m_{\pi_D}/f_{\pi-D})$ space for different choices of m_{V_D}/m_{π_D} assuming π_D makes up all the dark matter. Right: The branching ratio as a function of m_{π_D}/f_{π_D} . For HPS, the branching ratio in the parameter space of interest for the sum of ρ_D and ϕ_D is about $\sim 10\%$	182
712		
713		
714		
715	6.20 The SIMP reach estimate from the full 2016 Engineering Run dataset shown in $\epsilon^2 - m_{A'}$ space for $\alpha_{dark} = 0.01$ and for Left: $m_\pi/f_\pi = 3$ and Right: $m_\pi/f_\pi = 4\pi$. The ratio of the masses is kept constant at $m_{A'} : m_\rho : m_\pi = 3.0 : 1.8 : 1.0$ for simplicity. The contours are drawn at 2.3 expected events and the dataset is projected to set new limits in previously unprobed territory. These figures need to be replaced. . . .	183
716		
717		
718		
719		

720 This thesis is dedicated to...

₇₂₁ **Chapter 1**

₇₂₂ **Introduction**

₇₂₃ The Standard Model of Particle Physics (SM) is the most successful attempt to explain matter, its
₇₂₄ interactions, and its origin at the most fundamental level possible. Shown in Fig. 1.1, the basic
₇₂₅ particle content of the SM contains a group of six quarks and 6 leptons which compose all the
₇₂₆ known matter as well as four gauge bosons which are responsible for the three fundamental forces
₇₂₇ in nature - electromagnetism, strong nuclear force, and weak nuclear force. The last piece of the
₇₂₈ SM is the Higgs Boson, the conjectured cause of elementary particle masses, and was triumphantly
₇₂₉ discovered in 2012 at the Large Hadron Collider (LHC) - a 27 km long circular particle accelerator
₇₃₀ and multi-billion dollar project. This is the largest machine ever built by mankind, and because of
₇₃₁ the scale and technology required, the SM Higgs Boson prediction and its discovery almost 50 years
₇₃₂ later remains one of the greatest intellectual accomplishments of humanity. For almost 60 years, the
₇₃₃ SM has proven to be robust in its agreement with data and has remained the best explanation of
₇₃₄ elementary particles and their interactions.

₇₃₅ However, modern cosmology has completely broken our understanding of particle physics. Through
₇₃₆ detailed astrophysical measurements, it has been shown that the universe contains an invisible type
₇₃₇ of matter that the SM fails to account for. Not only that, this invisible matter makes up about 85%
₇₃₈ of the total matter in the universe which dramatically shows the scale in which the SM is incorrect.
₇₃₉ This invisible matter is often referred to as “dark matter” due to its lack of interactions with light.

₇₄₀ The concept of dark matter actually dates back well before the advent of the SM to Lord Kelvin
₇₄₁ in 1884 where he established a relationship between the size of the Milky Way Galaxy and the
₇₄₂ velocity dispersion of its stars by modeling stars as gaseous particles under the influence of gravity.
₇₄₃ Using this dynamical model, he reported evidence of additional unobservable matter and concluded
₇₄₄ that many of the stars could be “dark bodies” [66]. Intrigued by this idea, Henri Poincaré applied
₇₄₅ Lord Kelvin’s idea to the Milky Way, but disagreed with Lord Kelvin’s general conclusions. Though
₇₄₆ Poincaré coined the term “matière obscure” (French for dark matter), he remained uncertain and
₇₄₇ concluded that there could be only as much missing matter as observable stellar matter [78]. Fritz

748 Zwicky extended this idea by applying the virial theorem to the Coma Cluster and showed evidence
 749 for extra-galactic missing matter that he called “dunkle Materie” [86]. It wasn’t until Vera Rubin’s
 750 measurements of galactic rotation curves in the 1970s that modern cosmologists and particle physi-
 751 cists began to understand the scale of the missing matter problem more quantitatively and precisely
 752 and as a result, slowly began to take the idea of dark matter seriously. A compelling case for dark
 753 matter with modern evidence will be constructed in more detail in Chapter 2.

754 The nature of dark matter is also linked to its origin, and there is a high probability that
 755 there is some interaction, at least indirect interaction, with SM particles that can be exploited to
 756 search for dark matter in the laboratory - either with accelerator experiments or so-called direct
 757 detection experiments. In fact, for a simple mechanism of thermal equilibrium, where collisions
 758 between dark matter particles annihilate into SM particles and vice-versa, the amount of dark
 759 matter remaining, called the “relic abundance”, is directly related to its annihilation cross-section.
 760 When one computes the expected mass and cross-section from such a mechanism, it gives rise to
 761 a remarkable coincidence in which the particle responsible for dark matter can have a mass and
 762 coupling similar to the SM weak-sector particles (W , Z , and Higgs Bosons) and achieve the correct
 763 relic abundance. These hypothetical particles are called for Weakly Interacting Massive Particles
 764 (WIMPs) and this coincidence is so extraordinary, that it is referred to as the “WIMP Miracle” and
 765 provides compelling motivation to search for a stable object on the weak scale through both direct
 766 detection experiments and at accelerators.

767 To date of publication, WIMPs have not been discovered and the accessible parameter space will
 768 be probed with next generation direct detection experiments. As an alternative, it is reasonable
 769 to complement these searches on the mass scale where known stable SM particles exist, such as
 770 electrons and protons. However at this mass scale, the MeV-GeV mass scale (or sub-GeV), the
 771 simplest mechanisms of thermal equilibrium mediated by SM bosons in the early universe gives an
 772 overproduction of dark matter, greater than the observed 85%. That is, assuming these SM-dark
 773 matter interactions are mediated by SM forces, once the mass scale is below the so-called “Lee-
 774 Weinberg Bound” at 2 GeV, dark matter with a thermal origin always overproduces the observed
 775 relic abundance. In order to circumvent this bound, dark matter models on the sub-GeV scale called
 776 “light dark matter” require at least one additional comparably light mediator. One such natural
 777 candidate is called a heavy photon (or dark photon or A').

778 First considered by Bob Holdom in the 1985, heavy photons arise as the massive mediator from
 779 a model comprised of an additional $U(1)$ symmetry in nature [61]. This model was given new life
 780 by the results of the PAMELA satellite in 2008 that reported an excess in the flux of cosmic ray
 781 positrons originating from the center of the Milky Way Galaxy [10] and was explained by Arkani-
 782 Hamed as dark matter annihilations through a heavy photon mediator [21]. ¹ In this model, heavy

¹Though dark matter annihilations have been ruled out as an explanation the observed anomaly of by PAMELA, heavy photons are still strongly motivated by a variety of models of sub-GeV dark matter as a way to circumvent the Lee-Weinberg bound as well as a variety of other anomalies discussed in Sec. 2.4.

783 photons act like a bridge, or “vector portal”, in which dark matter and SM can indirectly interact
784 in highly dense and energetic regions such as the galactic center and the early universe. In order
785 to probe heavy photons in the parameter space most relevant to dark matter at accelerator-based
786 experiments, Bjorken, Essig, Schuster, and Toro (B.E.S.T.) developed a variety of clever strategies
787 using colliders, beam dumps, and fixed target experiments based on potential signatures of heavy
788 photons [34]. The two main signatures of a heavy photon that can be used as methods of discovery
789 are through a sharp resonance peak in the invariant mass spectra of its daughter particles or, since
790 heavy photons with small couplings can have a finite livetime, searches for secondary vertices are
791 possible. A variety of existing experiments, including both colliders and beam dump experiments,
792 could easily probe large regions of theoretically-favored heavy photon parameter space.

793 However, several models of sub-GeV dark matter highly motivate a region of heavy photon
794 parameter space in which heavy photons have both a low production cross-section and short decay
795 length (on the scale of mm-cm), proving impossible to probe for existing experiments. Probing the
796 short decay lengths of heavy photons on the scale of \sim 1 - 10 cm is the main goal of the Heavy
797 Photon Search Experiment - a precision vertexing fixed target experiment at Jefferson Laboratory.
798 Probing short decay lengths introduces a variety of technical challenges. For instance, the HPS
799 particle tracker must balance the detector acceptance of the highly boosted heavy photons with
800 excellent mm-scale vertex resolution. As a result, the most sensitive detector material (silicon from
801 the tracker) is placed at an unprecedented 500 μ m from the beam plane. Positioning the silicon any
802 closer will result in significant radiation damage to the silicon sensors from a very intense electron
803 beam, while a more conservative placement will render this type of search infeasible. In addition,
804 because of the small production cross-section and large background rates, the analysis will require
805 a separation of $\sim 10^8$ prompt (i.e. processes that originate from the target) SM processes from a
806 small number of true long-lived heavy photons - a critical but challenging task.

807 From HPS and a few other “flagship” experiments specifically designed to search for heavy
808 photons, the field known as “dark sectors” (i.e. the set of particles belonging to dark matter)
809 was born. Over the course of the past decade, dark sector models have become more generalized
810 extending beyond the simple vector portal from heavy photons to a limited set of additional portals
811 (such as Higgs-like, axion-like, and neutrino-like portals) in which the dark sector can indirectly
812 interact with SM particles. These models also allow arbitrary complex structure and interactions
813 amongst particles in the dark sector much like the matter and interactions in the SM sector.

814 Probing short-lived heavy photons through a precision vertexing experiment is the subject of this
815 dissertation and I place emphasis on the method and results of the displaced vertex search for the
816 2016 Engineering Run for HPS. The remainder of this dissertation details the motivations and theory
817 of heavy photons, detector and experimental setup, physics reconstruction process, displaced vertex
818 analysis and results, and future of HPS including generalized displaced vertices and projections of
819 the latest dataset.

STANDARD MODEL OF ELEMENTARY PARTICLES

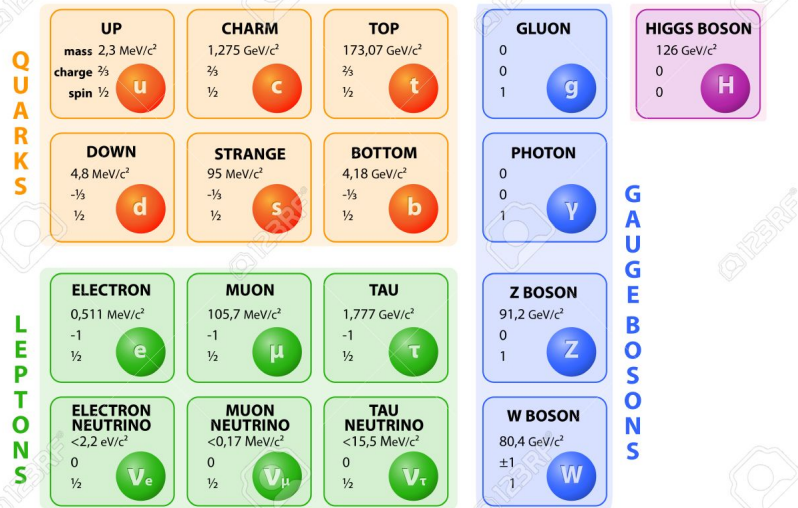


Figure 1.1: The Standard Model of Particle Physics is a group of the known elementary particles which is composed of six quarks, six leptons, four gauge bosons (which are responsible for the three fundamental forces), and the Higgs Boson (which is the origin of mass of many of the fundamental particles). **Find a picture without a watermark**

820 **Chapter 2**

821 **Motivation**

822 The Standard Model of Particle Physics (SM) has remained the best description of elementary parti-
823 cles and their interactions since its formulation. However, there are several observations, particularly
824 measurements from cosmology, that show that the Standard Model is incomplete.

825 **2.1 Observations**

826 The modern evidence for invisible matter beyond the SM stems mainly from galactic rotation curves,
827 weak gravitational lensing, the cosmic microwave background (CMB), big bang nucleosynthesis
828 (BBN), and type 1a supernovae.

829 **2.1.1 Galactic Rotation Curves**

830 The first modern evidence for invisible matter comes from Vera Rubin's measurements of galactic
831 rotation curves (i.e. the velocity at which stars orbit their galactic center) in the 1970s. Based
832 on kinematics and the gravitational inverse square law, in the absence of invisible matter, one
833 expects the speed at which stars orbit their galactic center to scale with the the distance from the
834 center r as $1/\sqrt{r}$. However, Vera Rubin's measurements show that these velocities were flat with
835 increasing r even for stars far away from the galactic center [80]. This discrepancy between theory
836 and measurements can be explained by the presence of matter that cannot be visibly detected. This
837 effect is shown in Fig. 2.1.

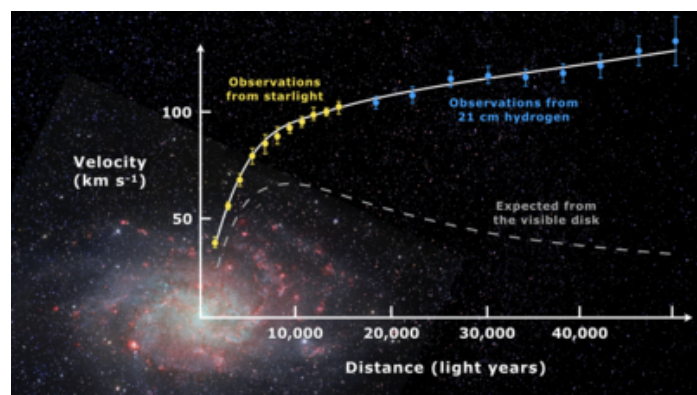


Figure 2.1: Galactic rotation curves show stars far from the galactic center are orbiting the galactic center far faster than they should gives evidence for invisible matter.

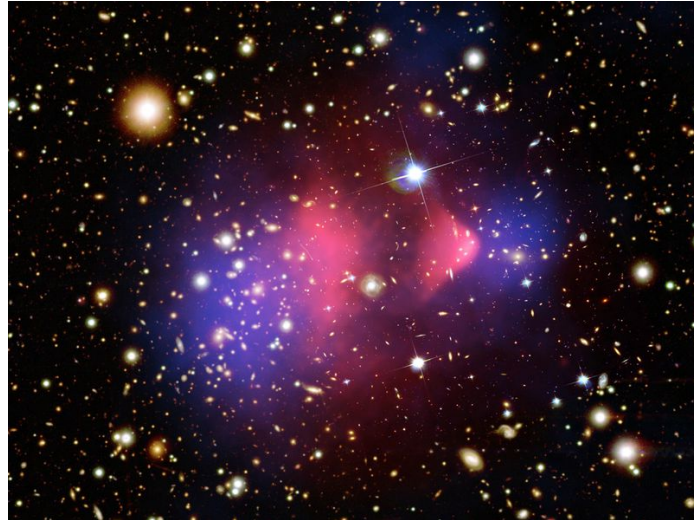


Figure 2.2: The Bullet Cluster shows visible matter from X-rays (highlighted in blue) and total matter from gravitational lensing (highlighted in pink).

838 2.1.2 Weak Gravitational Lensing

839 One could suppose that, since no independent tests of gravity are applied at the galactic scale,
840 gravity could simply be poorly understood at this scale. This is a possibility, in fact throughout the
841 history of astronomy, there is often the tension between a new theory of gravity and the presence of
842 some form of unseen matter as a resolution to an anomaly.

843 However, in addition to galactic rotation curves, measurements from gravitational lensing - the
844 bending of light in the presence of matter - provide evidence for invisible matter that cannot be
845 accounted for by the SM. The measurement the bending of light originating from distant galaxies
846 provides a measurement of the total mass in large regions of galactic clusters. This can be compared
847 with the distribution of X-rays from colliding galactic clusters, which is thought to be proportional
848 to the distribution of visible matter in the galactic cluster. In a measurement of two colliding
849 galactic clusters known as the Bullet Cluster shown in Fig. 2.2, the distribution of visible matter
850 from X-ray measurements (reconstructed in pink) does not agree with the distribution of the total
851 amount of matter as inferred from weak gravitational lensing (reconstructed in blue) [43]. This is
852 clear indication that there is invisible matter located within the Bullet Cluster that is non-baryonic
853 and cannot be accounted for by a different theory of gravity.

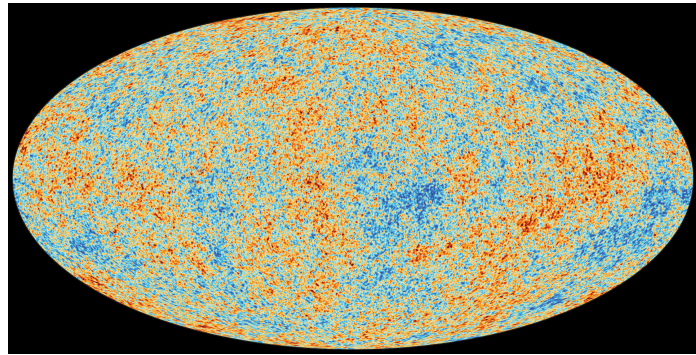


Figure 2.3: The Cosmic Microwave Background has temperature fluctuations consistent with extra invisible matter in the early universe.

854 2.1.3 Cosmic Microwave Background

855 The existence of invisible matter, or dark matter, is supported by the anomalies of both galac-
856 tic rotation curves and gravitational lensing. However, these evidences alone do not rule out the
857 possibility of a SM explanation of this invisible matter, or being particulate in nature at all. For
858 instance, black holes are a possible form of a non-particulate invisible matter that involves neither
859 new particles beyond the SM or a particle nature of dark matter. Despite this, there are several
860 other pieces of evidence that extend the case for dark matter.

861 The cosmic microwave background (CMB), the thermal “afterglow” of the Hot Big Bang, shows
862 evidence for invisible matter in the early universe that cannot be explained by the SM shown in
863 the bottom of Fig. 2.3. Specifically, the correlations in the temperature fluctuations in the CMB
864 spectrum, called CMB anisotropies, provide a measurement of sound waves in the early universe
865 (called baryon acoustic oscillations, or simple BAO). This provides a quantitative measurement of
866 both the amount of total matter and the amount of baryonic matter in the early universe. Of the
867 total matter in the early universe, precision BAO measurements gives about $\sim 15\%$ baryonic matter
868 (which is representative of the total SM matter in the early universe) and 85% of an additional type
869 of matter. This matter discrepancy is in agreement with the anomalies described by the galactic
870 rotation curves and gravitational lensing suggesting that the same invisible matter that is observed
871 in the universe today is the same type of invisible matter that existed in the early universe. John
872 says I lump BAO and CMB together. I always thought these were one in the same. If not, I could
873 use some guidance for their distinction.

874 This does not explicitly rule out the possibility of primordial black holes, that is those that
875 existed and were formed in the early universe. (Is this true? I remember hearing this at a talk
876 somewhere, I could use a source.). However, these are not favored because they require unnatural
877 fine tuning to get the models to produce observed results are do not explain the next anomaly - the
878 upper bound on baryonic matter set by Big Bang Nucleosynthesis.

879 2.1.4 Big Bang Nucleosynthesis and Type 1a Supernovae

880 Measurements from Type 1a Supernovae, known as a “standard candle” because of their well-defined
 881 and easily identifiable light curves, provide a measurement of the total matter in the universe. In
 882 the framework of the Λ CDM Model, a comparison of the redshift and luminosity of these supernovae
 883 gives a measurement of 30% matter of the total energy budget of the universe which is in agreement
 884 with CMB measurements [18].¹

885 On the other hand, Big Bang Nucleosynthesis (BBN), the description of production of hydrogen,
 886 deuterium, helium, and lithium nuclei in the early universe, constrains the current observed density
 887 of these nuclei with the primordial nucleon density. The observed density of all these nuclei are in
 888 agreement if the relative density of primordial baryonic matter in the universe is $<\sim 5\%$ ($\Omega_b <\sim 0.05$)
 889 [81]. This is far below the total mass measurement from Type 1a Supernovae at 30% suggesting much
 890 of matter in the universe is non-baryonic, and hence beyond the SM. The measurements from Type
 891 1a Supernovae and BBN are shown in Fig. 2.4

892 2.1.5 Some Properties of Dark Matter

893 From these measurements, one can constrain the properties of this missing matter. Any potential
 894 explanation of this missing matter must account for the following.

- 895 1. Since it has evading all detection mechanisms other than gravitational effects thus far, this
 896 missing matter is invisible and does not interact appreciably with SM photons. Hence, the
 897 common term for this matter is “dark matter.”
- 898 2. Measurements of the amount of dark matter from the early universe, particularly from the
 899 CMB, agree with present measurements. This indicates that dark matter is stable with a
 900 livetime far greater than the 13.8 billion year age of the universe.
- 901 3. Measurements from different regions of the universe are consistent with the idea of missing
 902 matter. This, together with the Cosmological Principle, provides compelling evidence that
 903 dark matter is present everywhere in the universe, including here on Earth.
- 904 4. The density of dark matter in the universe is similar to the density of SM matter (i.e. they
 905 have the same order of magnitude). A natural explanation for this coincidence is that there is
 906 some interaction, even indirect, between dark matter and SM matter in the early universe that
 907 connects their origins. This is the basis for the concept of “thermal dark matter” in which dark
 908 matter and SM matter were in thermal equilibrium in first few nanoseconds of the universe
 909 **How long is DM actually in thermal equilibrium? I don't know where I got nanoseconds from..**

¹The Λ CDM Model (dark energy and cold dark matter) is the standard model of cosmology built on the framework of General Relativity. Dark energy is the energy responsible for the accelerated expansion of the universe as measured by the Type 1a Supernovae and CMB. The fundamental nature and origin of dark energy is also a mystery and will not be discussed further.

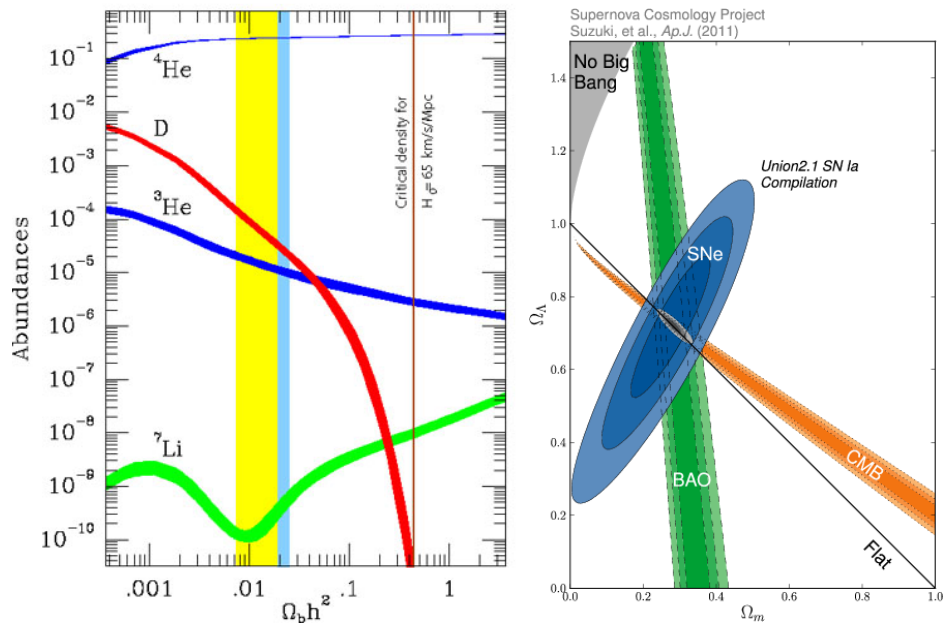


Figure 2.4: Left: Big Bang Nucleosynthesis puts an upper bound on the Standard Model matter density in the universe at about 15% of the total energy budget [81]. Right: Measurements from Type 1a supernovae (shaded in blue) together with the CMB and BAO measurements put the total mass in the universe at 30% of the total energy budget along with dark energy at 70% (from the intersection in gray) [18]. A combination of these measurements show that the Standard Model cannot account for most of the matter in the universe.

910 These measurements, specifically the CMB and Type 1a Supernovae measurements, together
911 with the Λ CDM Model also provide a quantitative breakdown of the energy budget of the universe.
912 Matter itself only composes about 30% ($\Omega_m = 30\%$) of the energy budget. The remaining 70% is
913 due to dark energy ($\Omega_\Lambda = 70\%$). Within the matter budget, dark matter comprises about 85% of
914 the total mass ($\Omega_{DM} = 26\%$) while SM matter, which includes our everyday atoms and molecules,
915 comprises only 15% of the total mass in the universe ($\Omega_{SM} = 4\%$). Furthermore, any model of
916 dark matter must respect this observed value of Ω_{DM} called the “relic density” (any model that
917 overproduces dark matter can be immediately ruled out).

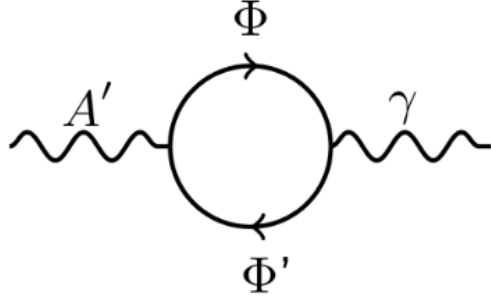


Figure 2.5: A one-loop kinetic mixing process where an A' mixes with the SM photon through an interaction of massive fields that couple to both photons.

918 2.2 Theory Summary

919 Heavy photons appear in dark matter models carrying forces between dark matter particles as well
 920 as providing indirect interactions with SM matter, and detailed motivations for dark matter with
 921 a heavy photon hypothesis will be described in detail in Sec. 2.3 and Sec. 2.4. But first, it is
 922 important to understand the basics of heavy photon formalism.

923 A theory that has gained interest over the past few years is that of an additional Abelian gauge
 924 symmetry $U'(1)$. This was first proposed by Holdom in 1985 and is the basic assumption behind the
 925 existence of a heavy photon where the additional broken symmetry interacts with the SM hyper-
 926 charge via kinetic mixing [61]. Suppose nature does contain this additional Abelian gauge symmetry
 927 $U'(1)$ which contains a massive gauge boson A' . This would produce the following Lagrangian:

$$\mathcal{L} = \mathcal{L}_{SM} + \frac{1}{4} F'^{\mu\nu} F'_{\mu\nu} + m_{A'}^2 A'^{\mu} A'_{\mu} + \epsilon F^{\mu\nu} F'_{\mu\nu} \quad (2.1)$$

928 where \mathcal{L}_{SM} is the Standard Model Lagrangian, $F_{\mu\nu}$ is the electromagnetic field strength, $F'_{\mu\nu} =$
 929 $\partial_{\mu} A'_{\nu} - \partial_{\nu} A'_{\mu}$ is the heavy photon field strength tensor (SM hypercharge), and ϵ is a dimensionless
 930 coupling constant also called the kinetic mixing parameter. This additional symmetry gives rise
 931 to a kinetic mixing term $\epsilon F^{\mu\nu} F'_{\mu\nu}$ with ϵ as the kinetic mixing parameter where the Standard
 932 Model photon mixes with the a new gauge boson, an A' , through an interactions of massive fields
 933 M_{Φ} and $M_{\Phi'}$ as shown in Fig 2.5. These intermediate particles could be massive far above the
 934 Supersymmetry-breaking scale, but the kinetic mixing will persist down to much lower mass scales.
 935 Due to kinetic mixing, the fields are non-orthogonal, but orthogonality can be restored by redefining
 936 the electromagnetic field as $A^{\mu} \rightarrow A^{\mu} + \epsilon A'^{\mu}$. By removing all the resulting ϵ^2 terms, this diagonalizes
 937 the gauge terms in the Lagrangian in Eq. 2.1 as

$$\mathcal{L}_{gauge} = -\frac{1}{4} F'^{\mu\nu} F'_{\mu\nu} - \frac{1}{4} F^{\mu\nu} F_{\mu\nu} \quad (2.2)$$

938 The redefinition of the gauge field also changes the interaction term of the Lagrangian $\mathcal{L}_{int} =$
939 $A^\mu J_\mu^{EM}$ to

$$A^\mu J_\mu^{EM} \rightarrow (A^\mu + \epsilon A'^\mu) J_\mu^{EM} \quad (2.3)$$

940 This induces an effective coupling between the heavy photon field and the electromagnetic current
941 that is proportional to a factor ϵ . Perturbativity requires $\epsilon < 1$, thus ϵ suppresses the effective charge.
942 One loop processes such as the one shown in Fig. 2.5 can be naturally generated by heavy multiplets
943 that are charged under both the SM electric charge and a dark charge (the charge resulting from
944 the new symmetry) [22] [34]. This process motivates ϵ to be in the range $\sim 10^{-2} - 10^{-4}$ and can be
945 related to several parameters by the following:

$$\epsilon \sim \frac{eg_D}{16\pi^2} \log\left(\frac{M_\Phi}{M_{\Phi'}}\right) \sim 10^{-2} - 10^{-4} \quad (2.4)$$

946 where e is the electric charge and g_D is the hypercharge dark coupling. If the theory does not
947 contain these additional particles that are charged under both $U(1)$ symmetries, additional loop
948 processes are possible and motivated by Grand Unification Theories (GUT) generally in the range
949 $\epsilon \sim 10^{-3} - 10^{-6}$ [22]. Finally, some versions of string theory motivate ϵ as low as 10^{-12} from Eq. 2.11
950 [54] [53] [42]. Models of light dark matter, where the dark matter mass is below the Lee-Wienberg
951 bound as described in Sec. 2.4, as well as certain models of supersymmetry motivate mass scales of
952 MeV-GeV. String theories connect ϵ to the mass scale resulting in a motivated mass region down to
953 the meV scale.

954 The existence of a new gauge boson arising from an additional massive $U'(1)$ symmetry that
955 can couple to charged SM particles leads to interesting possibilities. This idea has gained particular
956 interest as a potential way for an indirect coupling between SM fermions and a dark sector, that could
957 lead to a way to probe the possible structure of this dark sector. These heavy photon masses and
958 coupling ranges can be probed by both current and future experimental programs (including HPS)
959 and will provide insight on a variety of outstanding mysteries in particle physics and astrophysics
960 which are described in the following sections.

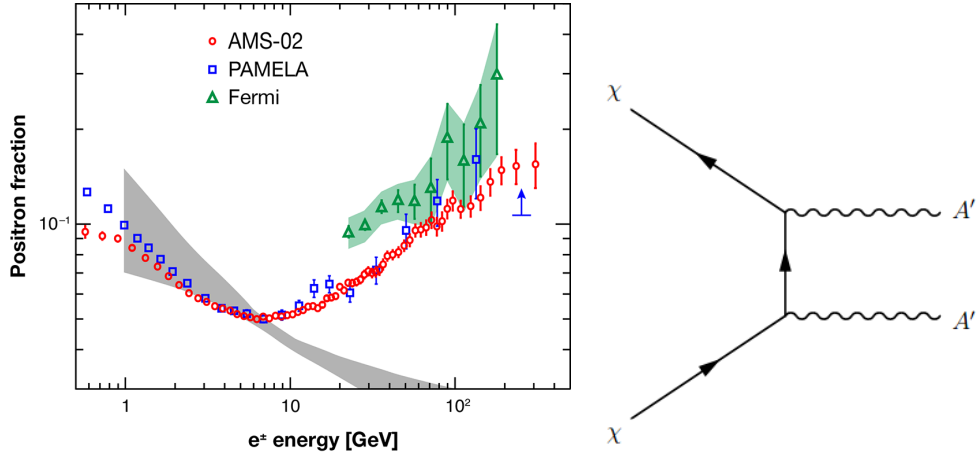


Figure 2.6: Left: The results from PAMELA, AMS, and Fermi-LAT showing the positron fraction excess (above the expected calculation from cosmic rays in grey) at above ~ 10 GeV [45]. Right: The Feynman diagram for the dark matter annihilation into two A' 's which subsequently decay into e^+e^- pairs. This provides an explanation for positron fraction excess. This explanation has since been disfavored.

2.3 Historical Motivations for A' 's

There are two specific historical anomalies that generated much interest in the heavy photon hypothesis among the communities of particle physicists and astrophysicists. In 2008, the Payload for Antimatter Matter Exploration and Light-nuclei Astrophysics (PAMELA) measured an anomalous excess of positron fraction $\phi(e^+)/(\phi(e^+) + \phi(e^-))$ above ~ 10 GeV that was inconsistent with the expectation from secondary production from cosmic-ray nuclei interactions with interstellar gas [10] [5]. Further measurements from the Fermi Large Area Telescope and the Alpha Magnetic Spectrometer (AMS) not only confirmed this anomaly, but extended it to even higher energies of ~ 200 GeV [13]. These measurements are shown in Fig. 2.6.

The implied annihilation cross-section from the observed positron fraction excess is larger than one would expect from a dark matter thermal relic ($\langle\sigma v\rangle \sim 3 \times 10^{-26} \text{ cm}^3 \text{s}^{-1}$). However, the scenario in which dark matter annihilation occurs through a heavy photon mediator shown in Fig. 2.6 is particularly appealing since a so-called ‘Sommerfeld enhancement’ can occur in which the cross-section is dependent on the inverse of velocity ($\langle\sigma v\rangle \sim 1/v$) [21]. Thus low-velocity interactions (e.g. dark matter collisions in the galactic halo) are enhanced while still preserving the dark matter freeze-out scenario (described in Sec. 2.4) with the observed dark matter relic abundance. In addition, this annihilation cross-section is much larger than observed for hadrons, which motivates heavy photons with $m_{A'} < 2m_p$ where decays to proton-antiproton pairs are kinematically forbidden. Thus, the MeV-GeV heavy photon mass range is highly motivated by both the Sommerfeld enhancement and observations of annihilation into hadrons.

981 This anomaly is now disfavored for several reasons. A larger AMS dataset shows softer positron
982 spectrum that is more consistent with a pulsar origin for cosmic ray positron excess than a heavy
983 photon interpretation; however, this does not exclude the possibility of heavy photons decaying into
984 intermediate states before an e^+e^- final state [41]. In addition, measurements by the Planck satellite
985 put strong constraints on the dark matter annihilation rate at recombination, thus making the heavy
986 photon explanation of the PAMELA anomaly unlikely [18] [7].

987 In addition to the positron cosmic ray excess, heavy photons were originally motivated by the
988 measurement of the magnetic momentum of muons ($a_\mu = (g - 2)/2$, or simply known as $g - 2$)
989 which deviates by more than 3 standard deviations away from the predicted value from the SM.
990 This can be explained by a contribution of the heavy photon to the muon magnetic moment for a
991 heavy photon within a certain range of parameter space shown in green in Fig. 6.15. In addition,
992 the excellent agreement between the corresponding magnetic moment of the electron and the SM
993 excludes the region in red. This favored region for a heavy photon explanation of the anomalous
994 magnetic moment of the muon has since been ruled out by several experiments both for visible and
995 invisible decays.

996 A heavy photon hypothesis for these two anomalies have since been ruled out. Even though
997 some of the original motivations for dark sector searches such as the anomalous positron excess from
998 PAMELA and the muon G-2 anomaly are no longer favored, motivations for searching for such a
999 particle remain particularly in models involving light dark matter.

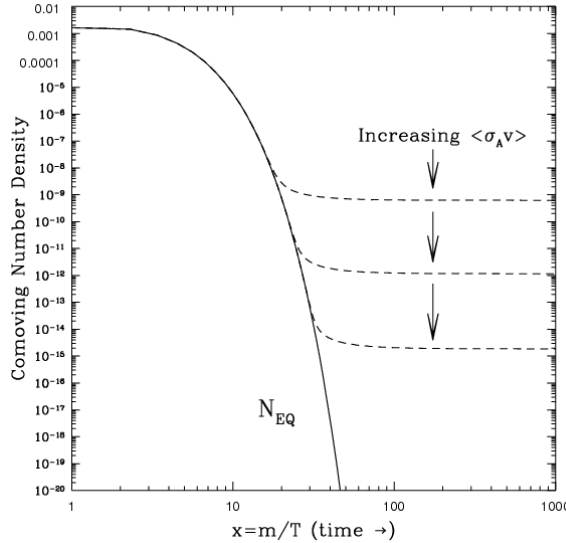


Figure 2.7: The mechanism of thermal freeze-out in which dark matter and SM matter are in thermal equilibrium in the early universe. As the universe cools (x -axis), the relic abundance of dark matter (y -axis) is depleted by self-annihilation until enough cooling occurs and the dark matter relic abundance is set.

2.4 Light Dark Matter

1001 **There are many references missing in this subsection.**

1002 Heavy photons are connected to a variety of models of light dark matter, that is dark matter
1003 on the MeV-GeV scale (or sub-GeV scale) where stable massive SM particles are known to exist, as
1004 well as self-interacting dark matter. In order to understand the potential connection between light
1005 dark matter and heavy photons, one must first understand the mechanisms of thermal dark matter
1006 and its connection to the amount of dark matter relic abundance. This connection is referred to
1007 as “thermal freeze-out” (which was alluded to in Chp. 1) and the simplest mechanism of thermal
1008 freeze-out as shown in Fig. 2.7 goes as follows.

- 1009 1. The whole universe began in a hot dense state with some amount of SM matter (Ω_{SM}) and
1010 some relic density of dark matter (Ω_{DM}) colliding in thermal equilibrium.
- 1011 2. Through an unspecified mechanism, dark matter particles annihilate with one another into
1012 SM particles and through the same mechanism SM also annihilate into dark matter particles.
1013 This occurs in thermal equilibrium. For simplicity, dark matter self-interactions are assumed
1014 to have no effect on this mechanism.
- 1015 3. Throughout this mechanism, the universe expands and cools which decreases the rate of dark
1016 matter-SM interactions. Eventually, the universe cools enough to stop the SM annihilation

1017 into dark matter particles; however, the dark matter annihilation into SM particles persists.
 1018 Thus, over this short time the amount of dark matter is continually depleted.

1019 4. As the universe continues to cool, eventually these dark matter annihilations stop as dark
 1020 matter completely decouples from the SM. At this point, the amount of dark matter called the
 1021 “relic abundance” is set at a fixed value. Measurements from a variety of astrophysical sources
 1022 described in Sec. 2.1 put the relative relic abundance $\Omega_{DM} = 85\%$ of the total matter in the
 1023 universe. In addition, there is an inverse relationship between the annihilation cross-section
 1024 and the relic abundance ($\langle\sigma v\rangle \propto \frac{1}{\Omega_{DM}}$) such that the larger the dark matter annihilation
 1025 cross-section the longer it will be in thermal equilibrium and the more it will be depleted.

1026 From the observed relic abundance (measurements from the CMB and Type 1a Supernovae),
 1027 using the inverse relationship the expected annihilation cross-section can be computed as $\langle\sigma v\rangle \sim$
 1028 $3 \times 10^{-26} \text{ cm}^3 \text{s}^{-1}$. In addition, the annihilation cross-section can be related to the dark matter
 1029 particle mass and the mass of mediator (such as the Z boson in this case) as follows:

$$\langle\sigma v\rangle \propto \frac{m_{DM}^2}{m_Z^4} \quad (2.5)$$

1030 One can solve for the dark matter particle mass and see that such a mechanism gives a mass
 1031 in the 100 GeV range. This mass scale and cross-section is typical and of what one would expect
 1032 from weak sector particles such as W bosons, Z bosons, or Higgs bosons providing a hint that
 1033 a dark matter particle could be a particle that interacts weakly with SM particles. These dark
 1034 matter candidates are named “Weakly Interacting Massive Particles” (WIMPs), and this mass and
 1035 cross-section computation is such a remarkable coincidence that this is famously referred to as the
 1036 “WIMP Miracle.” However, a major difference between WIMPs and weak-scale SM particles is that
 1037 WIMPs must be stable in order to be a dark matter candidate whereas weak-scale SM particles are
 1038 unstable. In addition, in order to resolve the hierarchy problem, models of Supersymmetry (SUSY)
 1039 were developed and many models described WIMP-like objects.

1040 Because of this, over the past few decades much of the focus of the particle physics and astro-
 1041 physics communities has been on both direct detection experiments and colliders such as the Large
 1042 Hadron Collider (LHC) searching for WIMP-like dark matter and SUSY on the ~ 100 GeV-scale.
 1043 However, to date of publication, neither WIMPs nor SUSY have been discovered and accessible pa-
 1044 rameter space for these models is shrinking. Specifically, direct detection experiments are approach-
 1045 ing the so-called neutrino floor where the direct detection of neutrino with the detector medium
 1046 become indistinguishable from dark matter recoils, thus searches of this type will no longer be pos-
 1047 sible, while the LHC will probe the most favorable models of SUSY within the next few years **How**
 1048 **do I make this claim more precise?**.

1049 As a way to complement the SUSY-WIMP dark matter searches, it is reasonable to search for
 1050 dark matter at the mass scale where known stable SM particles, such as electrons and protons,

1051 exist. If one naively computes the relic abundance of potential dark matter particles on the MeV
 1052 - GeV scale with an electroweak mediator using Eq. 2.5, the calculation results in an annihilation
 1053 cross-section far smaller than is expected from the simplest mechanisms of thermal equilibrium.
 1054 And because the annihilation cross-section is proportional to the inverse of the relic abundance, this
 1055 mass scale crosses the threshold of the so-called Lee-Weinberg bound at ~ 2 GeV such that dark
 1056 matter candidates below this bound will result in an overproduction of dark matter.² Of course, this
 1057 computation assumes only interactions mediated through SM bosons such as W bosons, Z bosons,
 1058 and Higgs bosons.

1059 As a way to circumvent the Lee-Weinberg bound, one could postulate an annihilation mechanism
 1060 through a new, comparably light mediator. This would provide another degree of freedom in Eq. 2.5
 1061 and allow for this simple mechanism to produce the observed dark matter relic abundance. Thus, any
 1062 thermal dark matter model on the MeV-GeV scale, called “light dark matter”, requires an additional
 1063 boson beyond the SM. A heavy photon is a simple and natural candidate that could mediate dark
 1064 matter annihilations in the early universe much like PAMELA’s observed positron cosmic ray excess
 1065 was explained (though collisions in the galactic halo occur at an enhanced rate because of the
 1066 Sommerfeld enhancement). Beyond this simple mechanism, heavy photons are connected with more
 1067 complicated models of dark matter that allow for more complex structure and interactions within
 1068 the so-called “dark sector” - the sector of all particles responsible for the 85% of dark matter. Due
 1069 to the kinetic mixing between the heavy photon and the SM photon, heavy photons would provide
 1070 an indirect mechanism to probe the particles and interactions in this dark sector. This mechanism
 1071 is also called a “vector portal.”

1072 In addition to mechanisms of thermal dark matter and a vector portal, heavy photons are often
 1073 motivated by a variety of self-interacting dark matter where dark sector particles are allowed to
 1074 interact with other dark sector particles.³ Excesses in both gamma ray and X-ray spectra can
 1075 provide hints of dark matter self-interactions potentially mediated by heavy photons. The Fermi-
 1076 LAT telescope has observed an extended emission in the gamma ray spectrum originating from
 1077 the galactic center. There are several models that explain this including pulsars, energetic protons
 1078 accelerated by a super-massive black hole, and dark matter annihilations into SM particles. The dark
 1079 matter annihilation can be explained through a heavy photon model, much like what was explained
 1080 for the original observed positron fraction anomaly by PAMELA. An excess in the X-ray spectra at
 1081 3.5 keV from several galaxy clusters has been explained in a model called “eXciting Dark Matter”
 1082 (XDM). In this model, self-interacting dark matter can collide via a heavy photon and excite dark
 1083 matter ($\chi^* \chi^*$) and its subsequent de-excitation emits an observable 3.5 keV X-ray ($\chi^* \rightarrow \chi\gamma$).

1084 Along the same lines of self-interacting dark matter, collisionless dark matter has historically

²When computing any mechanism of thermal origins of dark matter, and overproduction above the observed relic abundance is never allowed. However, an underproduction of dark matter is allowed since another mechanism can compensate the remaining dark matter relic abundance.

³These dark matter self-interaction can be mediated by heavy photons or by other additional mediators in the dark sector. In contrast, the minimal WIMP model does not allow for additional self-interactions.

1085 failed to account for detailed simulations of dark matter of galactic halos. Often these problems
 1086 can be resolved by self-interacting dark matter with a velocity-dependent cross-section which is
 1087 consistent with a heavy photon hypothesis which would otherwise be constrained by high-velocity
 1088 collisions such as the Bullet Cluster shown in Fig. 2.3 [74].

1089 For instance, there are observations in which Milky Way dwarf satellite galaxies have smaller
 1090 rotational velocities than predicted by these simulations for dark matter subhalos. This is called
 1091 the “too big to fail” problem and it suggests that the rotational velocities are actually smaller
 1092 than predicted, these massive subhalos fail to create these dwarf galaxies, or these massive subhalos
 1093 simply do not exist. Self-interacting dark matter provides a solution via the first possibility as it can
 1094 naturally reduce the central densities of subhalos (and hence reducing their rotational velocities). In
 1095 addition, collisionless dark matter fails to resolve the so-called “cusp-core problem” in
 1096 which the observed matter density profiles of galaxies are better modeled with a constant density core
 1097 from self-interacting dark matter than models from collisionless dark matter. There are, however,
 1098 other explanations of these phenomena that do not involve self-interacting dark matter such as
 1099 baryonic outflows in galaxies that may also produce similar cored distributions by transferring energy
 1100 to dark matter. As these simulations develop and improve over time, these conflicts of collisionless
 1101 dark matter may be resolved. **Is this still true?**

1102 **Also, what A' parameters motivate self-interacting DM in observed galactic halos? John and I
 1103 want to know**

1104 The Experiment to Detect the Global EoR Signature (EDGES) observed a strong absorption
 1105 profile of 21 cm hydrogen [50]. This indicates that hydrogen gas is colder than expected from
 1106 standard cosmological conditions. One possible explanation is dark matter on the ~ 10 MeV scale
 1107 scattering with SM matter through an A' mediator during the first stellar formation (the cosmic
 1108 dawn).

1109 Finally, heavy photons are motivated as an explanation of an anomaly from nuclear physics in
 1110 which a significant excess was observed in the angular spectrum for the internal pair creation for an
 1111 excited state to ground state transition of Be8 nuclei [71]. This was interpreted as a new protophobic
 1112 (a different coupling to different quark flavors) boson at called “X17” [49]. A similar anomaly was
 1113 found by the same group for He3 nuclei which could be explained by the same hypothetical boson
 1114 [70]. However, recent results from NA64 at CERN have taken a large portion of parameter space
 1115 out of this though have not completely ruled it out yet [27].

1116 **Should Be8 go in its own subsection?**

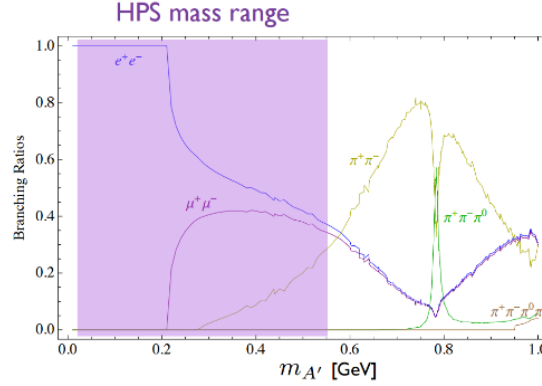


Figure 2.8: The branching ratio for heavy photon decays to SM particles as a function of mass. This assumes no decays into dark sector particles.

1117 2.5 Signatures of A's

1118 According to the minimal heavy photon model, kinetic mixing is the only coupling to the SM. One
 1119 can also assume decays to dark sector particles are forbidden (i.e. $2m_d > m_{A'}$), thus the focus
 1120 will be on visible decays (i.e. SM particles).⁴ Under this assumption, the branching ratio of heavy
 1121 photon decays to visibles as a function of mass in the MeV-GeV range is shown in Fig. 2.8 which
 1122 are derived by the ratio of cross sections as a function of center-of-mass energy for different final
 1123 states of e^+e^- interactions.

1124 The heavy photon decay width is given by:

$$\Gamma = \frac{N_{eff} m_{A'} \alpha \epsilon^2}{3} \quad (2.6)$$

1125 where $N_{eff} = 2 + R(m_{A'})$ and the function $R(Q)$ is given by

$$R(Q) = \frac{\sigma(e^+e^- \rightarrow \text{hadrons}, Q)}{\sigma(e^+e^- \rightarrow \mu^+\mu^-, Q)} \quad (2.7)$$

1126 For $m_{A'} < 2m_\mu$, $N_{eff} = 1$ since the only kinematically allowed SM decay is to e^+e^- pairs.⁵
 1127 Since the fractional decay width $\Gamma/m_{A'}$ is proportional to $\alpha \epsilon^2$, the small ϵ^2 will result in a very
 1128 narrow decay width, and the heavy photon will appear as a sharp resonance.

1129 The corresponding product of livetime and the speed of light (the $c\tau$ value) is related to the
 1130 inverse of the decay width in Eq. 2.6 by:

⁴If one relaxes this assumption, the possible decay scenarios become more complicated. Decays to invisible particles become possible and searches for missing mass or missing momentum must be performed.

⁵This is true for most of the parameter space covered by HPS, though the mass range at higher beam energies for HPS does cross the dimuon threshold.

$$c\tau = \frac{\hbar c}{\Gamma} = \frac{3\hbar c}{N_{eff} m_{A'} \alpha \epsilon^2} \quad (2.8)$$

1131 The decay length in the laboratory frame is related to $c\tau$ value by a factor of relativistic γ but is
 1132 not universal as it will depend on the type of experiment (e.g. fixed target experiment vs. a collider
 1133 experiment). But, for sufficiently small ϵ , the decay length becomes measureable by both experiments
 1134 with excellent vertex resolution (typically fixed target experiments, but sometimes colliders as well)
 1135 and beam dump experiments.

1136 Finally, the rate of heavy photon production is directly proportional to the corresponding process
 1137 for virtual photons at a given heavy photon mass. Thus, there exist an irreducible background with
 1138 identical kinematics for a given heavy photon production. The only directly distinguishable feature
 1139 is the fact that the heavy photon is on-shell and can have a finite, and hence measureable, livetime.
 1140 The ratio of the A' differential cross-section for a given $m_{A'}$ and ϵ to the cross-section of the
 1141 corresponding virtual photon process integrated over the narrow mass range $m_{A'} \pm \frac{\delta m}{2}$ is given by
 1142 [34]:

$$\frac{d\sigma(X \rightarrow A'Y \rightarrow ZY)}{d\sigma(X \rightarrow \gamma^*Y \rightarrow ZY)} = \left(\frac{3\pi\epsilon^2}{2N_{eff}\alpha} \right) \left(\frac{m_{A'}}{\delta m} \right) \quad (2.9)$$

1143 The specific virtual photon process related to HPS is discussed in more detail Sec. 2.8. If an
 1144 experiment can directly measure the rate of the corresponding virtual photon process, the expected
 1145 rate of heavy photon production can be normalized in a data-driven way.

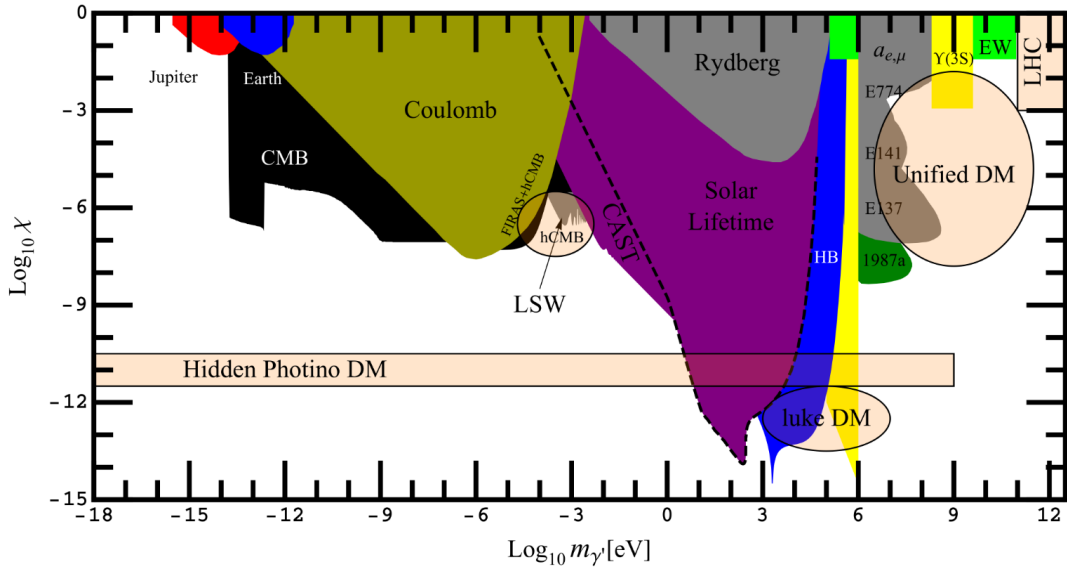


Figure 2.9: Existing constraints of heavy photons on the whole parameter space [64]. The constraints come from a variety of sources including astrophysical measurements, precision QED, and particle accelerator-based experiments. The regional labeled “unified DM” is of particular interest to dark matter for reasons described in Sec. 2.4 and Sec. 2.3 and will be the focus. Note that the notation on this plot is such that $\epsilon \rightarrow \chi$ and A' is denoted as γ' .

2.6 Overview of Searches

The parameter space for heavy photons is large, and current heavy photon constraints from various astrophysics measurement, precision QED, and accelerator-based experiments are summarized in Fig. 2.9 [64]. There is a much narrower region of partially unexplored parameter-spaced that is theoretically favorable with sub-GeV dark matter models. This parameter space is typically probed by accelerator-based experiments in which a beam of high energy particles (e.g. electron, protons, etc.) are collided with material or another beam in order to produce heavy photons.

The common production methods are through dark bremsstrahlung ($e^- Z \rightarrow e^- ZA'$), Drell-Yan ($q\bar{q} \rightarrow \gamma A'$), e^+e^- annihilation ($e^+e^- \rightarrow \gamma A'$), and meson decays (such as $\pi^0 \rightarrow \gamma A'$, $\eta \rightarrow \gamma A'$, $\phi \rightarrow \eta A'$). Once heavy photons are produced, experiments are designed and built to detect heavy photons often by measuring their decay products. Common detection signatures include a mass resonance of the SM decay products, missing mass or momentum (heavy photons decay to dark sector particles and cannot be detected directly), and displaced vertices from long-lived heavy photons.

Different types of experiments and facilities are designed to utilize these production and detection methods. These include complementary searches from colliders, thin fixed targets, and beam dumps from facilities that utilize proton beams, ion beams, electron beams, and positron beams. In general, fixed targets and beam dump experiments are higher luminosity and able to probe smaller ϵ while

1163 colliders with a high center-of-mass energy can probe larger masses.

1164 2.6.1 Colliders

1165 Searches for heavy photons at colliders mostly come from flavor factories that produce heavy photons
1166 through meson decays, but also through e^+e^- annihilation, Drell-Yan, and even displaced vertices.

1167 Among the experiments that utilize high-luminosity e^+e^- colliders to search for heavy photons
1168 are BaBar, KLOE and KLOE-II, and Belle-II. Each of these experiments were run at different
1169 center-of-mass energies and thus searched at complementary masses. BaBar was run at the PEP-II
1170 B-Factory at SLAC and heavy photon searches were performed using upsilon decays ($\Upsilon \rightarrow \gamma A'$)
1171 and then heavy photon decays into $\mu^+\mu^-$ final states [23]. In addition to visible final states, BaBar
1172 has search for heavy photon decays into invisibles [72]. In the future, Belle-II will also be able to
1173 search for invisible decays and is projected to improve upon the results from BaBar [77]. KLOE and
1174 KLOE-II were run at the DAΦNE ϕ factory and search for *phi* meson decays ($\phi \rightarrow \eta A'$) and then
1175 heavy photon decays into e^+e^- and $\mu^+\mu^-$ final states as well as dipion decays [24] [20] [73].

1176 Proton colliders such as the Large Hadron Collider (LHC) at CERN which houses experiments
1177 such as ATLAS [1], CMS [40], and LHCb can search for meson decays and forms of “dark showering”.
1178 Since these experiments are run at a higher center-of-mass energy than any other current experiment,
1179 these experiments can probe the largest A' mass space.

1180 Specifically, for heavy photon masses below the dimuon threshold LHCb can search for heavy
1181 photons in the $D^* \rightarrow D^0 A'$ channel decays into e^+e^- final states [63] [62] [2]. For heavy photon
1182 masses above the dimuon threshold, LHCb can search for heavy photon decays into a $\mu^+\mu^-$ final
1183 state. In addition, LHCb can perform a displaced vertex search for η decays in a heavy photon and
1184 ($\eta \rightarrow \gamma A'$) then for a long-lived heavy photon that decays into a $\mu^+\mu^-$ final state. Future upgrades
1185 to LHCb, specifically a trigger-less readout that allows for online reconstruction, will enable a search
1186 for displaced vertices with an e^+e^- final state with projected sensitivity competitive with the HPS
1187 displaced vertex search.

1188 Lower energy proton colliders such as WASA at COSY searched for neutral pion decays into
1189 heavy photons ($\pi_0 \rightarrow \gamma A'$) and heavy photon decays into e^+e^- final states. PHENIX at the
1190 Relativistic Heavy Ion Collider (RHIC) at Brookhaven uses both proton-proton and deuterium-
1191 gold nuclei ($d+Au$) collisions to produce neutral mesons that decay into heavy photons ($\pi_0 \rightarrow \gamma A'$
1192 and $\eta \rightarrow \gamma A'$) which then decay into e^+e^- final states [6].

1193 2.6.2 Beam Dumps

1194 As previously stated, heavy photons with sufficiently small couplings will be long-lived. This prop-
1195 erty can be exploited by beam dump experiments where a high intensity electron or proton beam
1196 is “dumped” onto a thick target, and a search for heavy photon decays to visible particles can be
1197 performed. If the beam dump is sufficiently thick enough, this will filter all SM background and any

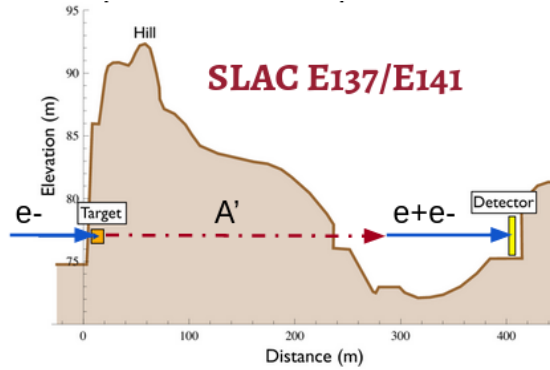


Figure 2.10: A schematic of beam dump experiments SLAC E137 and E141 which searched for long-lived particles that decay in a region several hundred meters from the target.

decay within a specific volume would be clear evidence for a new long-lived particle. Otherwise, the decay products must be reconstructed to measure their decay position to distinguish SM processes from potential new processes.

Several general-purpose electron beam dump experiments that were originally designed and run to search for axion-like and Higgs-like particles such as E137 and E141 at SLAC [33], E774 at Fermilab [38], KEK in Japan [68], and an experiment at Orsay reinterpreted previously taken data to show constraints for heavy photons [19]. NA64 is a recent electron beam dump at CERN [27]. These experiments produce heavy photons by dark bremmstrahlung, a process related to ordinary photon bremmstrahlung. Future electron beam dumps include the Beam Dump eXperiment (BDX) [29].

Similar constraints can be set from a proton beam dump experiment where heavy photons are produced by either the decay of neutral mesons produced at the target or proton bremsstrahlung such as the U70 accelerator. Future proton beam dump experiments include a SHiP at CERN [15] which is a general-purpose dark sector experiment, SeaQuest at Fermilab (soon to be SpinQuest or DarkQuest) which is typically used for nuclear physics experiments [52], and COHERENT at Oak Ridge [46]. Finally, several short-baseline neutrino experiments at Fermilab that utilize proton beam dumps such as MiniBooNe can search for heavy photons [14] [4].

2.6.3 Thin Fixed Target

Fixed target experiments are much like beam dump experiments; however unlike beam dump experiments, fixed target experiments are designed with a much thinner target to detect the decay products of relatively short-lived A' 's. As a result, fixed target experiments must have the ability to reconstruct vertices to distinguish the relatively short-lived A' 's from SM particles.

1220 Fixed target experiments utilize an electron beam to produce A' using the same dark bremm-
 1221 strahlung mechanism as beam dump experiments. A Prime EXperiment (APEX) is a fixed target
 1222 experiment at Jefferson Laboratory that uses an electron beam to detect the e^+e^- decay products
 1223 from an electro-produced heavy photon [48] [3]. It uses a septum magnet to separate e^+e^- pairs
 1224 into two calorimeters (HRS spectrometer in Hall A) whose measurements are used to compute the
 1225 invariant mass. In addition, the A1 spectrometer at the Mainz Microtron also searches for heavy
 1226 photon decays to e^+e^- pairs [76]. Several additional electron beam fixed target experiments are
 1227 planned including DarkLight using the Low-Energy Recirculator Facility at JLab and MAGIX at
 1228 the Mainz Energy-Recovering Superconducting Accelerator.

1229 Future experiments such as the Light Dark Matter eXperiment (LDMX) at SLAC search for
 1230 heavy photons through a production of dark bremmstrahlung and a subsequent decay into invisibles
 1231 [87]. The search is for a missing momentum signature by precision measurements of the recoil
 1232 electron momentum. Rare photo-nuclear processes that can mimic a missing momentum signature
 1233 are vetoed by a large hadronic calorimeter. The design of the LDMX apparatus is shown in Fig.
 1234 2.11.

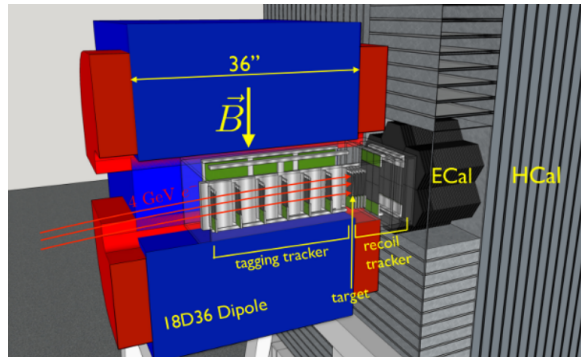


Figure 2.11: The Light Dark Matter eXperiment (LDMX) searches for heavy photon decays to invisibles by measuring the recoil electron momentum and searching for missing momentum. The apparatus includes a tagging tracker, recoil tracker, an Ecal, and an Hcal.

1235 In addition to electron beams, positron beams are also used in fixed target experiments to
 1236 search for heavy photons through e^+e^- annihilation. These searches utilize monophoton final states
 1237 ($\gamma A' \rightarrow \gamma \chi\chi^*$) such that a missing mass search can be performed. Proposed experiments of this
 1238 type include PADME at INFN Frascati and VEPP-3 at the Budker Institute at Novosibirsk [83].
 1239 The proposed Missing Mass A-Prime Search (MMAPS) at Cornell is a similar style missing mass
 1240 search with a $e^+e^-\gamma A'$ [16].

1241 Proton fixed target experiments such as NA48/2 at the Super Proton Synchrotron (SPS) at
 1242 CERN search for meson decays into heavy photons (specifically $K^\pm \rightarrow \pi^\pm \pi^0$; $\pi^0 \rightarrow A'$), that then
 1243 decay to e^+e^- pairs by utilizing a beryllium target to produce a Kaon beam (K^\pm) [28]. In addition,

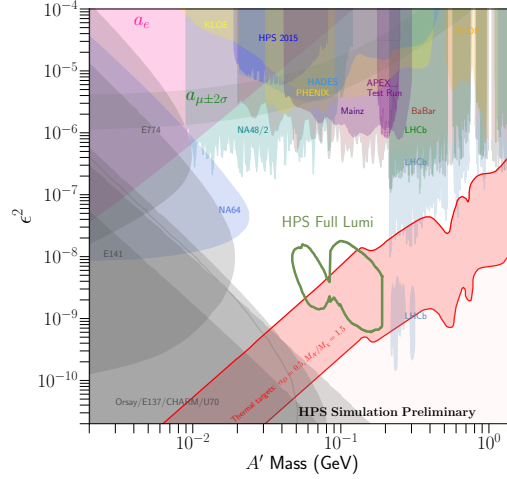


Figure 2.12: Existing constraints for heavy photons from experiments described in Sec. 2.6. The green contours show the projected sensitivity for HPS assuming the allotted 180 days of running time.

1244 the HADES measures potential heavy photons from meson decays (specifically $\pi_0 \rightarrow \gamma A'$, $\eta \rightarrow \gamma A'$,
 1245 $\Delta \rightarrow N A'$) and e^+e^- final states by using a variety of both hydrogen and niobium (Nb) targets
 1246 [11].

1247 Finally, the Heavy Photon Search (HPS) utilizes an electron beam to produce A' 's through dark
 1248 bremsstrahlung and searches for e^+e^- daughter particles from A' decays. HPS is unique in that it
 1249 reconstructs both the mass and vertex positions with excellent precision which enables searches for
 1250 both prompt decays and secondary vertices from heavy photons with a short decay length in the
 1251 range of 1-10 cm in the laboratory frame. The heavy photon theoretically favored parameter space
 1252 assuming visible decays as well as the existing constraints from the experiments described above and
 1253 future projections from HPS is shown in Fig. 2.12.

1254 **Did I miss any other experiments that should be mentioned?**

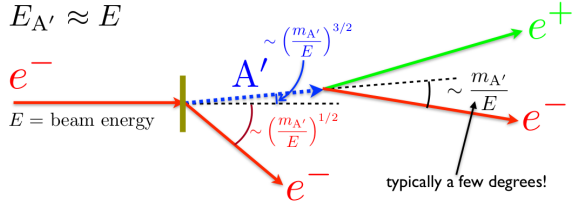


Figure 2.13: The kinematics for heavy photon (A') produced from an electron on a fixed target. In general, A' 's retain most of the incident beam energy, remain close to the beam axis due to a small recoil angle, and have a small opening angle.

1255 2.7 Heavy Photon Fixed Target Kinematics

1256 High luminosity fixed target experiments, that is experiments with a high intensity beam inci-
 1257 dent on a thin metal foil, can probe theoretically favored regions of the heavy photon parameter
 1258 space. Production mechanisms are analogous to that of regular photon bremsstrahlung, called “dark
 1259 bremsstrahlung”, albeit, with suppressed rates due to the weak effective coupling of the A' to electric
 1260 charge and significantly different kinematics because of the relatively large mass of the A' [82]. The
 1261 kinematics of heavy photons can be calculated from the Weizacker-Williams Approximation (WWA)
 1262 where the nucleus is replaced by an effective photon flux. This gives the production differential cross
 1263 section for an electron with energy E_0 incident on a fixed target as

$$\frac{d\sigma}{dx d \cos\theta_{A'}} \approx \frac{8Z^2\alpha^3\epsilon^2 E_0^2}{U^2} \frac{\chi}{Z^2} \left(1 - x + \frac{x^2}{2} - \frac{x(1-x)m_{A'}^2(E_0^2 x \theta_{A'}^2)}{U^2} \right) \quad (2.10)$$

1264 where E_0 is the beam energy, $x = E_{A'}/E_0$, $E_{A'}$ is the energy of the A' , and $\theta_{A'}$ is the angle from
 1265 the beam in the lab frame [34] [31]. The value χ/Z^2 is related to the electric form factor and is in
 1266 the range $\sim 5 - 10$ for the HPS range of interest. The function $U(x, \theta_{A'}) = E_0^2 x \theta_{A'}^2 + m_{A'}^2 \frac{1-x}{x} + m_e^2 x$
 1267 is related to the virtuality of the intermediate electron. The characteristic angle of emission is set
 1268 by $U(x, \theta_{A'}) - U(x, 0) \sim U(x, 0)$ which occurs at $\theta_{A'} \sim \frac{m_{A'} \sqrt{1-x}}{xE_0}$.

1269 Integrating over angle $\theta_{A'}$ and neglecting the mass of the electron m_e and assuming that $m_e \ll$
 1270 $m_{A'} \ll E_0$ and $x\theta_{A'}^2 \ll 1$, the differential cross section becomes

$$\frac{d\sigma}{dx} \approx \frac{8Z^2\alpha^3\epsilon^2 x}{m_{A'}^2} \frac{\chi}{Z^2} \left(1 + \frac{x^2}{3(1-x)} \right) \quad (2.11)$$

1271 This equation reduces to the photon bremsstrahlung cross section in the limit that $m_{A'} \rightarrow 0$.
 1272 Since $U(x, 0)$ is minimized, the A' production rate is maximum at $x \approx 1$, showing that A' 's take most
 1273 of the incident electron's energy $E_{A'} \approx E_0$. There is also a cutoff value of $1 - x$ at $\max\left(\frac{m_e^2}{m_{A'}^2}, \frac{m_{A'}^2}{E_0^2}\right)$
 1274 and a median of $\max\left(\frac{m_e^2}{m_{A'}^2}, \frac{m_{A'}^2}{E_0^2}\right)$. The A' emission angle cutoff is given by $\max\left(\frac{\sqrt{m_{A'} m_e}}{E_0}, \frac{m_{A'}^{3/2}}{E_0^{3/2}}\right)$
 1275 and is much smaller than the opening angle of the decay products $A' \sim m_{A'}/E_0$. The recoil electron

¹²⁷⁶ has a recoil angle of about $\theta_R \sim (\frac{m_{A'}}{E_0})^{1/2}$.

¹²⁷⁷ The overall A' rate is proportional $\frac{\alpha^3 \epsilon^2}{m_{A'}^2}$, thus decreasing with increasing A' mass, and is reduced
¹²⁷⁸ from ordinary photon bremsstrahlung by a factor of $\frac{\epsilon^3 m_e^2}{m_{A'}^2}$. A typical decay length as measured in
¹²⁷⁹ the lab frame $\gamma c\tau$ can be calculated from Eq. 2.8.

$$\gamma c\tau = \frac{3\hbar E_0}{N_{eff} m_{A'}^2 \alpha \epsilon^2 c} \quad (2.12)$$

¹²⁸⁰ For a fixed target experiment that attempts to reconstruct vertex positions, these kinematics
¹²⁸¹ provide significant challenges particularly from a highly boosted particle with a small opening angle.
¹²⁸² A schematic of the basic kinematics and A' production from an electron incident on a fixed target
¹²⁸³ is shown in Fig. 2.13.

1284 2.8 Fixed Target Backgrounds

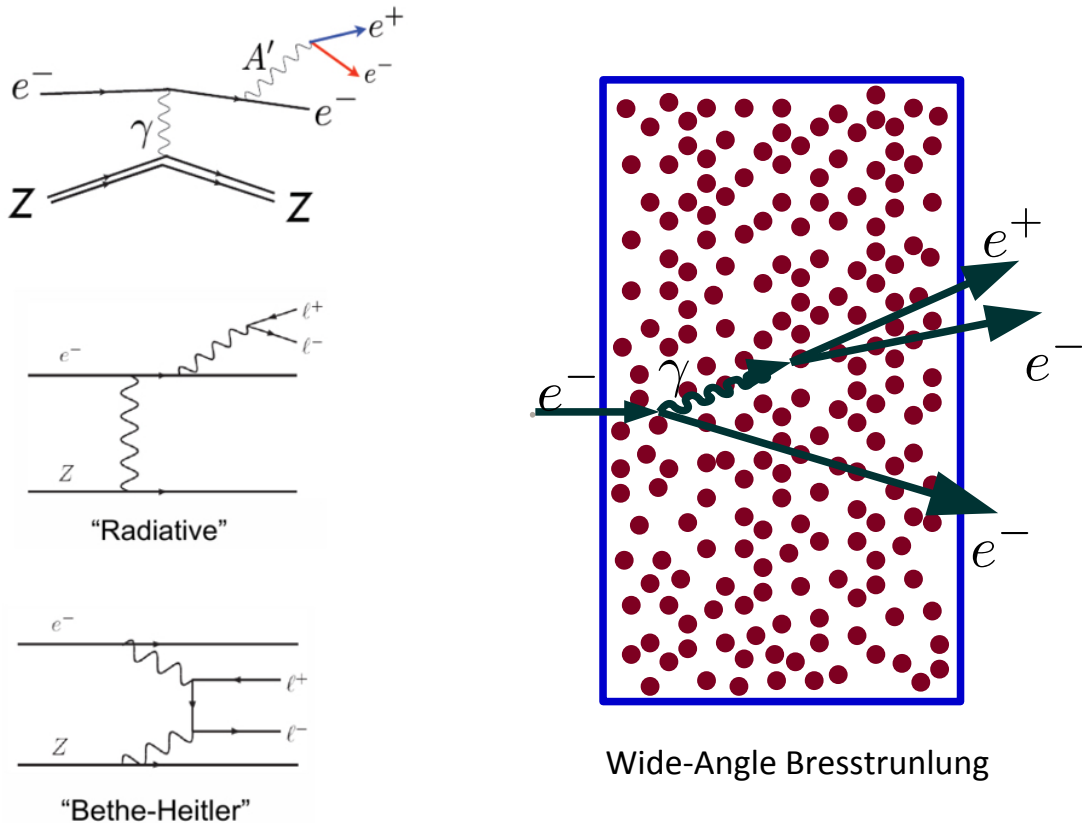


Figure 2.14: Left pictures show Feynman diagrams for A' (top), RAD (middle) and BH (bottom) events. Right picture shows WAB process.

1285 There are three main sources of physics backgrounds that are electro-produced in a fixed target
1286 that have an e^+e^- final state. The first two are prompt QED process ($e^-Z \rightarrow e^+e^-e^-Z$) called “tridents”
1287 because of the three-lepton final state. The other main e^+e^- background is bremsstrahlung
1288 production followed by pair conversion ($e^-Z \rightarrow e^-\gamma Z$ and then $\gamma Z \rightarrow e^+e^-Z$) which can recon-
1289 struct as trident-like due to the three-lepton final state. These are not necessarily prompt since the
1290 conversion can occur from an on-shell γ in either the target or any material in the detector. Their
1291 Feynman Diagrams are shown shown in Fig. 4.9.

1292 The two types of trident processes are called “radiatives” and “Bethe-Heitler” tridents. Radiative
1293 tridents have identical kinematics to A' s. Because of this, radiative tridents constitute an irreducible
1294 prompt background that can only be distinguished from A' s through either a mass resonance in the
1295 e^+e^- invariant mass spectrum or through a finite decay length for sufficiently small ϵ^2 . However,

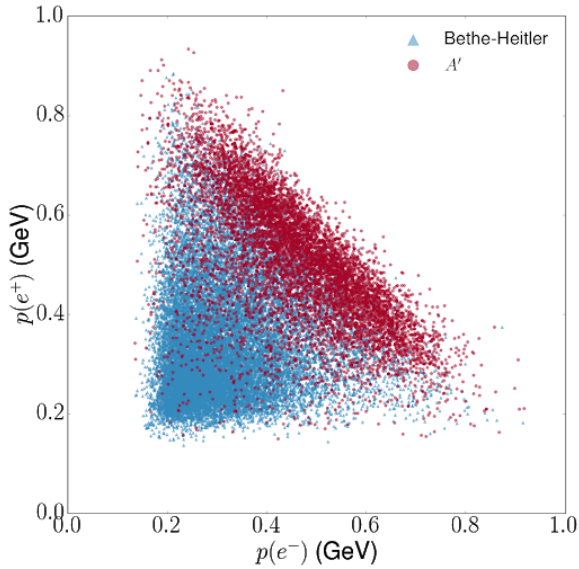


Figure 2.15: Positron momentum vs electron momentum comparing Bethe-Heitler tridents and A' 's (and hence radiative tridents). A' 's generally have a large x in comparison to Bethe-Heitler. This is for a beam energy of 1.06 GeV.

1296 the identical kinematics do provide a way to compute the expected A' rates directly from counting
 1297 e^+e^- pairs in the data and then using Eq. 2.9.

1298 Bethe-Heitler tridents can be kinematically distinguished from A' 's and radiative tridents and
 1299 generally have softer daughter e^+e^- pairs (e^+e^- pair is not peaked at high x). This difference in
 1300 kinematics is illustrated in Fig. 2.15. In addition, there are interference terms between radiative
 1301 tridents and Bethe-Heitler tridents which make a significant contribution to the overall cross-section,
 1302 but make it impossible to physically distinguish between recoil and daughter electrons where either
 1303 particle paired with a positron is a potential background. However, even when selecting only e^+e^-
 1304 pairs at high x where radiative tridents peak, the Bethe-Heitler tridents and cross terms (altogether
 1305 called “non-radiative” tridents) still dominate the rate of radiative tridents by nearly an order of
 1306 magnitude.

1307 The last main background are known as wide-angle bremsstrahlung (WABs) where a photon and
 1308 electron are both emitted from the target at large angles from the beam axis into the acceptance
 1309 of HPS. The photon can either convert in the target or a silicon plane in the tracker. There is
 1310 a very large rate of WABs; however, only a small fraction are in HPS acceptance. The WABs
 1311 that reconstruct a vertex with the daughter positron and the recoil electron are a background,
 1312 though it will reconstruct at the primary even though the converted photon itself can be a displaced
 1313 vertex. The rates of converted WABs with an e^+e^- pair in opposite halves of the detector after
 1314 reconstruction is comparable to radiative tridents.

1315 2.9 Overview of HPS

1316 The Heavy Photon Search (HPS) is a fixed target experiment at Jefferson Laboratory that searches
1317 for electro-produced heavy photons from a high energy electron beam and utilizes a compact for-
1318 ward acceptance spectrometer to capture the charged-lepton decay products of heavy photons and
1319 reconstruct their vertex positions and masses [30]. The main components of HPS consists of a silicon
1320 vertex tracker (SVT) used for reconstruction of particle trajectories and electromagnetic calorimeter
1321 (Ecal) used for timing and triggering.

1322 HPS searches for heavy photons using two distinct methods. The first method is a basic resonance
1323 search, or “bump hunt”, where a search for a resonance in the invariant mass spectrum of e^+e^-
1324 pairs at the heavy photon mass over a large background of QED processes is performed [9]. HPS
1325 offers comparable sensitivity with other experiments that can perform a similar search and offers a
1326 relatively wide mass range over e^- fixed-target competitors. However, HPS is not expected to probe
1327 new territory with the resonance search with the currently planned run time.

1328 The second search method is a displaced vertex search where a secondary vertex displaced from
1329 the target is distinguished from a large prompt QED background [8]. The fact that HPS can search
1330 for long-lived heavy photons by actually reconstructing the vertex instead of using a much simpler
1331 beam dump experiment makes HPS uniquely able to probe a region of phase space of particles with
1332 short $c\tau$ values on the order of 1 - 10 mm.

1333 In order to successfully perform these two searches, HPS must accomplish two difficult challenges.
1334 First, the heavy photon kinematics require large acceptance and excellent vertex resolution. This
1335 results in silicon from the first layer of the SVT to be 0.5 mm from an intense electron beam risking
1336 both highly non-linear radiation damage to the sensors and challenges of particle occupancy in the
1337 detector. The second challenge requires separating a large number of prompt QED process on the
1338 order of 10^8 that undergo multiple scattering in the tracker that may reconstruction downstream of
1339 the target from only a few true displaced vertices which are from a long-lived particle off the tail
1340 of its exponential distribution. The remainder of this thesis will focus on the methods and results
1341 from the displaced vertex search.

¹³⁴² **Chapter 3**

¹³⁴³ **The HPS Detector**

¹³⁴⁴ The Heavy Photon Search (HPS) is a precision vertexing experiment designed to measure both
¹³⁴⁵ prompt and long-lived heavy photons that decay to e^+e^- pairs. The HPS detector is a large,
¹³⁴⁶ compact forward acceptance spectrometer with three main components - a silicon vertex tracker
¹³⁴⁷ (SVT), an electromagnetic calorimeter (Ecal), and a three-magnet chicane. A rendering of the
¹³⁴⁸ detector is shown in Fig. 3.1. The SVT is used to track particles and measure their momentum, the
¹³⁴⁹ Ecal is used for timing and triggering, and the analyzing magnet (the middle magnet of the chicane)
¹³⁵⁰ bends charged particles for a momentum measurement and particle identification.

¹³⁵¹ The specific design of the detector components are optimized for the physics goals of HPS.
¹³⁵² To maximize A' 's signal yield, particularly low mass and displaced A' 's, the detector must have
¹³⁵³ acceptance to small angles. The search for displaced vertices is limited by vertex resolution that
¹³⁵⁴ is dominated by multiple scattering, thus the first layer must be placed as close to the target as
¹³⁵⁵ possible.

¹³⁵⁶ Beam electrons that are elastically scattered in the target are the dominant source of background
¹³⁵⁷ and can be eliminated with a selective trigger. The beam electrons that lose energy in the target due

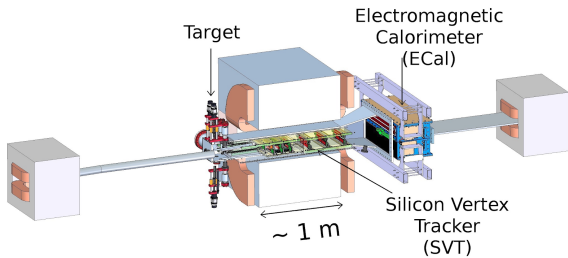


Figure 3.1: A 3D rendering of the HPS detector complete with the silicon vertex tracker (SVT), electromagnetic calorimeter (Ecal), and chicane.

Scattered Beam Background

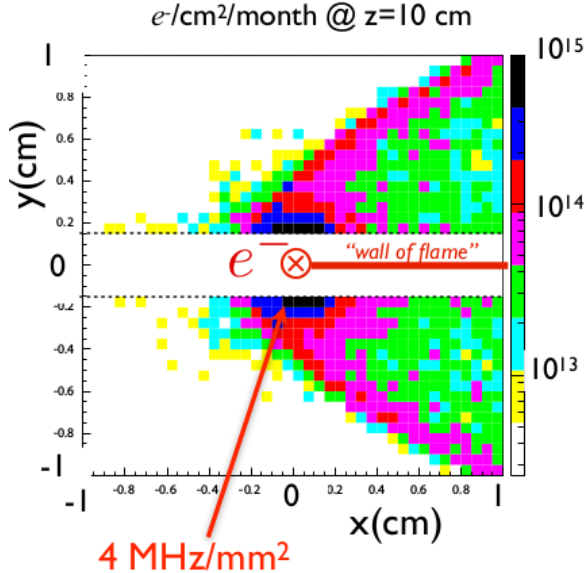


Figure 3.2: The rate of electrons in at the first layer of the SVT from the so-called “wall of flame” - beam electrons that lose energy due to bremsstrahlung in the target and bend in the magnetic field. To avoid the radiation damage from the wall of flame, the detector is split into top and bottom halves.

1358 to Bremsstrahlung bend in the presence of the magnetic field and form the so-called “wall of flame”
 1359 in the horizontal plane including the beam direction (referred to as the “beam plane”) that would
 1360 produce too much radiation damage in any detector component as shown in Fig. 3.2. Thus, the
 1361 SVT and Ecal are both split in top/bottom halves and placed as close to the beam plane as possible.
 1362 In order to balance between maximizing signal yield, optimizing vertex resolution, and minimizing
 1363 radiation damage, the detector is designed at an opening angle of 15 mrad from the beam plane for
 1364 both top and bottom halves.

1365 The last major design consideration is due to the fact that beam gas interactions have potential
 1366 to be a very significant background source increasing both detector occupancy and radiation damage.
 1367 For this reason, the SVT and the space between the Ecal halves are under vacuum. In addition, there
 1368 exist a possibility for a beam-gas interaction downstream of the target that will mock a downstream
 1369 decay and look very signal-like. A medium-level vacuum (10^{-6} Torr) is sufficient to mitigate these
 1370 effects and as a result, all materials must be vacuum compatible (and are tested in a high vacuum test
 1371 chamber). Lastly, all materials must be nonmagnetic because the SVT operates in a high magnetic
 1372 field.

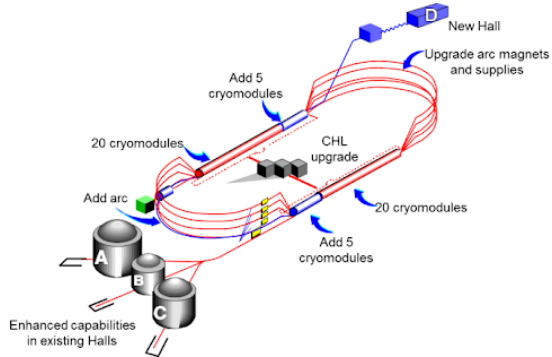


Figure 3.3: A schematic of the upgraded Continuous Electron Beam Accelerator Facility (CEBAF) at Jefferson Laboratory. The machine is a recirculating linear accelerator designed to send a beam of electrons of different currents and energies to four different experimental halls (Halls A - D).

1373 3.1 The Continuous Electron Beam Accelerator Facility (CE- 1374 BAF)

1375 The high energy electron beam used for A' production by bremsstrahlung on a thin target is provided
1376 by Jefferson Laboratory’s Continuous Electron Beam Accelerator Facility (CEBAF) [65]. CEBAF is
1377 able to simultaneously deliver intense and energetic electron beams of different energies and currents
1378 to three different experimental halls (Hall A, Hall B, and Hall C). The recent upgrade allows for
1379 CEBAF to deliver beam to four experimental halls (an additional Hall D) in multiples of 2.2 GeV
1380 up to 12 GeV [39] [47]. Beyond and including the 2015 Engineering Run, HPS runs have all been in
1381 the 12 GeV era - that is with the upgrades.

1382 CEBAF is a recirculating linear accelerator (linac) designed as a “racetrack” configuration where
1383 beam bunches are circulated multiple times through the same two linacs by arcs as shown in Fig.
1384 3.3. Each cycle, or pass, around the accelerator adds an additional 2.2 GeV of beam energy for a
1385 maximum of 5 passes to Hall A, Hall B, and Hall C and an additional half pass to Hall D. Thus,
1386 the energy in a hall will be $0.1 \text{ GeV} + n \times 2.2 \text{ GeV}$ for n passes (the addition 0.1 GeV comes from
1387 the energy from the injector). CEBAF can deliver a beam current of up to $85 \mu\text{A}$ to halls A and C
1388 and deliver up to $5 \mu\text{A}$ to halls B and D (HPS utilizes a current far less than the maximum).

1389 Electrons in the accelerator originate from the photoemission of a strained GaAs superlattice
1390 photocathode with an incident laser of 780 nm wavelength, which is equal to the band gap of the
1391 GaAs [75]. The incident laser is pulsed at 499 MHz for ≈ 40 ps. The photoemitted electrons are
1392 then brought to the the injector before finally entering the accelerator.

1393 CEBAF accelerates electrons using superconducting radiofrequency (RF) cavities operating at
1394 1500 MHz and by using an RF separator, can deliver beam pulses at either 500 MHz or 250 MHz,
1395 essentially a continuous duty cycle, to each of the four experimental halls. This short pulse time (2

₁₃₉₆ - 4 ns) results in a near-continuous duty cycle and is essential to HPS as it reduces pileup effects
₁₃₉₇ while maximizing luminosity. The 12 GeV upgrade included a 750 MHz RF separator which allowed
₁₃₉₈ the beam to be diverted to the new Hall D.

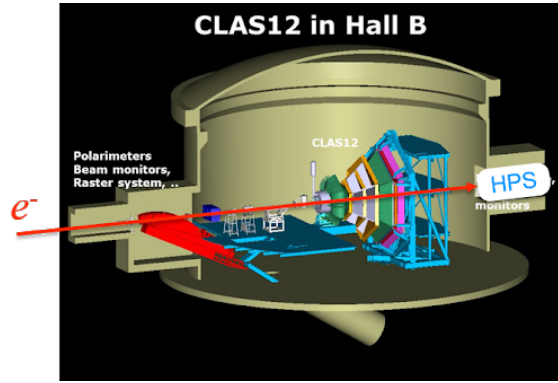


Figure 3.4: A schematic of Hall B including the CLAS-12 spectrometer and the HPS detector in the Hall B alcove. The electron beam enters the hall from the left in this picture.

1399 3.2 Hall B and HPS Beamline

1400 The HPS experiment is located in Hall B in an alcove behind the CLAS12 (CEBAF Large-Acceptance
1401 Spectrometer) detector, which is typically used for low-current precision nuclear physics. Hall B can
1402 receive either an electron or photon beam. In order to reduce pileup and beam background for
1403 the HPS experiment, the Hall B beam from CEBAF is a continuous beam structure with a bunch
1404 spacing at 2 ns (which is far shorter than the trigger window and comparable to the detector timing
1405 resolution).

1406 The Hall B beamline begins with a large tagger dipole magnet which is a dipole magnet which,
1407 when energized, steers the electron beam into the tagger dump below the beamline. The tagger
1408 magnet is far upstream of HPS and allows for tuning of the beam to an acceptable quality before
1409 delivering the beam to HPS. This is critical as the low acceptance of the tracker puts the silicon
1410 within 5 mm of the nominal beam plane even with the SVT fully retracted, thus a poor quality
1411 beam (one with a large spotsize, beam tails, or other instabilities) could cause unnecessary radiation
1412 damage to the detector. If a target is placed upstream of the tagger magnet, a photon beam can
1413 also be produced in Hall B which has been used for test runs for HPS in the past. The nominal
1414 configuration for HPS physics running is for the tagger magnet to be de-energized so that the electron
1415 beam can be delivered to HPS.

1416 The beamline between the tagger magnet and HPS consists of several beam position monitors
1417 (BPMs) which measure the passing beam bunches to provide an estimate of beam current and
1418 position. A series of quadrupole magnets and horizontal and vertical correctors on the beamline
1419 are used for fast automatic correction to beam trajectories based on the BPM measurements. The
1420 quadrupole magnets are also used to squeeze the beam spotsize as small as possible at the target.

1421 The Hall B beamline also includes several wire harps to measure the beam position and profile.
1422 These wire harps are composed of 2-3 thin metal wire connected to a motor and as the wires traverse

1423 the beam profile (which are at different angles to obtain both x and y profile measurements), it will
1424 scatter beam particles resulting in an increase of the count rate of downstream halo counters. The
1425 rate of these counters is proportional to the beam intensity, thus a beam position and profile can
1426 be constructed with knowledge of the wire positions and halo counter rates. This is used for beam
1427 tuning as well as to ensure the beam is safe enough to perform wire scans with the wires directly
1428 connected to the SVT as described below. An example of a harp scan from the 2H02 harp, which is
1429 the closest wire harp to the HPS target at 2.2 m upstream, from the 2016 Engineering Run is shown
1430 in Fig. 3.5. The general strategy to achieve a small spot size at the target is to use the measurements
1431 from the 2H02 wire harp as well as several wire harps further upstream in conjunction with a series
1432 of quadrupole magnets along the beamline. The magnetic fields of the quadrupole magnets can be
1433 finely tuned such that the waist, that is the minimum beamspot size in the y -direction, is precisely
1434 at the target.

1435 There are several collimators along the beamline to protect both HPS silicon sensors and elec-
1436 tronic components from radiation damage from either a stray beam or particles produced by a
1437 stray beam. When enough of a beam interacts with a collimator, it also produces many particles
1438 that trip the fast shutdown (FSD). The closest collimator to the SVT is a 1 cm thick tungsten plate
1439 with machined slots of different widths connected to a linear shift and placed 2.9 m upstream of
1440 target (referred to as the “SVT collimator”). With the exception of the inner strips of layer 1 of the
1441 SVT, this protects most of the detector from beam tails and beam halo. The collimator can also
1442 force an FSD trip such as when the beam is mis-steered or scrapes the collimator which can produce
1443 enough secondary particles for the FSD counters to cross threshold. For the 2016 Engineering Run,
1444 the 4 mm slot was used ([Is this true??](#)).

1445 Downstream of HPS, there are two fluorescent screens and a screen used for optical transition
1446 radiation (OTR) that are useful for viewing the beam position. Finally, the beam is terminated in a
1447 Faraday cup in the Hall B beam dump. The Faraday cup provides the most accurate measurement
1448 of the total beam charge and is used to normalize the data for the analysis. A beam blocker must be
1449 put in front of the Faraday cup at beam currents above 50 nA to avoid overheating, and the actual
1450 measurement of integrated charge must be re-scaled.

1451 A schematic of the HPS beamline in the Hall B alcove is shown in Fig. 3.6. The HPS apparatus
1452 is a large, compact forward spectrometer that consists of a three-magnet chicane system, SVT, Ecal,
1453 and a vacuum chamber. On the exterior of HPS, there are several halo counters (plastic scintillators)
1454 that monitor the stability of beam conditions. If these halo counters measure particle rates above
1455 their set threshold, most likely due to an obscured beam, a fast shut down (FSD) is applied to the
1456 Hall B beam within 1 ms to prevent further radiation damage to the HPS detector components.

1457 Thin wires are attached to both the top and bottom of the SVT as described in Sec. 3.3.2 and
1458 are used to measure the beam position and profile with respect to the SVT as close to the target
1459 as possible. Each half the SVT contains a horizontal and a diagonal wire (oriented $\approx 10^\circ$ from

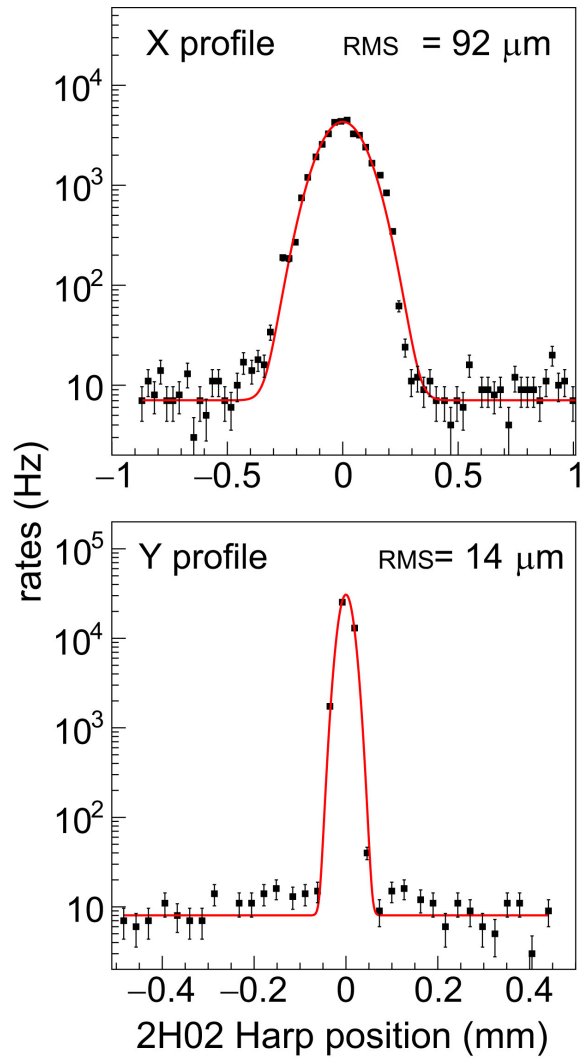


Figure 3.5: An example of a scan from the 2H02 wire harp from the 2016 Engineering Run. This provides a measurement of the beam profile that is useful as input to tuning the beam to its optimal profile at the target. The profile shows a width of $92 \mu\text{m}$ in x and $14 \mu\text{m}$ in y with minimal beam tails.

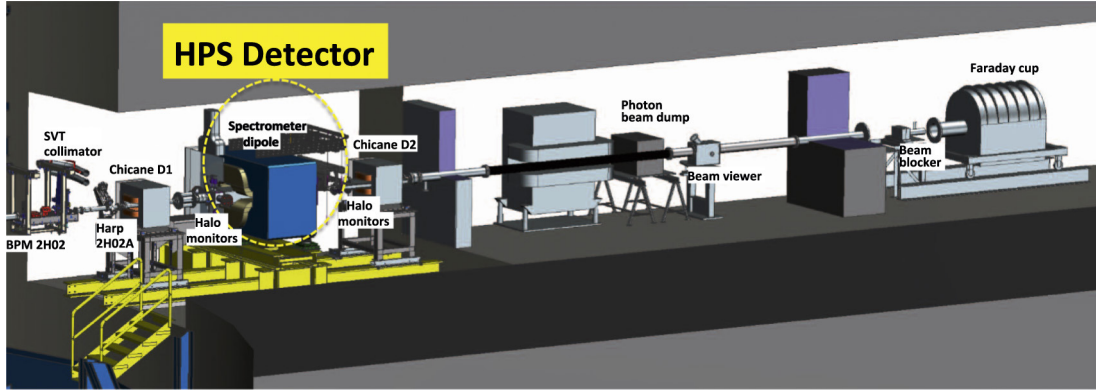


Figure 3.6: A schematic of the HPS beamline inside the Hall B alcove.

horizontal) for a vertical and horizontal position measurement. These wires move with the SVT and, as they traverse the beam profile, beam particles are scattered into the halo counters on the exterior of HPS. The rate of beam particles counted by the halo counters is proportional to the intensity of the beam, thus through a mapping of the wire position and count rate a beam profile can be produced. In order to ensure safe operation of the SVT, the beam profile in the y -direction is required have a width less than $50\mu\text{m}$ with minimal beam tails and a mean within $50\mu\text{m}$ of the midplane between the top and bottom halves of the SVT. However, a beamspot as small as possible is desired as a smaller spot size will aid the constraint of vertices to the beamspot, thus improving the displaced vertex analysis by more efficiently rejecting tracks and vertices that are inconsistent with the beamspot. The beamspot size and position in the x -direction is less important since the resolution is far worse due to the small stereo angles between the SVT strip sensors, so a width of less than $150\mu\text{m}$ is sufficient. An example of a wire scan measurement from the 2016 Engineering Run is shown in Fig. 3.7.

The SVT wire scans are unable to effectively measure the beam halo - beam electrons in the far tails of the Gaussian beam profile. This is important to understand for the purposes of long term radiation damage in the SVT. A measurement of beam halo from the 2015 Engineering Run by measuring occupancies in layer 1 of the SVT without the target is shown in Fig. 3.8. The beam halo intensity is $< 10^{-5}$ of the beam intensity which is sufficiently below the rate due to elastically-scattered beam electrons in the target, and thus is acceptable for HPS.

The chicane contains a single 18D36 analyzing magnet (or central magnet of pair spectrometer) with a pole length of 91.44 cm and a gap size of $45.72 \times 15.24\text{ cm}^2$. The analyzing magnet operated with a maximum field strength of 0.24 T for the 2015 Engineering Run and 0.50 T for the 2016 Engineering Run (the field strength scales linearly with beam energy and a maximum field strength of 1.5 T). In addition, two H-dipole Frascati magnets are set on either side of the analyzing magnet such that the total $\int \vec{B} \cdot d\vec{l}$ for the chicane system is 0 (each Frascati magnetic has half the bending

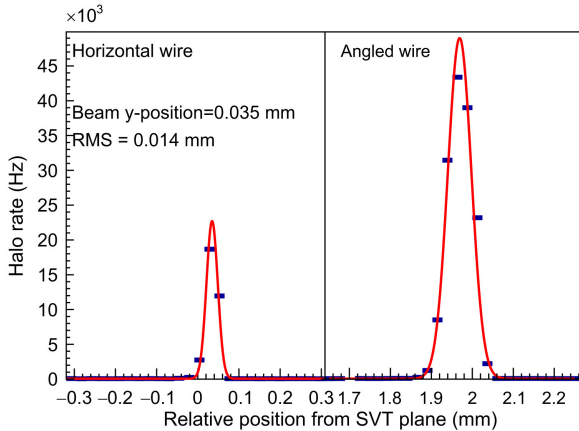


Figure 3.7: An example of an SVT wire scan measurement from the 2016 Engineering Run. This provides a measurement of the beam profile as close to the target as possible. This scan shows a beam with a $14 \mu\text{m}$ width in the y -direction with minimal tails and $35 \mu\text{m}$ from the nominal beam plane. This is an excellent beam profile for HPS.

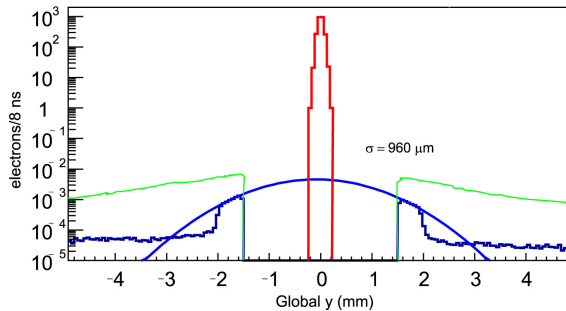


Figure 3.8: A measurement of the beam halo from 2015 Engineering Run using the occupancy of the first layer of the SVT in a no target run. The beam halo shows a width of $960 \mu\text{m}$ and 5 orders of magnitude less than the peak of the beam.

1485 power of the analyzing magnet with opposite sign) which ensures the beam trajectory downstream
1486 of the chicane is independent of whether or not the chicane is powered.

1487 The vacuum box has flanges upstream of the analyzing magnet for penetration of linear motion
1488 systems, cooling lines, and power and signal cables. The HPS target can be moved remotely by a
1489 linear shift from a stepper motor on the vacuum flange and is cantilevered at a ceramic support
1490 rod. There are several target options that can be selected based on the linear position of the target
1491 mount - $4 \mu\text{m}$ tungsten (0.125% radiation length design and 0.116% radiation length measured), 8
1492 μm tungsten (0.25% radiation length design and 0.223% radiation length measured), and a carbon
1493 target for calibration. The targets are connected to a grounding wire in order to prevent discharge
1494 due to charge buildup from the incident beam. The Ecal is downstream of the analyzing magnet.
1495 More details of the Hall B and HPS beamlines can be found in the HPS Beamline paper [26].

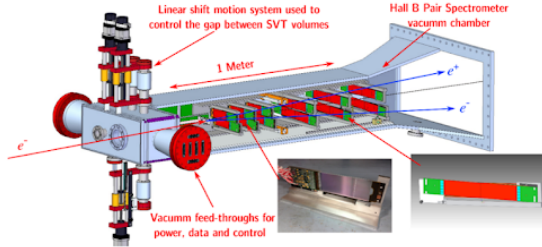


Figure 3.9: A schematic of the HPS silicon vertex tracker (SVT) which includes 6 layers of silicon microstrip sensors inside a vacuum and a uniform magnetic field. **Maybe find a better picture.**

1496 3.3 Silicon Vertex Tracker

1497 The silicon vertex tracker (SVT) provides a momentum measurement from charged particle trajectories that bend in the uniform magnetic field that can be used to reconstruct a vertex position.
 1498 The SVT is an array of silicon microstrip sensors consisting of six layers (or measurement stations).
 1499 Microstrips provide a 1D measurement along the direction of the sensor extending away from the
 1500 beam. In order to provide a 3D measurement, each layer contains two components - an axial sensor
 1501 with strips parallel to the beam plane and a stereo sensor rotated at a small angle. A large stereo
 1502 angle would provide improved hit resolution in the direction along the axial strip, and hence im-
 1503 proved momentum resolution.¹ However, a large stereo angle would also cause the stereo sensors
 1504 to dip significantly into the beam plane, lose acceptance, and be prone to ghost hits (falsely recon-
 1505 structed 3D hits). In addition, since resolution effects are limited by multiple scattering, improving
 1506 resolution in the x direction by increasing the stereo angle is not necessary. Thus, the stereo angle
 1507 is intentionally small and designed to be 0.100 mrad for the first three layers and 0.050 mrad for the
 1508 last three layers. The axial/stereo sensor pairs reconstruct a 3D hit position at each of the six layers
 1509 that are used for track finding. The difference in stereo angle between the first and last three SVT
 1510 layers breaks the degeneracy in pattern recognition that could have generated more ghost hits.
 1511

1512 The SVT is split into top/bottom halves to avoid the very high flux of electrons near the beam
 1513 plane due to the “wall of flame”. Both the top and bottom halves are designed at a 15 mrad
 1514 opening angle with respect to the primary. This opening angle must be as small as possible in order
 1515 to capture as many A 's as possible which are typically highly boosted with a small opening angle.²
 1516 The last three layers of the SVT are double wide (i.e. two sensors end to end) to increase acceptance
 1517 for charged particles that are bending due to the uniform magnetic field.

1518 The six layers are arranged such that the distance between the first and second layer (layer 1
 1519 and layer 2) and the second and third layer is about 10 cm. The distance between the remaining
 1520 layers is about 20 cm. Layer 1 is placed as close to the target as possible at about 10 cm in order

¹The resolution in the bend plane is simply the resolution in the non-bend plane divided by the stereo angle.

²This becomes even more critical for displaced A 's which, for a given opening angle, lose acceptance rapidly as the decay vertex increases along the beam direction.

1521 to provide the best possible vertex resolution, and subsequently the second layer is placed close to
 1522 the first layer to maximize pointing resolutions of tracks back to layer 1. The limiting factor of the
 1523 first layer placement is the fact that the sensors cannot be closer to $500 \mu\text{m}$ from the beam plane
 1524 in order to avoid significant radiation damage from both elastically scattered electrons in the target
 1525 and beam tails. Thus for a given opening angle of 15 mrad and a 1 mm guard ring (inactive silicon)
 1526 where the active sensor begins at $0.5 + 1.0 \text{ mm} = 1.5 \text{ mm}$, the closest the first layer can be placed
 1527 downstream of the target is $\approx 1.5 \text{ mm} / 15 \text{ mrad} = 10 \text{ cm}$.³ This approaches the maximum allowed
 1528 occupancy for the silicon sensors of $\sim 1 - 2\%$. The sensors are designed to be as thin as possible
 1529 to reduce the material budget and hence the effects due to multiple scattering. A summary of the
 1530 some of the important design features of the SVT is shown in Table 3.1.

Layer Number	1	2	3	4	5	6
Distance z from target (mm)	100	200	300	500	700	900
Dead Zone Distance y (mm)	± 1.5	± 3.0	± 4.5	± 7.5	± 10.5	± 13.5
Number of Sensors	4	4	4	8	8	8
Stereo Angle (mrad)	100	100	100	50	50	50
Bend Plane Resolution (μm)	≈ 60	≈ 60	≈ 60	≈ 120	≈ 120	≈ 120
Non-Bend Plane Resolution (μm)	≈ 6	≈ 6	≈ 6	≈ 6	≈ 6	≈ 6
Material Budget ($\%X_0$)	0.7%	0.7%	0.7%	0.7%	0.7%	0.7%
Module Power Consumption (W)	6.9	6.9	6.9	13.8	13.8	13.8

Table 3.1: A summary of the basic parameters for different layers in the SVT.

³The next subsection described a 1 mm inactive part of the sensor, so the active region begins at 1.5 mm from the beam plane.

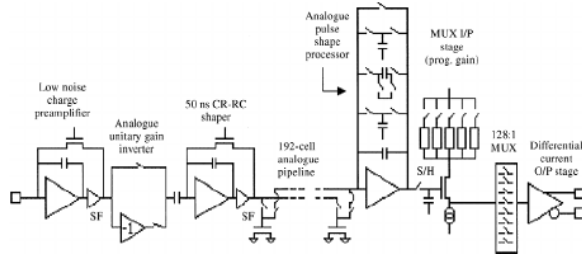


Figure 3.10: A schematic of the APV25 deep submicron readout chip that was originally designed for CMS detectors but is used for the HPS SVT.

1531 3.3.1 Sensors and Readout

1532 HPS utilizes the silicon microstrip sensors originally designed and procured for the upgraded DØ
 1533 detector at Fermilab for run IIb, which was cancelled in favor of an insertable Layer 0 [44]. The
 1534 sensor technology was chosen to minimize material budget to mitigate multiple scattering effects
 1535 and to be highly tolerant to radiation. These sensors are single-sided p+n with AC-coupled readout
 1536 with a bulk that is lightly doped n-type silicon. The strip implants are strongly p-type doped. The
 1537 bias of the strips comes from polysilicon resistors at the end of the strips which are capacitively
 1538 coupled to aluminum readout strips that run on top of the silicon strips.

1539 The sensor cut dimensions are 100 mm × 40.34 mm with an active area of 98.33 mm × 38.34 mm.
 1540 The silicon strip pitch is 30 μm ; however, only every other strip is readout (i.e. the readout pitch is
 1541 60 μm). When a particle is incident on an intermediate strips (a sense strip), the charge will split
 1542 between the neighboring readout strips and this charge sharing will improve single hit resolution.
 1543 Each sensor has 640 readout strips.

1544 The useful sensor lifetime is limited by radiation damage where the sensor strips closest to the
 1545 beam plane are expected to undergo a large electron flux of $> 10^{15}$ electrons per cm^2 over the duration
 1546 of the experiment. Specifically, incident particles can displace silicon nuclei from their crystal lattice
 1547 which causes an effective type inversion, where the n-type bulk is converted to p-type. The radiation
 1548 damage leads to an increase in depletion voltage which means the charge collection efficiency for a
 1549 given bias voltage will decrease. Thus as a sensor undergoes radiation damage over the course of
 1550 the run which is highly non-uniform and concentrated on the beam edge of the sensor (mostly from
 1551 elastically scattered beam electrons in the target), the bias voltage must be increased to keep the
 1552 same charge collection efficiency. Eventually, this bias voltage will approach the breakdown voltage
 1553 and will no longer be usable in the experiment. In addition, radiation damage leads to increased
 1554 leakage current, and thus sensor heating. For these sensors, the nominal operating bias voltage is
 1555 180 V. The design specifications required a breakdown voltage greater than 350 V; however, only
 1556 sensors with a breakdown voltage greater than 1000 V were used. For the 2015 and 2016 Engineering
 1557 Runs, radiation damage was not an issue.

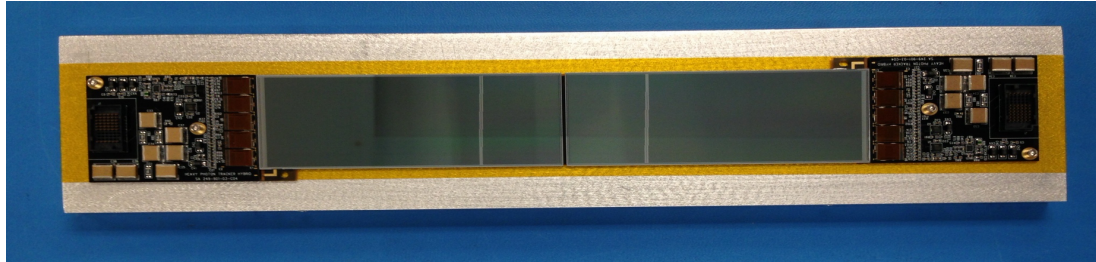


Figure 3.11: A picture of the two SVT sensors (end to end) with each sensor. The sensors are readout by APV25 chips which are housed on a hybrid circuit.

1558 These sensors are readout by the APV25 readout chip which was developed for the silicon mi
 1559 crostrip sensors in the CMS tracker [79] [51]. A schematic is shown in Fig. 3.10. The APV25 chip
 1560 has high hit time resolution and has the ability to readout multiple consecutive samples of its shaper
 1561 waveform, thus it is useful for pileup rejection - an essential requirement for HPS. The APV25 chip
 1562 has 128 input channels, thus each sensor has $640 / 128 = 5$ readout chips. Each channel contains
 1563 a charge-sensitive preamplifier with an optional inverter, CR-RC shaper, and a 192-cell-deep analog
 1564 pipeline. Only 160 out of 192 of these cells are used to buffer samples and the remaining 32 cells
 1565 buffer the addresses of samples waiting to be readout. A picture of two SVT sensors with APV25
 1566 chips is shown in Fig. 3.11.

1567 The clock is designed for a clock period of 25 ns which is equivalent to the LHC bunch crossing.
 1568 However, HPS adapted this chip to run on a clock period of 24 ns (41.6 MHz) since it is an even
 1569 multiple of the both the JLab and Ecal clocks, which are 2 ns and 4 ns, respectively. Each channel
 1570 samples the shaper output and stores it in a cell of its pipeline on each clock. Once a trigger is
 1571 received, the pipeline cell of each channel is readout, and the chip multiplexes the 128 signals onto a
 1572 single differential current output. A configurable latency (the distance between the read and write
 1573 pointers) setting determines which pipeline cells are readout.

1574 The samples are readout by the Analog Pulse Shape Processor (APSP) which has the ability to
 1575 operate in two distinct modes - deconvolution mode and multi-peak mode. For each trigger signal,
 1576 the deconvolution mode allows for three consecutive pipeline cells to be readout and combined
 1577 into a weight sum whereas the multi-peak readout mode allows for three consecutive pipeline cells
 1578 to be readout without any additional operations. In order to mitigate pile-up effects from large
 1579 occupancy, HPS is operated in multi-peak readout mode and for each trigger, the APV25s are
 1580 sent two consecutive trigger signals for a total of six samples. These six samples are fit to a pulse
 1581 shape predetermined from offline calibration and reconstructed offline in order to obtain the pulse
 1582 amplitude and hit time. This is described in detail in Sec. 4.3.

1583 During the 2015 Engineering Run, the nominal settings of the APV25 were utilized. For the
 1584 2016 Engineering Run, these same parameters were used with the exception of the input parameters
 1585 of the pulse shaper which were optimized to have a sharp rise time for optimal time resolution and

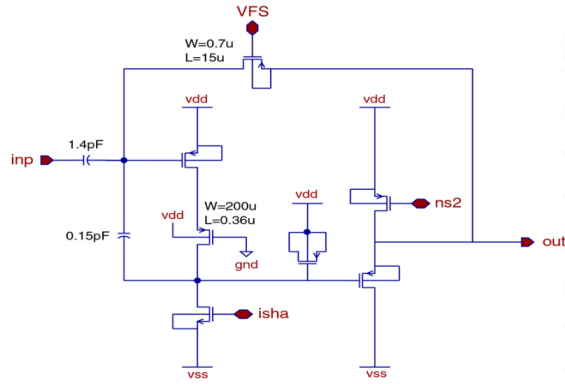


Figure 3.12: The APV25 Shaper schematic. The parameters VFS (related to the input voltage) and isha (related to the input current) were optimized for improved time resolution and reduced pileup.

₁₅₈₆ quick fall time to further reduce pileup effects. A schematic of the APV25 shaper and the parameter
₁₅₈₇ which were optimized is shown in Fig. 3.12.

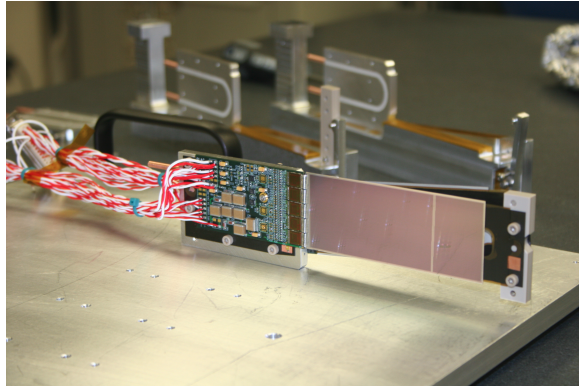


Figure 3.13: A single SVT module which comprises of two silicon microstrip sensors which are axial (front) and stereo (back) to the beam plane. Each sensor is supported by a carbon fiber support structure can be seen protruding from the right of the axial sensor.

3.3.2 SVT Mechanics

1588 Each sensor is part of a base unit referred to as a “half-module” and is comprised of a single or
 1589 double sensor, carbon fiber support structure, and hybrid readout circuit boards. The first three
 1590 layers 1-3 are composed of a single sensor and hybrid while the last three layers 4-6, since they are
 1591 double wide, are composed of double sensors and hybrids. Each of these half-modules can be used
 1592 as the axial or stereo components of the detector.

1593 The carbon fiber, in addition to support for the sensor, acts as ground plane for the half-module
 1594 while a layer of Kapton insulation isolates the carbon fiber from the back of the sensor which is
 1595 at high voltage. The Kapton and carbon fiber are kept as thin as possible, much thinner than the
 1596 silicon sensors, to avoid adding additional unnecessary material that increases multiple scattering in
 1597 the tracker.⁴

1598 The hybrid circuit boards house the APV25 readout chips, five per half module, and provides
 1599 a connection of the sensor to the rest of the DAQ. The APV25 power, control lines, and output
 1600 channels are wirebonded to the hybrid while the input channels are wirebonded directly to the
 1601 sensor. The hybrid contains temperature sensors and carries filter capacitors for the sensor bias.

1602 Two of these half-modules are paired to create a module with one axial and one stereo half-
 1603 module. The axial half-modules are parallel to the beam plane and the stereo half-modules are
 1604 rotated at a small angle and dips into the beam plane on the positron side (beam left, the side
 1605 opposite to where beam background is bent). These modules are mounted on aluminum support
 1606 modules which hold the half-modules from both sides and, in addition to mechanical support, these
 1607 supports also pull heat generated by the hybrids. The half-modules and the support undergo thermal
 1608 contraction at different rates, thus the module support applies a constant tension from a spring pivot

⁴A window was machined into the carbon fiber support such that the material in the middle of the sensor, where most of the physics of interest is expected, is further minimized.

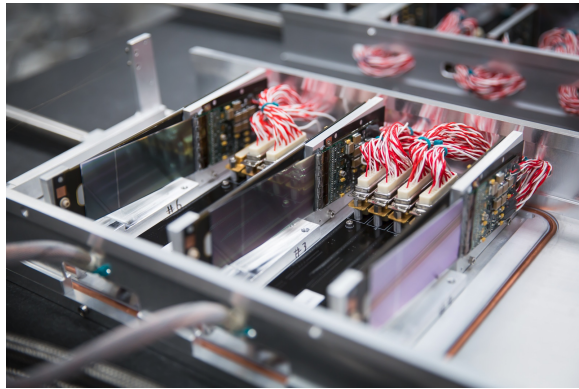


Figure 3.14: Layers 1 - 3 modules of the SVT (from left to right) are place in one of the U-channels. Copper cooling lines and electrical lines can be seen. The wire frames and scan wires can also be seen on the left.

1610 in order to keep the half-modules flat at operating temperature ($\sim 0^\circ \text{ C}$). A picture of a complete
 1611 module is shown in Fig. 3.13.

1612 Three of these modules are mounted on an aluminum support structure called a “U-channel”.
 1613 The SVT contains a total of four of these U-channel for each top and bottom of L1-3 and L4-6
 1614 (which are larger). Each U-channel is supported by kinematic mounts which guarantee reliable and
 1615 repeatable positioning when the U-channels are installed and re-installed. The L1-3 U-channels rest
 1616 on two downstream kinematic mounts, which act as a hinge, and is supported at the upstream end
 1617 by motion levers which guide the L1-3 U-channels towards and away from beam. Finally, the L1-3
 1618 modules house scan wires as close to the target position as possible to measure the beam position
 1619 and profile relative to the SVT to assess beam quality. Each U-channel has two wires - one parallel
 1620 to the beam plan and one rotated at a slight angle - in order to obtain 2D position information. A
 1621 picture of a L1-3 U-channel is shown in Fig. 3.14.

1622 The SVT underwent a mechanical survey before installation using a coordinate-measuring ma-
 1623 chine which utilized both optical and touch probe measurements to locate 3D target points. The
 1624 survey ensures the SVT was assembled as designed and allows adjustment for the adjustable com-
 1625 ponents if necessary, and it provides an initial alignment for track reconstruction whose quality
 1626 depends strongly on precise knowledge of the sensor positions and orientations. This is sufficient
 1627 for initial knowledge, but the sensor is later aligned using the data as described in Sec. 4.7. Lastly,
 1628 the survey provides a measurement of the edge of the L1 axial sensor relative to the wire on the
 1629 U-channel to ensure that the sensor edge is placed at $500 \mu\text{m}$ from the beam plane. A picture of the
 1630 SVT installed in the SVT vacuum box is shown in Fig. 3.15.

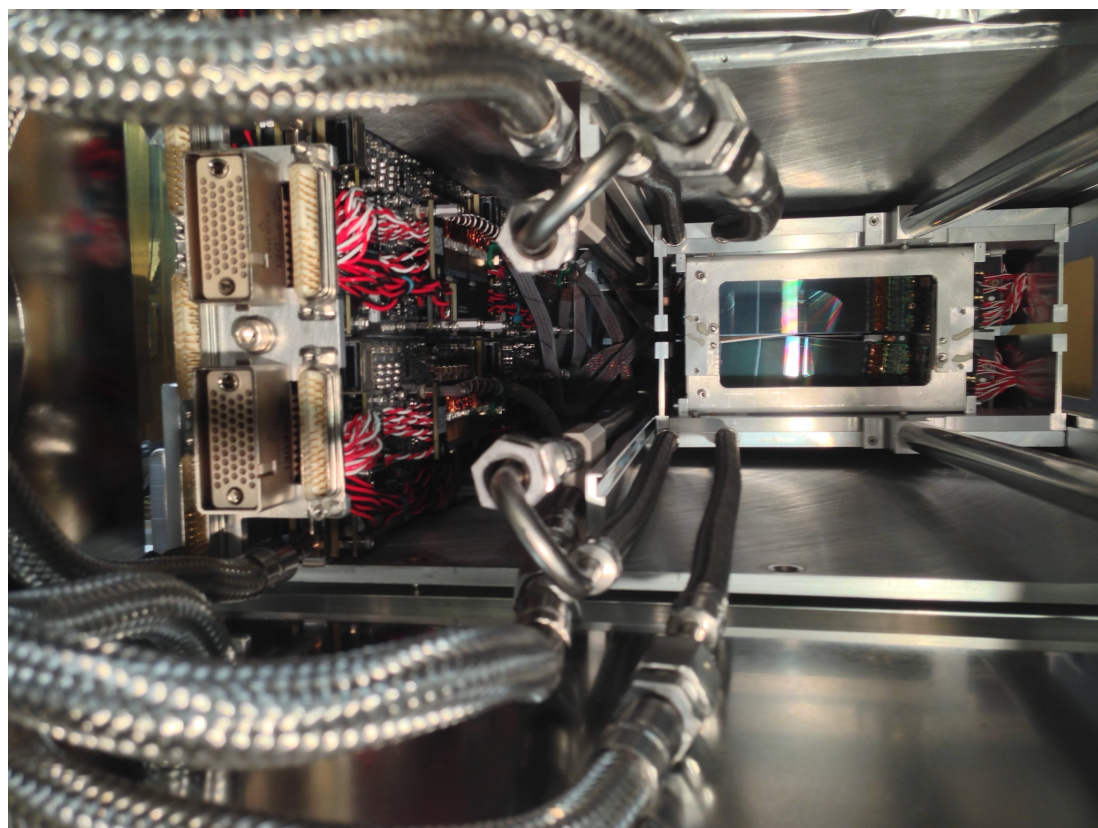


Figure 3.15: A picture inside the SVT vacuum chamber with everything installed except for the target. The frontend boards (FEBs) and FEB cooling plate are on the left. The SVT cooling lines protrude outward in the picture. The first layer of the SVT can be seen in the back behind the wire frames. The SVT is in its closed position and the beam must go through the 1 mm gap between the top and bottom sensors.

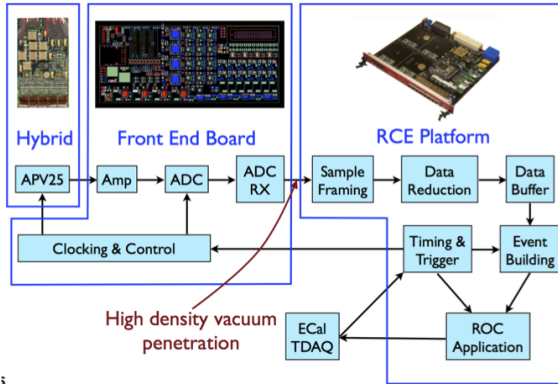


Figure 3.16: A schematic of the SVT DAQ system described in Sec. 3.3.3.

1631 3.3.3 SVT Data Acquisition, Power, and Services

1632 HPS must have a method to pass power and data to the detector given the constraints of the detector
 1633 design as described previously. In addition, the nearest rack that can contain the data acquisition
 1634 (DAQ) and power supplies is located about 20 m from where HPS is installed thus requiring the
 1635 analog signals from the APV25 readout chips to be converted to optical digitized signals. As a
 1636 result, the signal digitization and low-voltage regulation is performed inside the vacuum on front end
 1637 boards (FEBs) located on a cooling plate alongside the SVT. And because the SVT and front end
 1638 boards (FEBs) are in vacuum, all power and DAQ must pass through a pair of 8-inch vacuum flanges
 1639 upstream of the dipole magnet, thus requiring the reduction of the number of signals.

1640 Each of the 10 FEBs can service either a pair of L1-3 modules or a single L4-6 modules totalling
 1641 four hybrids which is connected by a single bundle of impedance-controlled twisted pair magnet wire
 1642 (which reduces crosstalk and electromagnetic interference between the lines). This carries the analog
 1643 APV25 output signals, digital controls, trigger signals, low-voltage power, and high-voltage sensor
 1644 bias. The data and control signals are carried by a mini-SAS cable on a high-speed data link. The
 1645 FEBs digitize the output signals from 20 APV25 chips (4 hybrids \times 5 APV25 chips). A preamplifier
 1646 on the APV25 converts a differential current signal to voltage and is digitized to a value between
 1647 0 and 16384 by an AD9252 14-bit analog to digital converter (ADC) which samples the signal at
 1648 41.667 MHz.⁵ Each FEB contains a Xilinx Artix-7 FPGA that sends the ADC data upstream to
 1649 multi-gigabit receivers and controls and monitors the hybrid state and configuration.

1650 The digitized data, low-voltage power, and high-voltage bias from the FEBs is transferred to
 1651 electronic boards on the penetration of the vacuum flange (called “flange boards”) through mini
 1652 SAS cable for data and twisted pair cables for power and bias.⁶ There are two flange boards on

⁵The 14-bit samples for each of the 23040 APV25 channels is too much data to store. The DAQ requires a readout threshold of three out of six samples above a threshold (three times the channel noise above the mean) that is predetermined from offline calibration.

⁶The flange boards are custom-made since the number of required connections is too high for conventional vacuum

1653 the beam right side - one for high voltage and the other for low voltage. The four flange boards
1654 located on the beam left side convert the digitized signal to optical using fiber transceivers so the
1655 signal can be transferred a large distance to the general-purpose Reconfigurable Cluster Elements
1656 (RCE) platform. The RCE platform was developed at SLAC and is housed in a standard Advanced
1657 Telecommunications Computing Architecture (ATCA) crate. The data from the FEBs is distributed
1658 on a Cluster on board (COB) between two ATCA blades housed inside the crate. Each COB contains
1659 8 RCE processing nodes which use Xilinx Zynq-7000 series FGPAs to apply data reduction to signals
1660 from the flange boards and build events.

1661 Each COB houses several generic hardware daughterboards common to RCE platforms including
1662 four Data Processing Modules (DPM) and one Data Transport Module (DTM). The DPMs process
1663 and reduce data at high speed while the DTM is responsible for timing and trigger distribution.
1664 The only HPS-specific hardware on the COB is the Rear Transition Module (RTM) which interfaces
1665 the optical fibers from the signal flange boards to the COB. The SVT DAQ utilizes a total of two
1666 COBS and two RTMs. In addition to the core of the DAQ, the rack also contains the low and high
1667 voltage Wiener MPOD power supplies which are commonly used for a variety of JLab experiments.
1668 A schematic of the SVT DAQ system is shown in Fig. 3.16.

1669 The SVT services - motion, cooling, and power - are supplied from outside the vacuum through
1670 several flanges located upstream of the vacuum chamber. The SVT is cooled through 2 independent
1671 cooling loops one for the silicon sensors and the other for the FEBs. The silicon sensors must be kept
1672 below 0° C in order to avoid further radiation damage due to higher temperature (called reverse
1673 annealing). They are cooled through a hydrofluoroether compound circulating through copper lines
1674 embedded into the U-channels where top and bottom are split and L1-L3 and L4-L6 are connected
1675 in series. The specialized fluid is necessary since its low viscosity maintains high flow rates at low
1676 temperatures.

1677 Only the heat produced from operating the FEBs themselves needs to be dissipated. Thus,
1678 distilled water is sufficient as a cooling fluid and is circulated through copper lines embedded in the
1679 FEB cooling plate. The FEBs themselves are cooled through direct thermal contact with the cooling
1680 plate. A picture of the FEBs on the cooling plate is shown in Fig. 3.17.

1681 In addition to cooling components, there are three linear shift stepper motors that provide
1682 independent motion control of the top and bottom U-channels as well as the target frame. The
1683 motors are powered and controlled by a Newport XPS controller. All three motors have both a
1684 hardware and software safety stop, while the two motors that control the U-channel linear motion
1685 also include a precision limit switch to ensure the SVT is not accidentally driven into the beam.



Figure 3.17: The FEB cooling plate complete with 10 FEBs fastened to the front and back of the plate.

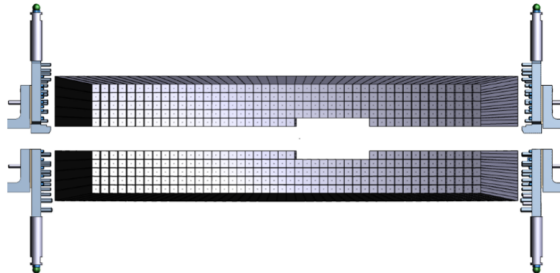


Figure 3.18: A rendering of the beam's eye view of the HPS Ecal. Each segment is one of the 442 lead tungstate crystals and the Ecal is split in half to avoid radiation damage from the most intense parts of the beam.

3.4 Electromagnetic Calorimeter and Trigger

The electromagnetic calorimeter (ECal) is an array of 442 lead tungstate scintillating crystals (PbWO_4) and is used primarily for precision timing and triggering [25]. The crystals are reused from the CLAS Inner Calorimeter (IC). The crystals have front faces of size $1.3 \times 1.3 \text{ cm}^2$, are 16 cm long, and are tapered such that the back faces have dimensions $1.6 \times 1.6 \text{ cm}^2$ for acceptance purposes. The Ecal itself is split into top and bottom halves much like the SVT to avoid the most intense parts of the beam plane. Each half contains 5 rows of 46 crystals with the exception of the removal of 9 crystals in the innermost row to avoid large occupancy from beam background. This is referred to as the Ecal hole or electron gap. The innermost rows are positioned 2 cm from the beam plane to maintain the 15 mrad design opening angle. The face of the Ecal is positioned 139.3 cm from the target position. Scintillation light from each crystal is detected by an avalanche photodiode (APD) on the back face of the crystal (specifically, a Hamamatsu S8664-1010 APD). One blue and one red LED are positioned on the front face of each crystal and are used for monitoring purposes (specifically radiation damage and stability of readout gain). Since the scintillator response is temperature-dependent, the Ecal is surrounded by a thermal enclosure.

The primary purpose of the Ecal is to trigger the experiment. Jefferson Laboratory has developed general-purpose readout boards called the FADC250 digitizer boards, or simply FADC. APD signals are amplified by a preamplifier that outputs signals through a motherboard. Each FADC board has 16 input channels and are continuously digitized at 250 MHz to a 12-bit precision which are then stored in 8 μs deep pipelines to await being readout if a trigger signal is received. There are several readout modes available, but HPS utilizes the readout mode that outputs a window of 100 samples that allows pulse fitting with optimal time resolution.

The FADC boards are located in VXS crates also developed by Jefferson Laboratory as a general-purpose trigger framework. An algorithm that continuously looks for threshold crossings and integrates the digitized signal from the FADC within a fixed window converts the integration to an

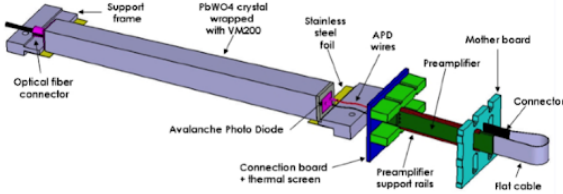


Figure 3.19: A schematic of a PbWO_4 crystal in the Ecal.

1711 energy from previously calibrated values from cosmic rays. This gives a crystal position, energy, and
 1712 time of the threshold crossing which are then passed to the Global Trigger Processor (GTP) every
 1713 32 ns. Each Ecal half has a GTP board which clusters hits by looking at a 3×3 block around
 1714 a center crystal with a least a 50 MeV ([Is this number still accurate??](#)) and the surrounding hits
 1715 within 16 ns of the center hit. This defines a cluster with a center crystal, hit time, number of hits,
 1716 and total energy. Each GTP reports these clusters to the Single Subsystem Processor (SSP) board.

1717 The SSP uses these clusters to make a decision on the Trigger. For the 2016 Engineering Run, we
 1718 have 5 triggers. The first is a “pulser” trigger which fires at a fixed rate of 100 kHz. Next, there are
 1719 two triggers that fire on single clusters that are called “singles1” and its corresponding trigger which
 1720 has looser requirements “singles0”. Finally, there are two triggers that fire on a pair of top-bottom
 1721 clusters (at least one cluster in each GTP). These are called “pairs1” and “pairs0” triggers, where
 1722 pairs0 is the looser version of pairs1. The pairs1 is our nominal trigger that is used for the physics
 1723 analysis. In order to prevent the other triggers from triggering at a rate higher than the DAQ can
 1724 handle, the singles triggers and the pairs0 trigger are prescaled such that one trigger in 2^n triggers
 1725 are accepted where n is in the range of 10 to 13.

1726 Once the SSP makes a trigger decision, if a cluster or pair of clusters meets the requirements
 1727 above a trigger is sent to the Trigger Supervisor board (TS) and distributes the trigger to the Trigger
 1728 Interface (TI) boards. The TS can reject the trigger if a subsystem is not ready to accept a trigger
 1729 or the trigger follows too closely to another trigger.

1730 The livetime of the DAQ, that is the fraction of time the DAQ is willing to receive triggers,
 1731 must be understood in order to properly normalize the data. One way to measure the livetime is to
 1732 use the pulser trigger. Since the pulser trigger fires at a constant rate, the ratio of the number of
 1733 pulser triggers recorded to the number of pulser triggers that should have been recorded based on
 1734 the 100 Hz rate is a direct measurement of the livetime. Another way to measure the livetime is to
 1735 combine the measurement of integrated charge from the Faraday cup as described in Sec. 3.2 with
 1736 a measurement of the integrated charge with the DAQ live. This is called the “gated Faraday cup
 1737 scaler”, and the ratio of this scalar to the total integrated charge is the DAQ livetime. [What do we](#)
 1738 [actually use for 2016?](#)

1739 The HPS physics trigger is designed to maximize efficiency for A' s, or more generally e^+e^- pairs

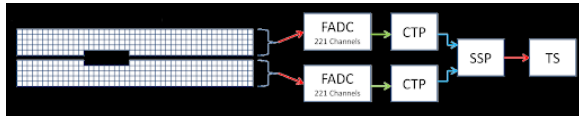


Figure 3.20: A schematic of the trigger for the Ecal. Top and bottom halves of the Ecal are each readout by FADC readout boards, and then sent to the SSP where a trigger decision is made.

near the beam energy, while sufficiently suppressing backgrounds to avoid overwhelming the DAQ systems. The most significant one-cluster background is elastically-scattered electrons in the target. Thus a trigger requiring at least two clusters will eliminate a large fraction of these. The largest source two-cluster backgrounds is wide-angle bremsstrahlung (WABs) followed by elastically-scattered electrons in the target in coincidence with WABs. These can be eliminated by first requiring top and bottom coincident clusters as well as further timing and energy cuts.

The time coincidence between top and bottom clusters are required to be within 12 ns and is corrected for time walk. In addition to timing requirements, there is a coplanarity requirement that requires two clusters on opposite sides of the beam axis. It is intended to select only e^+e^- coincident pairs which are expected on average to be symmetric about the beam axis. The azimuthal angle ϕ relative to the beam axis of the top and bottom cluster is required to be within $\pm 30^\circ$ of 180° .

Furthermore, the trigger requires some basic energy requirements. First, a maximum energy sum requirement eliminates a large fraction of coincident beam scattered electrons. For the minimum energy requirements, it is important to note that there are substantial energy losses from a variety of sources in the Ecal such as the absorption of energy by the vacuum flange, gaps between crystals, or the back of the Ecal. As stated previously, this is accounted for in the reconstruction by detailed MC studies, but is not accounted for in the trigger. In addition, particles can hit the innermost row of the Ecal and lose energy where much of the shower is lost in the beam gap. This is especially important since a large fraction of signal, particularly at lower mass due to the smaller opening angle, occurs at the beam edge of the calorimeter. For this reason, there are only loose requirements on the minimum energy on individual clusters and minimum energy sum that are below the truth energy threshold of what one would expect from an A' .

Finally, it is expected that the lower energy decay particles from A' 's will have be further from the beam axis due to increased bending of the lower momentum particle from the magnetic field. The energy-distance cut rejects particles that are both low energy and close to the beam axis. This cut has the effect of first rejecting wide-angle bremsstrahlung which is a photon that is typically lower energy and closer to the beam axis and second, rejecting beam electrons that scrape the Ecal edge where most energy is lost. The cut is based on the cluster energy E_{low} and the cluster distance from the beam axis r_{low} and is expressed as $E_{low} + (5.5 \text{ MeV / mm}) r_{low} > 0.7 \text{ GeV}$.

The pairs1 trigger requirements - including the timing, cluster energy, cluster size, energy sum, cluster energy difference, coplanarity, and energy-distance requirements - are summarized in Table

₁₇₇₁ 3.2.

Trigger Description	Value
Time Difference	$ t_{top} - t_{bot} \leq 12$ ns
Cluster Energy	$0.15 < E < 1.4$ GeV
Cluster Size	$N_{hits} \geq 1$
Energy Sum	$0.6 < E_{top} + E_{bot} < 2.0$ GeV
Energy Difference	$ E_{top} - E_{bot} < 1.1$ GeV
Coplanarity	$ \phi_{top} - \phi_{bot} - 180^\circ < 35^\circ$
Energy-Distance	$E_{low} + (5.5 \text{ MeV / mm}) r_{low} > 0.7 \text{ GeV}$

Table 3.2: Summary of the pairs1 Trigger Selection from the 2016 Engineering Run.

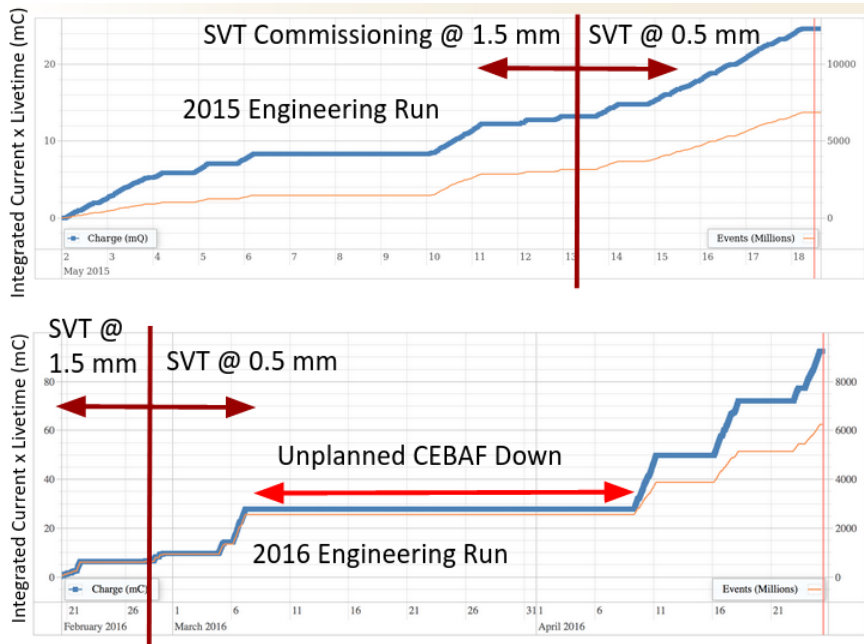


Figure 3.21: A summary for the integrated charge over time for the Top: 2015 Engineering Run and Bottom: 2016 Engineering Run. **Replace these figures**

1772 3.5 Datasets

1773 To date, HPS has three data taking runs - an engineering run in 2015, and engineering run in 2016,
 1774 and a physics run in 2019. The 2015 engineering run was taken with a beam energy of 1.056 GeV
 1775 and beam current of 50 nA incident on a 4 μm target. The total luminosity taken over opportunistic
 1776 nights and weekends amount to 1166 nb^{-1} which corresponds to 1.7 PAC days. A broken cryogenic
 1777 helium liquifier (CHL) shortly before the run began resulted in the operation of only a single CEBAF
 1778 linac for this run (as opposed to the usual two linacs). This gave HPS a unique opportunity to run
 1779 at this beam energy equivalent to half a pass which would have otherwise been unavailable.

1780 The 2016 Engineering Run was taken with a beam energy of 2.3 GeV and beam current of 200
 1781 nA incident on a 8 μm target. The total luminosity taken over weekends amount to 10753 nb^{-1}
 1782 which corresponds to and 5.4 PAC days. Much of the analysis is performed on a blinded $\sim 10\%$
 1783 sample (1101 nb^{-1}) before the final results over the whole dataset are produced. The data for the
 1784 2016 Engineering Run was collected by running on weekends over the span of several months.

1785 A summary of the accumulated luminosity over time for the 2015 and 2016 Engineering Runs is
 1786 shown in Fig. 3.21. The focus of this thesis is the displaced vertex analysis from the 2016 engineering
 1787 run. The 2019 Physics Run was undertaken with an upgraded detector, described in Sec. 6.

1788 **Chapter 4**

1789 **Event Reconstruction & Selection**

1790 Reconstruction is the process in a given event of building actual physics processes, such as an A' decay,
1791 from the raw hits of the detector channels readout by the trigger. The HPS event reconstruction
1792 is based on the lcsim software toolkit [56] and uses both reconstructed energy clusters from the Ecal
1793 and tracks from the SVT, which are done independently until Ecal clusters and tracks are matched
1794 by extrapolating the track state at the last layer of the SVT to a cluster in the Ecal for particle
1795 identification. These objects, mainly e^+e^- pairs or e^-e^- pairs, are used to reconstruct vertices used
1796 for the physics analysis. The multiple stages of the HPS reconstruction - SVT hit reconstruction,
1797 tracking, vertexing, and Ecal clusters - are as follows in the proceeding sections.

1798 **4.1 HPS Coordinate Systems**

Coordinate System	<i>x</i>	<i>y</i>	<i>z</i>
JLab Coordinates	Beam left	Vertical	Beam direction
Detector/HPS Coordinates	Beam left rot. -30.5 mrad	Vertical	Beam direction rot. -30.5 mrad
Tracking/lcsim Coordinates	Beam direction	Beam left	Vertical

Table 4.1: Basis for several different coordinate systems used in the HPS reconstruction and analysis.

1799 There are three coordinate systems utilized in the HPS reconstruction process - the global coor-
1800 dinates (JLab coordinates), the HPS coordinate system (detector coordinates), and tracking coor-
1801 dinates (lcsim coordinates). Each coordinate system is used in a different part of the reconstruction
1802 process since each has simplifying features. First, the JLab coordinate system is defined globally
1803 by the Hall B beamline where the the *x*-axis points beam left in the bend plane, the *y*-axis points
1804 vertically upwards, and the *z*-axis points along the direction of the beam. The origin is set at the
1805 intersection of the nominal beam and nominal target position. Due to the asymmetry of HPS with

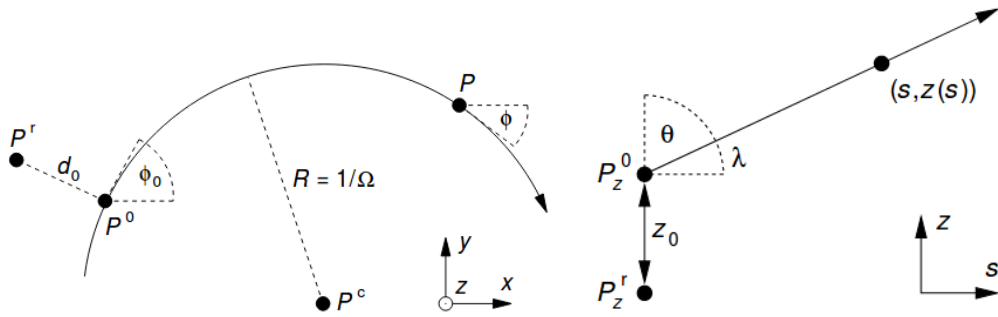


Figure 4.1: A schematic of the linear collider tracking parameters 4.1 [69].

respect to the chicane, where the beam is bent due to the first dipole magnet in the chicane by 30.5 mrad about the y -axis in the $-x$ -direction, the HPS z -axis and x -axis are also rotated by 30.5 mrad. Since the beam travels in the $+z$ -direction in HPS coordinates at the target, this is the natural reference frame for reconstructed particles and, unless otherwise stated, the physics analysis including positions and momenta will be performed in this frame.

The entire HPS SVT lies within a roughly uniform vertical magnetic field, thus a charged particle trajectory will form a helix. Unfortunately, the coordinate systems for track reconstruction and analysis on HPS are different. HPS utilizes perigee parametrization of tracks that fixes a magnetic field along the z -axis (which is the y -axis in HPS coordinates). The tracking coordinates are oriented approximately such that the x -axis points along the direction of the beam, the y -axis points beam left, and the z -axis points vertically upwards. In addition, each track is defined by 5 track parameters - Ω , d_0 , z_0 , $\tan\lambda$, and ϕ - and are briefly described below and shown in Fig. 4.1 [69].

1. Ω is the signed curvature of the track (i.e. the inverse of the radius $C = -q/R$).
2. d_0 is the signed impact parameter in the xy tracking plane. In the HPS detector frame, this translates to the impact parameter along the x (horizontal) direction.
3. z_0 is the tracking z position at the point of closest approach to the reference point. This is the key tracking parameter for the isolation cut. In the HPS detector frame, this approximately corresponds to the impact parameter in the y (vertical) direction.
4. $\tan\lambda$ is the slope of the straight line in the sz tracking plane. In the HPS detector frame, this translates to the slope of the track dy/dz in the yz plane.
5. ϕ is the azimuthal angle of the momentum of the particle at point of closest approach to the reference point.

Due to multiple scattering in the silicon sensors, each segment of the track between scattering planes is described by a separate helix, called a track state. Thus, each track segment will have its

1830 own set of unique 5 track parameters as well as a unique 5×5 covariance matrix of these track
 1831 parameters, and a track will have 11 or 13 track states depending on the number of hits on track.
 1832 This process is described in Sec 4.3.3. The last importnat tracking parameter is the path length of
 1833 the helix, denoted as s , which is useful for parametrization of the helix.

1834 4.2 Ecal Reconstruction

1835 Electromagnetic particles that are incident on the Ecal and shower within the Ecal deposit energy
 1836 in several crystals which can then be clustered together to give both the total energy deposited and
 1837 an estimate of the hit position on the front face of the Ecal. The Ecal reconstruction is the process
 1838 of building particle clusters from the waveforms readout in single crystals of the Ecal for a given
 1839 event. Ecal crystals that are readout store 100 samples in 4 ns intervals relative to the trigger time.
 1840 The pulse shape is fit with a three-pole function

$$F_{3pole}(t) = \frac{t^2}{2\tau^3} e^{-\frac{t}{\tau}} \quad (4.1)$$

1841 The time constant τ is calibrated offline for each channel and is typically ~ 2.4 ns. From this
 1842 function, the pedestal, time of the pulse, and amplitude are fit in offline reconstruction and pileup is
 1843 ignored. From the amplitude, the pulse is converted to energy by two types of channel calibrations
 1844 - cosmic rays and elastic scatters in the target ([cite](#)). Cosmic rays, which pass downward through
 1845 the Ecal and deposit a calculable amount of energy in the crystals, are used for a preliminary
 1846 Ecal calibration before data taking. After data taking, cluster energy is calibrated from elastically
 1847 scattered electrons from the target, which are very near the beam energy, and the gain constants for
 1848 every crystal are adjusted until the energies match what is observed in MC. Both cosmic ray MIPs
 1849 and elastically scattered electrons populate the full range of interest in energy.

1850 Cosmic rays are calibrated before data taking with the beam off through the detection of mini-
 1851 mum ionizing particles (MIPs), which have a known rate of energy loss, passing downwards through
 1852 the Ecal.

1853 In order to form clusters in the Ecal, individual hits are grouped together using a clustering
 1854 algorithm adapted from the CLAS Inner Calorimeter [[cite](#)]. A crystal which has the most energy in
 1855 a local group of hits becomes the seed for a cluster, and the algorithm looks for hits in neighboring
 1856 crystals which are within 8 ns of the seed to build the cluster. Since higher energy hits have better
 1857 timing resolution, the seed hit time is defined as the time of the cluster.

1858 The energy of the cluster is initially the sum of the individual hit energies. However, this energy
 1859 does not account for parts of the electromagnetic showers that are lost on the Ecal edges or energy
 1860 absorbed in the vacuum flanges ([Cite these.](#)). In addition, particles generally enter an Ecal crystal
 1861 at an angle off axis from crystal axis and electromagnetic showers deposit energies at all Ecal depths
 1862 resulting in the fact that maximum energy deposition may not occur in the same crystal as the

1863 crystal whose front face the particle has traversed. As a result, energy corrections are based on
1864 detailed MC studies and the energy is corrected as a function of particle type (photon, electron, or
1865 positron), energy, and angle, where the particle type must be determined by track-cluster matching
1866 later in the reconstruction described in Sec. 4.4. In addition, the position of the cluster is initially
1867 determined by a logarithmically weighted centroid. For the same reason as energy, the position must
1868 also be corrected and is done so in the same MC studies as energy. [cite these MC studies](#)

1869 4.3 SVT Reconstruction

1870 The SVT reconstruction is the process of building particle tracks from the collection of waveforms
1871 readout from all the single strips in the SVT which have been hit. These tracks are used to form
1872 electron and positron objects (tracks matched with Ecal clusters), which are then used to form
1873 vertices used in the final analysis.

1874 4.3.1 SVT Hit Reconstruction

1875 For each trigger, SVT channels where at least three of the six samples are above the readout thresh-
1876 old, that was determined by offline calibration before data taking in calibration runs (for reasons
1877 described in Sec. 3.3.3), are readout. For each strip in the SVT that is readout, the APV25 reads
1878 out six samples of 24 ns intervals. The APV25 response is modeled as a four pole filter with three
1879 coincident poles (i.e. three of the poles with the same time constant). This gives the following
1880 transfer function with two time constants τ_1 and τ_2 .

$$\tilde{F}(\omega) = \frac{1}{(1 + i\omega\tau_1)(1 + i\omega\tau_2)^3} \quad (4.2)$$

1881 The inverse Fourier Transform of this transform function is the pulse shape given by

$$F(t, \tau_1, \tau_2) = A \frac{\tau_1^2}{(\tau_1 - \tau_2)^3} \left(e^{-\frac{t-t_0}{\tau_1}} - \sum_{k=0}^2 \left(\frac{\tau_1 - \tau_2}{\tau_1 \tau_2} (t - t_0) \right)^k \frac{e^{-\frac{t-t_0}{\tau_2}}}{k!} \right) \quad (4.3)$$

1882 The time constants are predetermined offline by fitting pulses in calibration runs and have typical
1883 values of $\tau_1 \approx 72$ ns and $\tau_2 \approx 12$ ns. t_0 is defined as the time the fit crosses 0 and is set as the time
1884 of the raw hit. A is related to the amplitude of the pulse in ADC counts. Both of these quantities
1885 are determined by the fit in offline reconstruction and an example waveform and fit is shown in Fig.
1886 4.2.

1887 The pulse is fit to a pileup algorithm where a fit to a single pulse is compared to a fit with a
1888 double pulse. If the single pulse fit has a $\chi^2_{prob} < 0.5$, a refit with two pulses is attempted. If this
1889 produces an improved χ^2_{prob} , the double pulse fit is accepted, else the single pulse fit is accepted.
1890 The time of the pulse is corrected after the fit for several effects including a run-dependent phase
1891 shift, trigger time, and time of flight.

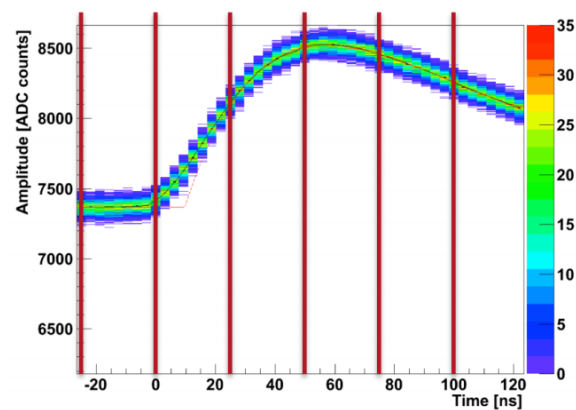


Figure 4.2: A plot of the digitized waveform that is stored from the DAQ and the fit using Eq. 4.3. The 6 samples used for the fit are in 24 ns intervals (between the red lines).

1892 4.3.2 SVT Cluster and 3D Hit Reconstruction

1893 After single strip hit reconstruction, the hits are clustered together with neighboring hits using
1894 the nearest neighbor RMS Clusterer algorithm. The algorithm uses the amplitudes in ADC counts
1895 (where it is not necessary to convert amplitude to energy deposition) and seeds hits whose amplitude
1896 are at least 4σ above the noise of the channel, where σ is the RMS of the noise of the channel. From
1897 there, it appends neighboring strips whose pulse times are within 8 ns of the seed strip and whose
1898 amplitudes are at least 3 RMS above the noise of the channel. In addition, each of the strips, whether
1899 seed or neighbor channel, must have a χ^2 probability for the fit in Eq. 4.3 greater than 3.20×10^{-6} .
1900 The position of the cluster is the amplitude-weighted centroid of the hits ($\sum x_i A_i / \sum A_i$). Typically,
1901 SVT clusters are composed of one or two strips hits in approximately equal proportion. Since time
1902 resolution is significantly degraded for hits with low energy deposition, the time of the SVT cluster
1903 is weighted by the square of the amplitude ($\sum t_i A_i^2 / \sum A_i^2$).

1904 The 1D strip clusters in each axial sensor in a given layer are then paired together with the
1905 corresponding stereo sensor in the same layer to form 3D hits. Only clusters within 12 ns of the
1906 trigger time and with at least an amplitude of 400 ADC counts are considered. As a reference, a
1907 minimally ionizing particle (MIP) will typically have an amplitude of ~ 1200 ADC counts. These
1908 clusters must cross physically in space from the perspective of the primary (with some tolerance)
1909 and be within a 16 ns coincidence of each other. A 3D hit is reconstructed at the intersection of
1910 the two strip clusters. Since this intersection depends on the track angle, the 3D hit position is
1911 recalculated every time the hit is used in a track fit to correct for parallax effects.

4.3.3 Track Reconstruction

The SeedTracker algorithm, which was developed for design studies with the SiD detector ([cite](#)), is performed as a simple method of track finding for HPS. Seed tracks, that is tracks that result from SeedTracker, are found using several different track finding strategies. The tracking strategies are as follows.

1. A track candidate is found using a particular three (of the six possible) 3D hits to form a helical track.
2. This helix is extrapolated to a confirm layer and, if this confirm layer has a 3D hit consistent with the helix, this hit is appended to the helical trajectory. Else, the track candidate is discarded.
3. Lastly this 4-hit track is extrapolated to the remaining two layers called the extend layers. The 3D hits in those layers that are consistent with the helix are appended. We require at least one of the extend layers to have a 3D hit consistent with the helix, thus requiring a minimum of five 3D hits on a track. If this extend requirement is not met, the track candidate is discarded.

Four tracking strategies are used because any single strategy using this method will not find tracks that happen to miss a seed or confirm layer. The four tracking strategies used in the reconstruction are s-345 c-2 e-16, s-456 c-3 e-21, s-123 c-4 e-56, and s-123 c-5 e-46 where s, c, and e are abbreviations for seed, confirm, and extend, respectively. As an example, s-345 c-2 e-16 seeds track candidates using 3D hits on layers 3, 4, and 5. Then, this helical fit is extrapolated to layer 2, followed by layers 1 and 6. The seed tracks from 345 that successfully append a hit in layer 2 and either layer 1 or 6 are stored as a track candidate to be used for the remaining reconstruction.

In addition, there are several other requirements the track must pass. The RMS time of all the hits on the track must fall within 8 ns. The track must have a χ^2 less than 100 (including an individual hit χ^2 less than 10), a distance of closest approach $d0$ less than 15 mm, an impact parameter $z0$ of less than 15 mm, and a minimum transverse momentum of 100 MeV.

The SeedTracker algorithm returns a helical track fit to 3D hits, but fails to take multiple scattering into account which results in an artificially worsened momentum resolution. In order to account for multiple scattering effects, the helical track fit is refit using the General Broken Lines (GBL) algorithm [35] [67]. For HPS, the GBL algorithm treats each sensor plane in the SVT as a source of scattering and fits a track segment (defined by 5 parameters described in Sec. 4.1 that define the track state) between each sensor plane and extrapolates a track segment on the first and last SVT sensor plane. For the reconstruction of the 2016 Engineering Run dataset, the GBL track is required to have a χ^2 per degrees of freedom less than 12. The GBL fit minimizes the hit residuals and scattering angles (called kinks) for each of these track segments and provides performance equivalent to a Kalman filter. However, the GBL implementation for HPS requires 3D

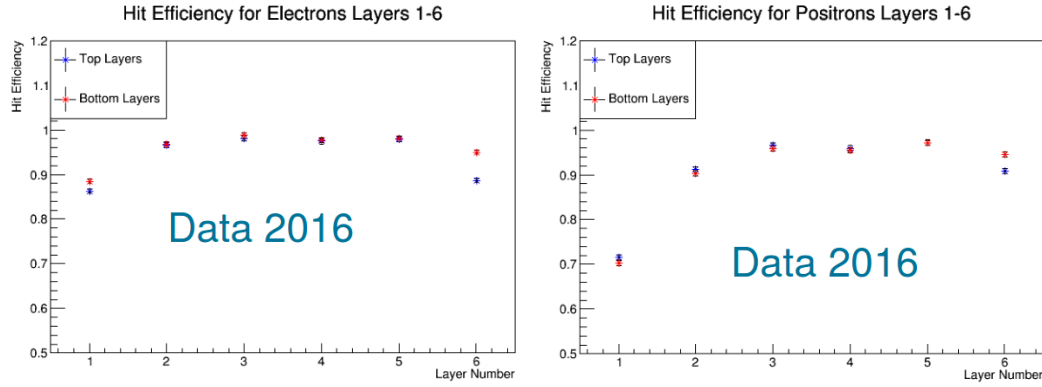


Figure 4.3: The hit efficiency for each top/bottom layer of the SVT for Left: electrons and Right: positrons. The decrease in efficiency in layer 1 and layer 6 can be attributed to increased occupancy and a large number of dead channels, respectively. The difference between electrons and positrons in layer 1 hit efficiency is a result of WABs, where a conversion occurs in layer 1 and fails to produce a hit in both axial and stereo sensors, which is measured as a hit inefficiency.

1947 hits from SeedTracker before inputting the track into the GBL algorithm. This 3D hit requirement
 1948 results in some efficiency loss due to acceptance for particles that only traverse either the axial or
 1949 stereosensor in a given layer. In addition, there are further efficiency losses due to the inherent
 1950 efficiency effects of individual sensors where an inefficiency in either the axial or stereosensor will
 1951 not form a 3D hit. For future track reconstruction for HPS, a Kalman filter that utilizes strip hits
 1952 for pattern recognition instead of 3D hits will be used to regain this loss of efficiency.

1953 A plot of the hit efficiency for each SVT layer separated by hemisphere and curvature is shown
 1954 in Fig. 4.3. Layer 1 has decreased hit efficiency due a larger occupancy than the rest of the detector,
 1955 while layer 6 has decreased hit efficiency due to a large number of dead channels in that layer.
 1956 Positrons also have a decrease layer 1 efficiency due to wide-angle Bremsstrahlung conversions in
 1957 layer 1. The methods of measuring hit efficiency as well as separating the measurement by channel
 1958 will be described in more detail in Sec. 4.6.

1959 4.4 Track Cluster Matching

1960 Tracks are matched to Ecal clusters by extrapolating the track state of the final SVT hit to the face
1961 of the Ecal though a non-uniform magnetic field map, which accounts for the dipole magnet’s fringe
1962 field, and comparing this extrapolated position to the Ecal cluster position. Matching a track to
1963 an Ecal cluster confirms the reality of the track since all particles of interest that produce a track
1964 should also form an Ecal cluster.¹ In addition, since the Ecal offers a better time estimate than a
1965 track, the time coincidence of two Ecal clusters can be used to reduce the effects of accidentals.

1966 The track is matched with the cluster with the minimum n_σ , where σ is the error on the ex-
1967 trapulated track position from layer 6 of the SVT to the front face of the Ecal , provided that the
1968 match is less than 30σ . Subsequent analysis imposes a stricter requirement. Electron objects are
1969 defined as a negatively curved GBL track that is matched to an Ecal cluster in the same detector
1970 volume. Similarly, positron objects are defined as a positively curved GBL track that is matched to
1971 an Ecal cluster in the same detector volume. The electron and positron objects are used as inputs
1972 to the vertex fitter. The remaining Ecal clusters that do not have an associated matching track
1973 are defined as photon objects. To potentially further reduce accidentals, one might expect the ratio
1974 of the energy of the Ecal cluster to the momentum of the matched track (E/p) to have a mean at
1975 one with a small σ corresponding to the energy and momentum resolutions. However, the particles
1976 near the edge of the Ecal, where much of the action occurs, typically only deposit a fraction of their
1977 energy into the Ecal crystals. Thus, E/p is non-Gaussian with a mean below 1 and as a result, no
1978 restriction on E/p is imposed.

¹In reality, particles of interest (typically electrons) can produce tracks but extrapolate to the so-called “Ecal hole” which was cut out to reduce occupancy from elastically-scattered beam particles. These tracks can be recovered by implementing a positron-only trigger and relaxing the requirement of an electron track matched to an Ecal cluster. This is done in the upgraded detector for future running described in Sec. 6.1.

Cut Description	Requirement
Cluster Time Difference	$ t_{e^+Cluster} - t_{e^-Cluster} < 2.5 \text{ ns}$
e^+ Track-Cluster Time Difference	$ t_{e^+Track} - t_{e^+Cluster} - 55 < 10 \text{ ns}$
e^- Track-Cluster Time Difference	$ t_{e^-Track} - t_{e^-Cluster} - 55 < 10 \text{ ns}$
Ecal clusters in opposite volumes	$y_{e^+Cluster} \times y_{e^-Cluster} < 0$
Loose track-cluster match	$\chi^2 < 15$
Beam electron cut	$p(e^-) < 2.15 \text{ GeV}$
Track Quality	$\chi^2/\text{dof} < 12$
Maximum Vertex Momentum	$V_{0p} < 2.8 \text{ GeV}$

Table 4.2: Requirements applied to V_0 particles during the reconstruction stage for data (i.e. pre-processing selection).

Cut Description	Requirement
Cluster Time Difference	$ t_{e^+Cluster} - t_{e^-Cluster} < 5 \text{ ns}$
Track-Cluster Time Difference	$ t_{e^+Track} - t_{e^+Cluster} - 43 < 10 \text{ ns}$
Track-Cluster Time Difference	$ t_{e^-Track} - t_{e^-Cluster} - 43 < 10 \text{ ns}$
Ecal clusters in opposite volumes	$y_{e^+Cluster} \times y_{e^-Cluster} < 0$
Loose track-cluster match	$\chi^2 < 15$
Beam electron cut	$p(e^-) < 2.15 \text{ GeV}$
Track Quality	$\chi^2/\text{dof} < 6$
Maximum Vertex Momentum	$V_{0p} < 2.8 \text{ GeV}$

Table 4.3: Requirements applied to V_0 particles during the reconstruction stage for MC (i.e. pre-processing selection).

4.5 Vertexing

Every pair of e^+ and e^- objects in an event is fitted to a Billior vertex fitter [32]. The Billior vertex fit is a fast vertex fit that finds the best-fit vertex position and track parameters based on the individual track parameters and covariance matrices of the e^+e^- pair. This provides a vertex with a reconstructed 3D position based on the distance of closest approach between the two tracks as well as a reconstructed mass and momentum that are determined based on the fitted track parameters at the fitted vertex position.

Given a collection of vertices made up of electron and positron tracks, additional constraints can be imposed to reduce backgrounds. Any real heavy photon decay vertex will have tracks in opposite hemispheres of the detector, point back to the beamspot, and have a vertex momentum (the sum of the momenta of the two tracks) consistent with heavy photon kinematics. If the e^+ and e^- objects are in the same hemisphere of the detector (most likely converted bremsstrahlung), they are placed in the Unconstrained Vc Collection and not considered for this analysis. If the e^+ and e^- objects are in opposite hemispheres of the detector and they pass the preprocessing selection (cuts in the reconstruction) describe in Tables 4.2 and 4.3, then they are placed in the Unconstrained

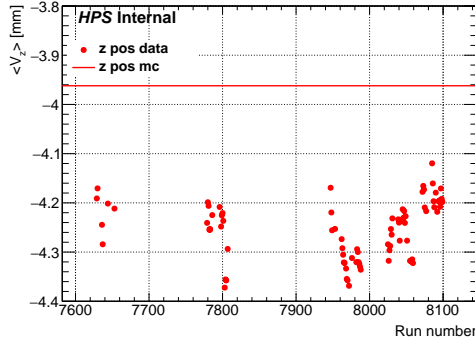


Figure 4.4: The run-dependent average position in z for unconstrained vertices fit represented by solid points and a solid line for data and MC simulation, respectively.

1994 V0 Particle Collection and considered for the analysis. These standard loose restrictions come from
 1995 previous analysis and will be stricter at the analysis stage. The descriptions and motivations for
 1996 these cuts are described in detail in Sec. 4.10.

1997 In addition, a target constraint (x , y , and z positions) and a beamspot (x and y components
 1998 of the V0 momentum) are placed on the V0 particle and placed in separate collections with a one-
 1999 to-one-to-one mapping between the three collections. Specifically, the target constraint requires the
 2000 vertex to be consistent with the z position of the target and the x and y positions and sizes of
 2001 the beamspot while the beamspot constraint requires the vertex momentum to point back to the
 2002 beamspot at the target z position. Unconstrained vertices are used for the displaced vertex analysis
 2003 while target constrained vertices are used for the resonance search.

2004 In addition, all electron object pairs are also fit with a Billior Vertex and placed in the un-
 2005 constrained Møller Candidate Vertex Collection. Møller candidates are also fit with target and
 2006 beamspot constraints in separate collections and mapped in the same way. The Møller candidates
 2007 are used for the studying the data/MC comparison of the mass resolution as described in Sec. 5.2.

2008 The beamspot and target constrained Billior vertices both use the beam position and size along
 2009 with the target position in z as an input. For data, a run-by-run beam parameters were selected
 2010 based on the fits of distributions. Plots for these beam parameters are shown in Fig. 4.4 and Fig.
 2011 4.5 where the data is shown as points and the MC is shown as a solid line. For MC, for simplicity
 2012 and the parameters chosen to be constant and are $b_x = -0.224$ mm, $\sigma_x = 0.125$ mm, $b_y = -0.08$ mm,
 2013 and $\sigma_y = 0.030$ mm. These parameters were used for both the actual simulated beam position and
 2014 profile as well as inputs to the Billior Vertexer. These parameters are also used as inputs to the
 2015 event selection described in Sec. 5.

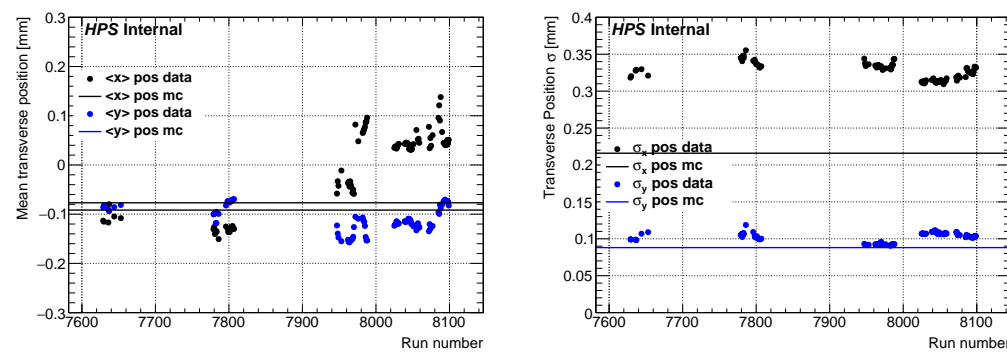


Figure 4.5: The run-dependent mean (left) and width (right) in x and y for the unconstrained vertex position in data. The MC is represented as a solid line.

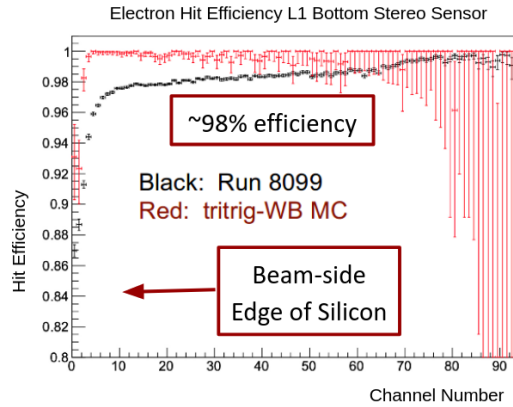


Figure 4.6: The measured SVT layer 1 efficiency for electrons in layer 1 bottom stereo sensor. The MC does not have the correct hit efficiencies.

4.6 Hit Efficiency

The HPS detector has hit efficiency effects that must be properly accounted for, particularly in the first layer of the SVT where occupancies are significantly higher than the other layers of the tracker. The main source of hit inefficiencies are wide angle bremsstrahlung conversions (WABs) in layer 1 of the SVT. Positrons from converted WABs are less likely to deposit sufficient energy into a silicon strip to pass readout threshold. This could result in a track that extrapolates to the active area of a layer 1 sensor that lacks a reconstructed hit, and thus will appear as a hit inefficiency in the method described below. This can be seen in a comparison of the hit efficiencies in layer 1 for positrons and electrons in Fig. 5.9 where the difference in efficiency between electrons and positrons can be attributed to converted WABs.

The remaining sources of hit inefficiencies are mostly unknown and are still under exploration. One hypothesis is some of the channels are readout, but the corresponding waveforms fail the fit requirements of the hit reconstruction stage described in Sec. 4.3. There is evidence of this from the fact that layer 1 hit inefficiencies occur at the strips nearest to the beam plane which have the highest occupancies due to elastically-scattered beam in the target and x-ray emissions from the target.

Hit efficiencies are measured using a track refit to a layer of interest, and an unbiased extrapolation to that layer to see if a hit lies within a certain window of the extrapolated position. As an example, in order to measure layer 1 efficiencies, the standard track reconstruction is performed on all layers except for layer 1. The tracks that meet basic quality requirements are extrapolated to both the axial and stereo sensor planes in layer 1. For the tracks that extrapolate to the active area of the sensor of interest, if a 1D hit is not found within 5σ of the extrapolation error it is counted as a hit inefficiency. The hit efficiency is defined as the ratio of the number of tracks with a hit within

2039 the defined extrapolation window to the total number of tracks sampled.

2040 Due to the highly non-uniform nature of occupancies on the sensors, the hit inefficiencies are
2041 studied in each sensor as a function of the extrapolated track position on the sensor. A sample of
2042 measured hit efficiency in data in comparison with MC as a function of channel number for the layer
2043 1 bottom stereo sensor is shown in Fig. 4.6. In addition, there are multiple scattering effects that
2044 result in a reduced measured hit efficiency on the edge of the sensors due to the fact that particle
2045 trajectories that don't traverse the active sensor area reconstruct a track that extrapolates to the
2046 active sensor area due to resolution effects (and thus counted as a hit inefficiency). This is most
2047 visible in MC which does not contain any hit efficiencies yet has a rapidly decreasing measured
2048 hit efficiency along the edge of the sensor. In principle, this can be corrected if errors on track
2049 extrapolations are computed correctly.

2050 Unfortunately hit efficiencies are not present in the MC, and methods of incorporating these
2051 effects are under investigation. However, hit efficiencies will affect the signal rate and distributions
2052 for a variety of variables of interest. To account for hit efficiencies in both a simple and reasonable
2053 way, a post-reconstruction hit killing algorithm based on track slope is applied to signal MC (and
2054 some background distributions). This method is described in detail in Sec. 5.3.2.



Figure 4.7: The target position is found to be -4.3 mm. I actually need to get these plots. Some placeholders are there for now.

2055 4.7 Tracker Alignment

2056 An initial mechanical survey is applied to the SVT as described in Sec. 3.3.2 which defines sensor
 2057 positions with a precision of $50 - 100 \mu\text{m}$. This level of imprecision will create systematic shifts
 2058 in track parameters and artificially degrade tracking and vertexing resolutions, thus is insufficient
 2059 to meet the HPS physics goals. In order to mitigate alignment-related effects, an offline alignment
 2060 using particle trajectories to find the sensor positions and orientations as close as possible to their
 2061 true values is performed.

2062 Detector alignment comes in two steps - internal alignment and global alignment. The internal
 2063 alignment finds the sensor positions relative to each other using the top and bottom volumes of the
 2064 SVT separately with the goal of minimizing the track χ^2 . The internal alignment utilizes Millepede-
 2065 II which was developed for fast alignment of large tracking detectors such as CMS [36] [37]. Each
 2066 sensor can be corrected by translation along or rotation about the three coordinate axis for a total
 2067 of six possible alignment corrections.

2068 These corrections are not equally important. For instance, track parameters are sensitive to
 2069 translations along the measurement direction in a given sensor but completely insensitive to trans-
 2070 lations along the non-measurement direction (other than minor acceptance affects for tracks on the
 2071 sensor edge). For simplicity, only translations along the measurement direction and beam direction
 2072 as well as rotations about the sensor normal were considered **Is this true?**. The sensor position and
 2073 orientations were found by iterating with different alignment configurations that float a single sensor
 2074 position or orientation until the optimal alignment constant is found.

2075 Global alignment involves fixing the so-called “weak modes” where sensors move coherently in

such a way that the track parameters and track quality are unaffected. Since there are 5 track parameters there are 5 weak modes - translating in the horizontal ($d0$) and vertical directions ($z0$), rotating tracks horizontally (ϕ) and vertically ($\tan\lambda$), and the horizontal quadratic shear (Ω).

Elastically-scattered electrons from the target ($e^-Z \rightarrow e^-Z$) have a known momentum at the beam energy, a known origin at the beam spot on the target, and sufficiently populate the full HPS angular acceptance making them ideal to study various weak modes. First the known curvature, provides a way to study the horizontal quadratic shear. Second, the known origin provides a way to study the translational weak modes as well as the z position of the target z_{targ} . In the yz -plane the extrapolated y position of any track can be parametrized as follows:

$$y(z) = y_{beam} + \tan\lambda \times (z - z_{targ}) \quad (4.4)$$

where $\tan\lambda$ is the track slope defined in Sec. 4.1. The equation contains two unknowns - the target position in z and the beam position in y_{beam} . This can be resolved by using both the top and bottom halves of the SVT by moving in the vertical direction until their measurements are in agreement. Similarly, the x position of the beamspot x_{beam} can be found using the same method.

Include the target position.

Møller-scattered electron pairs, that is beam electrons that scatter off of a target electron, have a known momentum equal to the momentum of the beam, including both magnitude and direction. This can be used to measure the beam angle deviation from the nominal beam axis. In addition, the two-body kinematics of Møller scattering is identical to Compton scattering and has the following relation:

$$m_e c^2 (1/E - 1/E_{beam}) = 1 - \cos \theta \quad (4.5)$$

where θ is the angle from the beam axis and E is the energy of the e^-e^- pair. As a result, all Møllers at a specific energy will scatter at the same angle from the beam axis which can be used to constrain both the rotational weak modes. Møller-scattered electrons are also useful as a “standard candle” for determining the mass scale and mass resolution as described in Sec. 5.2.

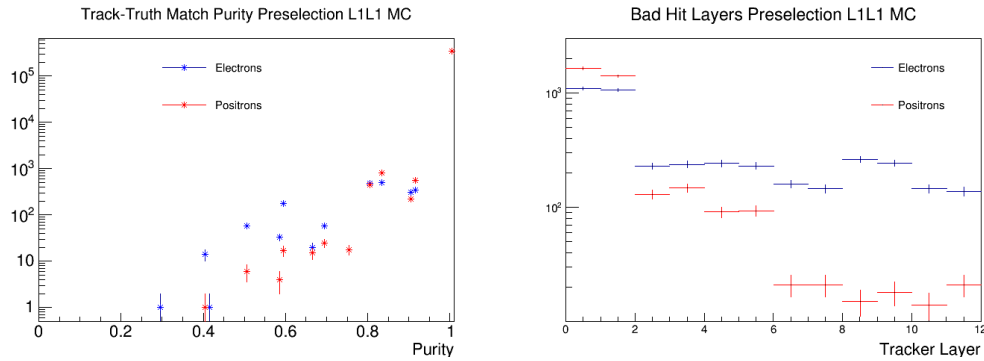


Figure 4.8: Left: The purity for e^+e^- tracks with preselection and layer 1 requirements for tritrig-wab-beam MC. Purity is a measure of how hit on track are associated with the truth matched particle. Right: Tracking layers (ordered in sensor number from upstream to downstream) that contain a hit on track not associated with the truth particle matched to the track (i.e. a bad hit).

4.8 Track-Truth Matching

In order to study backgrounds resulting from tracking errors, it is useful in the MC to match tracks with the particles that generated them, and study which tracks have incorrectly included errant hits (referred to as mistracking). This will enable a detailed study of mistracked backgrounds that can falsely reconstruct downstream of the target and appear signal-like. A simple track-truth matching algorithm is performed after reconstruction, and the algorithm is as follows:

1. In the reconstruction process, the hits on track (i.e. the tracker hits) are each mapped to a list of truth particles (called MCParticles) that contribute to the hit.
2. For each MCParticle, the number of tracker hits associated with a given track is tabulated.
3. The MCParticle with the highest score, that is the highest number of tracker hits on a given track, is considered to be the truth match.

If there is a tie in this score, the MCParticle with the inner most hits (closer to the target) is considered the to be the truth match. More precisely, a loop is performed over the tracker hits in order from first sensor to last sensor, and the MCParticle that does not contribute to a tracker hit first in this loop is no longer considered for the truth match.

If there is still a tie, the higher momentum MCParticle is considered to be the truth match. This last tie breaker is arbitrary and its occurrence is exceedingly rare, if ever.

Once an MCParticle is matched to a track, the quality of the match can be quantified by computing the purity of the match - which is defined as the ratio of hits the truth-matched MC particle contributes to the track to the total number of hits on track (a fraction of 10 for 5-hit tracks and a

fraction of 12 for 6-hit tracks). The purity of the preselection with layer one requirements of tritrig-wab-beam for positrons and electrons is shown in Fig. 4.8. In this sample, about 0.002% of e^+ and e^- tracks do not have a MCParticle match to track where the most likely explanation are particles with truth information that is not propagated to the reconstruction level. These truth-matched tracks are used to study backgrounds due to mistracking in detail.

2124 4.9 Monte Carlo Samples

Sample	Generator	Statistics
RAD	MadGraph5	~2.9M
Tritrig	MadGraph5	~8.0M
WABs	MadGraph4	~32k
A' prompt	MadGraph4	~3.8M
A' displaced	MadGraph4	~56k
Møller	EGS5	~500k
Beam	EGS5	—

Table 4.4: Event generators and statistics for MC samples.

2125 In order to be confident that the results from the analysis are well-understood, realistic Monte
2126 Carlo (MC) samples are run for particular physics processes. It is important to properly simulate
2127 all the physics processes that make up an appreciable fraction of the triggered data. The main
2128 e^+e^- physics backgrounds are tridents composed of radiatives (RAD), Bethe-Heitler (BH), and
2129 their cross terms as described in Sec. 2.8 as well as converted wide-angle bremsstrahlung (cWABs).
2130 WABs are the dominant triggered process since charged particles are not required in the trigger.
2131 Møller scattering occurs when a beam electron scatters off a target electron. This provides a useful
2132 “standard candle” for the mass scale and mass resolution as described in Sec. 4.7, thus a comparison
2133 between data and MC is necessary. Lastly, backgrounds from elastically-scattered beam electron in
2134 the target are present in the triggered data in large quantities. Even though a simple selection of a
2135 maximum electron momentum eliminates beam particles, beam particles can leave hits in the tracker
2136 and significantly affect the pattern recognition and track reconstruction. Thus, beam backgrounds
2137 need to be understood in detail, and all processes are overlaid with beam background.

2138 For event generation and cross-section computation, the HPS MC chain uses several generators
2139 depending on the specific physics process of interest including EGS5 [58] and MadGraph4 [17].
2140 Trident processes, wide-angle bremsstrahlung (wabs), and A' 's are generated using MadGraph4. The
2141 Feynman diagrams are shown in Fig. 4.9. Beam background, Møllers, and scattering in the target
2142 are simulated using EGS5. All prompt processes are passed through EGS5 to properly simulate the
2143 scattering in the target which produces EGS5 final state particles. From EGS5 final state particles,
2144 a package called Stdhep is used to persist truth information and build beam bunches using a Poisson
2145 distribution as well as account for the the beam size, orientation, and offset.

2146 The detector response is then simulated using a GEANT4-based package [12] called Slic (Simu-
2147 lator for the Linear Collider) [55]. The detector response, specifically for the SVT and the Ecal, is
2148 converted into raw hits with time stamps and energy deposition information.

2149 Next, the raw hit information must pass through the readout simulation which emulates that

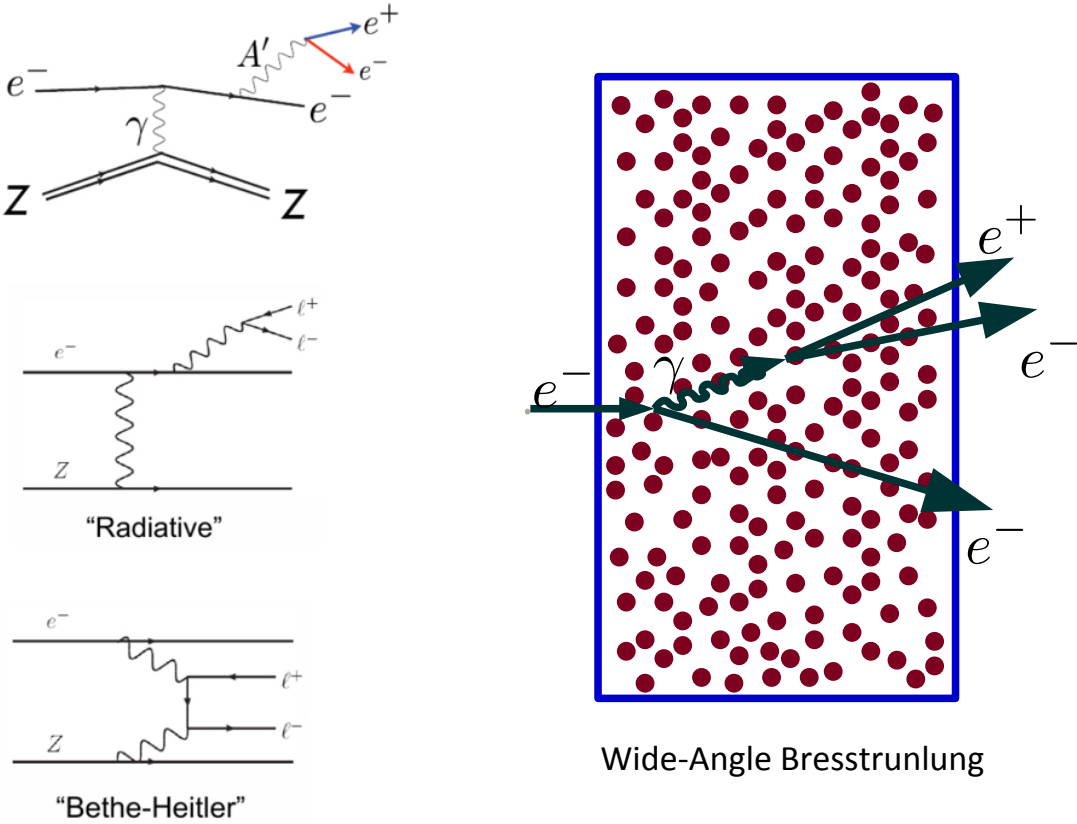


Figure 4.9: Left pictures show Feynman diagrams for A' (top), RAD (middle) and BH (bottom) events. Right picture shows WAB process.

trigger response including digitization and readout. Finally, the digitization from the readout simulation is used as input in the physics reconstruction software in hps-java in the same way the real experimental data is reconstructed. This provides a way for data and simulation to be directly compared, with MC able to be separated into different background components.

The MC samples produced as shown in Table 4.4 are background samples of RAD, tritrig, WAB, Møller, and beam background. The A' samples come in two different types - prompt and displaced from the target. Prompt A' samples are used for the resonance search and for an estimate of the mass resolution described in Sec. 5.2 (mass resolution is independent of displacement). The displaced A' 's are used to estimate the z -dependence of efficiency and geometrical acceptance. The detailed generator level requirements for each MC sample are shown in Table 4.5.

Both prompt and displaced A' samples are generated at specific mass points over the range of interest determined by the acceptance at a specific beam energy, and with close enough spacing such that interpolation of acceptance between mass points contains minimal error. The mass points

generated are between 50 MeV and 150 MeV in increments of 5 MeV as well as a high mass point at 175 MeV. The displaced A' samples must populate the decay range of interest ($\sim 0 - 150$ mm) with sufficient statistics. These samples are produced with a constant livetime at $c\tau = 10$ mm, which is large enough to sufficiently populate the decay range of interest for HPS, and then reweighted at a later step to reflect actual signal shapes.

Sample	Cut Description	Cut Requirement
RAD	Min energy of daughter particles	$E_{e^+} > 50$ MeV and $E_{e^-} > 50$ MeV
RAD	Min for y -direction of e^+e^- particles	$p_{e^+,y}/p_{e^+} > 0.005$ and $p_{e^-,y}/p_{e^-} > 0.005$
RAD	Min total energy of e^+e^- pair	$E_{e^+} + E_{e^-} > 500$ MeV
RAD	Min invariant mass of e^+e^- pair	$m_{e^+e^-} > 10$ MeV
Tritrig	Min energy of e^+	$E_{e^+} > 100$ MeV
Tritrig	Min for y -direction of e^+	$p_{e^+,y}/p_{e^+} > 0.005$
Tritrig	Min total energy of a e^+e^- pair	$E_{e^+} + E_{e^-} > 1000$ MeV
Tritrig	Min invariant mass of a e^+e^- pair	$m_{e^+e^-} > 10$ MeV
WABs	Min photon energy	$E_\gamma > 400$ MeV
WABs	Min for y -direction of e^+e^- particles	$p_{\gamma,y}/p_\gamma > 0.005$
Møller	Min energy of final state particles	$E > 10$ MeV
Møller	Min for transverse direction for f.s. particles	$\sqrt{(p_x/p)^2 + (p_y/p)^2} > 0.005$
Beam	Min energy of beam particles	$E_{e^-} > 0.005E_{beam}$
Beam	Min for transverse direction for f.s. particles	$\sqrt{(p_x/p)^2 + (p_y/p)^2} > 0.005$
Photon	Min for y -direction of γ	$p_{\gamma,y}/p_\gamma > 0.004$
Photon	Max for y -direction of γ	$p_{\gamma,y}/p_\gamma < 0.005$
A' 's Prompt	None	—
A' 's Displaced	None	—

Table 4.5: Basic generator level physics requirements for different physics processes. A' 's have no generator level cuts since knowledge of the geometrical acceptance is required to compute the expected number of A' 's for different mass and ϵ values.

Detailed steps on the production of beam particles are as follows:

- 1. Beam particles are produced in EGS5.
- 2. Beam rotation, beam size, and the target offset are all applied via stdhep. Beam particles are sampled and beam bunches are built in stdhep.
- 3. The beam bunches are passed through Slic.

Detailed steps on the remaining MC - RAD, tritrig, WAB, Møllers, and A' with beam overlay - are as follows:

- 1. Particles are produced in MadGraph. The exception is that Møllers are produced in EGS5.

- 2176 2. Final state particles from MadGraph are passed through the target via EGS5. Because dis-
2177 placed A' have no interaction with the target, only the recoil electron for these samples is
2178 passed through the target.
- 2179 3. Parent particles are added into each event of the EGS5 output.
- 2180 4. Beam rotation, beam size, and the target offset are all applied via stdhep.
- 2181 5. The events are passed through Slic.
- 2182 6. The output events from Slic are spaced apart by a fixed interval equal to the event window
2183 size in the trigger system.
- 2184 7. The sample is mixed with the beam sample or a WAB sample if desired.
- 2185 8. Readout and reconstruction is processed.

2186 Lastly, since the displaced vertex analysis is mostly concerned with a near-zero background region
2187 far beyond the target, the background shapes at the extreme tails of the reconstructed z distributions
2188 must be understood. In order to do this, a sample of tridents overlaid with beam and wabs, with
2189 the trident luminosity equivalent to the luminosity of the dataset, is generated. This gives some
2190 indication of the high z background due to both mistracking and large scatterings in the tracker and
2191 is used as a direct comparison to data in Sec. 5.

2192 In addition a sample of pure tridents with about three times the luminosity in data is used to
2193 further understand the tails of the z distributions due to prompt processes that undergo significant
2194 multiple scattering or single Coulomb scattering and reconstruct far downstream of the target. The
2195 pure trident sample is used for the high luminosity sample because overlaying a sample with beam
2196 is computationally expensive.

Cut Description	Requirement
Trigger	Pair1
Track-cluster match	$\chi^2 < 10$
Cluster Time Difference	$ t_{e^+Cluster} - t_{e^-Cluster} < 1.45 \text{ ns}$
Track-Cluster Time Difference	$ t_{e^+Track} - t_{e^+Cluster} - \text{offset} < 4 \text{ ns}$
Track-Cluster Time Difference	$ t_{e^-Track} - t_{e^-Cluster} - \text{offset} < 4 \text{ ns}$
Beam electron cut	$p(e^-) < 1.75 \text{ GeV}$
Track Quality	$\chi^2/\text{dof} < 6$
Vertex Quality	$\chi^2_{unc} < 10$
Minimum e^+ Momentum	$p(e^+) > 0.4 \text{ GeV}$
Minimum e^- Momentum	$p(e^-) > 0.4 \text{ GeV}$
Maximum Vertex Momentum	$V_{0p} < 2.4 \text{ GeV}$

Table 4.6: Requirements applied to V_0 after reconstruction as an initial set to study. The time offset for data is 56 ns and the time offset for MC is 43 ns. These requirements are referred to as preselection.

4.10 e^+e^- Preselection

After reconstruction, analysis can be performed. The goal of the displaced vertex analysis is to search for long-lived A 's produced in a fixed target that decay to e^+e^- pairs in the range $\sim 1 - 10$ cm in the lab frame. These rare signal processes must be distinguished from a large number of prompt QED tridents, and this search is limited by the vertex resolution of HPS and the quality of tracking. In this energy range, the vertex resolution is dominated by multiple scattering in the tracker, particularly in the first layer. In order to perform the search most effectively, a series of analysis cuts are utilized to separate the prompt background that reconstructs falsely downstream of the target from true long-lived particles. Because the expected relative signal rate is very low, a near-zero background region is required to make this search possible. Thus, these cuts aimed to eliminate nearly all background in a signal region that is sufficiently downstream of the target without sacrificing too much signal efficiency.

This section presents and describes the cuts from the reconstruction quality requirements to the quality cuts applied to define kinematic regions used for the background normalization and shape corrections evaluation and signal selection optimization. The reconstruction is run on V0 skims on the pass 4 dataset - which have at least one V0 candidate in the event (at least one e^+e^- pair in opposite halves of the detector which makes a reasonable quality vertex). The cut flow is separated into three parts - preprocessing selection (shown previously in Table 4.2 and Table 4.3), preselection (described in Table 4.6 and shown later in Fig. 4.10 - Fig. 4.16), and tight selection (described in Chp. 5) - each successive part contains stricter requirements to further eliminate backgrounds.

The physics trigger used by HPS was tuned to accept time coincident e^+e^- pairs, where the e^+ and e^- reside in opposite detector volumes. Therefore, as an initial requirement, the Ecal clusters associated with the e^+ and e^- are required to be in opposite halves of the detector, i.e. have a y

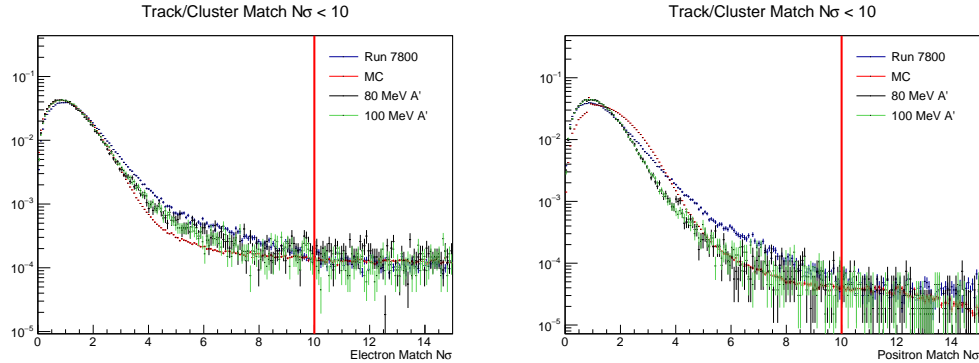


Figure 4.10: Track-cluster match number of σ for electrons (left) and positrons (right). A loose cut is placed at $N\sigma < 10$ for both electrons and positrons to eliminate poor track-cluster matches.

position which satisfies the following relation:

$$y_{+Cluster} \times y_{-Cluster} < 0. \quad (4.6)$$

In addition, several loose cuts were required at the reconstruction stage, the so-called pre-processing cuts which are shown in Table 4.2 for data and Table 4.3 for MC. The vertices contained in the events that pass the trigger requirement are selected by a set of cuts, tighter with respect to the reconstruction quality cuts but still loose enough to select signal-like higher-quality vertices with large statistics. This set of cuts is referred to as *Preselection*. Preselected events are used as a way to study trident rates and as a way to study the need for tighter cuts described in Sec. 5.4. At this stage only vertices reconstructed by an unconstrained fit are considered. In general, the preselection cuts are shared with the resonance search selection or were studied in the previous displaced vertex analysis from the 2015 Engineering Run.

The selection starts by requiring that the distance between the tracks and the matched electromagnetic clusters is less than 10σ , where σ is the error associated to the cluster position. This is shown in Fig. 4.10. This requirement guards against the case where a track is grossly mismatched to an Ecal cluster. To further reduce mismatching, the time difference between the calorimeter clusters matched to SVT tracks in opposite hemispheres is required to be less than 1.45 ns (the Hall B bunches are separated by 2 ns) to reduce out of time events. This cut aims to reduce the contamination due to accidentals to less than 1% PF::Cite Old BH analysis, and is studied in detail in the current resonance search (cite current BH). The cluster time difference cut is shown in Fig. 4.11.

In addition, the difference between the track time and the cluster time is required to be less than 4 ns. Before applying this cut, the track time distribution is shifted to zero by correcting the offset,

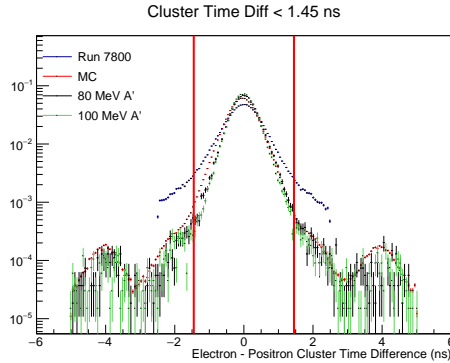


Figure 4.11: A cluster time difference cut between electrons and positrons is placed at 1.45 ns to eliminate accidentals from other beam bunches (Hall B bunches are spaced at 2 ns).

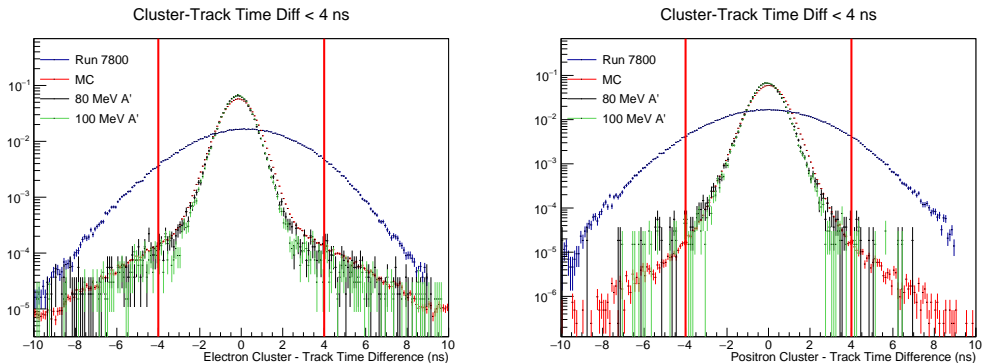


Figure 4.12: Cluster-track time difference (with the time offset from Table 4.6) for electrons (left) and positrons (right). A cut is placed at a time difference of 4 ns for both electrons and positrons to eliminate out of time tracks. There is significant mismodeling for the track time resolution; however, this is a data-driven cut.

which is approximately 56 ns in data and 43 ns in MC simulation². The cut is loose enough such that it is possible to use the same offset correction for each run in data without introducing run-by-run systematic effects, but it also further reduces e^+e^- pairs where one of the tracks is mismatched to the corresponding cluster. This is the same cut value for cluster-track time difference that was used in previous displaced vertexing and resonance search ([cite this](#)) and is shown in Fig. 4.12.

Electrons are required to have a momentum magnitude less than 1.75 GeV in order to remove the contribution from full energy electrons - that is electrons that scatter elastically off the nucleus of the tungsten target [PF::Cite Current BH analysis](#). In addition, loose cuts on the minimum

²The discrepancy in for the offset between data and MC can be attributed to the different conditions used. The is also a difference between the offsets in data for preprocessing cuts in Table 4.2 (55 ns) and Preselection cuts in Table 4.6 (56 ns). The correct offset is 56 ns; however, the window of 10 ns used for the MOUSE cuts is significantly wider than the 4 ns in the Preselection.

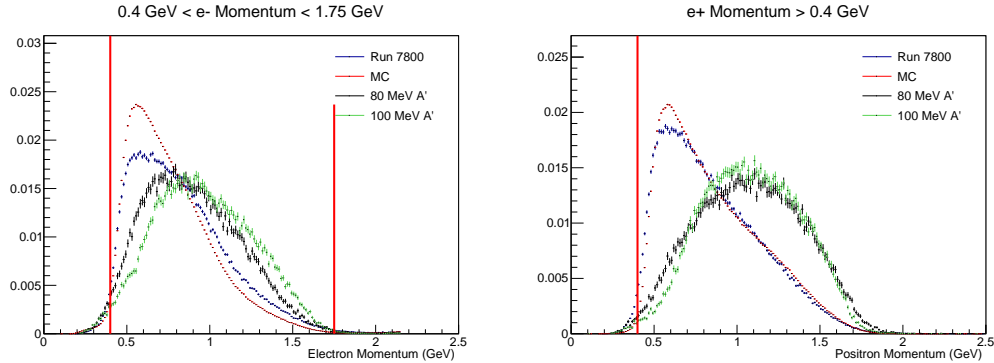


Figure 4.13: Electron momentum has a minimum momentum cuts at 0.4 GeV in order to reduce low momentum particles that have larger multiple scattering. A maximum momentum cut is placed at 1.75 GeV to eliminate V0s that reconstruct with elastically-scatter electrons in the target. Left: The plot of electron momentum after preprocessing. Right: A plot of the electron momentum used to study full-energy electrons (since most elastically-scatter electrons are cut away during preprocessing). There is some mismodeling for individual particle momenta particularly at low momentum. Replace figure on the right with electron momentum that include an FEE peak.

2249 particle momentum at 0.4 GeV, to eliminate low momentum particles which could have large multiple
 2250 scattering, and maximum V_0 momentum 2.4 GeV, above which no signal is expected, are also shared
 2251 with the resonance search. The electron momentum cuts are shown in Fig. 4.13 and the positron
 2252 momentum cut and the maximum V_0 momentum cut are shown in Fig. 4.14.

2253 Poorly fit tracks and vertices can lead to falsely reconstructed vertices downstream of the target.
 2254 Both tracks are required to have a track quality of χ^2/dof (degrees of freedom) less than 6 which is
 2255 a relatively loose requirement that was used for the 2015 Displaced Vertex Search [8]. Each vertex
 2256 is required to a vertex fit quality on the unconstrained vertex of at least have a $\chi^2_{unc} < 10$ which is a
 2257 loose requirement. The track and vertex quality are shown in Fig. 4.15 and Fig. 4.16, respectively.

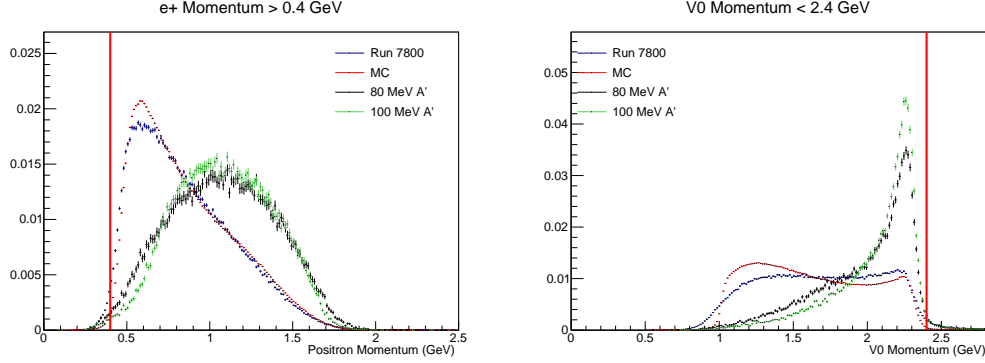


Figure 4.14: Left: Positron momentum has a minimum momentum cut at 0.4 GeV in order to reduce low momentum particles that have larger multiple scattering. Right: A maximum V0 momentum cut is placed at 2.4 GeV since signal is not expected far above the beam energy at 2.3 GeV.

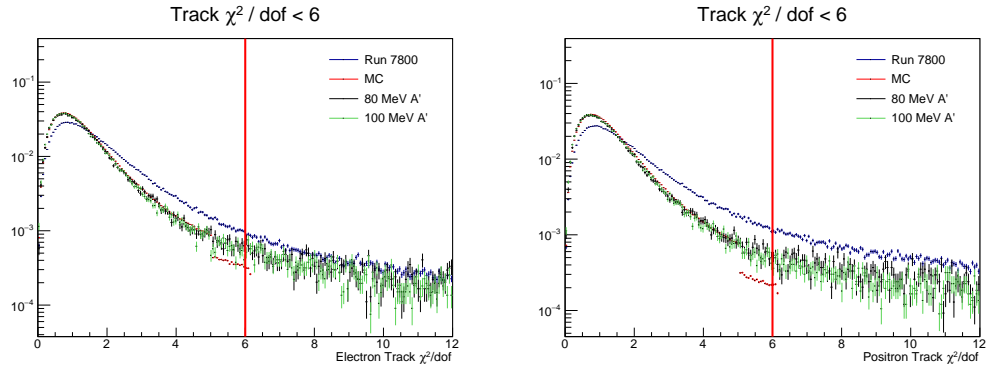


Figure 4.15: Track χ^2 per degrees of freedom (dof) for electrons (left) and positrons (right). A cut is placed at $\chi^2 < 6$ for both electrons and positrons to eliminate poor tracks that can falsely reconstruct downstream of the target.

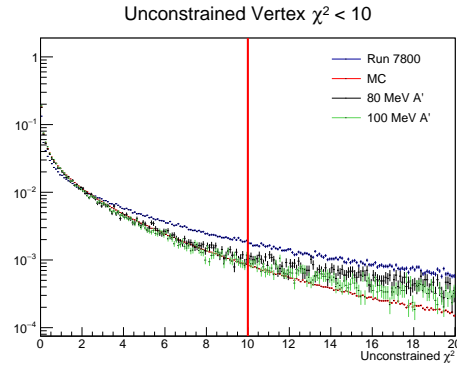


Figure 4.16: A loose cut on the unconstrained vertex fit χ_{unc} is placed at 10 to eliminate poorly reconstructed V0s that can incorrectly reconstruct downstream of the target. There is some mismodeling for the cluster time resolution, and there is some mismodeling in the vertex quality.

	data ϵ_{tot}	tridents ϵ_{tot}	WAB ϵ_{tot}	AP ϵ_{tot}
no-cuts	2.65672e+07	–	8.05260e+06	–
Trigger Pair1	2.65022e+07	0.998	0 0.0	0 0.0
$e^- \Delta_d(trk, clu) < 10\sigma$	2.63041e+07	0.99	7.96627e+06 0.989	31702 0.993 55363 0.989
$e^+ \Delta_d(trk, clu) < 10\sigma$	2.62441e+07	0.988	7.94766e+06 0.987	31473 0.986 55251 0.987
$\Delta_t(clue_e^-, clue_e^+) < 2\text{ns}$	2.49811e+07	0.94	7.83282e+06 0.973	31002 0.971 54665 0.977
$e^- \Delta_t(trk, clu) < 4\text{ns}$	2.26414e+07	0.852	7.78389e+06 0.967	30882 0.967 54463 0.973
$e^+ \Delta_t(trk, clu) < 4\text{ns}$	2.15004e+07	0.809	7.7633e+06 0.964	30440 0.954 54293 0.97
$p_e^- < 1.75\text{GeV}$	2.14217e+07	0.806	7.75548e+06 0.963	30379 0.952 54201 0.969
$e^- Track\chi^2 < 6$	2.06244e+07	0.776	7.58028e+06 0.941	29735 0.932 52652 0.941
$e^+ Track\chi^2 < 6$	1.9464e+07	0.733	7.42088e+06 0.922	27139 0.85 50983 0.911
$\chi^2_{unc} < 10$	1.53681e+07	0.578	6.9479e+06 0.863	13226 0.414 42929 0.767
$p_e^- > 0.4\text{GeV}$	1.5204e+07	0.572	6.88443e+06 0.855	13194 0.413 42474 0.759
$p_e^+ > 0.4\text{GeV}$	1.5204e+07	0.572	6.88443e+06 0.855	13194 0.413 42474 0.759
$p_{vtx} < 2.4\text{GeV}$	1.51465e+07	0.57	6.8777e+06 0.854	13128 0.411 42205 0.754

Table 4.7: Table showing the efficiency of each cut on 10% of the 2016 data sample and on MC simulation for tridents, WABs and 80 MeV A' displaced samples. The trident sample contains both Bethe-Heitler and radiative events.

2258 A summary of the *Preselection* cuts applied to the reconstructed vertices is presented in Table 4.6
 2259 while in Table 4.7 the cutflow and the cut efficiency on various samples for MC simulation are shown.
 2260 Fig. 4.17 shows a comparison of data and MC for preselected events while Fig. 4.18 - Fig. 4.20 show
 2261 the cutflows of the preselection. This initial selection is then used as a basic comparison of e^+e^-
 2262 rates and kinematic shapes between data and MC, and events will later have stricter requirements
 2263 to further reduce prompt backgrounds that reconstruct significantly downstream of the target.

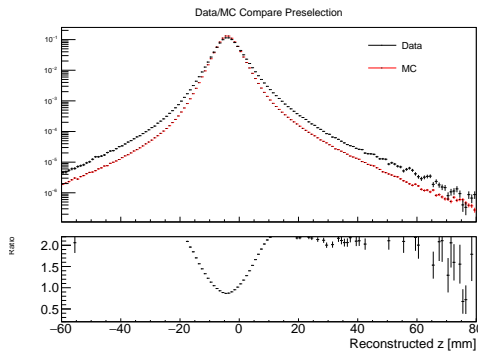


Figure 4.17: Comparison of 10% Data and tritrig-wab-beam for preselected events.

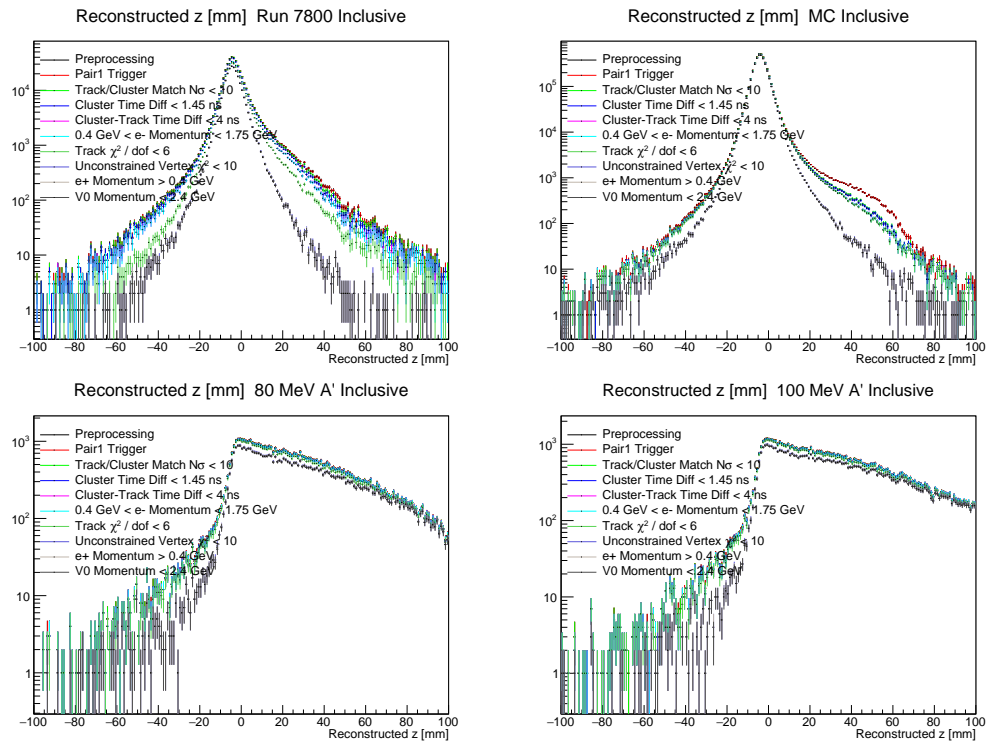


Figure 4.18: Preselection cutflow for as a function of reconstructed z . Top Right: Run 7800 in data. Top Left: a fraction of the tritrig-wab-beam sample. Bottom Left: 80 MeV displaced A' s. Bottom Right: 100 MeV displaced A' s.

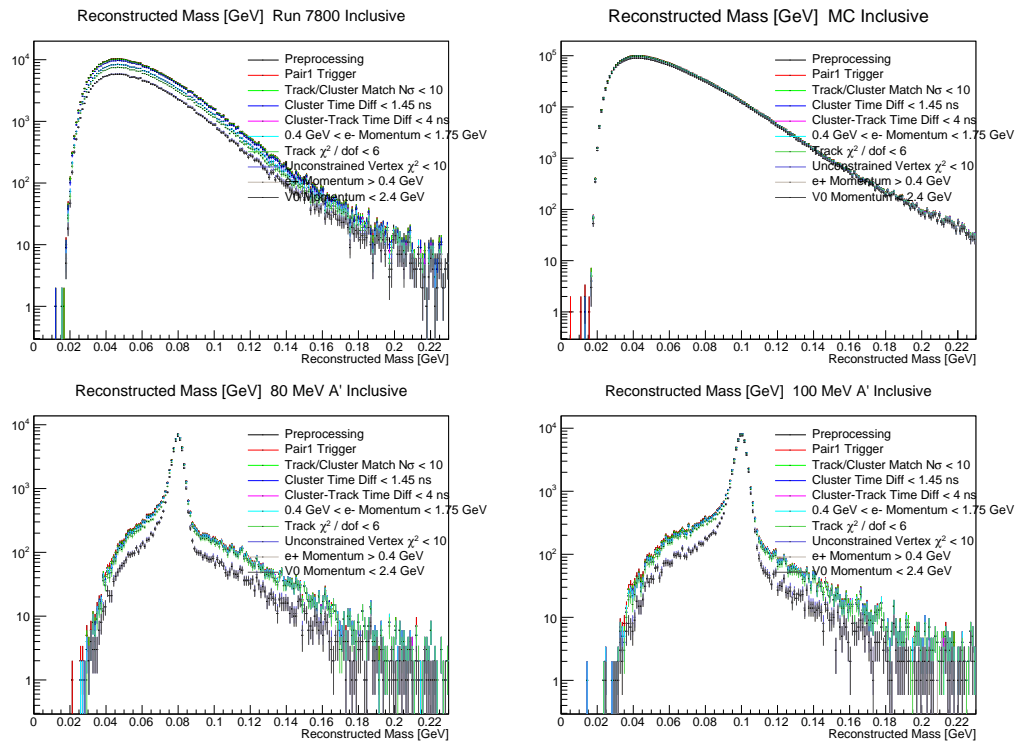


Figure 4.19: Preselection cutflow for reconstructed mass. Top Right: Run 7800 in data. Top Left: a fraction of the tritrig-wab-beam sample. Bottom Left: 80 MeV displaced A' 's. Bottom Right: 100 MeV displaced A' 's.

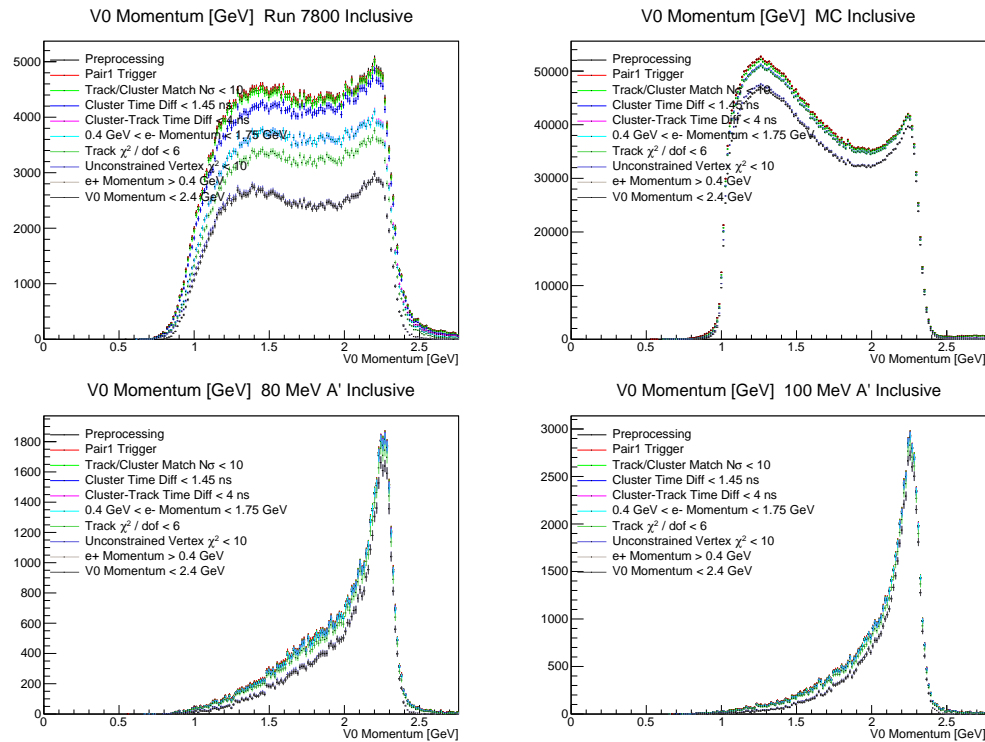


Figure 4.20: Preselection cutflow for as a function of reconstructed V0 momentum. Top Right: Run 7800 in data. Top Left: a fraction of the tritrig-wab-beam sample. Bottom Left: 80 MeV displaced A's. Bottom Right: 100 MeV displaced A's.

2264 4.11 Composition of the e^+e^- Sample & Normalization

2265 Understanding the normalization of the data is imperative to correctly compute the expected number
 2266 of detectable A' s as a function of mass and ϵ . This can be done by measuring the rate of radiative
 2267 tridents and then utilizing Eq. 2.9 to compute the expected rate of A' 's. The number of radiative
 2268 tridents in the data can be estimated by using MC to separate the e^+e^- pairs into their individual
 2269 contributions (radiatives, WABs, and tridents) and computing the fraction of e^+e^- pairs that are
 2270 due to radiative processes, the so-called “radiative fraction”. From the radiative fraction and the
 2271 number of e^+e^- pairs in data, the number of expected A' 's can be computed. A description of the
 2272 normalization for the composition of the e^+e^- pairs, a comparison to the overall e^+e^- rate to data,
 2273 and obtaining the radiative fraction is presented in the following subsections.

2274 4.11.1 MC Normalization

Sample	μ of ICS	σ of ICS	# of good files	# of generated events per file
RAD	81.61 μ b	0.08340 μ b	9940	10k
Trident-Trig	1.416 mb	0.004310 mb	9853	50k
WAB	0.1985 b	0.01973 b	9956	100k

Table 4.8: Normalization parameters for the RAD, Tritrig, and WAB samples. The mean μ and the σ are obtained from the distribution of integrated cross-sections (ICS) from the individual generated samples.

2275 Normalization for MC is computed by using the mean μ of the integrated cross section (ICS) for
 2276 each sample produced as shown in Fig. ?? and the total number of events generated (Luminosity =
 2277 Events Generated / Mean (μ) ICS). The results are shown in Table 5.7 and are used to separate the
 2278 rate of different e^+e^- production processes and as a comparison to the overall e^+e^- rate in data.
 2279 The ICS is computed after the cuts from Tab. 4.5.

2280 4.11.2 HPS e^+e^- Rates

2281 A dedicated study of the HPS e^+e^- composition from MC and overall rate compared with e^+e^-
 2282 data rates is documented in the 2016 sample composition note [57]. The study looked at both γe^-
 2283 (dominated by WABs) and e^+e^- (both tridents and cWABs) final states. The MCs used for this are
 2284 summarized in 4.9 and the data used is $\sim 10\%$ of run 7963. The selection used for the composition
 2285 study were chosen to be the same as those used the preselection defined in Tab. 4.6.

2286 Figure 4.21 shows the distributions of some kinematic variables for the e^+e^- events from the
 2287 composition study. In addition to the preselection, the events shown in these distributions have a
 2288 minimum e^+e^- momentum sum cut (referred to as the radiative cut in Sec. 5.4) but do not require
 2289 that the tracks have both L1 and L2 hits.

2290 From these studies, it appears that the MC overestimates the overall e^+e^- rate in data by ~ 0.20 ,
2291 thus scaling the overall MC cross-section by 80% shows excellent agreement.

2292 Generally, the agreement between data and MC for these distributions is reasonable with the
2293 exception of a $\sim 20\%$ overall scale difference which may have several sources. While the MC is
2294 generated with a single set of conditions, there is some run-to-run variation in the e^+e^- rates of
2295 order 5%. In addition, this MC does not account for tracking efficiencies which are of the order of
2296 $\sim 10\%$ as well as the hit efficiency effects (particularly in layer 1) described in Sec 4.6. There are
2297 also a few features in these plots (e.g. skew in track momentum, some differences in track slope)
2298 that may be attributed to the same causes as the overall rate discrepancy.

2299 It is an assumption that the overall discrepancy between e^+e^- rates in data and MC are the
2300 same as and the individual contributions. Thus, the fraction of e^+e^- pairs that are due to radiative
2301 tridents are the same in data and MC. In other words, these discrepancies cancel when taking the
2302 ratio of rates of different processes.

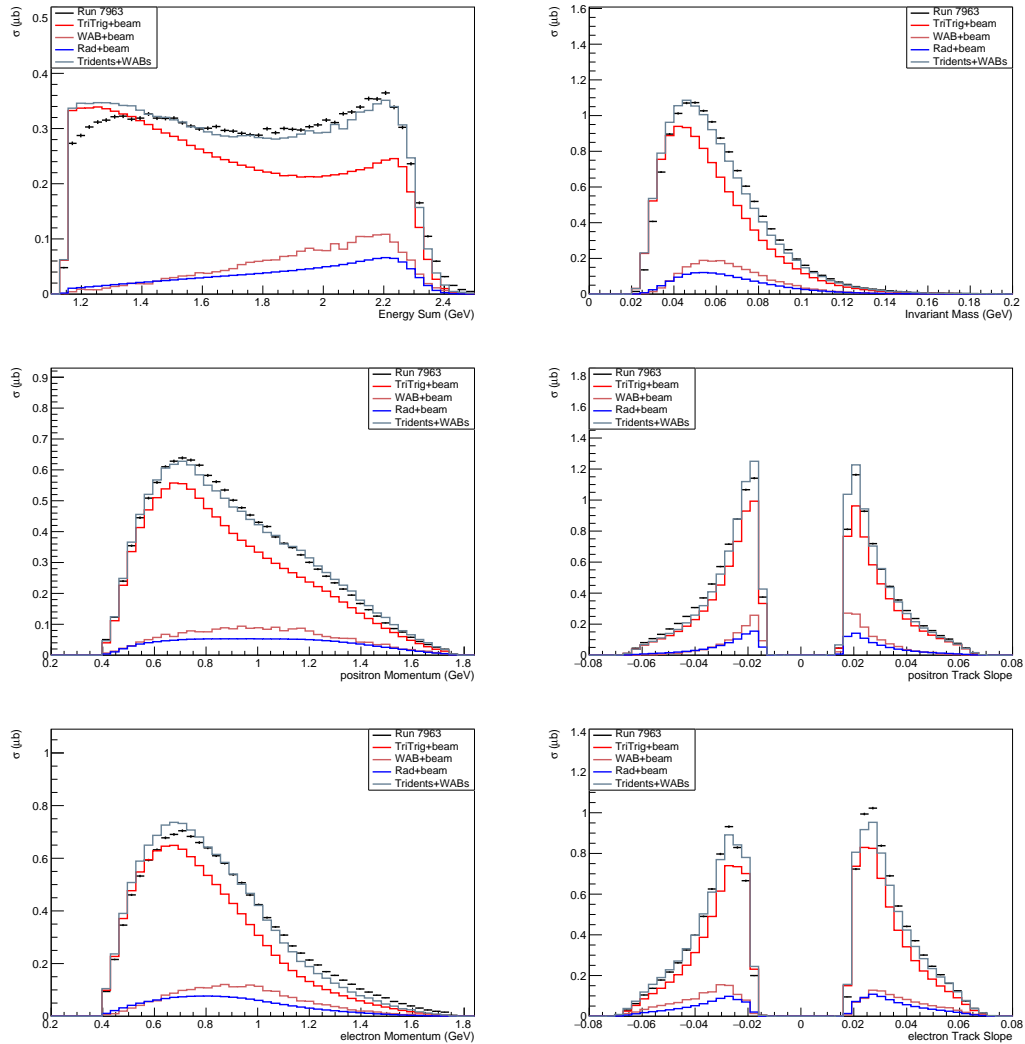


Figure 4.21: Distributions of e^+e^- events with scaling all MC cross-sections by 0.8. Upper Left: e^+e^- momentum sum. Upper Right: e^+e^- invariant mass. Middle Left: Positron momentum. Middle Right: Positron track slope. Bottom Left: Electron momentum. Bottom Right: Electron track slope.

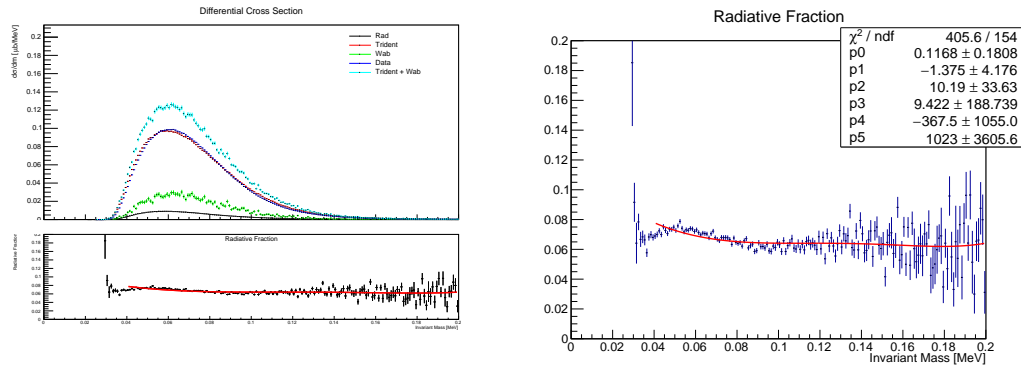


Figure 4.22: Left: The differential cross sections ($d\sigma/dm$) of wab, trident, and radiative trident components from MC as well as the measured cross section from 10% of the data. In principle, one would expect the tridents + wabs (turquoise) to agree with data (blue). The discrepancy is explained in Sec. 4.11.2. Right: The radiative fractions as a function of mass. It is fit to a 5th order polynomial and is used to determine the expected radiative trident rate from the number of e^+e^- pairs in a mass bin.

4.11.3 Radiative Fraction

A key component to translating the number of signal events to the coupling epsilon is the fraction of reconstructed events in our sample, after all selection requirements, that come from radiative tridents. This fraction, the so-called radiative fraction, is defined as a function of mass:

$$f_{rad}(m) = \frac{d\sigma_{rad}/dm(m)}{d\sigma_{tri}/dm(m) + d\sigma_{cWAB}/dm(m)} \quad (4.7)$$

While the total number of e^+e^- pairs can be taken from data the radiative fraction must be computed using MC. Therefore it is important that the composition of our data sample, namely, the relative contributions of trident events to converted WAB (cWAB) events is understood.

Each term in Eq. 4.7 is computed from MC by taking each individual process after running through the full trigger and detector simulation (which incorporates acceptance and efficiency effects) and weighting it by the cross-section from the respective MC generator. This is done as a function of mass, specifically in narrow mass bins. As stated previously, it is assumed that the overall e^+e^- rate discrepancy between data and MC have negligible effects on the radiative fraction.

For the numerator (i.e. the radiative component), the e^+e^- pairs from radiative processes are truth-matched and only events in which the true e^+e^- daughter pairs reconstruct from the decay of the γ^* are used. This is done to eliminate e^+e^- pairs in which the positron falsely reconstructs with the recoil electron (which gives an incorrect reconstructed mass) and to utilize the truth mass. The truth mass is computed from the invariant mass from these truth-matched e^+e^- pairs using the truth momentum components of the particles. Using the truth mass reduces the systematic uncertainty associated with signal leaking in or out of the narrow mass bins.

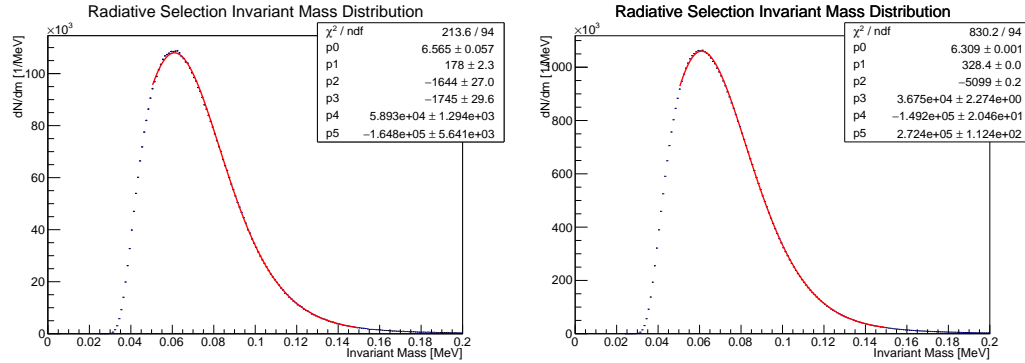


Figure 4.23: The invariant mass for Left: 10% of the data and Right: 100% of the data with the radiative cut selection. It is fitted to the an exponential to a 5th order polynomial. This is the number of e+e- pairs in a 1 MeV bin used to normalize the expected radiative trident rate, and hence the expected A' rate.

For the denominator (i.e. the sum of the total trident and converted WAB components), physics does not enable the differentiation between trident events that are reconstructed with the true daughter electron as opposed to the recoil electron (even if using truth information from MC due to the cross terms between the Bethe-Heitler and radiative diagrams). As a result, these events cannot be truth-matched and the reconstructed mass must be used in a mass bin in the denominator. The total denominator is representative of the total composition in data which also must rely on reconstructed masses.

Cut Description	Requirement
Preselection	-
Layer 2 Requirement	e^+ and e^- have L2 hit
Radiative Cut	$V_{0p} > 1.85$ GeV

Table 4.9: A list of cuts that are used to determine the radiative fraction and the number of e+e- events within a mass bin. The cuts are composed of the preselection cuts from Sec. 4.10 with the addition of a few extra cuts including the radiative cut (the cut on e^+e^- momentum sum).

The selection that is used for the radiative fraction for the displaced vertex search are the preselection cuts from Sec. 4.10 as well as the layer 2 requirement and the e^+e^- momentum sum cut (radiative cut) and is shown in Table 4.9. From these selections, the radiative fraction is computed as the number of truth-matched radiative tridents in a narrow bin of truth mass divided by the sum of trident and wab process in the same narrow bin of reconstructed mass, and normalized by their cross sections, as a function of mass as in Eq. 4.7. Both the radiative fraction and differential cross sections of various background components and data are shown in Fig. 4.22. The radiative fraction is parametrized using a 5th order polynomial.

$$f_{rad}(m[GeV]) = 0.1168 - 1.375m + 10.19m^2 + 9.422m^3 - 367.5m^4 - 1023m^5 \quad (4.8)$$

Using the radiative fraction and the number of e+e- pairs in a given narrow mass bin N_{bin} will provide a way to compute the expected number of radiative tridents in that mass bin ($N_{rad}(m) = f_{rad}(m)N_{bin}(m)$). The invariant mass plot using the radiative fraction selection from Table 4.9 using 1 MeV bins ($\delta m_{A'}$), which gives the number of e+e- events in that bin, is shown in Fig. 4.23. This is parametrized as using an exponential to a 5th order polynomial. For the 10% blinded sample this gives

$$N_{bin}(m[GeV]) = e^{4.903+208.3m-1880m^2-1868m^3+6.870e4m^4-1.980e5m^5} \quad (4.9)$$

and for the full 100% of the data this gives

$$N_{bin}(m[GeV]) = e^{6.309+328.4m-5099m^2+3.675e4m^3-1.492e5m^4+2.724e5m^5} \quad (4.10)$$

Using these equations and the radiative fraction, the expected number of radiative tridents in a given mass bin can be computed. From there, rearranging Eq. 2.9 gives the expected A' production rate at the target as a function of mass and ϵ .

$$S(m_{A'}, \epsilon) = f_{rad}N_{bin} \frac{3\pi\epsilon^2}{2N_{eff}\alpha} \frac{m_{A'}}{\delta m_{A'}} \quad (4.11)$$

This result normalized to both 10% of the dataset and the full dataset is shown in Fig. 4.24. The last step is to displace the A' 's over a range in z based on their expected decay distributions and then perform the proper accounting based on whether or not the e^+e^- pair is within acceptance of layer 1 while correctly incorporating hit efficiency effects and tighter selection cuts. This is discussed in detail in Sec. 5.3.2.

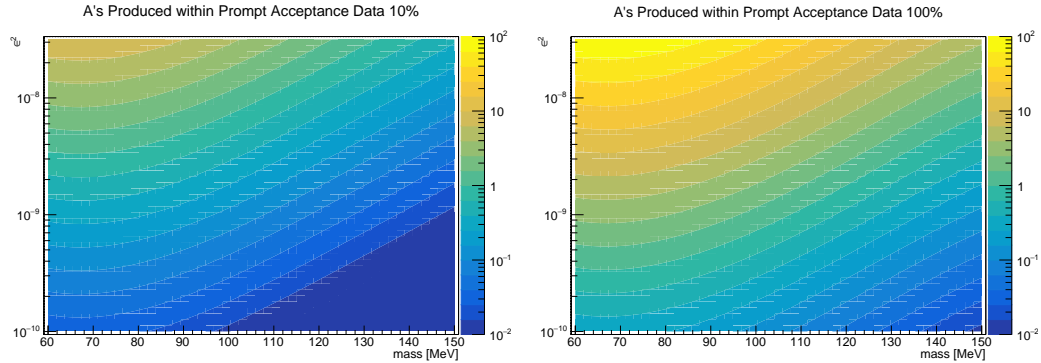


Figure 4.24: Left: The number of A's produced for each mass and ϵ^2 in prompt acceptance including all efficiencies for 10% of the data. In other words, the term in front of the integral in Eq. 5.18. Right: The number of A's produced for each mass and ϵ^2 in prompt acceptance including all efficiencies for 100% of the data.

2352 **Chapter 5**

2353 **Search for A' Displaced Vertices**

2354 As stated previously, the basic premise of the displaced vertex search is to search for long-lived
2355 A' 's that reconstruct far enough away from the target to distinguish from prompt processes. The
2356 expected rate of A' 's is on the order of $\sim 10^{-7} - 10^{-8}$ relative to the large prompt trident background
2357 rate requiring a search in a near-0 background region.

2358 Since the expected decay shape is exponential, a larger signal region closer to the target dramatically
2359 improves the expected number of detectable A' 's. Thus, the effectiveness of the search is
2360 limited by the detector vertex resolution, which itself is limited by multiple scattering of particles
2361 in the tracker (particularly layer 1 of the SVT). There are key differences, both kinematically and
2362 with features of the tracks and vertices, between the signature of an A' and prompt backgrounds
2363 that falsely reconstruct downstream of the target. These features can be exploited to effectively
2364 distinguish between signal and background and are described in the sections that follow.

2365 After utilizing these distinguishing features, the remaining prompt background can be characterized
2366 in such a way that the expected background at a given z position downstream of the target can be predicted.
2367 This can be used to define a z -value that delineates a region downstream of which a near-0 background
2368 is expected. This value is denoted as z_{cut} and the signal region is defined as the
2369 reconstructed $z > z_{cut}$. Even though a near-0 background region is defined, it is often the case that
2370 much larger backgrounds appear in these regions than predicted by the background characterization
2371 in both data and MC. These events are called “high z events” and their study is important to the
2372 current and future success of this type of search. These high z backgrounds must be understood
2373 and mitigated by orders of magnitude in order to see a signal.

2374 This chapter describes a summary of the results from the 2015 Engineering Run, the details of
2375 analysis cuts used to distinguish between signal and background, a procedure of determining z_{cut}
2376 and the signal region, the final results of the 2016 Engineering Run, and a detailed discussion on
2377 high z events in both data and MC.

2378 5.1 Previous Results from 2015 Engineering Run

2379 The first displaced vertex search for A' 's on HPS was performed on the 2015 Engineering Run [8].
 2380 As previously described, events were selected to eliminate prompt backgrounds that reconstruct
 2381 downstream from the target where signal is expected, and the final event selection that was used in
 2382 this analysis in both data and MC is shown in Fig. 5.1.

2383 The final results of this analysis consist of estimating the expected number of signal events in the
 2384 signal region and setting a limit on the A' model. The maximum number of expected A' events is
 2385 0.097 events at an A' mass of 43.6 MeV and $\epsilon^2 = 2.4 \times 10^{-9}$. Unfortunately, this signal expectation
 2386 is insufficient to set a limit on the canonical A' model; However, a limit a factor times the A' cross-
 2387 section can be set. The best limit set for this dataset is at an A' of 51.4 MeV and $\epsilon^2 = 1.7 \times 10^{-9}$
 2388 in which an A' -like model with 35.7 times the cross-section is excluded with 90% confidence at this
 2389 point in parameter space.¹ Though there is no known motivation for such a model, this provides an
 2390 estimate for expected sensitivity for future runs. These final results are shown in Fig. 5.2.

2391 Even though the displaced vertex search from the 2015 Engineering Run did not provide a
 2392 physically meaningful result, it provided essential information about backgrounds, particular those
 2393 at high z . Through a detailed analysis of both the full dataset and in MC at truth level, it was
 2394 determined that there were two main sources of high z events. The first are due to large scatters in
 2395 layer 1 of the tracker in which both e^+e^- particles each have a large scatter away from the beam
 2396 plane. This can either be a result of multiple Coulomb scattering, which dominates the cores and
 2397 tails of the distribution, or from single Coulomb scattering whose angular scattering distributions
 2398 have an even longer tail. This process can reconstruct a vertex far downstream from the target with a
 2399 small error, and though most of these can be mitigated, a few of these processes are indistinguishable
 2400 from a true displaced signal. Coulomb scattering in the first layer of the tracker remains the known
 2401 fundamental limit of the experiment.

2402 The second main source of high z backgrounds are due to mis-tracking in which the tracking
 2403 algorithms pick up an incorrect hit in layer 1 (i.e. a hit that is not a result of the particle that
 2404 produced the other hits on track), usually from a scattered beam particle, which pulls the vertex
 2405 downstream. This situation is usually accompanied by a large scatter away from the beam plane in
 2406 the corresponding particle (even though it is tracked correctly) which results in a vertex reconstruc-
 2407 tion even further downstream. A schematic of these two backgrounds is shown in Fig. 5.3. The
 2408 knowledge obtained from this dataset was used to further improve the displaced vertex analysis for
 2409 the 2016 Engineering Run.

¹One may be tempted to interpret this result as a simple scaling in luminosity. However, scaling luminosity also changes the signal region such that the expected A' rate does not scale linearly. The exclusion of the A' model times a certain factor of the cross-section is the better interpretation of this exclusion.

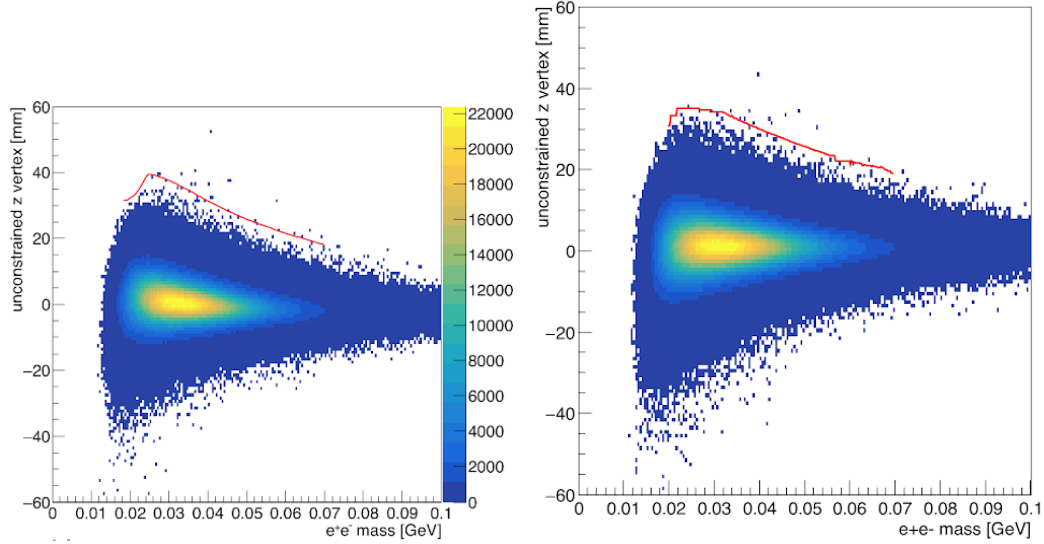


Figure 5.1: Final event selection for the displaced vertex search in the 2015 Engineering Run for Left: Data and Right: a luminosity-equivalent tritrig-wab-beam MC sample. The z_{cut} is shown in red.

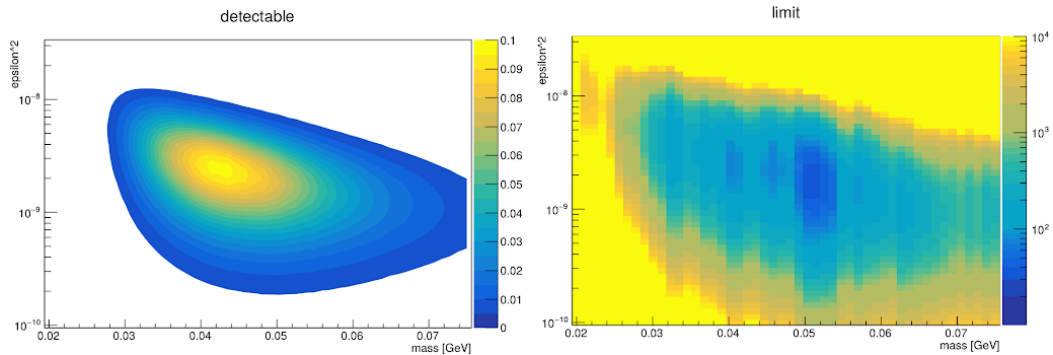


Figure 5.2: Final results for the displaced vertex search for the 2015 Engineering Run. Left: The number of expected A' events after all analysis cuts and z_{cut} as a function of mass and ϵ^2 . The maximum number of expected A' events is 0.097 events at an A' mass of 43.6 MeV and $\epsilon^2 = 2.4 \times 10^{-9}$. Right: The limit on the A' cross section as a function of mass and ϵ^2 where the best limit set is at an A' of 51.4 MeV and $\epsilon^2 = 1.7 \times 10^{-9}$ in which an A' -like model with 35.7 times the cross-section is excluded with 90% confidence.

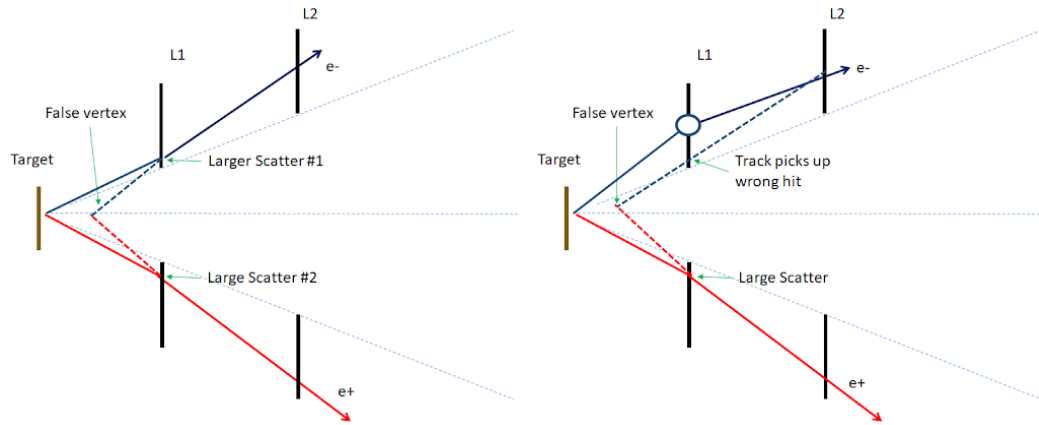


Figure 5.3: From detailed MC studies, it was shown that the backgrounds are due to two main processes. We seek to further mitigate these backgrounds in the 2016 Engineering Run. Left: A vertex is falsely reconstructed downstream of the target due to two large scatters of the e^+e^- pairs away from the beam plane. Right: A vertex is falsely reconstructed downstream of the target due to a track picking up the incorrect layer 1 hit (mis-tracking). These events are usually accompanied by a large scatter in the other particle that is tracked correctly.

2410 5.2 Mass Resolution

2411 The displaced vertex search is performed in bins of reconstructed mass for a given A' mass hypothesis.
 2412 In order to accurately estimate the expected A' yield in a given mass bin, it is important to have
 2413 an accurate estimate of the mass resolution as a function of mass in order to compute the amount
 2414 of signal yield by searching in a finite mass window. The uncertainty of the mass resolution can
 2415 result in more signal leaking out of a given mass bin than into the bin and is a source of systematic
 2416 uncertainty described in Sec. 5.7.

2417 In order to provide a standard mass point directly from data, the known mass of scattered e^-e^-
 2418 Møller pairs are used. However, unfortunately, comparing the mass resolution for Møllers between
 2419 data and MC shows dramatically different results which can be attributed to the discrepancy in the
 2420 momentum resolutions. In order to account for this, the momentum of the tracks is smeared and
 2421 the mass resolution is re-scaled. Lastly, the mass resolution is shown to be independent of decay
 2422 length, thus the mass resolution for a given A' mass can be kept constant.

2423 5.2.1 Møller Event Selection

2424 Møllers, that is elastically-scattered e^-e^- pairs, provide a convenient standard mass point for HPS.
 2425 The invariant mass of Møllers is a function of beam energy and can be computed from the total
 2426 energy in the center of mass frame at a beam energy of 2.3 GeV.

$$M(e^-e^+) = \sqrt{S_{\text{cm}}} = \sqrt{2m_{e^-}^2 + 2E_{\text{beam}}m_{e^-}} \approx \sqrt{2E_{\text{beam}}m_{e^-}} = 48.498 \text{ MeV} \quad (5.1)$$

2427 The basic selections involve selecting on e^-e^- pairs in opposite detector volumes within a small
 2428 time window and in a fiducial region of the Ecal. These selections reduce the backgrounds due to
 2429 out of time electrons and elastically-scattered electrons off a target nuclei. However, at this beam
 2430 energy the moller mass results in an opening angle that is near the edge of the HPS acceptance, and
 2431 it is rare for both electrons to fall within the acceptance of the Ecal (although one electron must
 2432 interact with the Ecal for the trigger). The electron that does not interact with the Ecal often times
 2433 falls into the so-called “Ecal hole” where 5 crystals on both top and bottom halves were removed
 2434 to reduce occupancy from elastically-scattered beam particles. Despite this, both electrons can be
 2435 within the tracker acceptance since the tracker acceptance still covers the acceptance over the Ecal
 2436 hole (where the other electron usually propagates through).

2437 Thus, the Møller event selection must be track-based using both the track times and the extrap-
 2438 olation of the track to the face of the Ecal. Unfortunately, both the track extrapolation resolution
 2439 and timing resolution are different between data and MC, thus a different set of cuts is utilized
 2440 between the them. The Møller event selection for data is summarized in Table 5.1, and the MC
 2441 Møller event selection is summarized in Table 5.2. The Møller mass resolution for data, MC, and
 2442 MC with track momentum smearing (described in the next section) using the unconstrained e^-e^-

Cut Description	Requirement
Time Difference Min	$\Delta t > -2.94$ ns
Time Difference Max	$\Delta t < 1.69$ ns
P_{sum} Min	$P_{sum} > 2.0$ GeV
P_{sum} Max	$P_{sum} < 2.45$ GeV
Δx_{top} Min	$\Delta x_{top} > -4.72$ mm
Δx_{top} Max	$\Delta x_{top} < 6.15$ mm
Δx_{bot} Min	$\Delta x_{bot} > -7.51$ mm
Δx_{bot} Max	$\Delta x_{bot} < 2.98$ mm

Table 5.1: Møller event selection for data on e^-e^- pairs. Since electron tracks are not required to match to Ecal clusters, the time difference is between track times and position differences are based on track extrapolations to the Ecal.

Cut Description	Requirement
Time Difference Min	$\Delta t > -1.44$ ns
Time Difference Max	$\Delta t < 1.54$ ns
P_{sum} Min	$P_{sum} > 2.15$ GeV
P_{sum} Max	$P_{sum} < 2.42$ GeV
Δx_{top} Min	$\Delta x_{top} > -4.89$ mm
Δx_{top} Max	$\Delta x_{top} < 4.82$ mm
Δx_{bot} Min	$\Delta x_{bot} > -4.98$ mm
Δx_{bot} Max	$\Delta x_{bot} < 4.52$ mm

Table 5.2: Møller event selection for MC on e^-e^- pairs. Since electron tracks are not required to match to Ecal clusters, the time difference is between track times and position differences are based on track extrapolations to the Ecal.

²⁴⁴³ vertex is shown in Fig. 5.4.

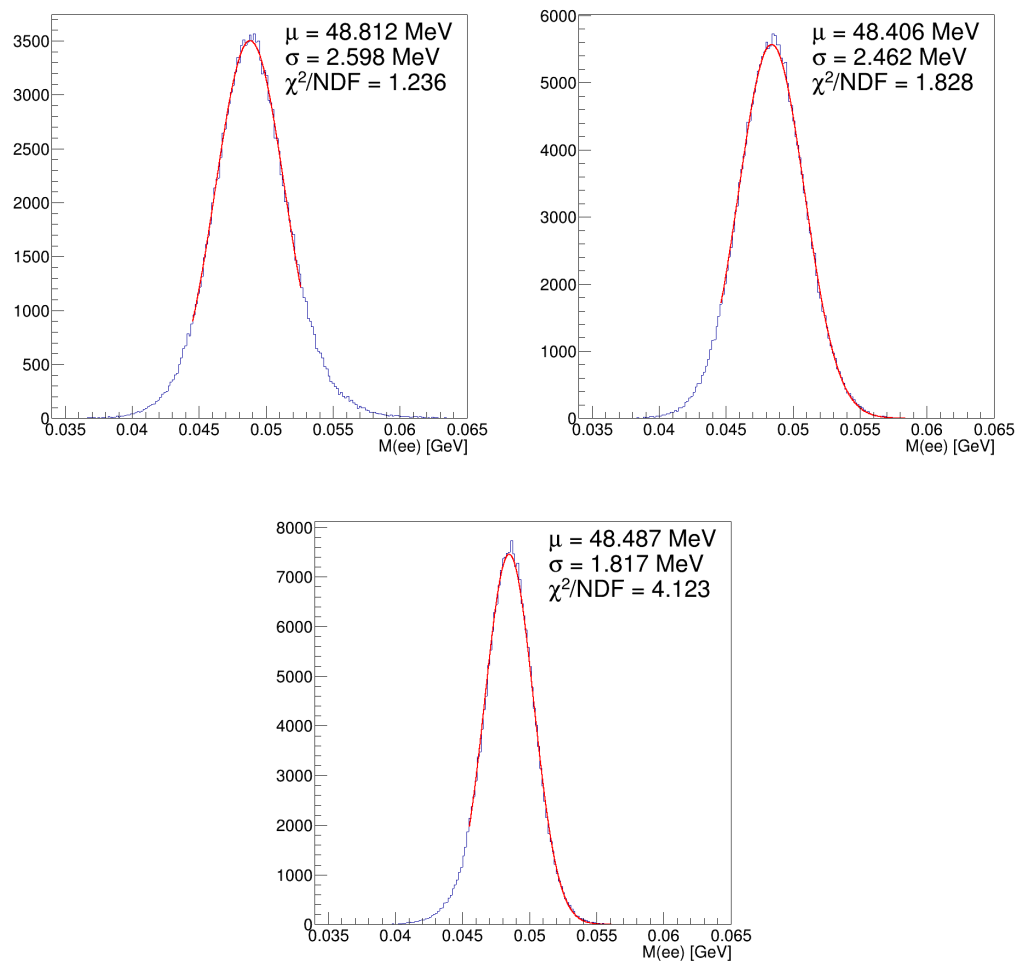


Figure 5.4: Fitted e^-e^- spectrum using the Møller selection for Upper Left: Data, Upper Right: Møller MC with track momentum smearing, and Bottom: Møller MC.

2444 5.2.2 Mass Resolution

2445 As stated previously, there is a discrepancy in the Møller mass resolution between data and MC that
 2446 can be attributed to the difference in momentum resolution of individual tracks which is $\sim 20\%$.
 2447 To approximate the effect of a momentum resolution difference on the mass resolution discrepancy,
 2448 a small-angle approximation for the opening angle can be used. The invariant mass and mass
 2449 resolution is given by

$$M_{e^+e^-} = 2\sqrt{p_1 p_2} \sin\left(\frac{\theta}{2}\right) \sim \frac{1}{\sqrt{2}}\theta\sqrt{p_1 p_2} \quad (5.2)$$

$$\sigma_m = \frac{1}{\sqrt{2}}\theta\sqrt{p_1 p_2} \left(\frac{\sigma_{p_1}}{p_1} + \frac{\sigma_{p_2}}{p_2} + \sigma_\theta\sqrt{p_1 p_2} \right) \quad (5.3)$$

2450 2451 From equation 5.3, it can be seen that a 20% increase in momentum resolution results in an in-
 2452 crease of $\sim 20\%$ in mass resolution, which would largely account for much of the mass resolution
 2453 discrepancy (the angular resolution discrepancy is small and can be ignored). In order to correct for
 2454 this discrepancy, a smearing technique on the track momentum is utilized and the mass resolution
 2455 is re-scaled.

2456 This smearing factor is calculated using the discrepancy between the data and MC full-energy
 2457 electron (FEE) momentum distributions where a narrow peak near the beam energy is expected.
 2458 The smearing factor deconvolutes the difference in Gaussian widths of data and MC such that the
 2459 widths agree when smearing. It is assumed that the relative momentum discrepancy does not change
 2460 appreciably with particle momentum and that the dominant effect in the data. The momentum
 2461 smearing factor is a function of detector hemisphere and the number of hits on track. These factors
 2462 are used to smear momentum on a track-by-track basis and the resulting smeared momentum is
 2463 denoted as $p_{1,sm}$ and $p_{2,sm}$. From the smeared momentum, the invariant mass can be re-scaled
 2464 using the original momenta and mass.

$$M_{e^-e-,sm} = 2\sqrt{p_1 p_2} \sin\left(\frac{\theta}{2}\right) = 2\sqrt{\frac{p_{1,sm}}{p_1} p_1 \frac{p_{2,sm}}{p_2} p_2} \sin\left(\frac{\theta}{2}\right) = \sqrt{\frac{p_{1,sm}}{p_1} \frac{p_{2,sm}}{p_2}} M_{e^-e-} \quad (5.4)$$

2465 This smeared invariant mass $M_{e^-e-,sm}$ is then refit with a Gaussian distribution, the width of
 2466 which is the smeared mass resolution. This smeared mass resolution is in excellent agreement with
 2467 data over the entire mass range of interest.

2468 An example of a 100 MeV displaced A' in the L1L1 category comparing the MC with and
 2469 without momentum smearing as well as the decay length dependence is shown in Fig. 5.5. An
 2470 example of a 100 MeV displaced A' in the L1L2 category comparing the MC with and without
 2471 momentum smearing as well as the decay length dependence is shown in Fig. 5.6. In general, there
 2472 is little dependence of the mass resolution on the decay length. This is because the precision of
 2473 the momentum measurement, and hence the mass resolution, is a result of the final layers of the

2474 SVT (layers 4 - 6) where the curvature of charged particles is maximum and can be more precisely
 2475 measured. Thus, mass resolution is a function of the number of layers hit, not of the decay position.

2476 Because of this, the prompt A' 's can be used which offer an advantage of more statistics partic-
 2477 ularly at low mass. In addition, for simplicity, the same cuts as the radiative fraction in Table 4.9
 2478 with the appropriate layer requirements are used to determine the mass resolution as any further
 2479 cuts are used to eliminate falsely reconstructed vertices downstream of the target and has little effect
 2480 on the core.

2481 The mass resolution for both the L1L1 and L1L2 categories comparing MC, MC scaled by the
 2482 Møller mass resolution in data and MC, and MC with track momentum smearing is shown in Fig.
 2483 5.7. Note that the L1L2 category is not final. What is shown here is the results from the displaced
 2484 in the L1L2 category. The plan is to still use prompt, but it will be different than L1L1 due to
 2485 different proportions of 5-hit and 6-hit tracks, and I have to take that proportion into account. I of
 2486 course have to show this.

2487 Lastly, the mass resolution is parametrized as a function of mass using a 4th order polynomial
 2488 fit to the mass resolution with track momentum smearing. This parameterization is used as an input
 2489 to the size of the mass search windows. For L1L1, the parametrization is

$$\sigma_m(m[\text{MeV}]) = 0.9348 + 0.05442 m - 5.784 \times 10^{-3} m^2 + 5.852 \times 10^6 m^3 - 1.724 \times 10^{-8} m^4 \quad (5.5)$$

2490 and for L1L2, the parametrization is

$$\sigma_m(m) = 0.04906\text{MeV} + 0.04694m \quad (5.6)$$

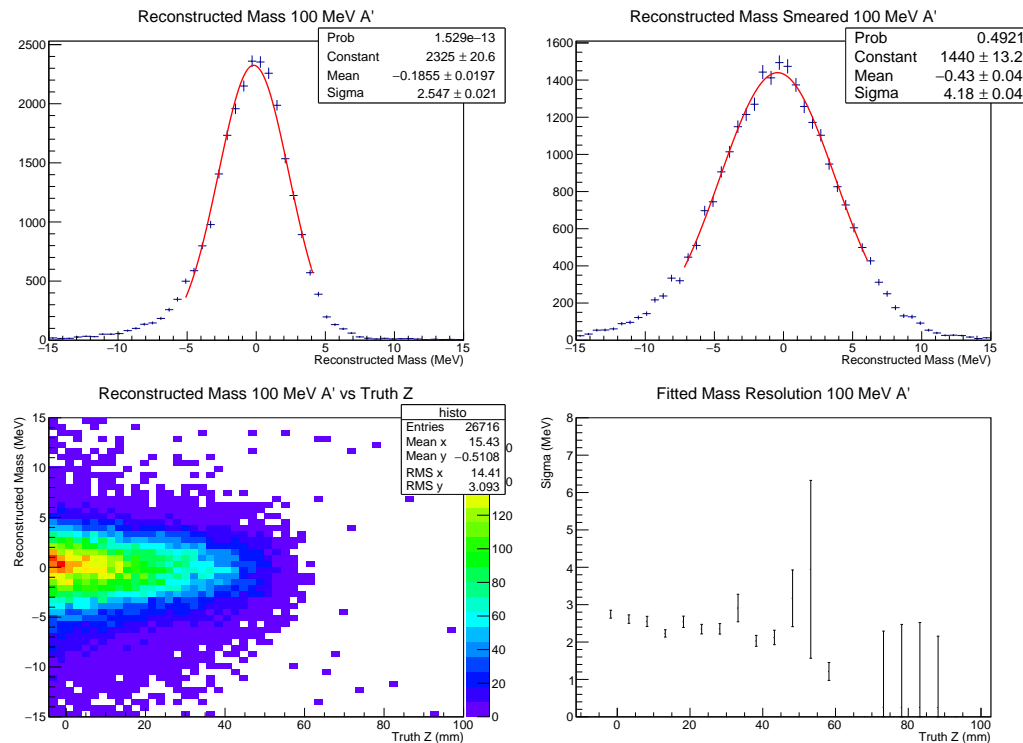


Figure 5.5: Upper Left: Fitted reconstructed mass spectrum for a 100 MeV displaced A' . Upper Right: Fitted reconstructed mass spectrum for a 100 MeV displaced A' with track momentum smearing. Lower Left: Reconstructed mass vs truth z decay for a 100 MeV displaced A' . Lower Right: The fitted mass resolution for 100 MeV displaced A' 's as in slices of truth z . Mass resolution is approximately independent of decay length. These plots are for the L1L1 category.

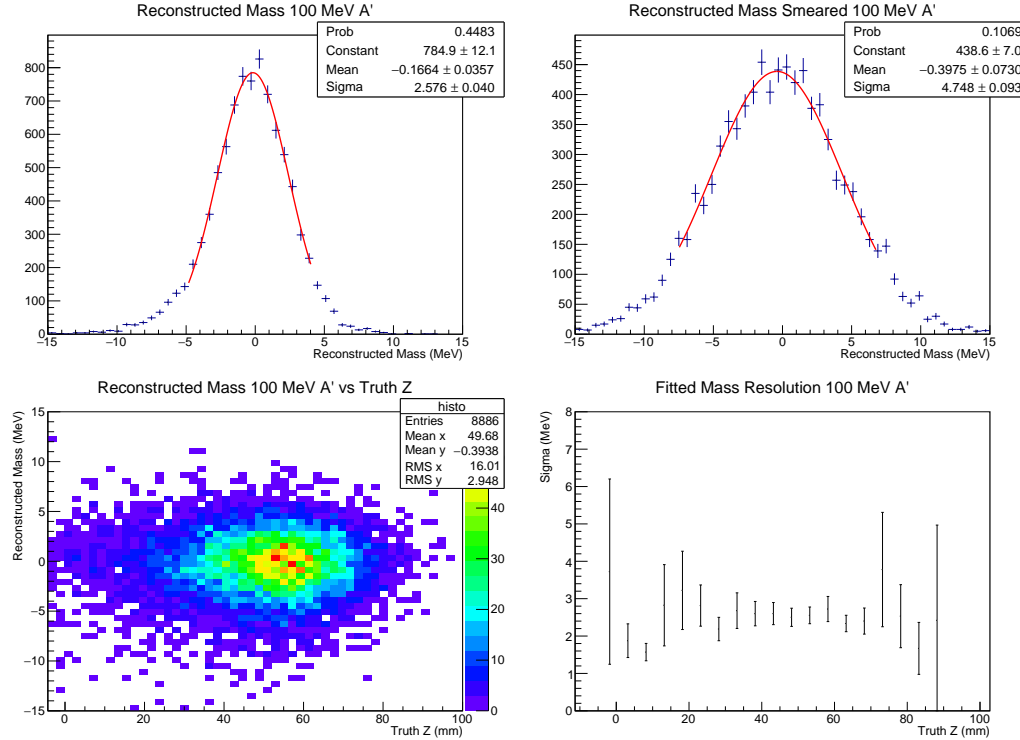


Figure 5.6: Upper Left: Fitted reconstructed mass spectrum for a 100 MeV displaced A' . Upper Right: Fitted reconstructed mass spectrum for a 100 MeV displaced A' with track momentum smearing. Lower Left: Reconstructed mass vs truth z decay for a 100 MeV displaced A' . Lower Right: The fitted mass resolution for 100 MeV displaced A' 's as in slices of truth z . Mass resolution is approximately independent of decay length. These plots are for the L1L2 category.

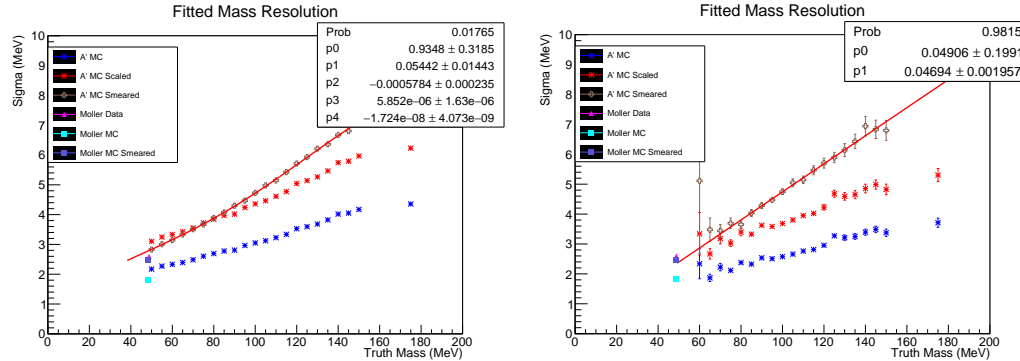


Figure 5.7: A' mass resolution as a function of mass comparing A' MC, A' MC scaled using the ratio of the Møller mass resolution in data to MC, and A' MC with smearing for the Left: L1L1 category and the Right: L1L2 category. The mass resolution is fitted to a straight line to the MC with track momenta smearing and is used as an input to the size of the mass bins in the final results.

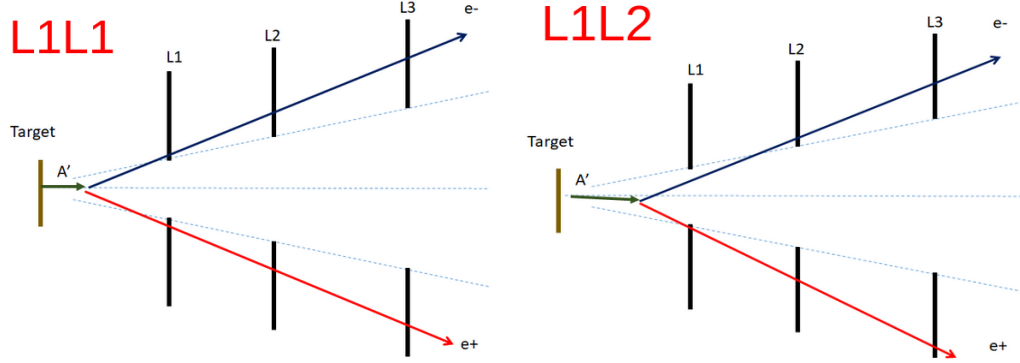


Figure 5.8: Left: Schematic of a relatively short A' decay length in which both daughter particles have a layer 1 hit. This is referred to as L1L1. Right: Schematic of a relatively long A' decay length in which one of the daughter particles misses layer 1 (but hits layer 2) and the other daughter particle hits layer 1. This is referred to as L1L2.

2491 5.3 Displaced A' Rates

2492 The process of computing the expected number of radiative events was shown in Sec. 4.11.3 as the
 2493 product of the radiative fraction f_{rad} and the number of e^+e^- events in a given narrow mass bin
 2494 N_{bin} . From there, the number of expected A' 's as a function of mass and ϵ was easily computed by
 2495 Eq. 4.11 and shown in Fig. 4.24. From the production rate of A' 's at the target, which has the same
 2496 event selection as Table 4.9, the next step is to displace the A' 's as a function of $m_{A'}$ and ϵ and do
 2497 the proper accounting for geometrical acceptance effects.

2498 5.3.1 A' Acceptance Effects

2499 The SVT is designed to have a geometrical acceptance of 15 mrad for prompt decays. However,
 2500 downstream decays must have a larger opening angle to remain in the acceptance of the SVT, and
 2501 the further downstream the decay, the more likely the daughter particles will miss the SVT. Thus,
 2502 the geometrical acceptance drops dramatically with increasing decay length. Based on geometrical
 2503 acceptance, there are several possibilities for a long-lived A' .

- 2504 1. The A' has a finite, but relatively short decay length, and both of the A' daughter particles
 2505 have layer 1 hits in the SVT. This category is denoted as L1L1 (where the 1's denote the first
 2506 layer of the SVT that the A' daughter particles hit).
- 2507 2. The A' has a slightly longer decay length than those that fall into the L1L1 category causing
 2508 exactly one of the A' daughter particles to miss layer 1 but hit layer 2, whereas the other
 2509 particle hits layer 1. This category is denoted as L1L2.

- 2510 3. The A' has a longer decay length than the L1L2 category causing both of the A' daughter
2511 particles to miss layer 1, but both particles have hits in layer 2. This category is denoted as
2512 L2L2.
- 2513 4. The A' has a relatively long decay length or a small opening angle where at least one of the
2514 A' daughters misses both layer 1 or layer 2. In these cases, the A' is not reconstructed since
2515 track reconstruction requires a minimum of five 3-D hits.

2516 Since we require 5 hits on every track, these four mutually exclusive categories are the only viable
2517 possibilities. A schematic of the L1L1 and L1L2 categories is shown in Fig. 5.8. Once the displaced
2518 A' 's are placed in the correct category and the geometrical acceptances are properly incorporated,
2519 the last step is to properly account for hit efficiencies in the SVT. For instance, hit efficiency effects
2520 can cause an A' event that should fall into the L1L1 category based on geometrical acceptance to
2521 have a missing layer 1 hit due to an inefficiency. This example would cause the A' event to migrate
2522 into L1L2 category. Unfortunately, the hit efficiencies are not properly accounted for in the MC
2523 and their study is ongoing. However, as a quick post-reconstruction fit, a hit killing method is
2524 implemented and described in the following subsection in Sec. 5.3.2.

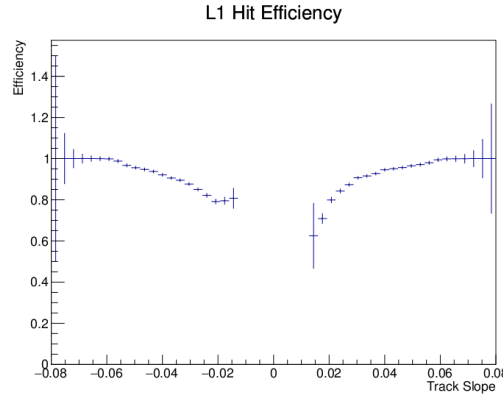


Figure 5.9: The layer 1 efficiency used for the hit killing algorithm as a function of track slope ($\tan\lambda$).

5.3.2 Hit Killing

The HPS detector has hit efficiency effects, particularly in the first layer of the SVT, as described in Sec. 4.6 that must be accounted for in the A' MC in order to properly normalize the expected signal rate. Hit efficiencies are measured as a function of channel number in the SVT, and although the eventual goal is to implement a hit killing algorithm based on channel number, a simple post-reconstruction hit killing algorithm based on track slope ($\tan\lambda$). The layer 1 efficiency used as a function of track slope is shown in Fig. 5.9. Since the hit efficiency in the other layers is $> 99\%$, the hit killing algorithm is only applied to layer 1 hits.

If a track passes the hit killing algorithm, nothing changes. However, if a track fails the hit killing algorithm, the layer 1 hit is removed and the A' can either migrate into another category or be eliminated. Details on several possibilities of an A' event passed through the hit killing algorithm are as follows:

1. Begin with the L1L1 category. Based on track slope, decide if each positron and electron track pass the electron efficiency cut. There are 4 possible scenarios.
 - (a) If both pass, the event remains in the L1L1 category.
 - (b) If either track fails to pass the cut and has 5 hits on track, the event is removed.
 - (c) If exactly one track fails to pass the cut and has 6 hits on track, the event is moved to the L1L2 category.
 - (d) If both tracks fail to pass the cut and both tracks have 6 hits on track, the event is moved to the L2L2 category.
2. Next move to the L1L2 category (excluding those events that have migrated into the L1L2 category from the L1L1 category). For this category, since only layer 1 inefficiencies are

2547 considered and exactly one track contains a layer 1 hit, only the track with the layer 1 hit is
 2548 considered. Again based on track slope, decide if the positron or electron track passes the hit
 2549 efficiency cut. There are 3 possible scenarios.

- 2550 (a) The track with the layer 1 hit passes the hit efficiency cut, it remains in the L1L2 category.
 - 2551 (b) The track with the layer 1 hit fails the hit efficiency cut and has 5 hits on track. This
 2552 event is removed.
 - 2553 (c) The track with the layer 1 hit fails the hit efficiency cut and has 6 hits on track. This
 2554 event is moved to the L2L2 category.
- 2555 3. Finally, no events are removed from the L2L2 category since only layer 1 efficiencies are
 2556 considered and L2L2 events have no layer 1 hit by definition. However, L2L2 gains some of
 2557 the A' events from L1L1 and L1L2 categories. As previously explained, L2L2 is not considered
 2558 for this analysis.
- 2559 4. Lastly, add the events that have migrated from L1L1 into L1L2, and add the events that have
 2560 migrated from L1L1 and L1L2 into L2L2.

2561 These steps complete the post-reconstruction track slope-dependent hit killing algorithm thus
 2562 incorporating the efficiency curves for A' 's as a function of z that includes both geometrical acceptance
 2563 and hit efficiency effects. An example of the efficiency curves divided into the three mutually exclusive
 2564 categories (and their sum) for two A' masses before and after the hit killing algorithm is shown in
 2565 Fig. 5.10.

2566 At this point, the efficiency curves denoted as $\epsilon_{vtx,sum}(z, m_{A'})$ are normalized to unity at the
 2567 target. More specifically, the sum of the mutually exclusive categories is fit and extrapolated to
 2568 the target position in and re-scaled such that $\epsilon_{vtx,sum}(z_{targ}, m_{A'}) = 1$. The fit is shown in Fig.
 2569 5.10. However, there are tight selection cuts to be applied described in Sec. 5.4, and these are
 2570 applied to the efficiency curves after normalization and shown in Fig. 5.11.². To complete the
 2571 efficiency curves, the signal region in must be defined and a description is given in Sec. 5.5. As a
 2572 summary of this procedure, a value of z (denoted as z_{cut}) is chosen downstream of which a near-0
 2573 background is expected. Thus $z > z_{cut}$ defines the signal region, and this requirement is applied to
 2574 the reconstructed z of efficiency curves shown in Fig. 5.11. Finally, to compute the actual expected
 2575 A' yield as a function of $m_{A'}$ and ϵ , a re-weighting method is applied to these efficiency curves and is
 2576 described in detail in Sec. 5.6.1. I am trying to build up to this, though I'm not sure to an outsider
 2577 it will be clear what I'm doing.

²There is about a 20% reduction in signal efficiency from the tight cuts which is why these curves are normalized to ~ 0.8 at the target.

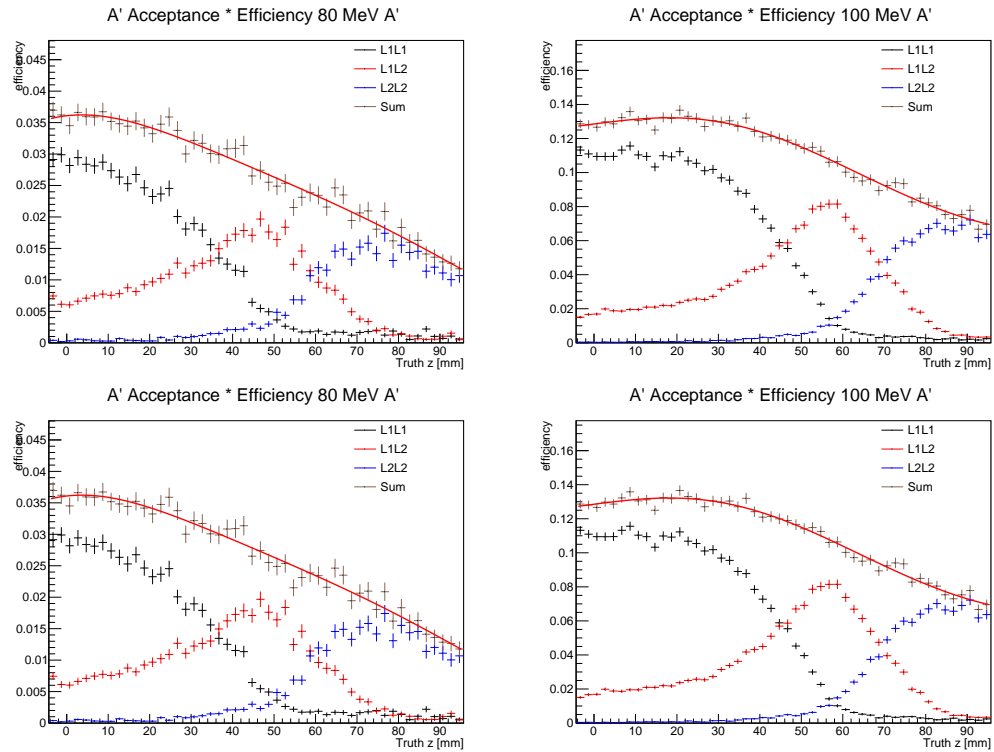


Figure 5.10: The product of geometrical acceptance and efficiency for displaced A' 's for the L1L1, L1L2, and L2L2 categories as well as there sums. 80 MeV displaced A' 's are on the left and 100 MeV displaced A' 's are on the right. The top is before hit killing and the bottom is with hit killing and a fit function fit to the sum of the categories. **The top plots I still have to make, I have the same plots there as the bottom as a placeholder.**

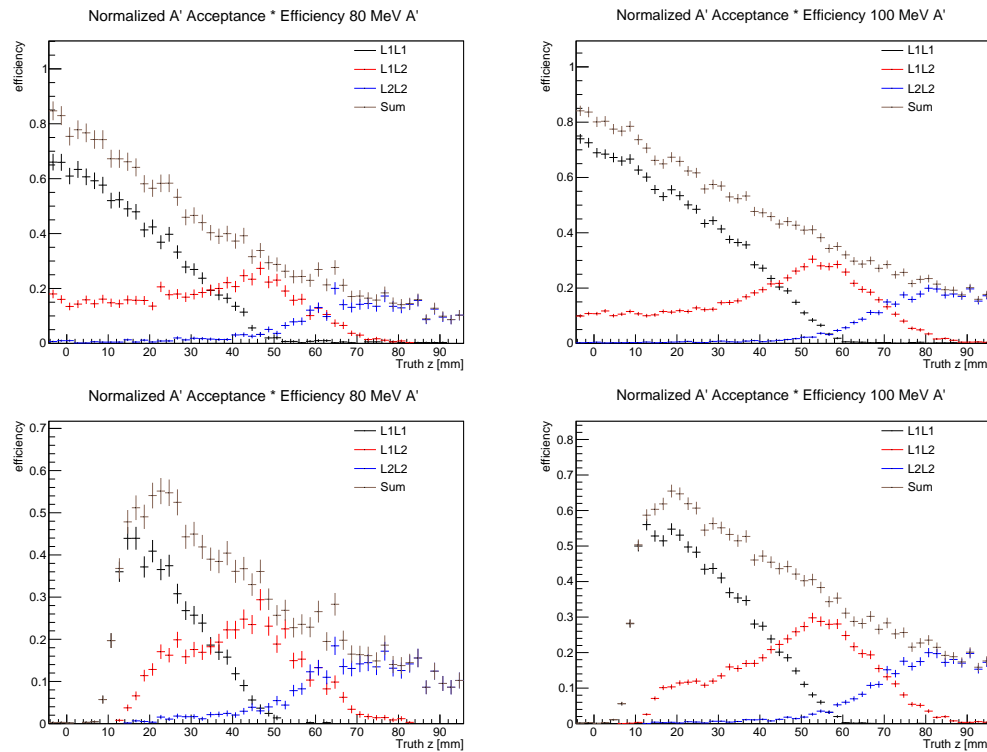


Figure 5.11: The product of geometrical acceptance and efficiency for displaced A' 's for the L1L1, L1L2, and L2L2 categories as well as there sums. These plot are normalized to unity at the target, where the sum is normalized before hit killing and further analysis cuts. 80 MeV displaced A' 's are on the left and 100 MeV displaced A' 's are on the right. The top is without the z_{cut} and the bottom is with the z_{cut} from 10% of the data.

2578 **5.4 Vertex Cuts**

2579 There was a bug in my plotting code in which some of the ratios in the cuts are simply just 1. I will
2580 fix and update when I get a chance.

2581 The goal of the displaced vertexing analysis is to find long-lived A 's beyond a background of
2582 prompt QED tridents. In order to achieve this, tighter cuts must be utilized such that the prompt
2583 background that reconstructs at large z , the so-called “high z background”, is reduced to manageable
2584 level such that A 's can potentially be discovered. Thus, beyond the Preselected events, several more
2585 cuts in order to further reduce backgrounds at high z that appear otherwise signal-like must be
2586 utilized.

2587 A majority of the large z backgrounds result from scattering in layer 1 of the tracker (both the
2588 active and dead detector material) or mis-reconstructed tracks. Because of this, there are a variety
2589 of handles that can be utilized to efficiently distinguish between a true displaced signal and a prompt
2590 background. In general, a true displaced signal will have a downstream reconstructed position with
2591 small error, will have a momentum point back to the beam spot, and be composed of clean tracks
2592 with large vertical impact parameters. This is not necessarily true for background. Thus, cuts
2593 on impact parameters, projections of the V0 momentum back to the target, and vertex quality are
2594 utilized. In addition, to guard against high z background due to mis-tracking the so-called “isolation
2595 cut” is implemented as well as a minimum V0 momentum cut to kinematically separate A 's from
2596 Bethe-Heitler tridents.

2597 These cuts are fairly easy to demonstrate the qualitative effectiveness of reducing background
2598 without sacrificing too much signal efficiency. Unfortunately, the current understanding of the
2599 background shapes and uncertainties in the background model are not known in detail. In order
2600 to tune actual cut values beyond the initial qualitative justification, we must rely on only 10% of
2601 the data, a luminosity-equivalent MC sample of tridents overlaid with simulated beam background
2602 and wabs, and a three times luminosity-equivalent sample of pure tridents. Although these samples
2603 are all informative, this limitation makes it difficult to specify some of the cut values in a rigorous
2604 quantitative manner.

2605 A 's with a relatively short decay length will have layer 1 hits for both daughter particles, while A 's
2606 with longer decay lengths may have one or both of these particles miss layer 1 due to geometrical
2607 acceptance as shown in Fig. 5.8. For prompt background, even though the SVT is designed to
2608 maintain the same acceptance in all layers at 15 mrad, several “real world” effects cause particles to
2609 sometimes miss a layer in the detector. First, hit efficiencies in layer 1 may cause particles to miss
2610 layer one even though the particle traverses the active sensor plane. In addition, daughter particles
2611 (or photon conversions) can interact with the dead material in layer 1 and force the particle to
2612 scatter into the acceptance of the detector. These effects are shown in Fig. 5.12.

2613 Thus, the analysis is divided into several mutually exclusive categories based on the first hits on
2614 track of the two daughter particles similar to how signal is divided in Sec. 5.3. If both particles have

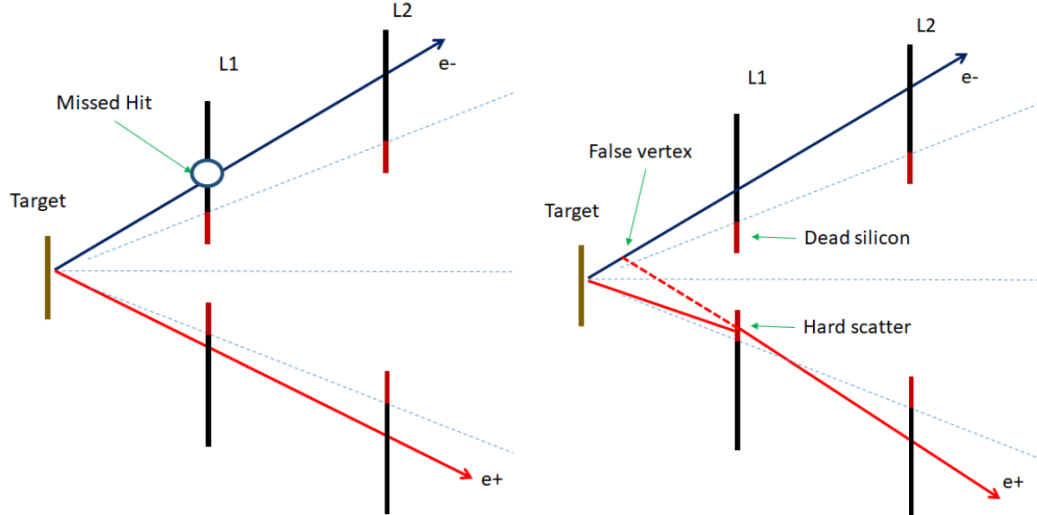


Figure 5.12: Left: A schematic of a prompt background process that has a hit inefficiency in layer 1 and is placed in the L1L2 category. Right: A schematic of a prompt background process in which one of the daughter particles scatters away from the beam in the inactive silicon of layer 1 and into the acceptance of the tracker. This process is placed in the L1L2 category and also reconstructs a false vertex downstream of the target.

2615 a layer 1 hit, the event is placed in the so-called L1L1 category. If exactly one particle hits layer
 2616 1 and the other particle misses layer 1, the event is placed in the L1L2 category. If both particles
 2617 miss layer 1, event is placed in the L2L2 category. These are the only three categories since tracking
 2618 algorithms require 5 hit tracks in a 6 layer detector. For the purposes of this analysis, only the
 2619 L1L1 and L1L2 categories are used since the probability of further downstream decays decreases
 2620 exponentially such that the L2L2 category adds minimal significance to the analysis.

2621 Performing the analysis on these categories separately instead of together is done for several
 2622 reasons. First, the vertex resolution is highly dependent on which layers are hit first. The closer
 2623 the first hit to the target the better the vertex resolution (i.e. L1L1 has better vertex resolution
 2624 than L1L2 which has better resolution than L2L2). Second, the nature of the backgrounds between
 2625 the categories are different. The L1L1 category high z backgrounds are typically due to multiple
 2626 scattering in the active region of L1 sensors and mis-tracking. While backgrounds in the L1L2 and
 2627 L2L2 categories are typically due to hit efficiency effects, multiple scattering in both active and
 2628 inactive regions of layer 1, mis-tracking, and even trident production in layer 1.

2629 **5.4.1 L1L1**

2630 **L1L1 Layer Requirements**

2631 For the L1L1 category, layer 1 hits on both e^+e^- tracks are required. In addition to requiring
2632 layer 1 hits, layer 2 hits are also required which improves the resolution for extrapolating tracks to
2633 the correct hit in layer 1. This has the effect of reducing mis-tracking which can result in high z
2634 backgrounds (see isolation cut subsection). Layer 3 hits are not explicitly required by the analysis,
2635 rather they are implicitly required by the SeedTracker algorithm. Thus, all events in this category
2636 have hits in layers 1-3. A summary of the tight selection cuts in the L1L1 category is shown in Table
2637 5.3 and described in the following subsections.

Cut Description	Requirement
Layer 1 Requirement	e^+ and e^- have L1 hit
Layer 2 Requirement	e^+ and e^- have L2 hit
Radiative Cut	$V_{0p} > 1.85$ GeV
V0 projection to target	Fitted 2σ cut
Isolation Cut	Eq. 5.9
Impact Parameters	Eq. 5.12

Table 5.3: A summary of the tight cuts for the L1L1 category.

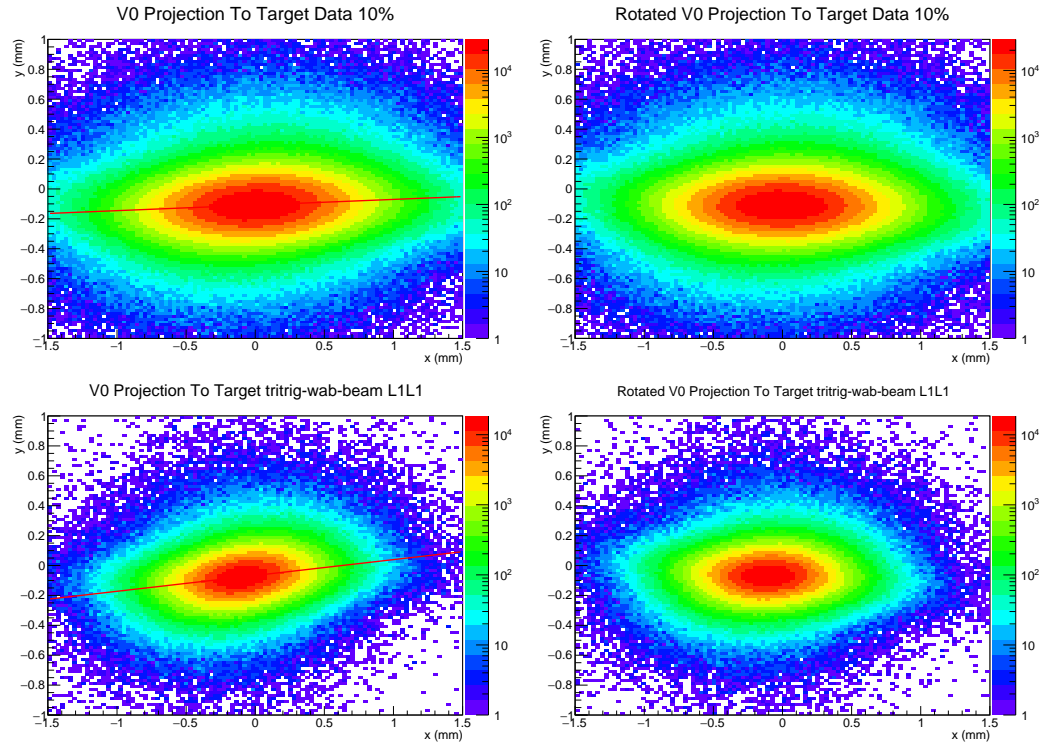


Figure 5.13: The V0 projection back to the target for Preselection in the L1L1 category. Upper Left: 10% Data with a linear fit to the $x-y$ correlation Lower Left: 10% tritrig-wab-beam with a linear fit to the $x-y$ correlation. The V0 projection back to the target for L1L1 Preselection with rotated $x-y$ coordinates for Upper Right: 10% Data and Lower Right: 10% tritrig-wab-beam. The angle of rotation is $\theta_{data} = 0.0387$ rad in data and $\theta_{MC} = 0.1110$ rad in MC.

Projection of the vertex to the target

As mentioned previously, in order to reduce the number of downstream high z background events, it is required that vertices project back to the beamspot position. The vertex projection to the target in the $x - y$ plane is computed by taking the direction of the vertex momentum, computed as the vector sum of the momenta of the e^+e^- pair, and extrapolating the vertex position to the target location (at $z = -4.3$ mm in detector coordinates). While in MC simulation the beamspot is generated in a fixed position, the position of the unconstrained vertices in the $x - y$ plane in data depends on the beam conditions, leading to run-by-run biases that need to be corrected before applying the target projection cut.

The longitudinal and transverse spatial distributions of the vertices that pass the *Preselection* cuts are used to estimate the run-by-run position of the beamspot in data and MC simulation. The spatial distributions are fit with a Gaussian function in the interval $[-1.5\text{RMS}, 1.5\text{RMS}]$, where RMS is the root mean square of the distributions. The same procedure is applied to the distributions for

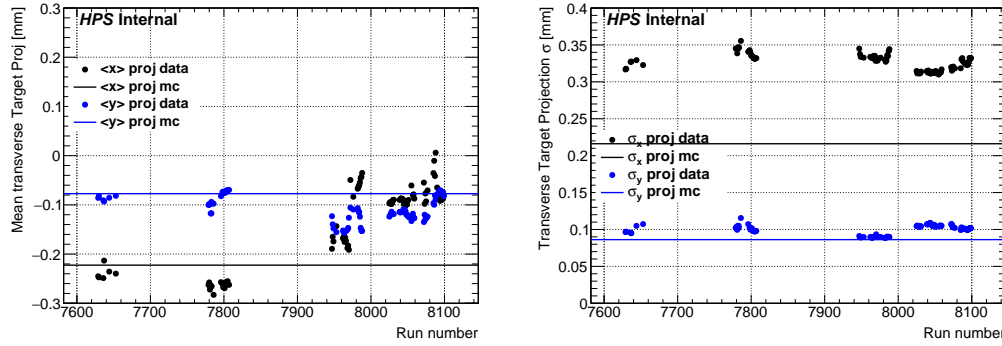


Figure 5.14: The run-dependent mean (left) and width (right) for x and y target projection for the unconstrained vertex in data.

2651 the transverse projections of the vertex to the target surface.

2652 The transverse projections show correlation between the x and y coordinates of the extrapolations
2653 in Fig. 5.13 in both data and MC, although different correlations. The linear correlation was fit in
2654 the interval [-0.5 mm, 0.5 mm] in order to fit the correlation in the core of the distribution. The
2655 angle in data, across all 10%, is $\theta_{data} = 0.0387$ rad and in a subset of tritrig-wab-beam $\theta_{MC} = 0.1110$
2656 rad. The rotation is also shown Fig. 5.13. The new rotated coordinates are then refit using the
2657 method above to determine the rotated x and y fitted means and sigmas in MC and on a run-by-run
2658 basis for data. These values are used to form an elliptical cut on the rotated x and y coordinates in
2659 units of n_σ from the mean.

2660 In Figure 5.14, the mean and width of the transverse projection to the target surface, with
2661 rotations for the x and y coordinates are shown for data and MC. These are used for the run-by-run
2662 corrections in data. The actual cut value, which is reduced to a single tuneable parameter n_σ from
2663 the mean, is difficult to demonstrate quantitatively for reasons described previously. However as a
2664 quick study, the cut value was floated and the ratio of the expected signal yield (at two optimal
2665 mass and ϵ points) to the background (taken across the entire signal range) was computed. It was
2666 determined by this metric that the final result is generally independent in the cut range from $n_\sigma = 2$
2667 to $n_\sigma = 3$. From this study, the cut is selected as $n_\sigma = 2\sigma$ and is shown in Fig. 5.15. The effect
2668 of the V0 projection cut is shown in Fig. 5.16 including the final selection with and without the
2669 projection cut (i.e. an $n - 1$ plot).

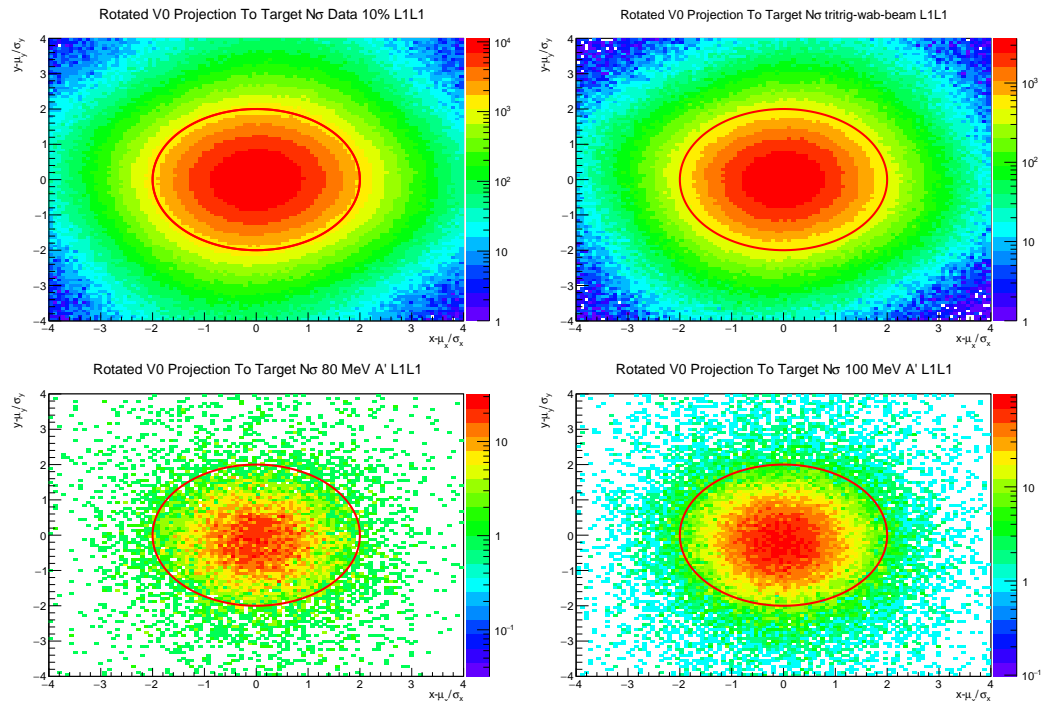


Figure 5.15: The V0 projection back to the target significance ($x(y) - x_{\text{mean}}(y)/x_{\sigma}(y)$) using the rotated coordinates for L1L1 Preselection for Upper Left: 10% data Upper Right: 1% tritrig-wab-beam Lower Left: Displaced 80 MeV A' Lower Right: Displaced 100 MeV A' . The elliptical cut at 2σ is shown in red.

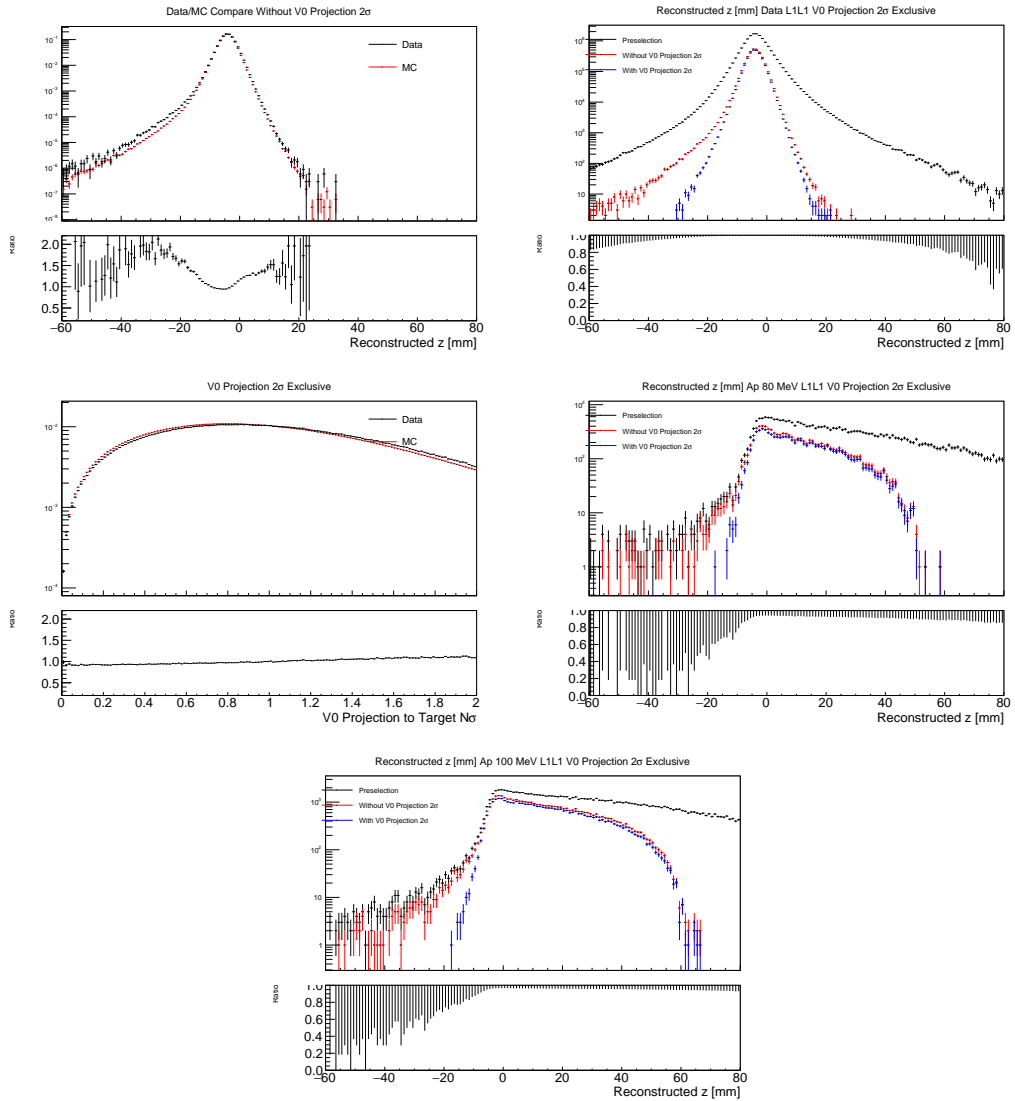


Figure 5.16: Plots showing the effect of with and without the V0 projection to the target cut for the L1L1 category. Upper Left: Comparison of VZ distributions for 10% Data and 100% tritrig-wab-beam MC for all tight cuts except for the V0 projection to the target cut. Upper Right: Comparison of preselection, tight cuts, and tight cuts without the V0 projection to the target cut for 10% Data. Middle Left: Comparison of the V0 projection to the target in units of $n\sigma$. for 10% Data and tritrig-wab-beam MC using all tight cuts except the V0 projection to the target cut. Middle Right: Comparison of preselection, tight cuts, and tight cuts without the V0 projection to the target cut for displaced 80 MeV A's. Bottom: Comparison of preselection, tight cuts, and tight cuts without the V0 projection to the target cut for displaced 100 MeV A's.

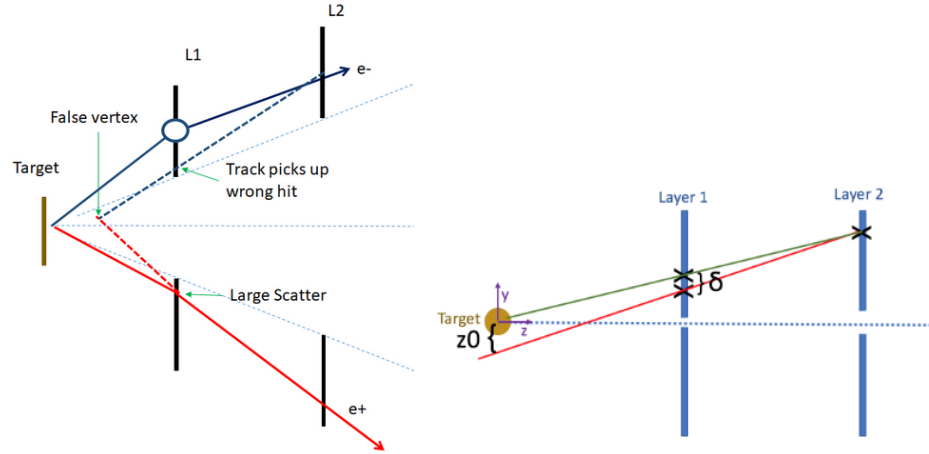


Figure 5.17: Left: Example of mistracking from a layer 1 bad hit that falsely reconstructs downstream of the target. Right: Geometric picture of the isolation cut comparing the distance between the nearest hit away from the beam δ and the track longitudinal impact parameter of the track z_0 where the correct track is in green and the incorrect track found by the tracking algorithm is in red.

2670 Isolation Cut

2671 Mis-reconstructed tracks, or mis-tracking, are tracks that contain at least one hit on track that
 2672 is not associated with the particle responsible for the majority of other hits on track. For instance,
 2673 a track can reconstruct from a real particle trajectory but with an additional hit from a beam
 2674 electron, recoil electron, photon, or noise hit. This incorrect hit is also called a “bad hit.” And
 2675 when this additional hit is in layer 1 and is closer to the beam than the true hit (or if the true
 2676 hit doesn’t exist), this can falsely reconstruct a downstream vertex, often significantly downstream,
 2677 that appears signal-like as shown in Fig. 5.17. Often this occurs as a result of scattering in the
 2678 second layer causing the track to extrapolate to the incorrect hit in layer 1 (often times having a
 2679 better track quality than a track with the true hit) and occurs at a significant enough rate that it
 2680 needs to be mitigated.

2681 The isolation cut is performed on tracks, and unfortunately as discussed in Sec. 4.1, the co-
 2682 ordinate systems for track reconstruction utilizes perigee parametrization while the analysis uses
 2683 detector coordinates.

2684 The isolation cut utilizes a post-reconstruction strategy designed to eliminate high z backgrounds
 2685 due to mis-tracking from bad hits in layer 1. In particular, tracks that mis-reconstruct the 3D hit
 2686 in the first layer of the SVT where the hit on track is closer to the beam plane than the true hit can
 2687 reconstruct a downstream vertex that appears to be signal-like. The isolation cut offers a simple
 2688 method to test if fitting a track with another hit in layer 1 is more consistent with the track coming
 2689 from the primary than the secondary vertex without re-running track reconstruction (even if the
 2690 original track would have better track quality). If the track is more consistent with the primary, the

2691 event is eliminated.

2692 The most basic form of this cut is a simple geometric cut that compares the distance of the next
 2693 closest hit in the sensor, called the isolation value δ , to the track longitudinal impact parameter z_0
 2694 (tracking z is in the vertical direction y in the detector frame). First, since the track parameter
 2695 z_0 is recorded at the origin and the target position is upstream from the origin at $z_{targ} = -4.3$
 2696 mm, the value of z_0 is corrected to the impact parameter at the target z_{0corr} using a simple linear
 2697 extrapolation of the track state to the target.

2698 The isolation value δ is the distance along the measurement direction for each sensor between
 2699 the 1D cluster hit on track and the next nearest 1D cluster hit in the direction away from the beam
 2700 plane. By sign convention, δ is always positive, and the 1D cluster hits closer to the beam plane
 2701 are not considered since these will reconstruct the vertex further downstream (and we are testing if
 2702 a track fit with another hit is more consistent with the primary). Furthermore, only the minimum
 2703 isolation value between the axial and stereo sensor in a given layer is considered.

2704 Comparing this value to the impact parameter, the geometrical condition of the isolation cut is
 2705 such that, for the track to pass the cut, the isolation value must be greater than the product of the
 2706 impact parameter and the ratio of the distance between first 2 measurement points and the distance
 2707 between the second measurement and the primary (i.e. $\frac{z_{L2}-z_{L1}}{z_{L2}-z_{targ}}$). In the case of a layer 1 isolation
 2708 cut, since the ratio of the distance between layer 2 and layer 1 and layer 2 and the target is about one
 2709 half, the ratio used in this condition is $\frac{1}{2}$. Otherwise, this “refitted” track is more consistent with
 2710 the primary and the event is eliminated. This concept is shown in Figure 5.17, and this condition
 2711 can be expressed with the following inequality.

$$\delta + \frac{1}{2}z_{0corr} > 0 \quad (5.7)$$

2712 It has been shown in the previous displaced vertexing analysis from the 2015 engineering run that
 2713 this simple geometric cut eliminates a large fraction of high z events due to mistracking, but fails to
 2714 account for multiple scattering in layer 1 [8]. Thus, the high z backgrounds of this nature were not
 2715 mitigated to the full potential in previous analysis. In other words, there were high z backgrounds
 2716 observed in both data and MC that were near the edge of this basic isolation cut, and shifting the simple
 2717 cut by even a small amount would have further reduced high z background. Extending the simple
 2718 geometric cut by incorporating an error on the impact parameter z_{0corr} accounts for the multiple
 2719 scattering in the tracker.

2720 In order to take multiple scattering into account, the z_{0corr} term in Equation 5.7 is modified by
 2721 adding the estimate of its error at the target position, effectively shifting the value of the isolation
 2722 cut.

$$z_{0corr} \longrightarrow z_{0corr} + \Delta z_{0corr} \quad (5.8)$$

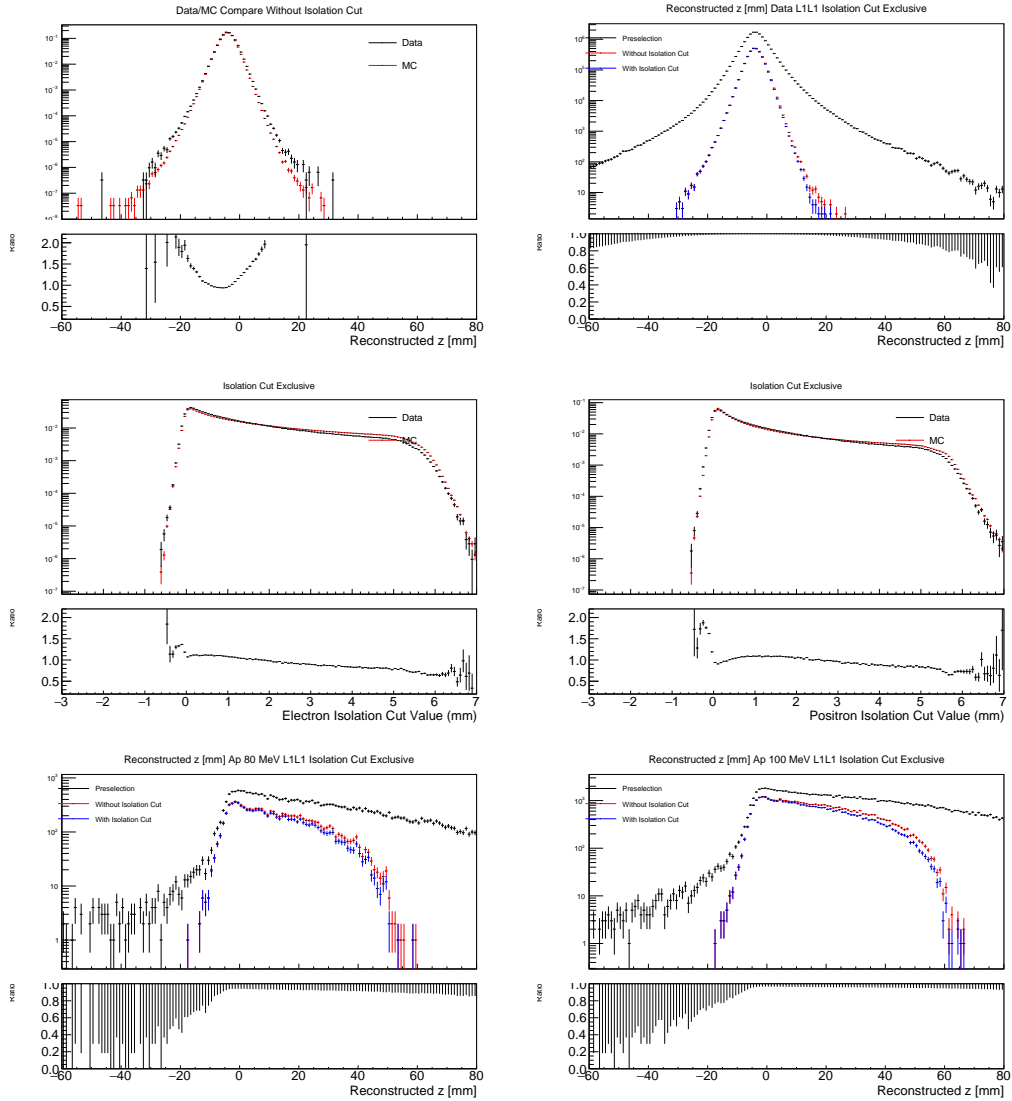


Figure 5.18: Plots showing the effect of with and without the isolation cut for the L1L1 category. Upper Left: Comparison of VZ distributions for 10% Data and 100% tritrig-wab-beam MC for all tight cuts except for the isolation cut. Upper Right: Comparison of preselection, tight cuts, and tight cuts without the isolation cut for 10% Data. Middle Left: Electron isolation cut value for 10% Data and tritrig-wab-beam MC using all tight cuts except the isolation cut. Middle Right: Positron isolation cut value for 10% Data and tritrig-wab-beam MC using all tight cuts except the isolation cut. Bottom Left: Comparison of preselection, tight cuts, and tight cuts without the isolation cut for displaced 80 MeV A's. Bottom Right: Comparison of preselection, tight cuts, and tight cuts without the isolation cut for displaced 100 MeV A's.

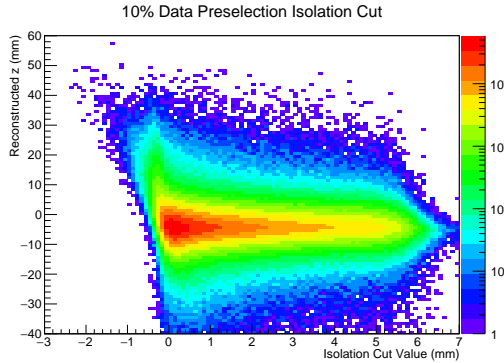


Figure 5.19: Reconstructed z vs. the isolation cut value in eq. 5.9 for 10% of the data with preselection and layer 1 requirements. This isolation cut value combines positrons and electrons for both top and bottom, but only uses the minimum positive isolation value for the axial and stereo pair in layer 1.

2723 Typically, the errors of the impact parameter at the target are ~ 0.1 mm. In order to take into
 2724 account large scatters in the L1 material, the isolation cut takes into account the errors in the track
 2725 extrapolation on a track-by-track basis by shifting the cut value up to a specified n_σ on z_0 leading
 2726 to a final isolation cut value given by I refer to the entire left side of the equation as the “isolation
 2727 cut value”. This may be confusing, but I didn’t have time to change the name on the plots so I’ll
 2728 find a better way to denote it later.

$$\delta + \frac{1}{2} (z_{0,corr} - n_\sigma \Delta z_{0,corr}) > 0 \quad (5.9)$$

2729 The last step in finalizing the isolation cut is to select the number n_σ to use in the cut. In general,
 2730 the signal efficiency is fairly insensitive to (since $\Delta z_{0,corr} \sim 100\mu\text{m}$). A reasonable value on the error
 2731 is 3σ which eliminates all high z background due to mis-tracking according to MC (a simple study
 2732 analyzing the signal efficiency shows that the result is generally independent between the range of
 2733 $n_\sigma = 2.5$ to $n_\sigma = 3.5$). The effect of the cut on 10% data, 100% tritrig-wab-beam, and 80 MeV and
 2734 100 MeV displaced A' 's is shown in Fig. 5.18.

2735 In order to better understand the effect of the isolation cut, it is important to see its affect on
 2736 both good tracks (tracks in which all hits on track are a result of its truth match) and bad tracks
 2737 (or mis-tracks, those with at least one bad hit) which can be determined by truth-matched tracks in
 2738 MC as described in Sec. 4.8. For preselected events with a layer 1 hit, the reconstructed z positions
 2739 vs the isolation cut value in eq. 5.9 for 10% of the data, 100% the tritrig-wab-beam MC sample
 2740 separating good and bad tracks, and displaced A' MC at two different mass points are shown in Fig.
 2741 5.19, Fig. 5.20, and Fig. 5.21, respectively.

2742 Finally, a comparison of the reconstructed z distribution for 100% tritrig-wab-beam for V0 par-
 2743 ticles with 100% pure e^+ and e^- tracks and V0 particles with at least one e^+ or e^- track with a

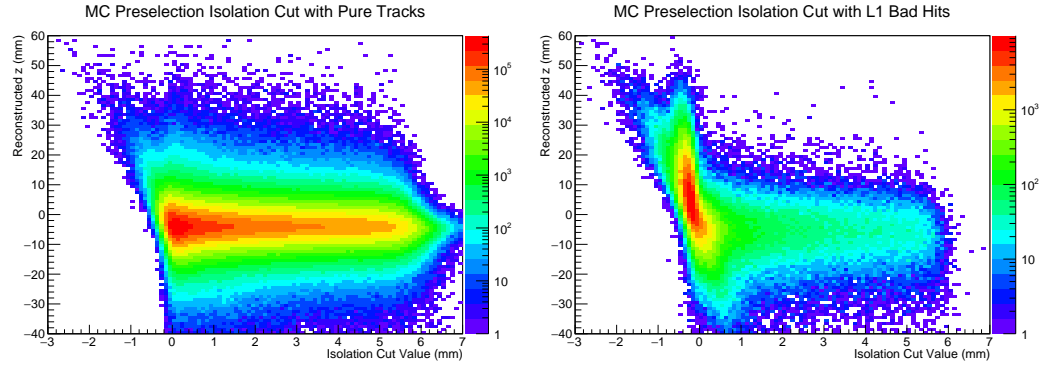


Figure 5.20: Reconstructed z vs. the isolation cut value in eq. 5.9 for 100% of the tritrig-wab-beam MC sample with preselection and layer 1 requirements. This isolation cut value combines positrons and electrons for both top and bottom, but only plots the minimum positive isolation value for the axial and stereo pair in layer 1. The left plot only selects tracks that match to the same MCParticle, while the plot on the right only selects V0 particles that contain either an e^+ or e^- track that have an incorrect layer 1 hit.

2744 bad hit in L1 is shown in Fig. 5.22. For tritrig-wab-beam, 98.8% of the V0 particles have 100% pure
 2745 tracks for both e^+ and e^- tracks while 0.95% of the V0 particles have either e^+ or e^- with a bad
 2746 L1 hit. The remaining fraction of V0 particles have either an e^+ or e^- bad hit in a layer other than
 2747 L1 (with good hits in L1) or have no track to truth match for either the e^+ or e^- particle.

2748 The isolation cut is not sensitive to sensor inefficiencies as it has been developed under the
 2749 assumption that a real 3D hit has been reconstructed. Therefore tracks that are reconstructed by
 2750 with an incorrect 3D hit because the true hit has failed the reconstruction cannot be eliminated by
 2751 this cut. The possible effects of hit efficiencies on high z backgrounds is discussed in more detail in
 2752 Sec. 5.8.

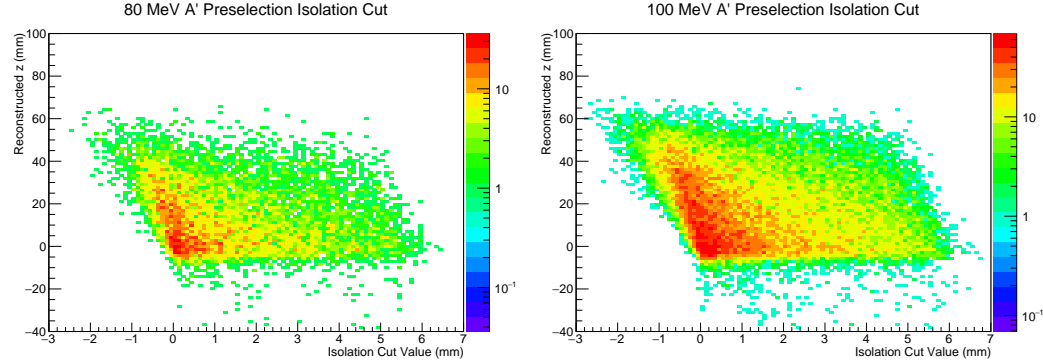


Figure 5.21: Reconstructed z vs. the isolation cut value in eq. 5.9 for an 80 MeV (left) and 100 MeV (right) displaced A' with preselection and layer 1 requirements. This isolation cut value combines positrons and electrons for both top and bottom, but only plots the minimum positive isolation value for the axial and stereo pair in layer 1.

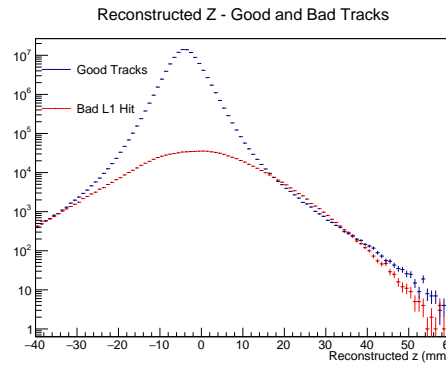


Figure 5.22: A comparison of the reconstructed z distribution for V0 particles with 2 tracks that have all the hits matched to an MC particle (blue) and those with either an e^+ or e^- track with a bad layer 1 hit.

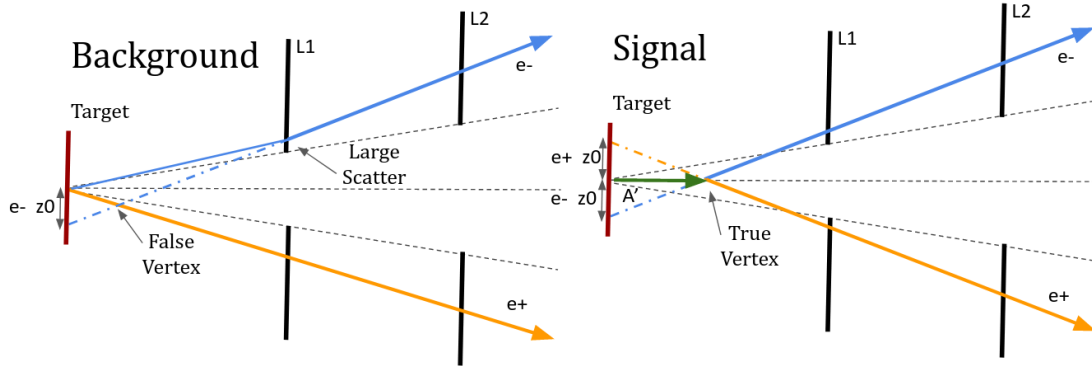


Figure 5.23: Left: Prompt background that falsely reconstructs at a large z due to an e^- particle with a large scatter away from the beam plane in layer 1 of the SVT. The corresponding e^+ does not have a large scatter and the track point back near the primary. A cut on the impact parameter can eliminate such background. Right: A true displaced vertex will have a large impact parameter for both e^+e^- pairs that is correlated with reconstructed z .

Impact Parameters

For signal, a true displaced vertex will have large impact parameters (z_0) in the vertical direction for both electron and positron tracks. Furthermore, these impact parameters are correlated with z , where both electron and positron impact parameters increase with increasing z in well-defined bands. For prompt background that reconstructs at large z , this is not always the case. Instead, it is possible for one particle to have a large scatter away from the beam plane (and thus a large impact parameter) and the corresponding particle to either be consistent with the primary or have a smaller impact parameter than is expected from signal. With a cut on impact parameter on both e^+e^- tracks, such backgrounds can be eliminated. This concept is illustrated in Fig. 5.23.

In order to fully utilize an impact parameter as a method to discriminate between background and signal, this cut is performed as a function of reconstructed z in order to fit the signal bands shown in the z_0 vs. reconstructed z plots of Fig. 5.24. This figure also shows the same plot in 10% of the data with preselection and layer 1 requirements. This correlation in signal is approximately linear for the masses of interest (which can be seen for 80 MeV and 100 MeV), so there is a requirement that the cut is linear in z .

$$z_{0+}(m, z) > a_+(m) + b_+(m) z \text{ or } z_{0-}(m, z) < a_-(m) + b_-(m) z \quad (5.10)$$

Both the electron and positron are required to satisfy this condition of being above or below one of these lines, respectively. The difference in slope between the positive and negative functions (b_+ and b_-) is large enough such that they are different constants. Since the opening angle of an A' is mass-dependent, the slopes of these cuts (and also the z -independent term) also depends on mass. Thus, the constants a_{\pm} and b_{\pm} must be parametrized as a function of mass.

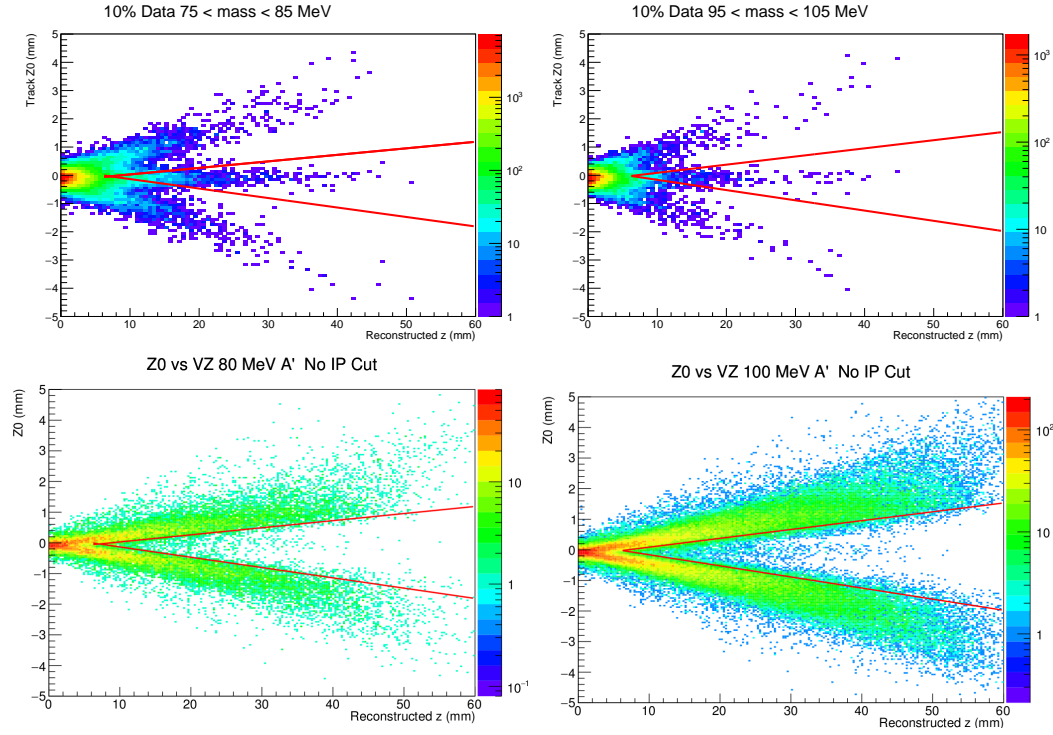


Figure 5.24: Impact parameter vs. reconstructed z for different mass values of 10% data and A' 's in the L1L1 category. The red lines indicate the impact parameter cut at the specified mass value. Upper Left: 10% data in mass range 75-85 MeV. Upper Right: 10% data in the mass range 95-105 MeV. Lower Left: 80 MeV Displaced A' 's. Lower Right: 100 MeV Displaced A' 's.

In order to obtain these constants for a given A' mass, a linear fit to the inner bands of the z_0 vs z distributions, combining both the electron and positron distributions, is performed for a single A' mass. Specifically, the z_0 distributions are sliced in overlapping bins of z and the point at which a certain fraction of the signal will be eliminated on the side closer to the beam plane (i.e. the “inner” portion of the z_0 distribution) is determined. This fraction of the signal that is chosen to be eliminated is a tuneable parameter denoted as α . This defines the constants a_{\pm} and b_{\pm} at a specific mass. This process is repeated for each mass point in the range 60 MeV - 150 MeV and a linear fit using the same α is performed at each mass.

As stated previously, each of these parameters that are linear in z must be parametrized as a function of mass. The fits show that the a_{\pm} parameter is generally within 25 μm across all masses including both the positive and negative fit. Thus, this parameter is fit to a constant across all masses such that $a_+ = a_- = a$. The relationship between the mass and the slope is non-linear and increases approximately asymptotically with increasing mass.

$$b_{\pm}(m) = b_{0\pm} + \frac{b_{1\pm}}{m} \quad (5.11)$$

2786 Finally, the cut equations can be summed up with 5 parameters a , b_{\pm} , and b_{\pm} that are set with
2787 a single tuneable parameter α .

$$z0_+(m, z, \alpha) > a(\alpha) + b_{0+}(\alpha) z + b_{1+}(\alpha) \frac{z}{m} \text{ or } z0_-(m, z, \alpha) < a(\alpha) + b_{0-}(\alpha) z + b_{1-}(\alpha) \frac{z}{m} \quad (5.12)$$

2788 In addition, since there is a mass-dependent target position for data (but not for MC) as shown
2789 in Fig. 5.38, and these constants must be determined from MC, the reconstructed z for this cut in
2790 data is shifted by a value dz determined by the difference in fitted mean between 10% data and MC
2791 preselection.

$$dz = -0.377 + 13.79m - 55.84m^2 + 84.00m^3 \quad (5.13)$$

2792 In addition to the shift in z , there are shifts in the y -direction due to changing beam conditions.
2793 The beam position in y can shift by as much as 50 μm which can have a significant impact on
2794 the signal efficiency of the impact parameter cut. To mitigate this effect, a run-dependent beam y
2795 position is utilized in the same way that the V0 projection back to the target is run-dependent.

2796 Next, the tuneable parameter α must be chosen. A simple study showed that the final result is
2797 generally independent of α in the range 10% - 20%, and $\alpha = 15\%$ was selected. At this α , the value of
2798 the 5 parameters are: $a = -2.018e10^{-1}$, $b_{0+} = 5.199e10^{-2}$, $b_{1+} = -2.301e10^{-3}$, $b_{0-} = 4.716e10^{-2}$,
2799 and $b_{1-} = -1.086e10^{-3}$. The effect of the impact parameter cut including $n - 1$ plots is shown in
2800 Fig. 5.25.

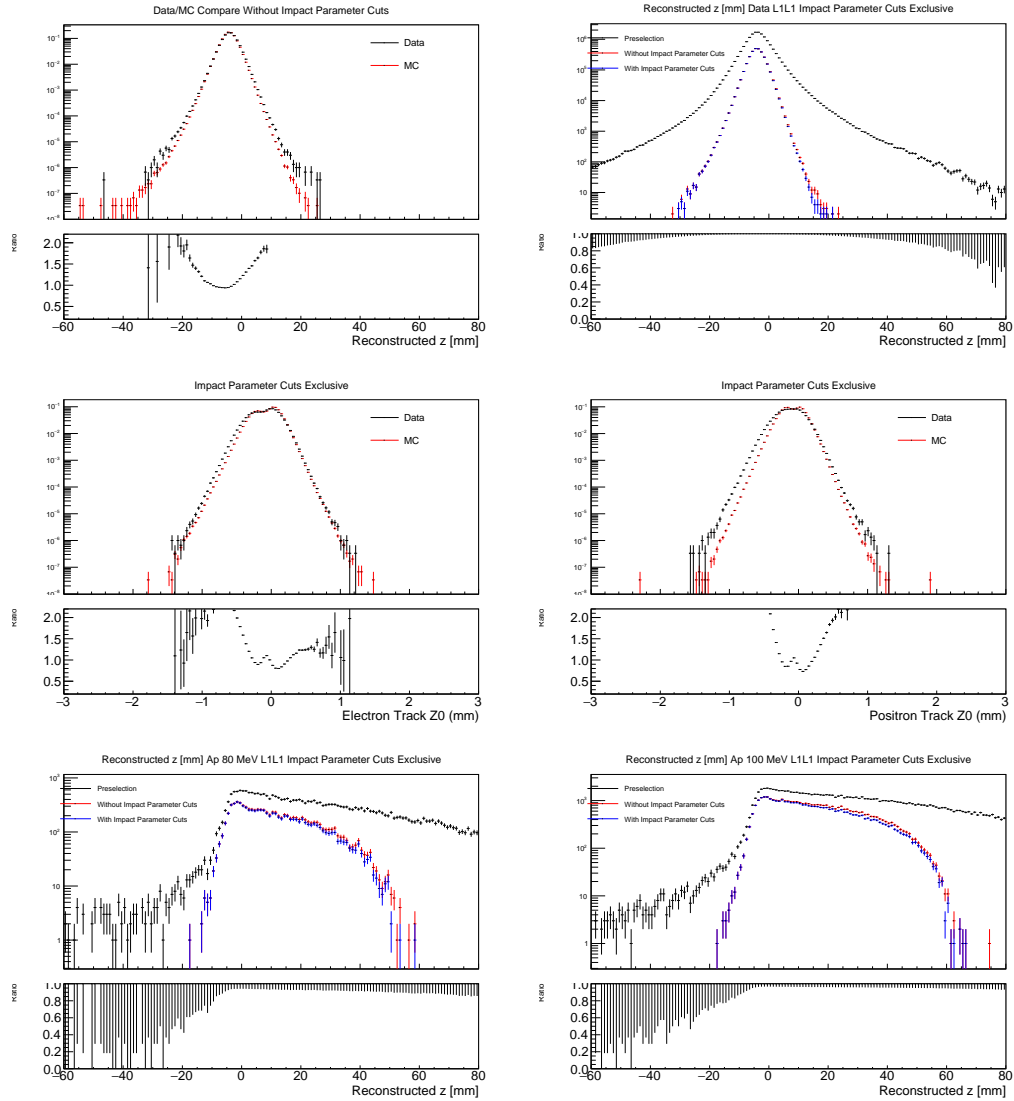


Figure 5.25: Plots showing the effect of with and without the impact parameter cut for the L1L1 category. Upper Left: Comparison of VZ distributions for 10% Data and 100% tritrig-wab-beam MC for all tight cuts except for the impact parameter cut. Top Right: Comparison of preselection, tight cuts, and tight cuts without the impact parameter cut for 10% Data. Middle Left: Electron track z_0 for 10% Data and tritrig-wab-beam MC using all tight cuts except the impact parameter cuts. Middle Right: Positron track z_0 for 10% Data and tritrig-wab-beam MC using all tight cuts except the impact parameter cuts. Bottom Left: Comparison of preselection, tight cuts, and tight cuts without the impact parameter cut for displaced 80 MeV A's. Bottom Right: Comparison of preselection, tight cuts, and tight cuts without the impact parameter cut for displaced 100 MeV A's.

2801 Radiative Cut

2802 As stated previously, the kinematics of A 's are such that the recoil electron is generally soft
2803 while A 's take most of the beam energy (i.e. have a large $x = E_{A'}/E_{beam}$). Thus, only V0s with
2804 momentum near the beam energy are selected, and a minimum V0 momentum cut (in addition to
2805 the maximum V0 momentum cut from preselection), the so-called radiative cut, is implemented.

2806 The figure of merit used to tune the radiative cut is the optimal ratio of the signal to background
2807 in the same way the V0 projection to the target cut was tuned. In order to provide sufficient statistics
2808 for the background term, the entire mass range of interest is used for the background (from 50 MeV
2809 - 150 MeV). It is an assumption that the entire mass range is representative of each individual mass
2810 slice. The results show that in general the final result is insensitive between the cut ranges of 1.7–2.0
2811 GeV. However, this figure of merit has a peak at about 1.85 GeV ($x \approx 0.8E_{beam}$), and the radiative
2812 cut is selected to be at this value. The effect of the radiative cut on 10% of the data, signal MC,
2813 and background MC is shown in Fig. 5.26 including $n - 1$ plots.

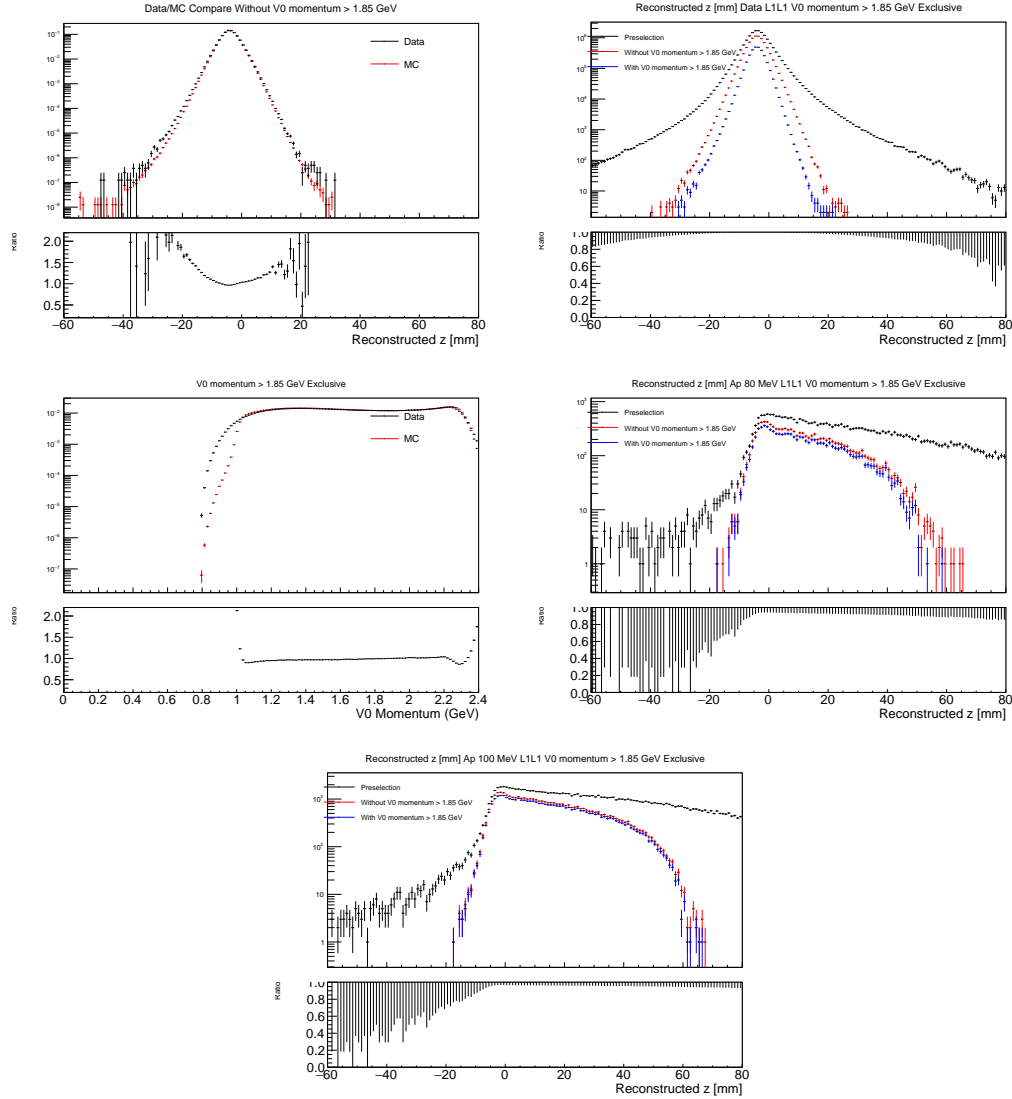


Figure 5.26: Plots showing the effect of with and without the V0 momentum cut for the L1L1 category. Upper Left: Comparison of VZ distributions for 10% Data and 100% tritrig-wab-beam MC for all tight cuts except for the V0 momentum cut. Upper Right: Comparison of preselection, tight cuts, and tight cuts without the V0 momentum cut for 10% Data. Middle Left: Comparison of the V0 momentum for 10% Data and tritrig-wab-beam MC using all tight cuts except the V0 momentum cut. Middle Right: Comparison of preselection, tight cuts, and tight cuts without the V0 momentum cut for displaced 80 MeV A's. Bottom: Comparison of preselection, tight cuts, and tight cuts without the V0 momentum cut for displaced 100 MeV A's.

	data	ϵ_{tot}	tridents	ϵ_{tot}	WAB	ϵ_{tot}	AP	ϵ_{tot}
Preselection	- -	- -	- -	- -	- -	- -	- -	- -
L1L1 + L2 Requirements	- -	-	0 0.0	0 0.0	0 0.0	0 0.0	0 0.0	0 0.0
V_0 Projection to Target $< 2\sigma$	- -	- -	- -	- -	- -	- -	- -	- -
$V_{0p} > 2.0\text{GeV}$	- -	- -	- -	- -	- -	- -	- -	- -
Isolation Cut	- -	- -	- -	- -	- -	- -	- -	- -
Impact Parameter Cut	- -	- -	- -	- -	- -	- -	-	-

Table 5.4: Table showing the efficiency of each cut on 10% of the 2016 data sample and on MC simulation for tridents, WABs and 80 MeV A' displaced samples for the L1L1 category. **TODO:** Update the cuts and numbers

2814 Selecting Single V0s

2815 A table of the effect of each tight cut in the L1L1 category for data and different MC components
 2816 is shown in Table 5.4.

2817 After the tight vertex selection, the last step is to remove both duplicate tracks and events with
 2818 multiple V0 particles. Tracks can share hits with other tracks, and these shared hits can be from
 2819 hits from another particle such as a recoil electron, beam electron, or photon or be a noise hit. There
 2820 is evidence in both data and MC that tracks with shared hits produce a small number of high z
 2821 background events. Because of the possibility of producing high z events, tracks with shared hits
 2822 are eliminated.

2823 The final requirement is each event must have exactly one V0 candidate that passes all cuts.
 2824 This will prevent duplicate V0s in an event which is not expected for signal. Those events that have
 2825 more than one V0 candidate that passes all cuts is eliminated. A comparison of the cut between
 2826 10% data, 100% MC, and displaced A' s is shown in Fig. 5.31. The final selection for the L1L1
 2827 category plotted as reconstructed z vs mass is shown in Fig. 5.30. The total effect of removing
 2828 tracks with shared hits and selecting single V0s eliminates about 10.3% of V0s in data and 8.4%
 2829 of V0s in both signal and background MC. Simply selecting single V0s while allowing tracks with
 2830 shared hits removes a total of about 6% of V0s in both data and MC which corresponds to about
 2831 3% of events (since nearly all events with multiple V0s that pass all selection cuts contain exactly 2
 2832 V0s).

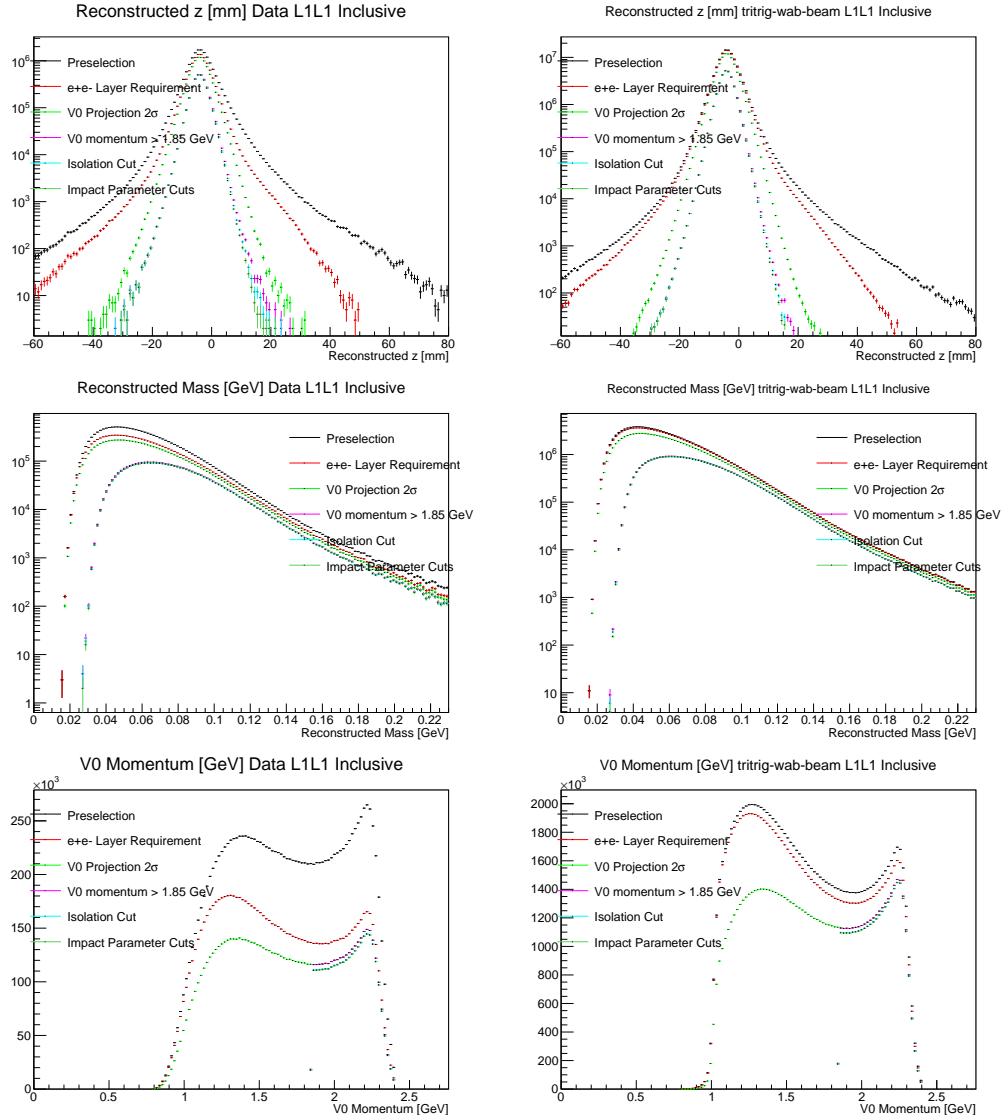


Figure 5.27: Upper Left: Comparison of 10% Data and tritrig-wab-beam MC for the final event selection in the L1L1 category. Upper Right: Comparison of 10% of the Data for before and after multiple V0 events are removed. Lower Left: Comparison of 80 MeV displaced A's for before and after multiple V0 events are removed. Lower Right: Comparison of 100 MeV displaced A's for before and after multiple V0 events are removed.

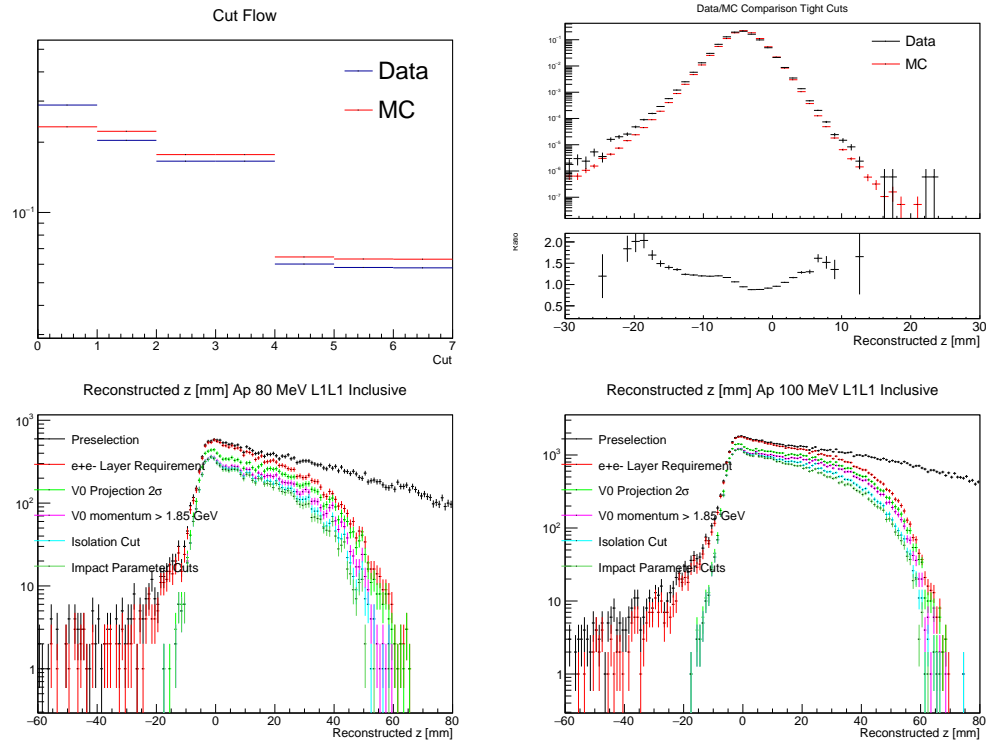


Figure 5.28: Comparisons of tight cuts for the L1L1 category. Upper Left: Comparison of the tight cutflow for 10% Data and tritrig-wab-beam. Upper Right: Comparison of 10% Data and tritrig-wab-beam for events with tight cuts. Lower Left: Tight cutflow for 80 MeV displaced A' 's. Lower Right: Tight cutflow for 100 MeV displaced A' 's.

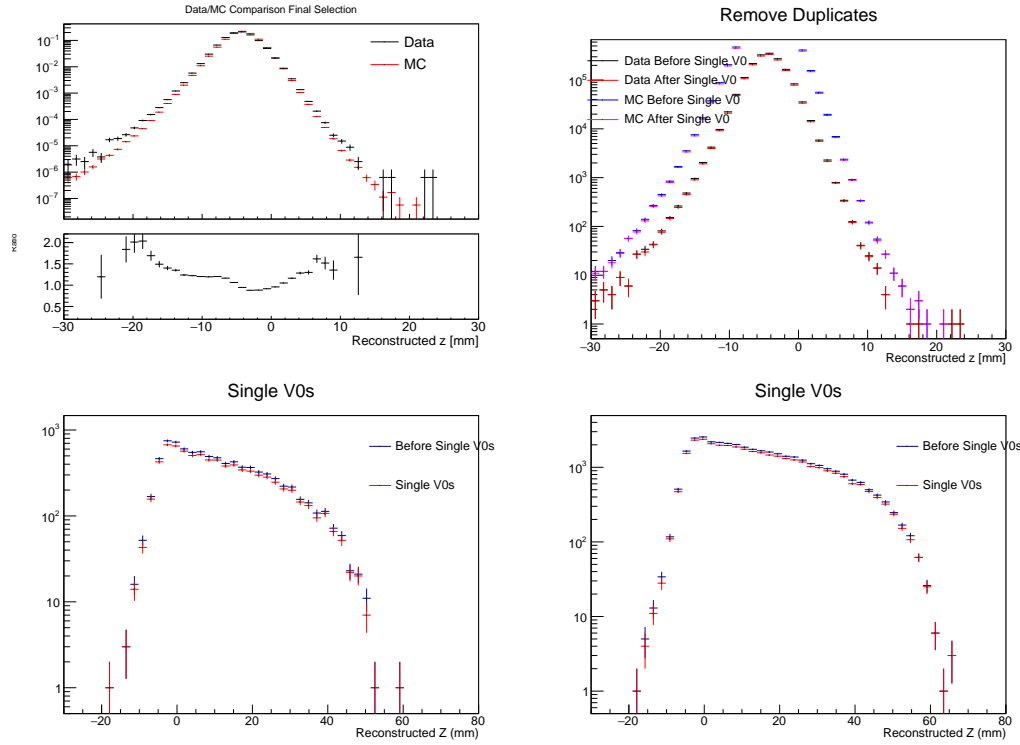


Figure 5.29: Upper Left: Comparison of 10% Data and tritrig-wab-beam MC for the final event selection in the L1L1 category. Upper Right: Comparison of 10% of the Data for before and after multiple V0 events are removed. Lower Left: Comparison of 80 MeV displaced A's for before and after multiple V0 events are removed. Lower Right: Comparison of 100 MeV displaced A's for before and after multiple V0 events are removed.

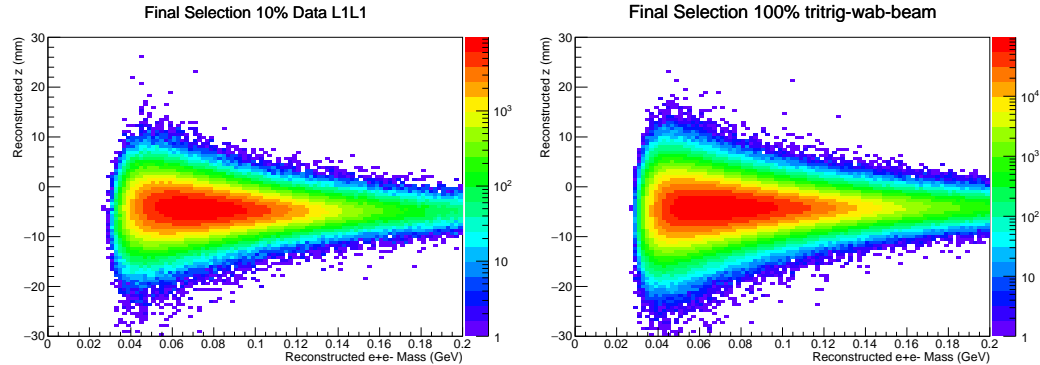


Figure 5.30: Upper Left: Comparison of 10% Data and tritrig-wab-beam MC for the final event selection in the L1L1 category. Upper Right: Comparison of 10% of the Data for before and after multiple V0 events are removed. Lower Left: Comparison of 80 MeV displaced A's for before and after multiple V0 events are removed. Lower Right: Comparison of 100 MeV displaced A's for before and after multiple V0 events are removed.

2833 **5.4.2 L1L2**

2834 **Ignore the L1L2 section. It is still being worked on.**

2835 As described in L1L1 section, longer-lived A's often have one or more daughter particles miss
2836 layer 1 of the SVT, and thus will be eliminated by requiring layer 1 hits. The strategy is to divided
2837 the analysis into several mutually exclusive categories by the first hit of the daughter particles - L1L1,
2838 L1L2, and L2L2. For this analysis, only L1L1 and L1L2 are utilized, and the proceeding subsections
2839 describe the tight cuts in the L1L2 category where exactly one daughter particle is required to have
2840 a layer 1 hit.

2841 Similar to the L1L1 category, in addition to the L1L2 requirement, layer 2 hits are also required
2842 to reduce mistracking and layer 3 hits are implicitly required by tracking algorithms. The effect
2843 of requiring either a layer 1 hit for the electron or positron (but not both) and requiring layer 2 is
2844 shown in Fig. ???. A summary of the cuts in the L1L2 category is shown in Table 5.5 and described
2845 in the following subsections.

Cut Description	Requirement
Layer 1 Requirement	e^+ xor e^- have L1 hit
Layer 2 Requirement	e^+ and e^- have L2 hit
Radiative Cut	$V_{0p} > 1.85$ GeV
V0 projection to target	Fitted 2σ cut
Isolation Cut	Eq. 5.9 or Eq. 5.14
Impact Parameters	Eq. 5.12

Table 5.5: A summary of the tight cuts for the L1L2 category.



Figure 5.31: Upper Left: Comparison of 10% Data and tritrig-wab-beam MC for the final event selection in the L1L1 category. Upper Right: Comparison of 10% of the Data for before and after multiple V0 events are removed. Lower Left: Comparison of 80 MeV displaced A 's for before and after multiple V0 events are removed. Lower Right: Comparison of 100 MeV displaced A 's for before and after multiple V0 events are removed.

2846 **Projection of the vertex to the target**

2847 Similar to signal events in the L1L1 category, signal events in the L1L2 category point back to
 2848 the beamspot. Thus, a cut on the projection to the target is warranted. The projection is shown in
 2849 Fig. ??.

2850 The procedure for the cut on the V0 projection is similar to the L1L1 category, in that there
 2851 is a run-by-run fit for the transverse projection for the data, but the degraded resolution due to a
 2852 missing layer 1 hit must accounted for. However, since the position and projection resolutions are
 2853 further degraded due to interactions with inactive material or active material (with hit inefficiencies),
 2854 deriving the resolution in the L1L2 category directly from data or background MC will artificially
 2855 inflate the position and projection resolutions from that of a true displaced vertex.

2856 Thus, the best way to obtain the resolutions in the L1L2 category is to compare the resolutions
 2857 from A' MC in the L1L1 and L1L2 category. For both categories, the projection resolution are
 2858 independent of reconstructed z , but the L1L2 category has about a 25% worse resolution in the x
 2859 direction and 50% worse resolution in y . This is shown in Fig. ??.

2860 For data, the run-by-run fitted means and sigmas for the rotated projection back to the target
 2861 are used from the L1L1 category and a single value is used for MC. However, for both data and MC,
 2862 the fitted sigmas are scaled by 1.25 for the x direction and 1.5 for the y direction, and an elliptical
 2863 cut at 2σ from the mean is cut. The cut is shown in Fig. ?? and the effect of the cut is shown in Fig.
 2864 ???. The effect of floating the cut value is shown in Fig. ?? and the effect on high z events (those
 2865 events greater than z_{cut} from 10% of the data) in data and MC is shown in Table ?? and Table ??.

2866 **Isolation Cut**

2867 Similar to the L1L1 category, the L1L2 category also has high Z events due to mistracking.
 2868 Specifically, when a track reconstructs with an incorrect hit, a so-called “bad hit”, in the first layer
 2869 that the particle hits. However by construction, for the L1L2 category, exactly one particle has its
 2870 first hit in layer 1 and the other particle has its first hit in layer 2. Thus, the isolation cut that is
 2871 applied to the particle with a layer 1 hit is the same as both the particles in the L1L1 category using
 2872 Eq. 5.9.

2873 However, the assumption in this equation is that layer 2 is about twice the distance from the
 2874 target from as layer 1 is. This is not true when the first hit is in layer 2. Layer 2 is about 2/3 the
 2875 distance from the target than layer 3. Thus the factor of 1/2 in Eq. 5.9 must be replaced by 1/3 to
 2876 get

$$\delta + \frac{1}{3} (z_{0corr} - 3 \Delta z_{0corr}) > 0 \quad (5.14)$$

2877 For the L1L2 category, if the track has its first hit in layer 2, then Eq. 5.14 is applied.

2878 Similar to L1L1, the cut is selected at 3σ .

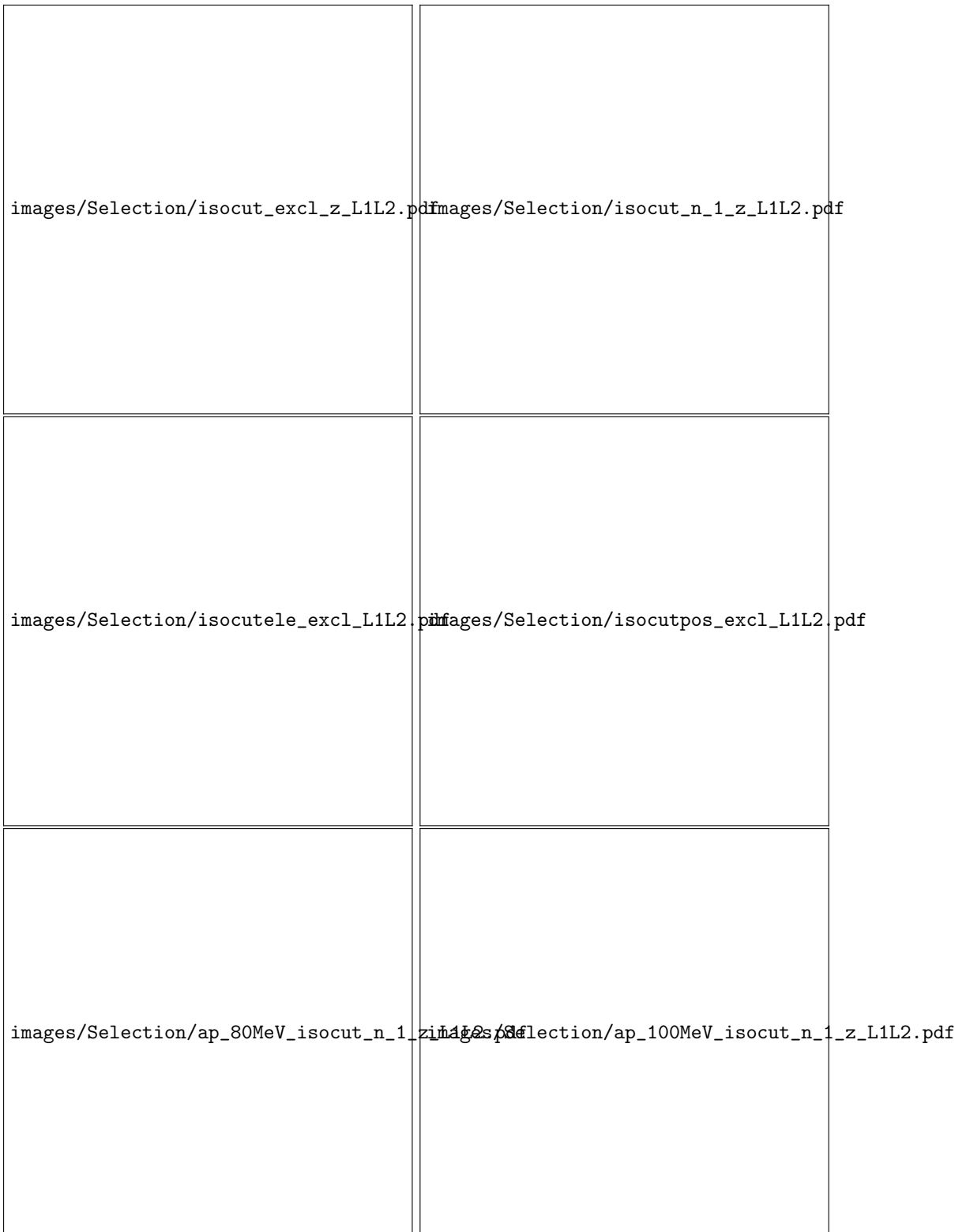


Figure 5.32: Plots showing the effect of with and without the isolation cut for the L1L2 category. Upper Left: Comparison of VZ distributions for 10% Data and 100% tritrig-wab-beam MC for all tight cuts except for the isolation cut. Upper Right: Comparison of preselection, tight cuts, and tight cuts without the isolation cut for 10% Data. Middle Left: Electron isolation cut value for 10% Data and tritrig-wab-beam MC using all tight cuts except the isolation cut. Middle Right: Positron isolation cut value for 10% Data and tritrig-wab-beam MC using all tight cuts except the isolation cut.

2879 **Impact Parameters**

2880 As with the L1L1 category, true displaced A' 's will have large vertical impact parameters z_0
 2881 that are correlated within well-defined band with reconstructed z . On the other hand, a prompt
 2882 background that has a large reconstructed z may have only one of the e^+e^- tracks with a large
 2883 impact parameter. Thus, a similar cut on the track impact parameters can be applied to events in
 2884 the L1L2 category.

2885 The method for the impact parameter cut in the L1L2 category is the same as the L1L1 category
 2886 where a tuneable parameter α is chosen to eliminate a certain fraction of signal events as a function
 2887 of z and fit to a linear function as in Eq. 5.10. An example of two mass slice in both 10% of the
 2888 data and signal MC is shown in Fig. 5.33. The linear constants are both parametrized in the same
 2889 way such that Eq. 5.12 is used. The value of reconstructed z for data is also shifted by the same
 2890 value dz from Eq. 5.13 to eliminate the mass-dependent target position in data.

2891 Table ?? and Table ?? show the number of high z events (events past z_{cut} for 10% data in the
 2892 L1L2 category) for 10% data, 100% tritrig-wab-beam, and x3 tridents as well as 80 MeV and 100
 2893 MeV displaced A' 's for varying values of α . From there a determination of α can be made based on
 2894 the amount of high z background it eliminates without reducing too much of the signal efficiency.
 2895 A value of $\alpha = 15\%$ was chosen as a reasonable value and is consistent with the L1L1 α value. The
 2896 corresponding constants are $a = -0.167438502208$, $b_{0+} = 0.016762652862$, $b_{1+} = 0.00033162637213$,
 2897 $b_{0-} = 0.0207347770085$, and $b_{1-} = 0.000331699098944$.

2898 The effect of the impact parameter cut is shown in Fig. ?? and the effect of floating the α value
 2899 is shown in Fig. ??.

2900 **Radiative Cut**

2901 As stated previously, the kinematics of A' 's are such that A' 's generally take most of the beam
 2902 energy and are accompanied by a soft recoil electron. The momentum sum distribution is indepen-
 2903 dent of the decay length. Because of this, the radiative cut (i.e. the minimum momentum sum cut)
 2904 in the L1L2 category can simply be the same as the L1L1 category and is set at 1.85 GeV. The
 2905 effects of the radiative cut in the L1L2 category are shown in Fig. ??, while the effects of floating
 2906 this cut are shown in Fig. ??.

2907 **Selecting Single V0s**

2908 A table of the effect of each tight cut in the L1L2 category for data and different MC components
 2909 is shown in Table ?? and the effect on the reconstructed z vs mass 2D plots are shown in Fig. ??.

2910 Similar to the events in the L1L1 category, the final selection in L1L2 requires only one remaining
 2911 V0 candidate that passes all cuts. That is, any event that has two or more remaining V0 candidates
 2912 after all cuts is eliminated. This is about XX% of events. The effect of removing tracks with shared
 2913 hits and removing duplicate V0 candidates is shown in Fig. ??.



Figure 5.33: Impact parameter vs. reconstructed z for different mass values of 10% data and A' 's in the L1L2 category. The red lines indicate the impact parameter cut at the specified mass value. Upper Left: 10% data in mass range 75-85 MeV. Upper Right: 10% data in the mass range 95-105 MeV. Lower Left: 80 MeV Displaced A' 's. Lower Left: 100 MeV Displaced A' 's.



Figure 5.34: Comparisons of tight cuts for the L1L2 category. Upper Left: Comparison of the tight cutflow for 10% Data and tritrig-wab-beam. Upper Right: Comparison of 10% Data and tritrig-wab-beam for events with tight cuts. Lower Left: Tight cutflow for 80 MeV displaced A's. Lower Right: Tight cutflow for 100 MeV displaced A's.



Figure 5.35: Upper Left: Comparison of 10% Data and tritrig-wab-beam MC for the final event selection in the L1L2 category. Upper Right: Comparison of 10% of the Data for before and after multiple V0 events are removed. Lower Left: Comparison of 80 MeV displaced A's for before and after multiple V0 events are removed. Lower Right: Comparison of 100 MeV displaced A's for before and after multiple V0 events are removed.

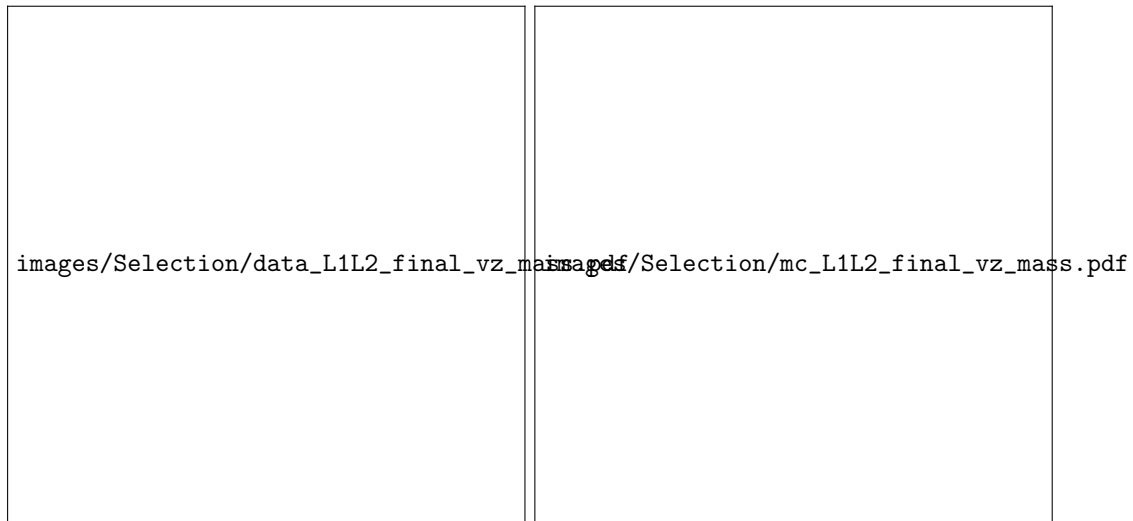


Figure 5.36: Upper Left: Comparison of 10% Data and tritrig-wab-beam MC for the final event selection in the L1L1 category. Upper Right: Comparison of 10% of the Data for before and after multiple V0 events are removed. Lower Left: Comparison of 80 MeV displaced A' 's for before and after multiple V0 events are removed. Lower Right: Comparison of 100 MeV displaced A' 's for before and after multiple V0 events are removed.

2914 **5.4.3 L2L2**

2915 L2L2 isn't part of the standard analysis, but I will include it in my thesis. Understanding the
2916 backgrounds here will be important for future analysis.

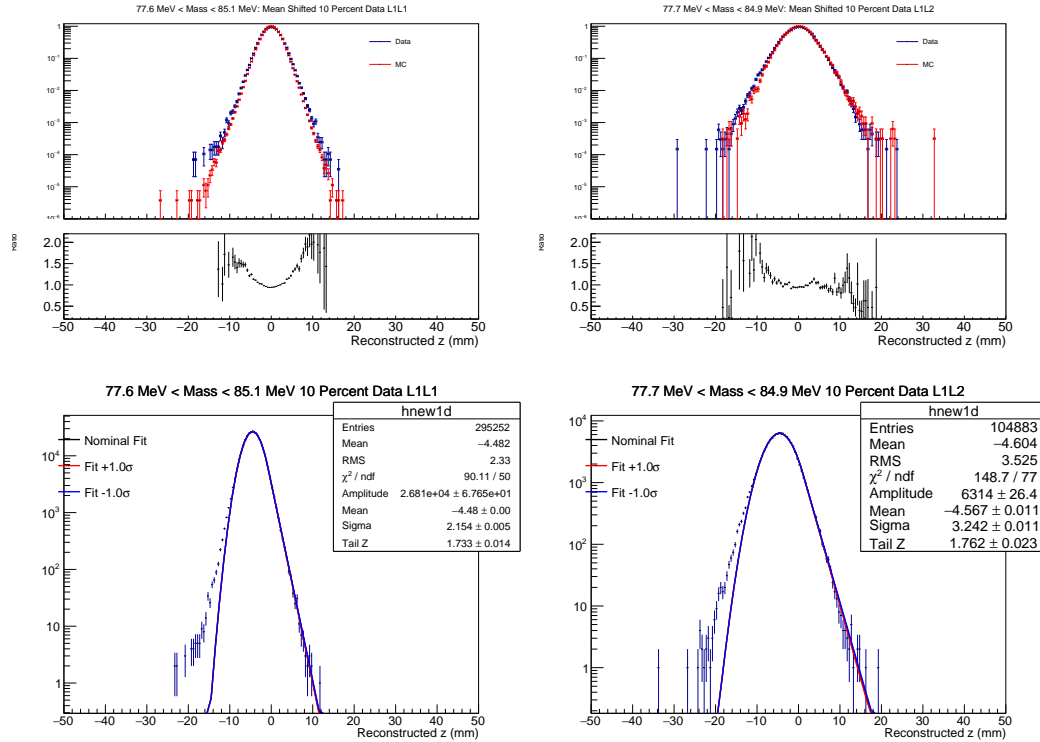


Figure 5.37: Upper Left: 10% Data and full MC comparison in reconstructed z for a slice in mass for L1L1. For both distributions, the fitted mean is shifted to 0. Upper Right: 10% Data and full MC comparison in reconstructed z for a slice in mass for L1L2. For both distributions, the fitted mean is shifted to 0. Lower Left: An example fit of a mass slice in 10% of the data using Eq. 5.15 for the L1L1 category. Lower Right: An example fit of a mass slice in 10% of the data using Eq. 5.15 for the L1L2 category. [Update these with 100% data.](#)

2917 5.5 Characterizing the Background & Defining the Signal 2918 Region

2919 The main goals for this analysis are to understand backgrounds, estimate our expected signal yield in
2920 a zero-background region (or a small well-characterized background), determine a method for signal
2921 significance, and set a limit. First, a signal region must be defined such that very little background
2922 is expected downstream of some large z value. Specifically, this is done as a function of mass since
2923 a signal is expected at a specific mass value and mass-dependent vertex resolution. With this in
2924 mind, the z vs mass distribution is sliced into overlapping bins equal to $1.9\sigma_m(m)$ for a mass m in
2925 the bin center. Each mass slice is fitted using the following continuous and differentiable function
2926 consisting of Gaussian core and exponential tail.

$$F\left(\frac{z - \mu_z}{\sigma_z} < b\right) = Ae^{-\frac{(z-\mu_z)^2}{2\sigma_z^2}} \quad F\left(\frac{z - \mu_z}{\sigma_z} \geq b\right) = e^{-\frac{b^2}{2} - b\frac{z-\mu_z}{\sigma_z}} \quad (5.15)$$

2927 The parameter b is the number of standard deviations from the mean that the fit function changes
 2928 from a Gaussian to an exponential tail. A comparison of 10% of the data and 100% of the tritrig-
 2929 wab-beam sample in a mass slice as well as a sample tail fit for both the L1L1 and the L1L2 category
 2930 is shown in Fig. 5.38. A comparison between the fit function parameters from Eq. 5.15 is shown in
 2931 Fig. 5.38.

2932 Using the results of the fit function, the z value at which the background fit function predicts
 2933 0.5 background events is the definition of the z_{cut} . Or more precisely defined

$$0.5 = \int_{z_{cut}}^{\infty} F(z) dz \quad (5.16)$$

2934 In order to roughly predict a z_{cut} for unblinding, the fit function can also be scaled up to 100% of
 2935 the data and the z_{cut} is solved for 0.5 background events in the same way. This is just a projection;
 2936 however, the final z_{cut} values is determined by a fit to 100% of the data. The z_{cut} for the full dataset
 2937 and the projection from the 10% sample as well as for the full tritrig-wab-beam sample is projected
 2938 over the final samples for both data and MC for both the L1L1 and L1L2 categories in Fig. 5.39.
 2939 The z_{cut} from data is used as the cut in the A' efficiency from Sec 5.3 and in Fig. 5.11. To be nearly
 2940 unbiased, the final fit is performed without the points in the mass bin of interest (i.e. using the mass
 2941 sidebands).

2942 As described in Sec. 5.3, the expected rate of A' 's produced at the target within prompt accep-
 2943 tance S as a function of mass and ϵ is given by Eq. 4.11. Further details of normalizing the A' rate
 2944 directly from the radiative cross section and the number of e^+e^- pairs in a small mass window of 1
 2945 MeV is described in Sec. 4.11.3. These expected rates are also shown in Fig. 4.24 for both 10% of
 2946 the data and the full dataset. Within a finite mass bin, the amount of expected signal S_{bin} needs to
 2947 be corrected by an efficiency factor ϵ_{bin} for an expected Gaussian distribution $S_{bin} = \epsilon_{bin} S$. The
 2948 bin sizes were selected to be $1.9\sigma_m$ and were optimized based on maximum signal yield past z_{cut}
 2949 for a few mass and ϵ points of interest, although this optimization procedure showed that the final
 2950 result is generally insensitive to mass windows between $1.8\sigma_m$ and $3.0\sigma_m$.

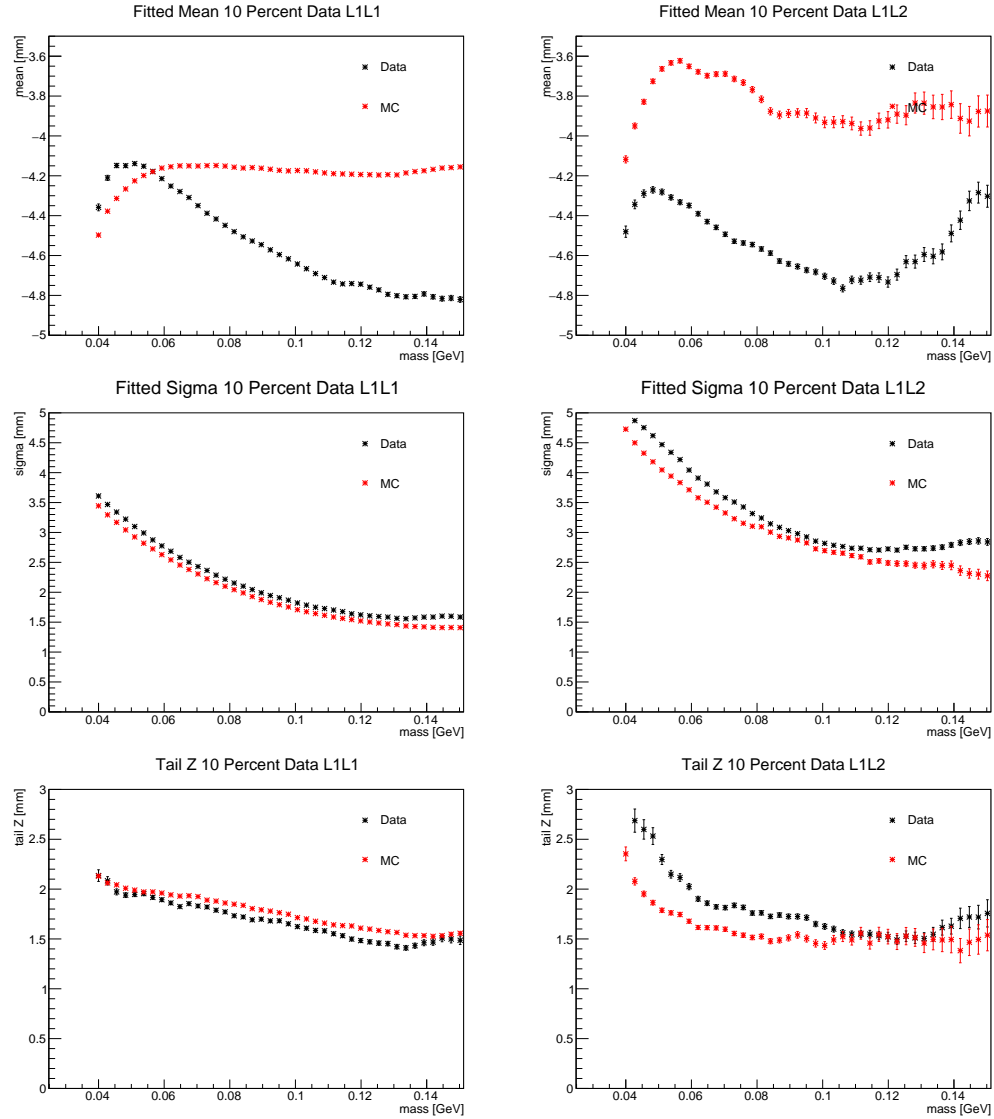


Figure 5.38: Top Left: Fitted mean as a function of mass comparing 10% of the data to the full tritrig-wab-beam sample for the L1L1 category. Top Right: Fitted mean as a function of mass comparing 10% of the data to the full tritrig-wab-beam sample for the L1L2 category. Middle Left: Fitted σ as a function of mass comparing 10% of the data to the full tritrig-wab-beam sample for the L1L1 category. Middle Right: Fitted σ as a function of mass comparing 10% of the data to the full tritrig-wab-beam sample for the L1L2 category. Bottom Left: Fitted “tail z” parameter (the number of σ from the mean the function transitions from Gaussian core to exponential tail) as a function of mass comparing 10% of the data to the full tritrig-wab-beam sample for the L1L1 category. Bottom Right: Fitted “tail z” parameter (the number of σ from the mean the function transitions from Gaussian core to exponential tail) as a function of mass comparing 10% of the data to the full tritrig-wab-beam sample for the L1L2 category.

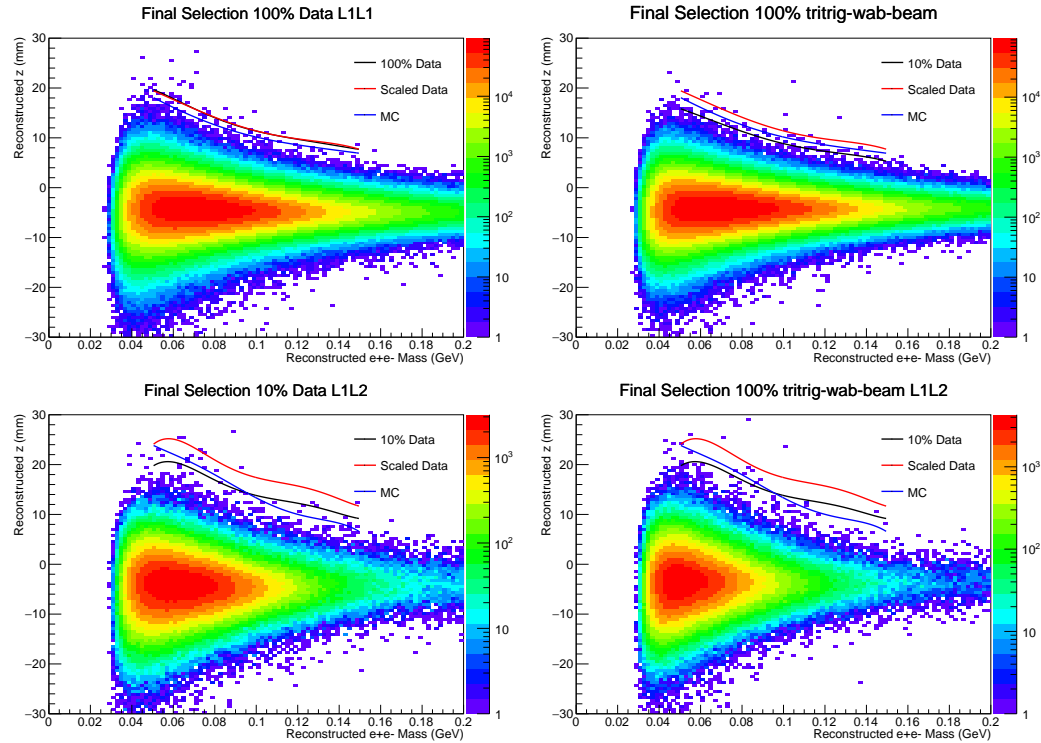


Figure 5.39: The final event selection with overlaid z_{cut} from 100% data, the full tritrig-wab-beam sample, and projected to the full dataset for Top Left: 100% data for the L1L1 category, Top Right: full tritrig-wab-beam sample for the L1L1 category, Bottom Left: 10% data for the L1L2 category, and Bottom Right: full tritrig-wab-beam sample for the L1L2 category.

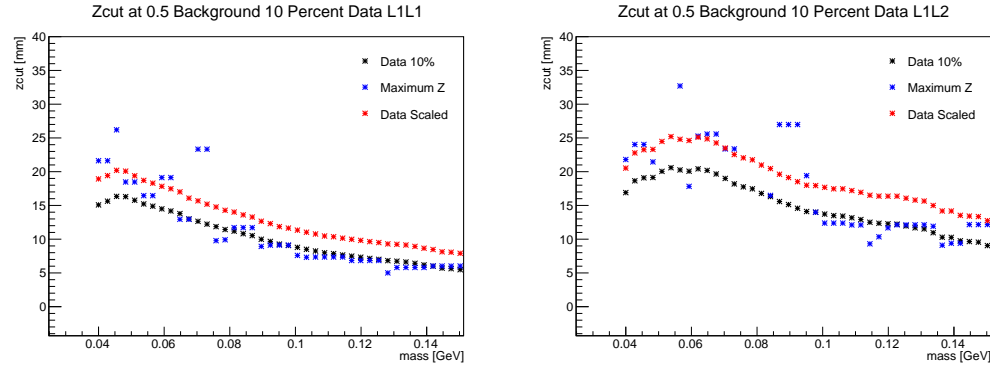


Figure 5.40: Left: A comparison of z_{cut} between 10% data and scaled to the full dataset to the maximum z value in a mass bin for the L1L1 category. Right: A comparison of z_{cut} between 10% data and scaled to the full dataset to the maximum z value in a mass bin for the L1L2 category.
Update with full dataset.

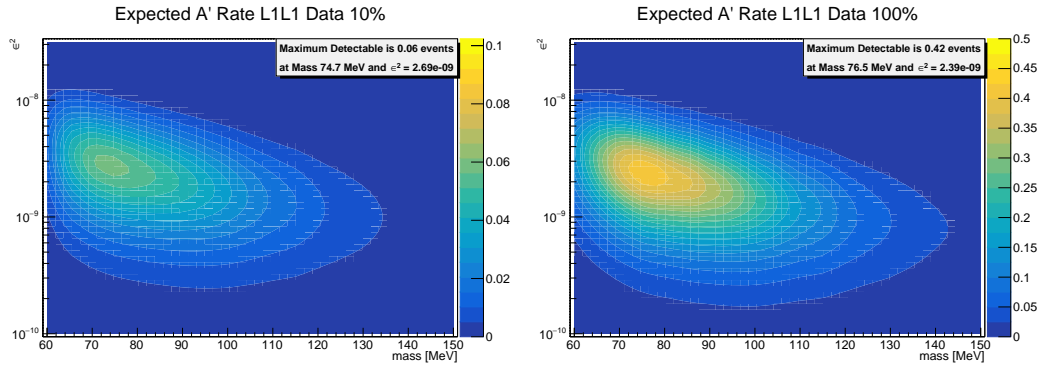


Figure 5.41: Left: The expected number of A' events past z_{cut} including all efficiencies for the L1L1 category for 10% of the data. Right: The expected number of A' events past z_{cut} including all efficiencies for the L1L1 category projected for the full dataset.

5.6 Results

5.6.1 Expected Signal Yield

The expected A' production rate at the target must be correctly “spread out” in the z -direction in order to obtain the truth signal distributions. The normalized truth signal shape as a function of $c\tau$ (which of course is computed from mass and ϵ) is an exponential given by

$$S_{truth}(z, m_{A'}, \epsilon) = \frac{e^{-(z_{targ} - z)/c\tau}}{\gamma c\tau} \quad (5.17)$$

This function is normalized such that integral from z_{targ} to infinity is unity (i.e. $\int_{z_{targ}}^{\infty} S_{truth}(z, m_{A'}, \epsilon) dz = 1$) so that it gives the expected signal density distribution. $\gamma = \frac{E}{m_{A'}}$ is the relativistic constant where the A' energy is assumed to be $E = 0.965 E_{beam}$ (which is the mean of the x distributions across all relevant masses).

At each point in reconstructed z , the truth signal shape must be multiplied by acceptance and efficiency affects. The details of incorporating these effects is explained in Sec. 5.3.2 where hit killing, further analysis cuts, and dividing events into mutually exclusive categories are taken into account. From this section, $\epsilon_{vtx,sum}(z, m_{A'})$ denotes the efficiency due to acceptance and preliminary analysis cuts and is normalized to unity at the target. While $\epsilon_{vtx,LiLj}(z, m_{A'})$ denotes further efficiency affects due to the hit killing algorithm, further analysis cuts and z_{cut} , and the separation due to the mutually exclusive categories. For this variable, i and j denote to the individual categories L1L1, L1L2, and L2L2 (i.e. $i = 1, 2$ $j = 1, 2$).

Finally, putting this all together and integrating the signal shape across the range of interest in z (note that the z_{cut} is already applied in the $\epsilon_{vtx,LiLj}(z, m_{A'})$ term) gives the formula for the expected signal past z_{cut} as a function of mass and ϵ .

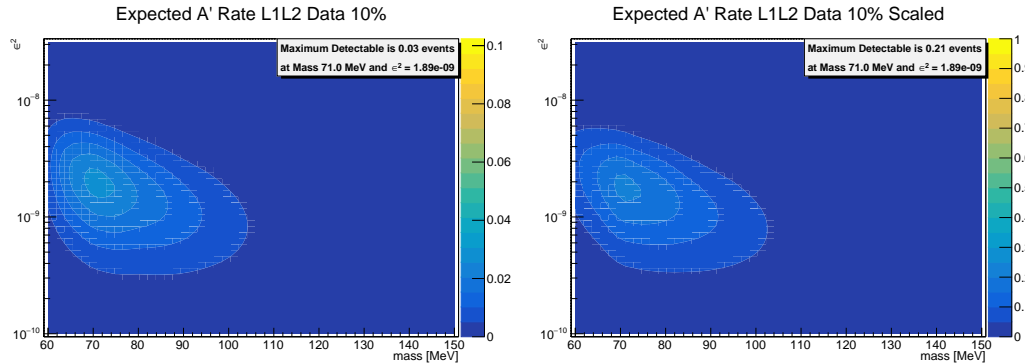


Figure 5.42: Left: The expected number of A' events past z_{cut} including all efficiencies for the L1L2 category for 10% of the data. Right: The expected number of A' events past z_{cut} including all efficiencies for the L1L2 category projected for the full dataset.

$$S_{bin,zCut,LiLj}(m_{A'}, \epsilon) = S_{bin}(m_{A'}, \epsilon) \int_{z_{targ}}^{z_{max}} S_{truth}(z, m_{A'}, \epsilon) \epsilon_{vtx,sum}(z, m_{A'}) \epsilon_{vtx,LiLj}(z, m_{A'}) dz \quad (5.18)$$

The amount of signal expected for the L1L1 category for 10% data has a maximum value of 0.06 events at $m_{A'} = 74.7$ MeV and $\epsilon^2 = 2.69 \times 10^{-9}$ while the amount of signal expected for the L1L1 category for the full dataset has a maximum value of 0.42 events at $m_{A'} = 76.5$ MeV and $\epsilon^2 = 2.39 \times 10^{-9}$. The full range of expected signal yield is shown in Fig. 5.41.

Also, L1L2.

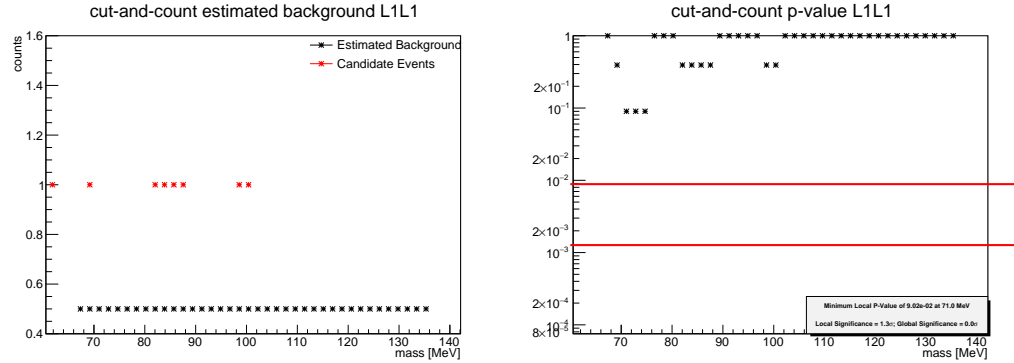


Figure 5.43: Left: The number of background events past z_{cut} based on the background model and the candidate events past z_{cut} for the L1L1 category. Right: The p-value for the L1L1 category

2976 5.6.2 Finding Signal Significance

2977 I am still working on this part. Feel free to skip. This still needs to be explored.

2978 Previous work in finding signal significance is best described in Sho's thesis ([cite Sho's thesis](#)).

2979 For each mass slice with n events past z_{cut} and the number of expected background events b , the
2980 probability (i.e. the p -value) of having at least n events from Poisson statistics is

$$P(n, b) = \sum_{k=n}^{\infty} \frac{b^k}{k!} e^{-b} \quad (5.19)$$

2981 From the definition of z_{cut} , we should expect the background b to be 0.5 events in each bin;
2982 however, we have backgrounds above this value and this must be estimated for data. In a similar
2983 way to how z_{cut} was determined, we can use the mass sidebands with a background model to fit
2984 and interpolate the model to the mass bin of interest. [Sho used a quadratic function, but we need](#)
2985 [to explore this..](#)

2986 Once this p -value is determined in each mass slice, we need to correct for the look-elsewhere
2987 effect. Finally, we need to convert the p -value to a significance.

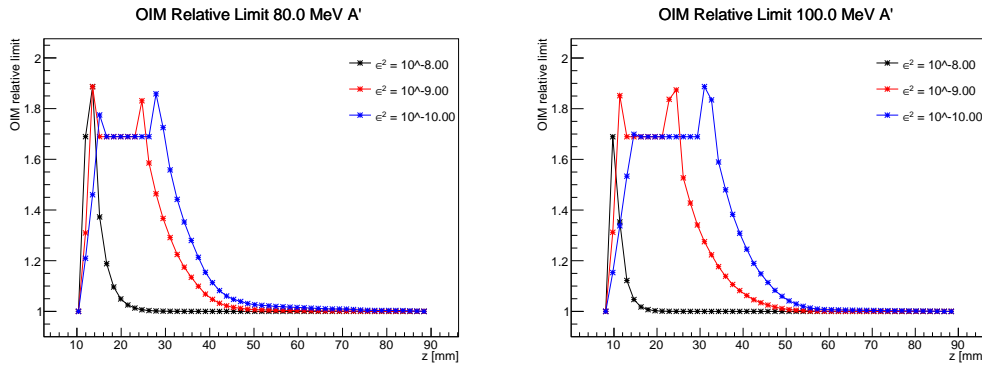


Figure 5.44: The effects of a single event on the Optimum Interval Method limit for several decay lengths for an 80 MeV mass bin (left) and a 100 MeV mass bin (right). The relative limit (relative to the background-free limit) is plotted as a function of reconstructed z of a single dummy background event. A single background event can result in up to about a 70% worse limit.

5.6.3 Setting Limits

The Optimum Interval Method (OIM) is used to set a limit on the cross-section of the canonical A' model [84]. OIM was originally developed for direct detection dark matter experiments in which one expects a small signal where the signal shape in one variable (reconstructed z for HPS) is known and there is a small, but not necessarily understood, background. The OIM is an extension of the Maximum Gap Method, which searches for the largest gap in signal space that has no background events (i.e. $x_i = \int_{z_i}^{z_{i+1}} S(z) dz$) in order to set a limit. The OIM generalizes this method to an arbitrary number of background events between any two events in signal space and sets a limit based on the optimum interval and automatically selects the interval to avoid experimenter bias. In addition, the absolute cross-section of the signal does not need to be known, instead the OIM finds the optimum interval and sets a limit at the smallest cross section at a specified confidence interval C_0 , 90% for this analysis.

In order to understand how a single event can potentially impact a limit, a dummy background was placed in an otherwise background-free signal region. The z position of the background event was varied from the z_{cut} to an arbitrarily large z value and the OIM limit relative to the background-free region is recorded. With a single background event, the optimum interval can either be the interval from z_{cut} to the background event, the background event to the maximum z , or the entire interval. A single background event can result in about a maximum of a 70% worse limit compared to the background-free region. These results for an 80 MeV and a 100 MeV displaced A' for several difference values of ϵ^2 are shown in Fig. 5.44.

The result for the OIM for the L1L1 and L1L2 categories on 10% of the data are shown in Fig. 5.45. For the full dataset in the L1L1 category, the best limit is set at $m_{A'} = 80.2$ MeV and $\epsilon^2 = 2.12 \times 10^{-9}$ with a factor of 6.05 times the canonical A' cross-section. The interpretation of

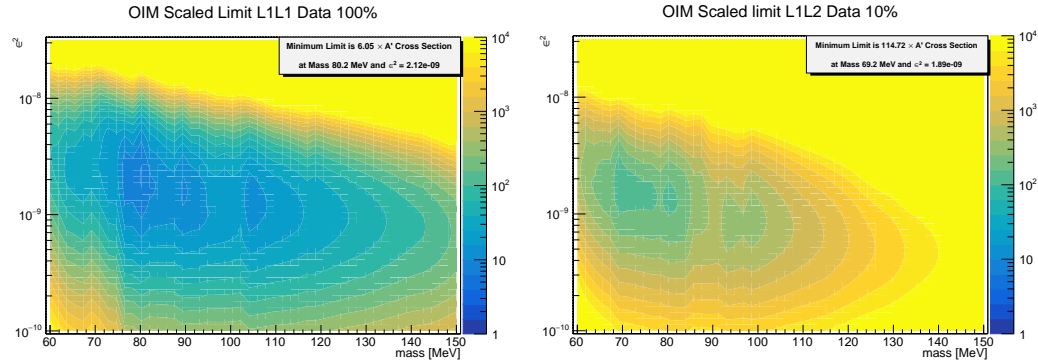


Figure 5.45: Left: The limit from Optimum Interval Method for the L1L1 category. Right: The limit from Optimum Interval Method for the L1L2 category.

³⁰¹¹ this value is for an A' -like model with 6.05 times the cross-section, the model is barely excluded at
³⁰¹² that mass and ϵ^2 with 90% confidence.

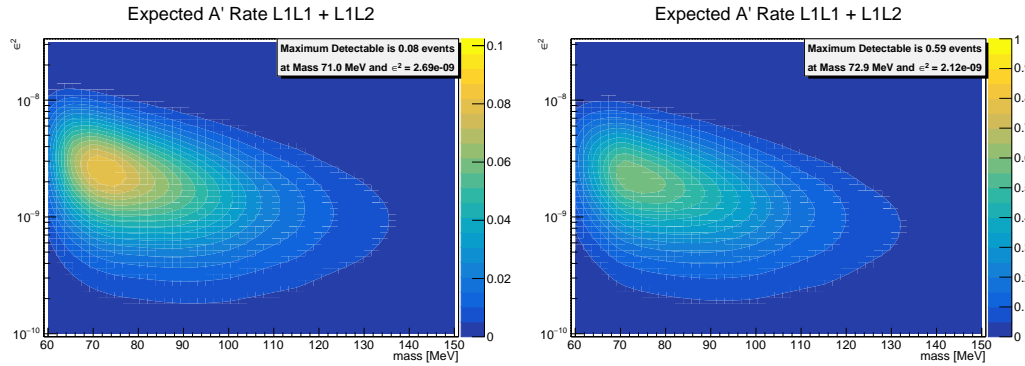


Figure 5.46: Left: The combined expected number of A' events past z_{cut} including all efficiencies for the L1L1 and L1L2 categories for 10% of the data. Right: The combined expected number of A' events past z_{cut} including all efficiencies for the L1L1 and L1L2 categories for the full dataset.
Report minimum value

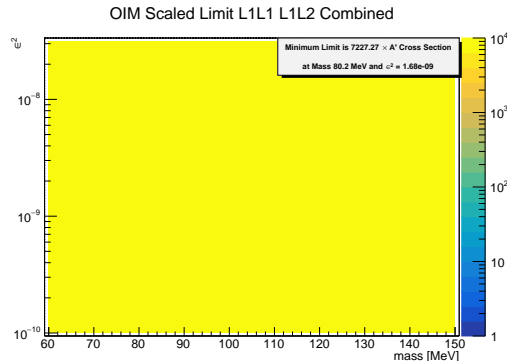


Figure 5.47: The combined limit from Optimum Interval Method for the L1L1 and L1L2 categories.
Report minimum value

3013 5.6.4 Combining Datasets

3014 I am still exploring these methods.

3015 Once we have results for both the L1L1 and L1L2 datasets, we can combine the results. First
3016 the expected signal yield can be trivially combined for both L1L1 (Fig. ??) and L1L2 (Fig. (XX))
3017 by simply adding the results which is shown in Fig. (XX).

3018 In order to combine the limits set individually by the Optimum Interval Method, we can treat
3019 them like two different experiments or the same experiment but with limits set with two different
3020 parts of the detector. There are six methods for providing a combined limit from the Optimum
3021 Interval Method shown here [85]. The L2L2 method is not included since it is not part of the
3022 standard analysis.

3023 **5.7 Systematic Uncertainties**

Systematic Description	Value
e^+e^- Composition	$\sim 7\%$
Mass Resolution	$\sim 1\%$
Analysis Cuts	$\sim 3\%$
A' Efficiency	$\sim XX\%$
Target position	$\sim 5\%$

Table 5.6: A summary of systematic uncertainties that impact the final result of the displaced vertex search.

3024 For a complete result, the systematic uncertainties from the experiment and analysis must be
3025 considered and quantitatively understood. These uncertainties are still being estimated; however, the
3026 systematic uncertainties considered to date from this analysis are described below and summarized
3027 in Table 5.6. Only the systematic uncertainties associated with the L1L1 category are considered
3028 so far; however, the L1L2 category will qualitatively have most of the same sources of systematic
3029 uncertainties.

3030 Several of the systematic uncertainties can be shared with the resonance search. For instance, the
3031 mass resolution affects the size of the search windows in both types of searches.³ An underestimate
3032 of the mass resolution would result in more signal leaking out of a mass bin than leaking into the
3033 mass bin. Thus, uncertainty in the mass resolution is a source of systematic uncertainty, and the
3034 main source of this uncertainty is a result of the errors on the momentum smearing used to estimate
3035 the mass resolution described in Sec. 5.2. Estimating the $\pm 1\sigma$ error on these parameters results in
3036 a conservative estimate of the error on the mass resolution of $\pm 1.5\%$ across all mass ranges. Using
3037 this 1σ uncertainty, the signal yield would be overestimated by about 1.0% for a window size of
3038 1.9σ .

3039 Another source of systematic uncertainty that is shared with the resonance search is the uncer-
3040 tainty in the e^+e^- composition that is expressed in the error of the radiative fraction. The main
3041 source of the uncertainty of the radiative fraction is the error on the cross-sections of the individual
3042 components which is shown in Table 5.7. The relative uncertainty is 1.0% for radiative tridents,
3043 0.3% for tridents, and 19.8% for WABS. The WABs have a relatively large uncertainty on the cross-
3044 section relative to the other components because of much lower statistics (the fraction of WABs that
3045 end up in the final sample is very small, thus a much larger sample of WABs is needed to obtain
3046 sufficiency statistics) and a much larger uncertainty on the cross-section from MadGraph4. Since

3Since the resonance search uses a target constrained vertex, the uncertainty in the target position also affects the mass resolution and must be considered; however, this effect can be neglected for the displaced vertex search since no such constraint is utilized.

3047 the uncertainty of the WAB cross-section is much greater than the uncertainty in the trident cross-
 3048 section, the uncertainty in the trident cross-section can be neglected. Combining the uncertainties
 3049 on the individual cross-sections, the total uncertainty in the radiative fraction is 6.4% and has been
 3050 rounded up to 7% for the estimate in the systematic uncertainty.

Sample	μ of ICS	σ of ICS	# of good files	# of generated events per file
RAD	66.36 b	0.6678 b	9940	10k
Tritrig	1.416 mb	0.004310 mb	9853	50k
WAB	0.1985 b	0.01973 b	9956	100k

Table 5.7: Normalization parameters for the RAD, Trident-Trig and WAB samples

3051 **Skip this paragraph, this still needs to be done.** There are systematic uncertainties associated
 3052 with the analysis cuts, particularly the tight selection after the hit killing method described in Sec.
 3053 5.3.2. There are only 4 tight cuts to consider - the isolation cut, the V0 projection to the target,
 3054 the impact parameter cuts, and the radiative cut A preliminary estimate for the impact parameter
 3055 cut systematic is about 1% - 2% as illustrated in Fig. ?? and Fig. ???. This is estimated by both
 3056 shifting and smearing the MC z_0 distributions to match what is seen in data. The radiative cut can
 3057 be neglected... In addition, one must consider the high V0 momentum cut. A conservative estimate
 3058 of the systematic on the analysis cuts is 3%.

3059 There is a potential source of systematic uncertainty associated with the background fit to the z
 3060 distribution in mass bins using Eq. 5.15. Performing a fit with $\pm 1\sigma$ on the parameters results in a
 3061 minuscule change in z_{cut} of less than 0.1 mm. The difference in signal yield from this error in z_{cut}
 3062 is small and can be neglected.

3063 From mechanical measurements, the target position is estimated to be known within ± 0.5 mm
 3064 from the nominal position. The uncertainty in the target position will result in an overall shift in z in
 3065 the truth distributions of displaced A' 's, and thus is a source of systematic uncertainty. For example,
 3066 if the target is 0.5 mm more upstream than assumed, the entire displaced A' truth distribution
 3067 will also shift upstream by 0.5 mm (without changing z_{cut}) resulting in the actual expected signal
 3068 yield that is less than calculated signal yield. For a given A' mass, this discrepancy will depend
 3069 significantly on ϵ because of varying decay length, and can be calculated by simply recomputing
 3070 both the signal yield and the limit at a different target position (± 0.5 mm). The ratio of the limit
 3071 from a target at 0.5 mm upstream of the nominal position to the target at the nominal position is
 3072 shown in Fig. 5.48. The mass and ϵ dependence will be used in the final estimate of systematic
 3073 uncertainties; however, over the parameter space of interest the systematic is < 5%, thus the value
 3074 5% is used for now. **This 5% value is a bit subjective for now...**

3075 The last source of systematic uncertainty considered is a result of the method of fitting and
 3076 normalizing the A' efficiencies as a function of z as described in Sec. 5.3. The function is extrapolated
 3077 to the target position and then normalized to unity. The uncertainty on this fit function results in

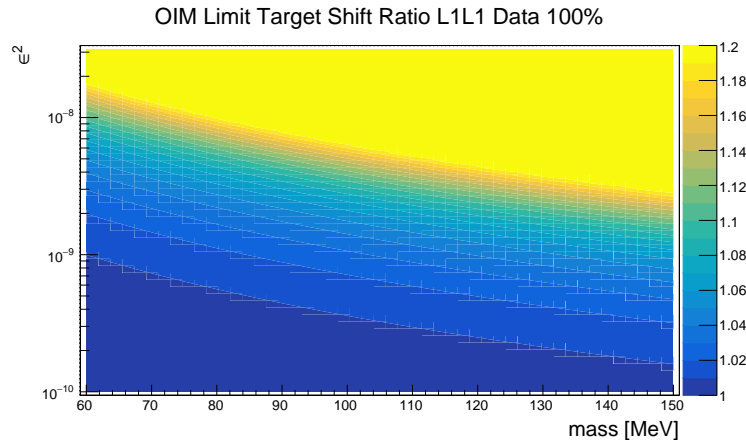


Figure 5.48: The ratio of the limit for the L1L1 category from the target 0.5 mm upstream of the nominal position to the target at the nominal position using the Optimum Interval Method. This ratio is used to estimate the systematic uncertainty associated with the error in the target position. This uncertainty is a function of mass and ϵ (because of the variable decay lengths), but a conservative estimate of 5% covers the entire parameter space of interest.

3078 an error on the estimated signal yield. Utilizing a fit with $\pm 1\sigma$ values of the fit parameters results
 3079 in a conservative estimate of XX% on the signal yield across the mass range of interest. **This still**
 3080 **needs to be done...**

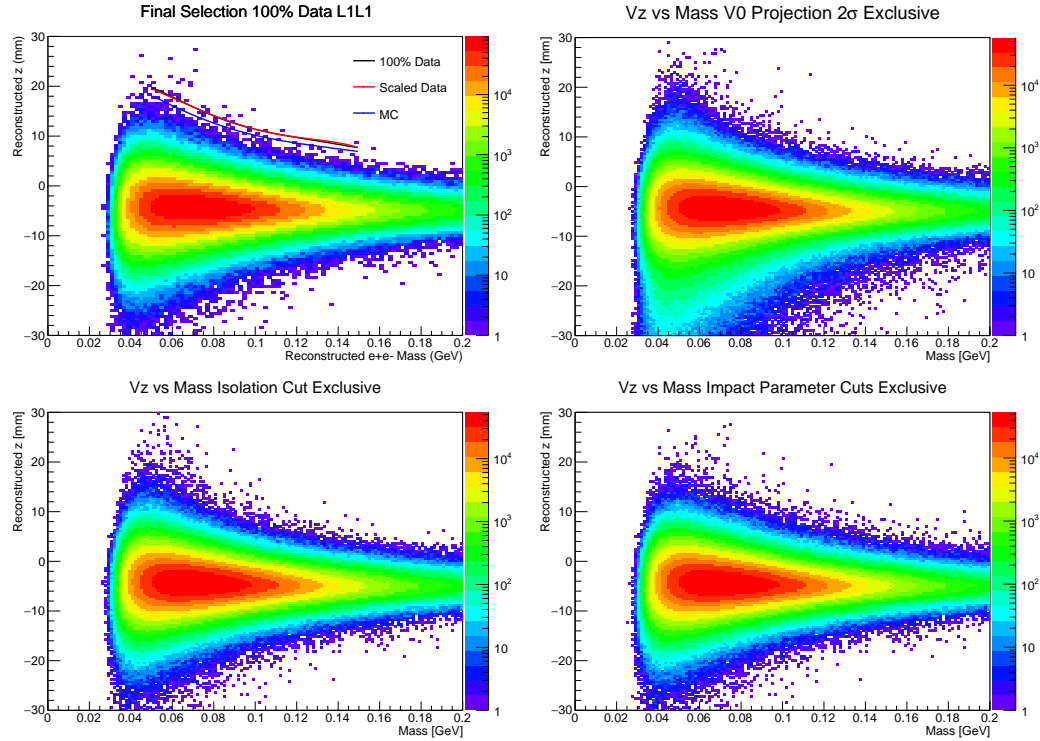


Figure 5.49: Upper Left: The final selection for the L1L1 category on the full dataset. The reconstructed z vs mass for the full dataset that includes all cuts with the exception of the (i.e. $n - 1$ plots) Upper Right: V0 projection to the target cut. Lower Left: Isolation cut. Lower Right: Impact parameter cut. The cuts are described in Sec. 5.4.

3081 5.8 Discussion of High z Backgrounds

3082 If there are any plots I can make to make these points clearer, let me know.

3083 One of the main goals of the displaced vertex analysis in the 2016 Engineering Run is a detailed
 3084 understanding of high z backgrounds, that is those that are past z_{cut} , in both data and MC. Under-
 3085 standing the nature of these backgrounds in detail will inform further background mitigation for
 3086 future analysis. The first step is to understand how well the tight vertexing cuts performed in this
 3087 analysis. This can be evaluated by comparing the final selection with all cuts against the near-final
 3088 selection with all cuts except the cut of interest ($n - 1$ plots) in the full dataset as shown in Fig.
 3089 5.49 for the L1L1 category.

3090 The next step is to understand the remaining high z events from the full dataset and the full 100%
 3091 tritrig-wab-beam sample that are not eliminated by the event selection and z_{cut} . It is understood
 3092 that the vertex resolution as well as the tails of the vertex distributions are dominated by multiple
 3093 scattering in layer 1 of the SVT. However, it is also known that single Coulomb scatters have a
 3094 longer tail in scattering angle when compared to multiple Coulomb scattering. It is suspected that

3095 many of these high z events could be due to large single Coulomb scatters away from the beam plane
 3096 in both e^+e^- particles. Similar to multiple scatters, one expects these events to in general have a
 3097 larger error on the vertex, have a momentum that misses the beam spot, fail to have large vertical
 3098 impact parameters for both e^+e^- tracks, etc. With this in mind, the remaining events past z_{cut}
 3099 for the full dataset and the full tritrig-wab-beam MC are printed with relevant variables of interest
 3100 in Table 5.8 and Table 5.9, respectively. These tables are informative because they displays all the
 3101 relevant information that can potentially distinguish between the large single Coulomb scatters and
 3102 a true displaced signal for a small number of events. The description of the table values, from left
 3103 to right, are as follows:

- 3104 1. The difference between reconstruction z and the z_{cut} ($V_z - z_{cut}$).
- 3105 2. The reconstructed z of the vertex.
- 3106 3. The reconstructed mass of the vertex.
- 3107 4. For data, the run number. For MC, the truth scattering angle away from the beam plane
 projected on the y -axis for the particle in the top hemisphere which is an indication of a large
 single Coulomb scatter. The angle is taken as the maximum scattering angle between the axial
 and stereo sensor in layer 1.
- 3108 5. For data, the event number. For MC, the truth scattering angle away from the beam plane
 projected on the y -axis for the particle in the bottom hemisphere. The angle is taken as the
 maximum scattering angle between the axial and stereo sensor in layer 1.
- 3109 6. The unconstrained vertex quality.
- 3110 7. The projection back to the target in the y direction expressed in the number of unsigned σ
 from the mean.
- 3111 8. The reconstructed y of the vertex expressed in the number of unsigned σ from the mean.
- 3112 9. The positive difference between the electron impact parameter z_0 and the impact parameter
 cut from Eq. 5.12 at the vertex mass and z .
- 3113 10. The positive difference between the positron impact parameter z_0 and the impact parameter
 cut from Eq. 5.12 at the vertex mass and z .

3114 From the full dataset, the high z events tend to fit into three different categories. The first
 3115 are those events within ~ 1 mm of the z_{cut} but are still downstream of the z_{cut} . These events are
 3116 consistent with the background model as one expects 0.5 background events per mass slice (though
 3117 of course one also expects signal to appear closer to the z_{cut} as well). There are 22 independent

Δz_{cut}	VZ (mm)	Mass (MeV)	Run	Event	χ^2_{unc}	V0 Proj Y (n_σ)	VY (n_σ)	Δe^-	z_0 (mm)	Δe^+	z_0 (mm)
0.08	12.62	89.95	7780	68384585	0.49	1.37		1.22	0.88		0.43
3.80	20.03	68.19	7781	138205858	4.63	0.28		0.55	0.74		1.10
3.54	15.05	98.57	7796	26862757	4.55	0.61		0.06	0.88		0.64
2.22	15.62	84.02	7800	134296298	8.65	0.68		1.04	0.90		0.60
0.32	11.12	105.89	7803	62089760	1.76	0.58		1.82	0.41		1.05
0.44	17.67	63.17	7803	105453502	8.55	0.65		0.18	0.84		0.74
0.28	13.62	84.37	7805	149492432	1.63	0.80		0.50	0.76		0.42
3.35	20.58	63.19	7947	47657629	2.25	1.78		0.54	0.78		1.26
0.50	17.12	66.21	7970	25752733	7.90	1.71		1.41	1.11		0.47
1.08	13.92	87.78	7988	97203933	1.92	0.79		0.17	1.03		0.66
7.75	23.33	71.48	8029	4393084	1.52	1.24		2.95	1.07		1.38
0.74	10.97	112.86	8040	62210614	2.24	0.78		0.51	0.71		0.43
11.74	27.27	71.71	8046	81085838	0.12	0.34		2.49	1.09		2.31
4.51	20.72	68.24	8055	9714720	0.13	1.08		3.61	0.67		1.25
2.24	14.27	93.91	8095	17884977	0.00	0.03		1.13	0.56		1.17

Table 5.8: A table of relevant variables for events past z_{cut} for 100% of the data in the L1L1 category.

3126 mass bins over the signal region (which means a total of 11 events is expected) and this expected
 3127 level of background above ~ 70 MeV is achieved.

3128 Next, there are events with a poor vertex quality (large $\chi^2_{unc} > 4$) and events in which the y -
 3129 position of the vertex reconstructs significantly away from the mean ($V_y > 2.5\sigma_y$). These properties
 3130 are not expected for signal and are more consistent with what one would expect from rare single
 3131 Coulomb scatters. Thus, there are distinguishing features between signal and background in nearly
 3132 all of these events that can be potentially exploited in future analysis.

3133 Below ~ 70 MeV, there is an excess of high z events in data above the expected background
 3134 that is not present in MC. Thus a detailed understanding is required where the cause is most likely
 3135 a process that is not properly simulated. One possible cause is a beam-gas interaction in which a
 3136 beam electron interacts with a gas particle downstream of the target and mocks a displaced vertex.
 3137 However, the vacuum level of $< 10^{-6}$ Torr suppresses these backgrounds such that < 0.1 events is
 3138 expected. Thus, beam-gas interactions cannot be the cause of these events.

3139 Another potential cause is a combination of mis-tracking and hit efficiency effects. As discussed
 3140 previously, the hit efficiency is not properly accounted for in MC. From Sec. 5.4, there is an isolation
 3141 to eliminate high z events due to mis-tracking. However, this cut is only effective when the true hit
 3142 is actually present in the reconstruction. It is possible for a mis-track and a hit inefficiency to occur
 3143 simultaneously. In this case, the true hit does not appear due to a hit inefficiency, thus the tracking
 3144 algorithm will pick up the incorrect hit, potentially resulting in a reconstructed vertex downstream
 3145 of the target, and the isolation cut will not be able to eliminate such events.

3146 The backgrounds due to mis-tracking tend to be at low mass between 40 - 70 MeV. As a simple
 3147 preliminary study, the post-reconstruction track slope-dependent hit killing algorithm described in

Δz_{cut}	VZ (mm)	Mass (MeV)	θ_1 (mrad)	θ_2 (mrad)	χ^2_{unc}	V0 Proj Y (n_σ)	VY (n_σ)	Δe^-	z_0 (mm)	Δe^+	z_0 (mm)
0.01	13.62	70.13	2.92	5.07	2.94	1.41	0.99	0.70	0.36		
1.00	10.03	108.39	6.37	2.04	1.94	1.28	1.16	0.29	0.54		
1.12	10.54	103.89	1.70	1.84	0.12	0.48	0.24	0.30	0.52		
0.92	10.06	107.01	8.18	1.71	3.90	0.88	1.34	0.58	0.62		
0.90	13.02	80.15	6.03	4.98	1.47	0.34	0.26	0.47	0.48		
0.43	8.67	119.19	6.87	6.86	0.82	0.34	0.24	0.42	0.35		
1.91	16.09	66.55	8.96	4.55	0.22	1.43	1.22	0.83	0.49		
12.08	21.38	105.27	15.71	10.54	0.14	0.23	1.48	1.70	1.48		
5.10	18.90	68.91	8.45	3.23	0.00	0.86	1.32	0.99	0.71		
0.18	10.81	91.95	3.70	3.35	3.97	1.90	0.38	0.46	0.40		
1.09	15.39	65.78	6.42	2.93	0.99	1.47	1.05	0.71	0.38		
0.58	15.40	62.68	10.12	1.82	3.95	1.85	1.82	0.80	0.32		
0.63	11.48	90.07	5.63	4.32	3.29	1.34	1.01	0.59	0.49		

Table 5.9: A table of relevant variables for events past z_{cut} for the full tritrig-wab-beam sample in the L1L1 category.

Sec. 5.3.2 was applied to those events which would otherwise be eliminated by the isolation cut. If such an event contains a track that fails the hit killing algorithm, the event is kept in the final sample which is effectively simulating the effect of the isolation cut failing to eliminate high z events due to mis-tracking. This study showed that it is possible that roughly between 1 - 3 events of this type can result in these high z events. This is a promising study; however, much more work needs to be done. For instance, a full understanding would require hit level inefficiencies to be incorporated into the full MC instead of the simpler track-slope dependent hit killing algorithm.

Finally, there is also the possibility that any of these events is a signal event. Since about 0.5 events is expected, it is reasonable to potentially expect a single A' event to appear in this dataset for a small range of A' parameter space. However, the present understanding of the background does not enable the distinction between a single background or signal event. Instead, the candidate events within a mass bin must be tested against expected signal distributions such as an exponential distribution in z (depending on livetime).

Add L1L2 tables also. Ignore below this sentence for now.

Understanding the high z events in the L1L2 category is similar to the L1L1 category, but has several added complications. The backgrounds in the L1L2 category are dominated by hit inefficiencies in layer 1 of the SVT, and since this is not simulated properly, we cannot completely rely on the MC to describe the high z backgrounds.

There is a single event out at ... trident production.

Similar to the L1L1 category, the L1L2 category candidate events must be tested against known signal distributions and against the corresponding mass bins in the L1L1 category.

Lastly, for the L2L2 category is similar to L1L2 in that it is tricky.

3170 5.9 A Machine Learning Approach

3171 A machine learning approach has been developed that solves all of our problems...

³¹⁷² **Chapter 6**

³¹⁷³ **Upgrades & the Future of HPS**

³¹⁷⁴ Beyond what was shown in this thesis which focused on the results of the 2016 Engineering Run,
³¹⁷⁵ the future of HPS is promising and includes much more running time with an upgraded detector.
³¹⁷⁶ The two engineering runs only account for about $\sim 4\%$ of the total allotted running time. In
³¹⁷⁷ addition, HPS has recently complete its first physics run during the summer of 2019. For this run,
³¹⁷⁸ the displaced vertex search result in both the 2015 and 2016 Engineering Runs motivated the need
³¹⁷⁹ for several upgrades. With the current detector configuration, it would take at least 8 weeks with
³¹⁸⁰ the displaced vertex search for any sensitivity to the canonical A' model. However, several simple
³¹⁸¹ upgrades that improve vertex resolution and increase A' acceptance make long-lived A' searches
³¹⁸² possible on a much shorter time scale.

³¹⁸³ In addition to upgrades, HPS is able to probe a unique region of parameter space involving short
³¹⁸⁴ livetimes and small cross-sections. Essentially, HPS is able to measure lifetimes, cross-sections, and
³¹⁸⁵ masses of long-lived particles and it can potentially probe any model containing electro-produced
³¹⁸⁶ long-lived particles that decay into e^+e^- pairs. There are other models that fit this requirement and

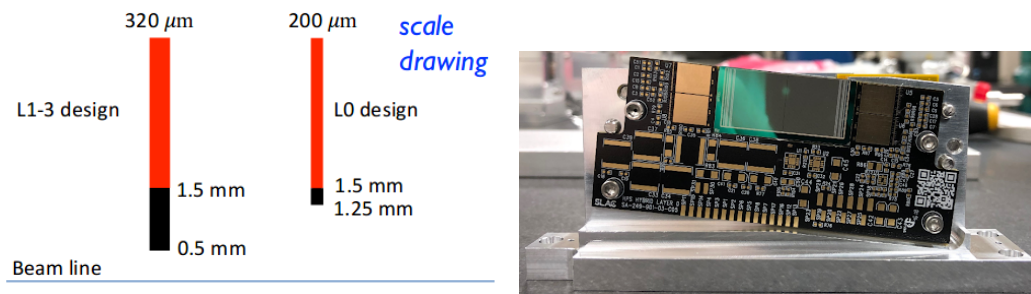


Figure 6.1: Left: A schematic comparing the upgraded L0 sensor dimensions to the nominal sensors used in the other layers. L0 sensors are thinner with far less dead material. Right: A picture of an L0 thin sensor full module (stereo side) and hybrid circuit.

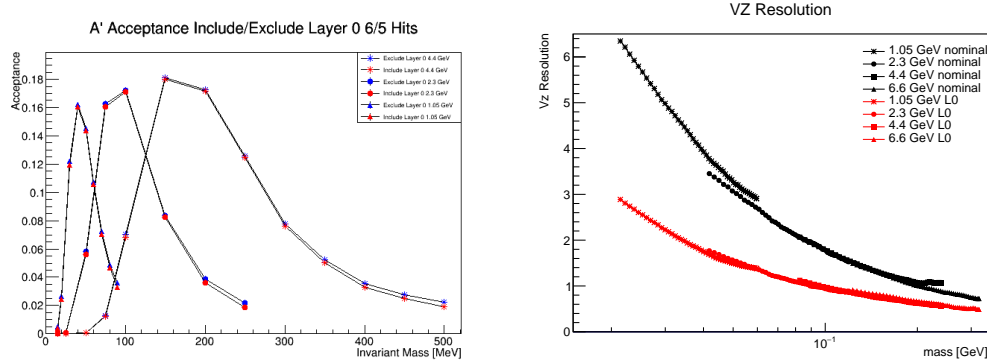


Figure 6.2: Left: A comparison of the acceptance for prompt trident events for the nominal detector and the upgraded L0 detector. The acceptance is remarkably close despite the smaller L0 sensor dimensions (the acceptance is concentrated on the center of the sensor near the beam edge). Right: A comparison of the vertex resolution with the nominal detector and upgraded L0 detector. The improvement in vertex resolution is about a factor of 2.

3187 in the future HPS will move to a generalize displaced vertex search to test all these models. One
 3188 such model is presented in this chapter.

3189 6.1 Upgrade Simulations and Installation

3190 In order to achieve the full effectiveness of HPS, several simple upgrades were implemented for the
 3191 most recent 2019 Physics Run. Informed by analysis from the previous two engineering runs, three
 3192 simple upgrades were added - the addition of a tracking layer between the current layer 1 and the
 3193 target, the implementation of a hodoscope which enabled a positron trigger, and the movement of
 3194 the current L1-L3 more towards the beam plane.

3195 The additional tracking layer, approximately halfway between the current layer 1 and the target
 3196 (hence the name “layer 0” or “L0”), improves the vertex resolution. Since the vertex resolution is
 3197 dominated by multiple scattering in the first layer and the additional tracking layer cuts the distance
 3198 between the target and the first measurement plane in half, the vertex resolution improves by about
 3199 a factor of two. The improvement of vertex resolution allows for a significantly larger signal region (a
 3200 z_{cut} closer to the target), and since the signal shape is exponential in z , this dramatically improves
 3201 the physics potential for the displaced vertex search. A comparison between the nominal detector
 3202 and the upgraded L0 detector for acceptance as well as a comparison of the vertex resolution is
 3203 shown in Fig. 6.2.

3204 There are several technical challenges associated with adding another tracking layer closer to the
 3205 target. In order to maintain the same geometrical acceptance for prompt processes at 15 mrad, the
 3206 active edge of the axial L0 sensor must be placed at half the distance from the current location of

3207 L1 (from 1.5 mm to 0.75 mm). However, this places the guard ring (i.e. the inactive silicon) directly
 3208 into the beam plane which is obviously not feasible due to radiation. To accommodate this, the
 3209 sensors were designed with a slim edge in which the dead region is only 0.25 mm instead of 1.0 mm.
 3210 This places the edge of the silicon at the original layer 1 vertical position of 0.5 mm from the beam
 3211 plane.

3212 The closer placement of the L0 active sensor to the beam plane presents challenges for occupancy.
 3213 For this reason, the sensors are split in two left-right halves such that each half contains strips and
 3214 the sensors are readout at both ends. This effectively cuts the occupancy in half to a similar level of
 3215 the layer 1 sensors in the nominal tracker. Lastly, the L0 sensor is thinner at 200 μm compared to
 3216 the nominal of 320 μm which further reduces multiple scattering effects. A schematic and picture
 3217 of the L0 sensors are shown in Fig. 6.1.

3218 In addition to the new tracking layer, layers 2 and 3 in the tracker were moved closer to the beam
 3219 plane in order to increase acceptance of A' s that live long enough and miss the first layer in the
 3220 tracker (L0 in this case). Specifically layers 2 and 3 were moved 700 μm closer to beam by placing
 3221 a simple mechanical shim in the U-channels underneath the layer 2 and 3 modules. The effect for
 3222 increasing acceptance for A' s that decay past about ~ 70 mm is shown in Fig. 6.4.

3223 After the initial studies described below were performed, in addition to moving layers 2 and 3
 3224 closer to the beam, it was decided that it would be beneficial for the current layer 1 modules to be
 3225 replaced with the thin sensor modules designed for layer 0. This has several advantages. First, the
 3226 thinner silicon material reduces multiple scattering. Second, the slim edge in these sensors allows
 3227 for a closer placement of the sensor to the beam plane thus increasing the acceptance to A' s that
 3228 decay beyond the L0 acceptance.¹ As a minor disadvantage, there is some acceptance loss to recoil
 3229 electrons (which are generally soft), though there is minimal acceptance losses for A' daughters.

3230 Lastly, a hodoscope was added between the tracker and the Ecal. As described in Sec. 3.4, the
 3231 nominal trigger was tuned to e^+e^- pairs of A' daughter particles. However, the Ecal was constructed
 3232 in such a way that five crystals at the beam edge in each of the top and bottom halves were removed
 3233 to decrease occupancy from beam particles. This is called the “Ecal hole” or “Ecal gap” and is
 3234 shown in Fig. 3.18. Unfortunately, about half of the prompt A' acceptance is contained in these
 3235 few crystals and more so for low mass A' s. And because there is still acceptance with the tracker in
 3236 this region, a positron-only trigger will recover the events where electrons are lost in the Ecal gap.
 3237 Adding a hodoscope on the positron side allows for matching with the Ecal that suppresses trigger
 3238 rates from single photons that is manageable for the DAQ to handle. This is shown in Fig. 6.5.

3239 In order to test the potential improvements of these upgrades, simulations were performed using
 3240 an upgraded detector model with a 1.06 GeV beam. This beam energy was chosen because the
 3241 analysis for the 2015 Engineering Run at 1.06 GeV was advanced at the time of these simulations
 3242 and a well-understood benchmark was needed. The initial simulations presented here do not include

¹After the nominal module was replaced by a thin sensor, layer 1 was moved 400 μm closer to the beam which means the silicon edge is still 850 μm from the beam plane.

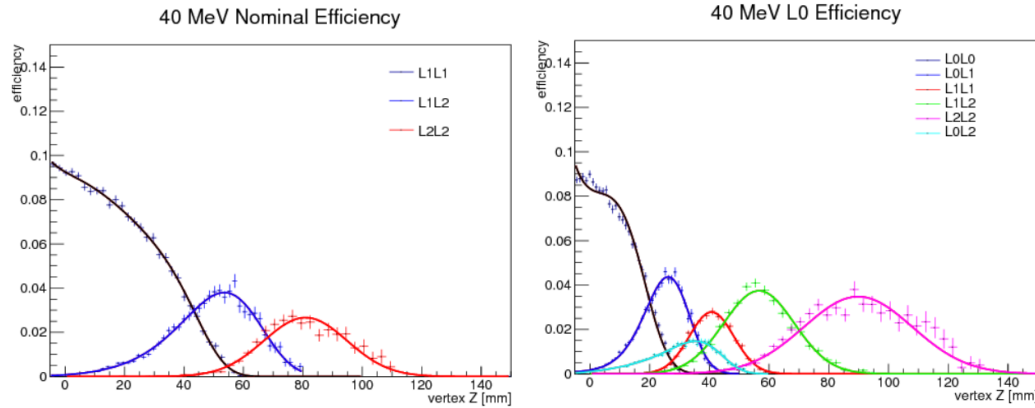


Figure 6.3: The efficiency of a displaced 40 MeV A' separated into different mutually exclusive categories based on the first layer hit by the positrons and electrons for both the nominal and L0 upgraded detector. Left: The nominal detector separated into L1L1, L1L2, and L2L2. Right: The upgraded L0 detector separated into L0L0, L0L1, L1L1, L0L2, L1L2, and L2L2.

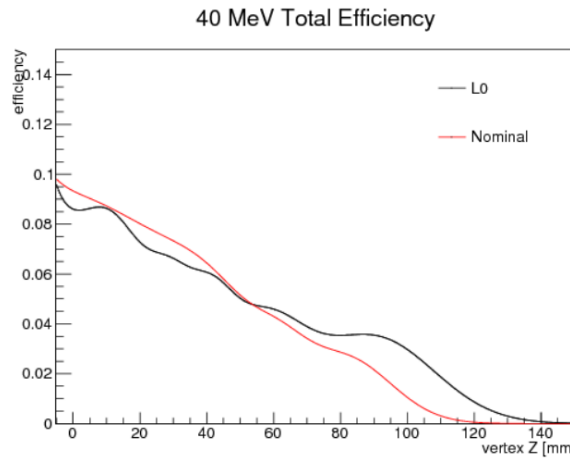


Figure 6.4: A comparison for a 40 MeV displaced A' of the total efficiency (including acceptance effects) between the nominal detector and the upgraded detector by adding the mutually exclusive categories in Fig. 6.3. The L0 has increased acceptance for large z due to layers 2 and 3 in the tracker being moved closer to the beam.

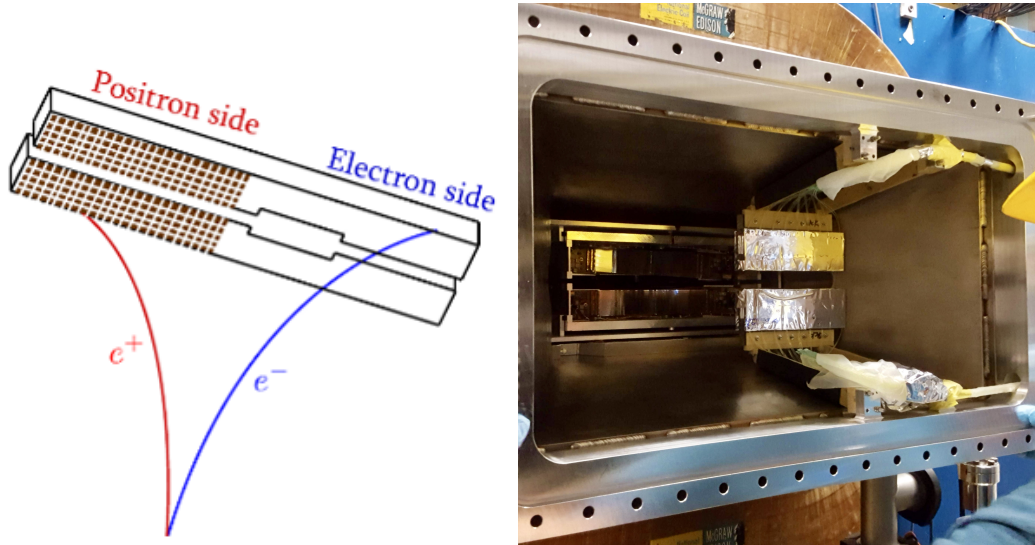


Figure 6.5: Left: A schematic of the Ecal showing the side in which positrons trigger. The positron trigger will recover events in which the electron falls in the gap. Right: A picture of the hodoscope which is located in the vacuum chamber behind layer 6 of the SVT and in front of the Ecal, but only on the positron side. Ecal-hodoscope matching enables a positron-only trigger with rates that are manageable for the DAQ.

3243 the hodoscope which adds an additional factor of ~ 2 to the signal yield. The goal of these simulations
 3244 is to obtain the number of A' 's in a near-zero background region, and hence a projected sensitivity.

3245 In order to obtain this reach estimate, the acceptance of displaced A' 's, a well-defined signal region,
 3246 and an overall normalization are all needed. From the simulations, the acceptance as a function of
 3247 z for a displaced 40 MeV A' in Fig. 6.3 and Fig. 6.4. The signal region is defined by projecting a
 3248 z_{cut} utilizing the same methods of background fitting discussed in Sec. 5.5. A comparison of the
 3249 z_{cut} between the nominal detector and the L0 upgraded detector at several different luminosities is
 3250 shown in Fig. 6.6. Since z_{cut} scales approximately with vertex resolution, there is an improvement
 3251 of about half the distance to the target with the upgraded detector. And since the signal shapes are
 3252 exponential in z , this additional signal region significantly closer to the target dramatically increases
 3253 the expected signal yield.²

3254 Finally, the overall normalization was found by using the radiative fraction from the ratio of the
 3255 event-weighted generator-level cross-sections of trident and WAB processes and multiplying by the
 3256 number of e^+e^- pairs in a small mass window as described in Sec. 4.11.3. After using this number
 3257 and Eq. [?] to compute the number of expected A' events, the projected sensitivity is derived by
 3258 drawing a contour at 2.3 expected signal events. This contour is shown in Fig. 6.7. The contours

²When requiring layer 0 hits for both e^+e^- particles, the geometrical acceptance drops off earlier in the upgraded detector than the nominal detector. However, since the signal shape is exponential, the signal gain from the more optimal z_{cut} far outweighs the signal loss due to acceptance. In addition, adding the L0L1 and L1L1 mutually exclusive categories nearly recovers this loss as shown in Fig. 6.4.

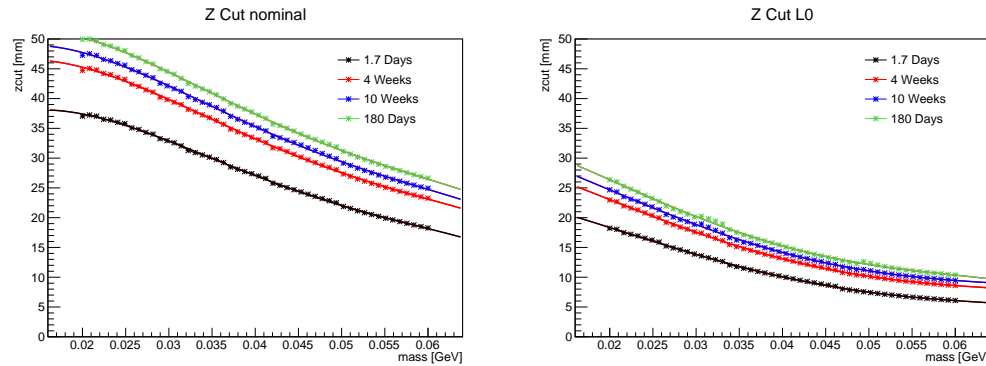


Figure 6.6: A comparison of the z_{cut} for several different luminosities (1.7 days, 4 weeks, 10 weeks, and 180 days) for Left: the nominal detector and Right: the upgraded L0 detector. The improvement in z_{cut} by a factor of ~ 2 for the L0 detector is a measure of the the improvement in the signal yield.

3259 are drawn for four weeks of continuous beam (reach is not expected in either detector configuration
3260 for the 2015 Engineering Run luminosity of 1.7 days of beam). The contour for the nominal detector
3261 is not drawn since the sensitivity is expected to begin at about 10 weeks.

3262 The construction of the upgraded SVT began at SLAC in the winter of 2019. A picture of a
3263 completed L0-3 U-channel on the mechanical survey table is shown in Fig. 6.8. After the mechanical
3264 survey was complete, each upgraded U-channel was placed in a test box for testing of the DAQ as
3265 shown in Fig. 6.8. These boxes were weather-sealed and pumped continuously with dry air to allow
3266 for cooling without condensation. The cooling system was hooked up to the nominal SVT cooling
3267 system. The humidity was monitored with humidity sensors and an Arduino-based readout system
3268 with a Twitter-based alert system as shown in Fig. 6.9 ([cite Twitter](#)).

3269 After testing at SLAC, the upgraded U-channels were shipped to Jefferson Laboratory and in-
3270 stalled in the HPS SVT box inside the analyzing magnet. The installation was performed in May and
3271 June of 2019, in time for the middle of June start of the run. A picture of the completely installed
3272 upgraded U-channels (without the target) for both the “open” and “closed” SVT configurations is
3273 shown in Fig. 6.10.

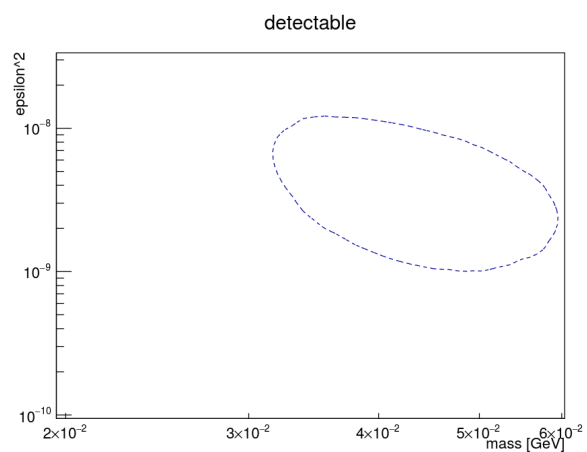


Figure 6.7: The estimated projection from early simulations for the upgraded L0 detector assuming 4 weeks of a continuous 1.06 GeV beam. The contour is drawn at 2.3 expected events and assumes layer 0 hits for both e^+e^- particles (L0L0).

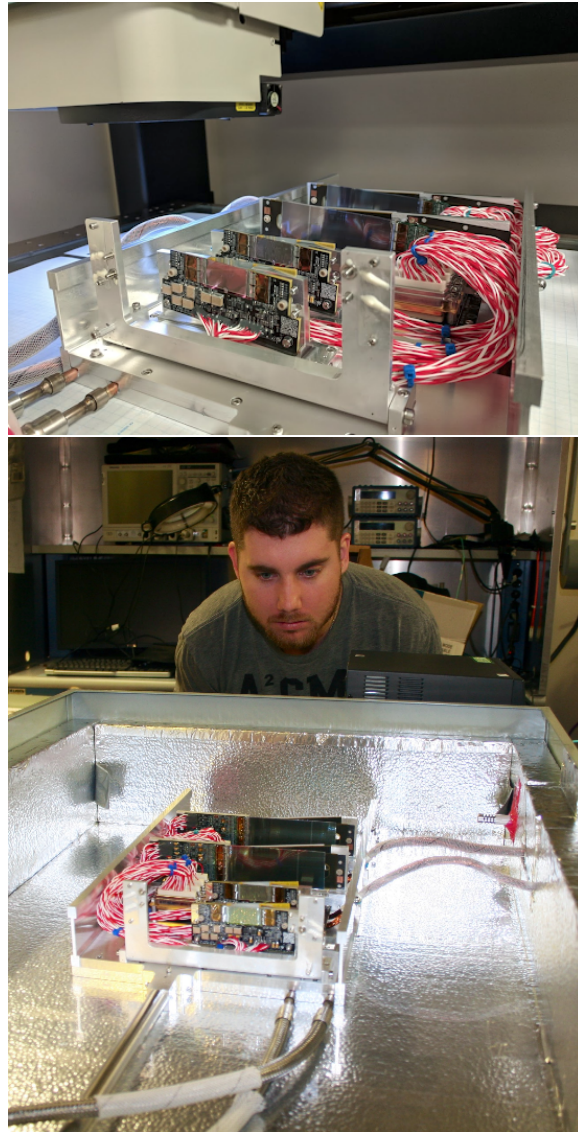


Figure 6.8: Left: A picture of an L0-3 U-channel on top of the mechanical survey table. Right: A graduate student peers over an L0-3 U-channel inside a test box at SLAC that was used for DAQ testing.

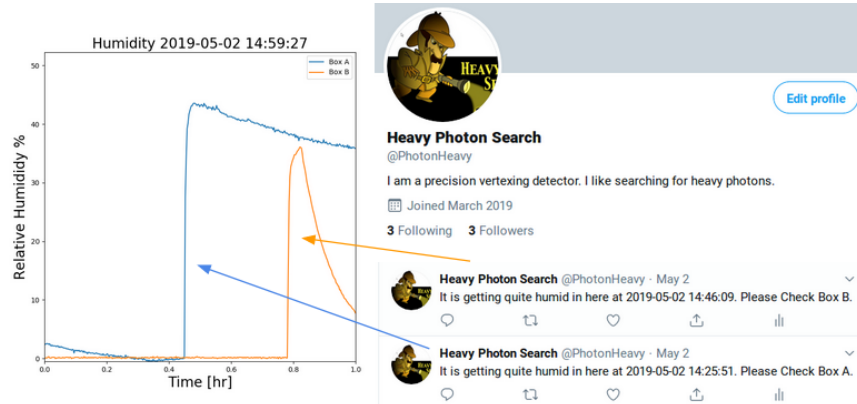


Figure 6.9: The upgraded U-channels were each placed in a test box at SLAC for DAQ testing. Since each box must be cooled and fed dry air, humidity monitoring is needed. Each box contained a humidity sensor which was readout via an Arduino and connected to a Twitter-based alert system. This picture shows an example of a sudden increase in humidity in both test boxes which was immediately followed by an alert tweet. In other words, someone opened the test boxes.

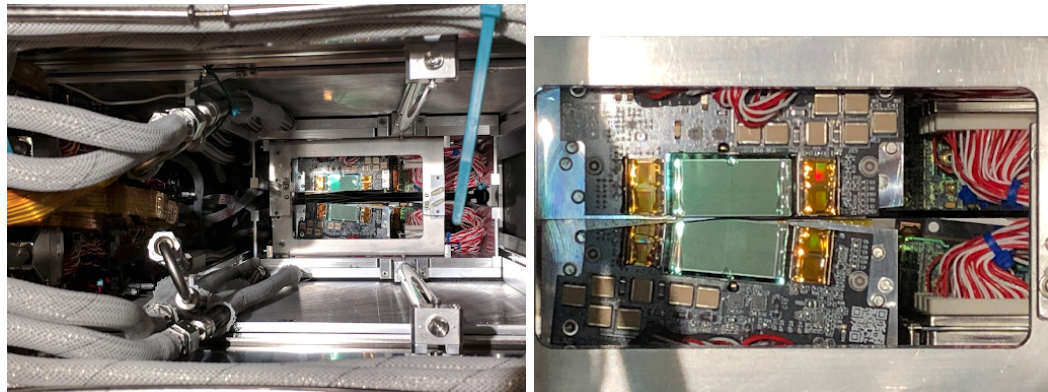


Figure 6.10: Left: A beam's-eye view of the installed L0 sensors inside the vacuum chamber. This is in the “open” configuration in which the sensors are far from the beam plane (~ 10 mm) so that the beam can be tuned without damaging sensors. Right: A zoomed in version in the “closed” (or operating) configuration where the L0 axial sensors are $500 \mu\text{m}$ from the beam plane.

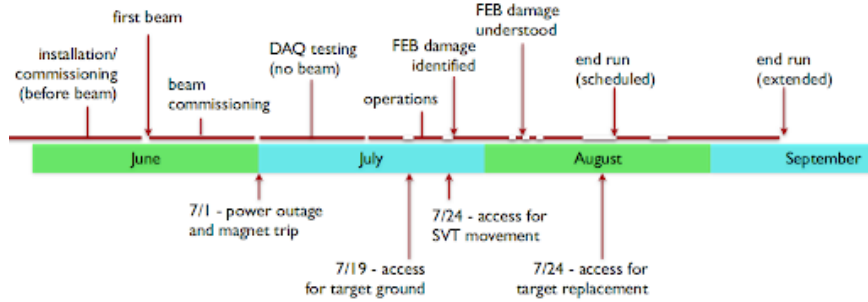


Figure 6.11: The approximate timeline for the major events that occurred over the course of the 2019 Physics Run. The first beam was delivered to the Hall B in the middle of June. Due to issues over the course of the run, the run was extended from the end of August to the middle of September.

3274 6.2 Preliminary Upgrade Performance & Reach Estimates

3275 Beam commissioning for the 2019 Physics Run began in the middle of June in 2019. This was the
 3276 first simultaneous running of Hall A, Hall B, and Hall C in the 12 GeV era (where each hall requested
 3277 unique beam requirements) which resulted in difficulty in delivering quality beam for several weeks.
 3278 In addition, several issues from HPS that interrupted data taking. First, a site-wide power outage
 3279 due to a storm caused a trip in the analyzing magnet which subsequently shifted the bottom U-
 3280 channel by more than 10 mm. Second, significant radiation damage from frequent beam tuning in
 3281 Hall B caused significant damage to the front end electronics, making a few of them barely usable.
 3282 Third, a broken grounding wire for the target (which was not identified until the vacuum chamber
 3283 was closed) caused charge to accumulate and then frequently discharge. A summary timeline of
 3284 important events over the 2019 Physics Run is shown in 6.11.

3285 Despite significant issues, excellent beam conditions were achieved at the end of July. An SVT
 3286 wire scan of one of the first beam profiles used for physics data taking is shown in Fig. 6.12 This
 3287 beam had a $\sim 22 \mu\text{m}$ spot size in y and was within $\sim 50 \mu\text{m}$ of the center of the detector. And
 3288 once beam quality was consistent, data was efficiently collected. In total, (XX mC and XX days)
 3289 was accumulated as shown in Fig. 6.13. This is about three times the total luminosity of the 2016
 3290 Engineering Run.

3291 In order to evaluate the effectiveness of the upgrades, an improved vertex resolution in agreement
 3292 with MC and an e^+e^- rate increase from the hodoscope and positron-only trigger must be shown.
 3293 The preliminary results from the 2019 Physics Run shows nearly a 1 mm vertex resolution in the
 3294 mass range of interest which is about $\sim 25\%$ worse than current MC predictions. However, this is
 3295 far from the final tracker alignment and as the alignment converges on its optimal configuration, the
 3296 vertex resolution will improve. The effectiveness of moving L1-L3 closer to the beam plane is still
 3297 under evaluation.

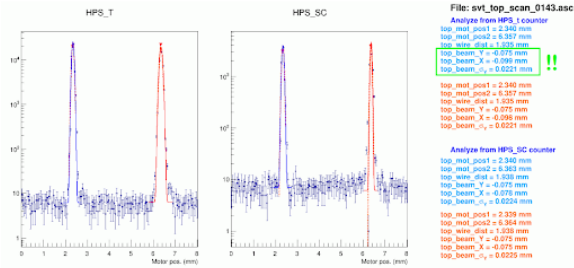


Figure 6.12: A measurement of the beam profile using the SVT scan wires with measures a beam profile of $22 \mu\text{m}$ in y within $50 \mu\text{m}$ of the center of the detector. This is a high-quality beam was the first successful beam for HPS with simultaneous operations of Hall A, Hall B, and Hall C in the 12 GeV era (upgraded CEBAF as described in Sec. 3.1).

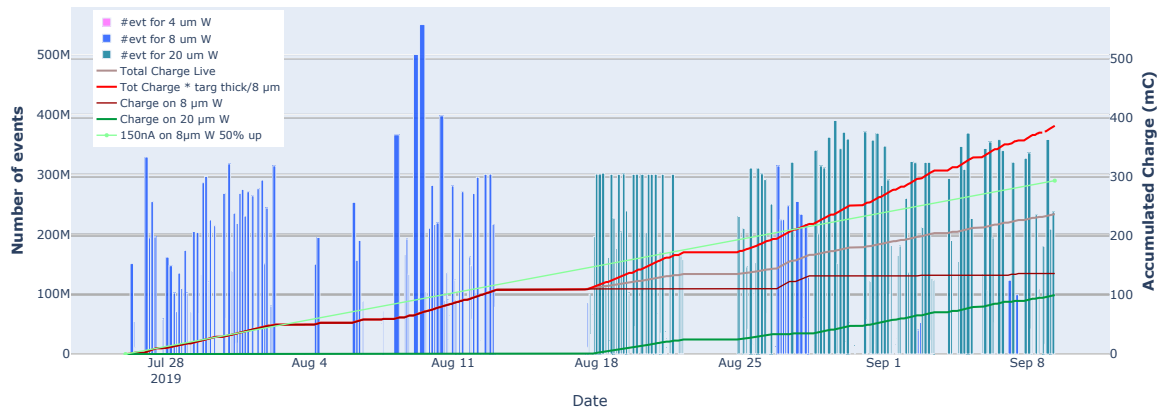


Figure 6.13: Accumulated charge over the course of the 2019 Physics Run. The red line is re-scaled to the luminosity-equivalent total charge from an $8 \mu\text{m}$ thick target since the target configuration was changed several times over the course of the run.

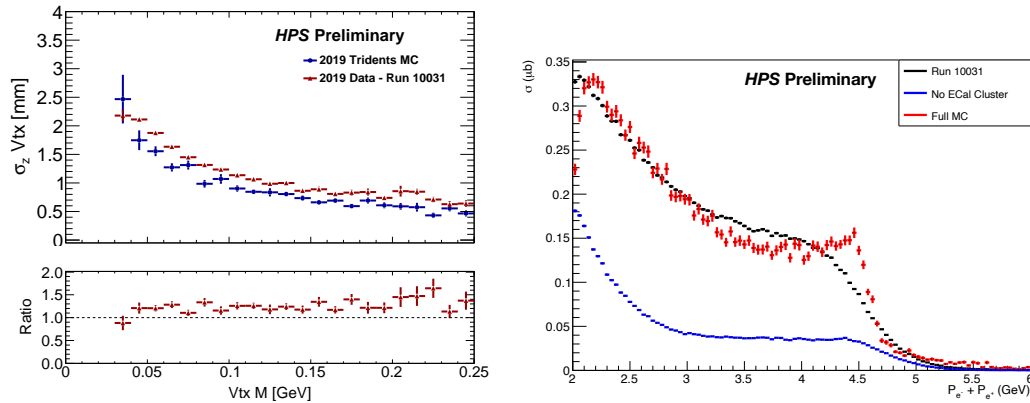


Figure 6.14: Left: A comparison of the vertex resolution for data and MC for with a 4.55 GeV beam. Data is within $\sim 25\%$ of MC and will improve as the tracker alignment is updated. Right: A comparison of data and MC measured cross-sections as a function of e^+e^- momentum sum. The blue line represents events in which the electron track does not match to a cluster in the Ecal. This is a measure of the effectiveness of the hodoscope which shows an increase in the rate of e^+e^- pairs by $\sim 30\%$ in the signal region (large momentum sum).

In terms of the effectiveness of the hodoscope, one can compare the total e^+e^- rate with the fraction of the e^+e^- rate that does not contain a match with an electron-side cluster. Preliminary results shown in Fig. 6.14 show an increase in rate of about $\sim 30\%$ in the momentum sum signal region. However, these preliminary results depend on the finding of an electron track. Track finding is expected to improve as both tracker alignment improves and as a Kalman Filter track finding algorithm is implemented.³

From the initial analysis in the data, one can project the expected sensitivity for the displaced vertexing analysis shown in Fig. 6.15. This projection is conservative since it requires layer 0 hits for both e^+e^- particles (L0L0). However, it is likely that adding the other mutually exclusive categories (L0L1, L1L1, etc.) to capture A' 's with longer lifetimes will add significance to the analysis. This is especially true in the upgraded detector since layers 1 -3 in the SVT were moved closer to the beam plane for increased A' acceptance of further downstream decays. The projected sensitivities of these additional categories have not been explored yet.

³For the 2015 and 2016 Engineering Runs, the SeedTracker algorithm was used for track finding as described in Sec. 4.3.3. However, several sensors were turned off over the course of the 2019 Physics Run due to issues with both the sensors and FEBs. SeedTracker relies on the use of 3D hits, thus incorporating a Kalman Filter which performs track finding at the strip hit level will recover a significant number of tracks.

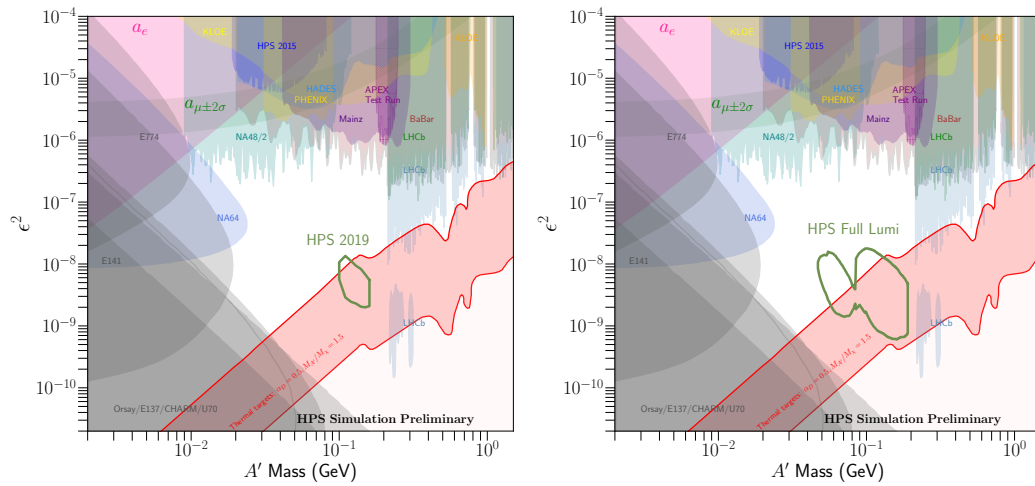


Figure 6.15: Left: Initial projections for the displaced vertex search from the 2019 Physics Runs with a 4.55 GeV beam. Right: Projections utilizing the full HPS run time of 180 days at both 4.55 GeV and 2.3 GeV. Both of these projections assume layer 0 hits for both e^+e^- particles (L0L0).

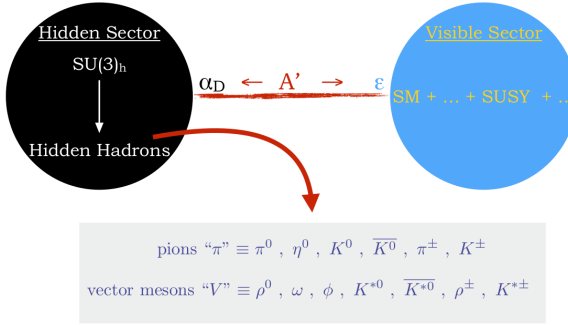


Figure 6.16: A hidden $SU(3)$ symmetry in a dark sector can contain hidden hadrons which include dark pions and dark vector mesons. One way for these particles to interact with SM matter is through an indirect interaction via kinetic mixing between an A' and the SM photon as described in Sec. 2.2.

3311 6.3 Generalized Displaced Vertices

3312 In addition to the minimal A' model described in Sec. 2.2, HPS can potentially probe any model
 3313 with an electro-produced long-lived mediator that decay to e^+e^- pairs and set limits on the mass,
 3314 livetime, and cross sections of long-lived particles that decay in the range $\sim 1\text{-}10$ cm.

3315 6.3.1 Strongly Interacting Massive Particles (SIMPs)

3316 Currently, the most appealing model for HPS beyond the canonical A' model are called Strongly
 3317 Interacting Massive Particles (SIMPs) which includes an additional $SU(3)$ symmetry to the SM
 3318 $SU(3)$ symmetry in addition to an additional $U(1)$ symmetry as shown in Fig. 6.16 [60]. This leaves
 3319 room for dark quark sector with dark mesons and dark vectors.

3320 The prime motivation for SIMPs is the so-called “SIMP Cosmology” in which dark matter
 3321 annihilations and cooling produces the correct dark matter relic abundance. Specifically, dark pions
 3322 undergo a $3 \rightarrow 2$ annihilation mechanism that depletes the dark pion relic abundance until the
 3323 universe expands and cools enough such that this mechanism ceases. These dark pion annihilations
 3324 heat up the dark sector but are able to dump heat into the SM sector through kinetic mixing of
 3325 the A' and the SM photon which produces the cold dark matter observed today. If one assumes
 3326 that the dark pions make up the entirety of dark matter, one gets a dark matter mass in the range
 3327 $\sim 1 - 100$ MeV. This is called the SIMP Miracle (analogous to the WIMP Miracle from Sec. 2.4)
 3328 and this mechanism is shown schematically in Fig. 6.17.

3329 The SIMP model contains six parameters, an additional four from the minimal A' model. The
 3330 six parameters are as follows:

- 3331 1. $m_{A'}$ - The mass of the A' . For the parameter space of interest, A' s are prompt.
- 3332 2. m_{V_D} - The mass to the dark vector which is the particle that is actually long-lived.

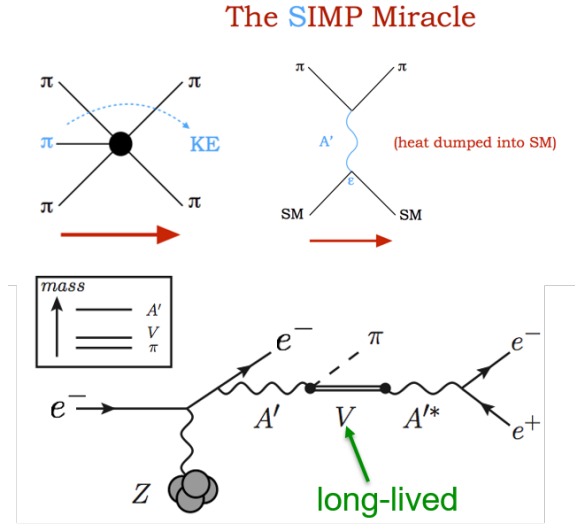


Figure 6.17: A mechanism in the early universe in which dark pions undergo a $3 \rightarrow 2$ annihilation mechanism followed by heat being dumped into SM sector to produce the cold dark matter observed today. This mechanism can be tuned to achieve the correct dark pion relic abundance of dark matter and is known as the “SIMP Miracle.” This motivates a dark matter mass in the range $\sim 10 - 100$ MeV. HPS can probe the production the mechanism $e^- Z \rightarrow e^- Z A'$ and then $A' \rightarrow \pi_D V_D$ and then $V_D \rightarrow e^+ e^-$ where the V_D is long-lived.

- 3333 3. m_{π_D} - The mass of the dark pion. This particle is not detected by HPS and shows up as
- 3334 missing energy. This particle is a candidate for dark matter.
- 3335 4. ϵ - The kinetic mixing parameter from the A' model.
- 3336 5. α_D - The dark sector $U(1)$ gauge coupling constant (analogous to the SM α).
- 3337 6. m_{π_D}/f_{π_D} - The dark sector pion decay constant.

3338 These parameters are not completely free and are bound by constraints, motivations, and de-
 3339 pendencies that arise from quantum field theory and cosmology. Additional constraints come from
 3340 the limitations of HPS and are as follows:

- 3341 1. The gauge coupling α_D is only constrained by perturbativity to be less than 1. Naturalness
 3342 arguments will put $\alpha_D \sim 10^{-2}$; however, this constraint can be easily be relaxed in order to
 3343 probe the full parameter space.
- 3344 2. The requirement from SIMP cosmology sets a lower bound on the kinetic mixing parameter
 3345 $\epsilon > 10^{-6.3} (m_{A'}/10^{-2} \text{ GeV})^{1/2}$ for $\alpha_D = 10^{-2}$ and the mass ratio used below. Larger couplings
 3346 ($\epsilon \sim 10^{-5} - 10^{-3}$) are allowed if a kinetic mixing loop arises from massive particles charged

under both the dark $U(1)$ and the SM hypercharge. For even larger couplings ($\epsilon > 10^{-2}$), the model approaches the standard scalar thermal dark matter scenario as π_D annihilations through the A' significantly impact the dark matter relic abundance.

- 3347 3. Pertubativity requires the ratio $m_{\pi_D}/f_{\pi_D} < 4\pi$. An additional constraint from the dark matter
3348 relic abundance from π_D together with fixed V_D and π_D masses also fixes the ratio m_{π_D}/f_{π_D}
3349 which is shown in Fig. 6.19.
- 3350 4. For SIMP cosmology to work, certain annihilations such as $\pi_D\pi_D \rightarrow A'^* \rightarrow \bar{f}f$ and $\pi_D\pi_D \rightarrow$
3351 $A'\pi_D$ should be suppressed which is achieved by requiring $\epsilon < 10^{-2}$ and $m_{A'} > 2m_{\pi_D}$, respectively.
3352
- 3353 5. HPS can only search for visible decays into e^+e^- pairs which this requires $V_D > 2m_e$. The A'
3354 decay channel requires $m_{A'} > m_{\pi_D} + m_{V_D}$.
3355
- 3356 6. Effective field theory provides a rough prediction relating the ratio of the dark vector mass to
3357 the dark pion mass.
3359

$$\frac{m_{V_D}}{m_{\pi_D}} \sim \frac{4\pi}{\sqrt{N_c}(m_{\pi_D}/f_{\pi_D})} \quad (6.1)$$

3360 where N_C is the number of colors in the dark QCD. As in the SM, $N_C = 3$ and vector mesons
3361 are heavier than pions. Enforcing this relationship further reduces the number of independent
3362 parameters and is shown to be generally independent of m_{π_D}/f_{π_D} in Fig. 6.19.

3363 Mass hierarchy and choice of mass ratios.

3364 Assuming the same dark bremsstrahlung production mechanism of A' s as described in Sec. 2.5.
3365 Once an A' is electro-produced, it can decay into some combination of dark vectors and dark pions
3366 [59]. The decay width of A' decaying into two dark pions π_D is:

$$\Gamma(A' \rightarrow \pi_D\pi_D) = \frac{2\alpha_D}{3} m_{A'} \left(1 - \frac{4m_{\pi_D}^2}{m_{A'}^2}\right)^{3/2} \left(\frac{m_{V_D}^2}{m_{A'}^2 - m_{V_D}^2}\right)^2 \quad (6.2)$$

3367 This mechanism leaves the recoil electron as the only visible particle in the final state. Thus,
3368 this A' decay cannot be probed with HPS. The decay width of an A' into a dark pion and a dark
3369 vector V_D is:

$$\Gamma(A' \rightarrow V_D\pi_D) = \frac{\alpha_D T_V}{192\pi^4} \left(\frac{m_{A'}}{m_{\pi_D}}\right)^2 \left(\frac{m_{V_D}}{m_{\pi_D}}\right)^2 \left(\frac{m_{\pi_D}}{f_{\pi_D}}\right)^4 m_{A'} \beta(x, y)^{3/2} \quad (6.3)$$

3370 where $x = m_{\pi_D}/m_{A'}$, $y = m_{V_D}/m_{A'}$, and $\beta(x, y) = (1 + y^2 - x^2 - 2y)(1 + y^2 - x^2 + 2y)$. The
3371 variable T_V is a function of the dark meson flavor.

$$T_V = 3/4, 3/2, 18 \quad (6.4)$$

3372 The dark pion is invisible and... Finally, for $m_{A'} > 2m_{V_D}$ the decay into two dark vectors is
3373 allowed with a decay width of:

$$\Gamma(A' \rightarrow V_D V_D) = \frac{\alpha_D}{6} f(r) m_{A'} \quad (6.5)$$

3374 where $r = m_{V_D}/m_{A'}$ and

$$f(r) = \left(\frac{1 + 16r^2 - 68r^4 - 48r^6}{(1 - r^2)^2} \right) \sqrt{1 - 4r^2} \quad (6.6)$$

3375 As will be described, each V_D will decay into $e^+ e^-$ pairs for $2m_e < m_{V_D} < 2m_\mu$ thus this last
3376 decay will have a four lepton final state. The acceptance of HPS to a four lepton final state is
3377 small, but has not been carefully evaluated. To increase the difficulty for HPS, such a mechanism
3378 would include two secondary vertices which would be challenging to resolve if only a fraction of the
3379 particles are in HPS acceptance. For these reasons, this mechanism is not explored and the focus is
3380 on the $e^+ e^- \pi_D$ final state.

3381 Finally, the same decay width of $A' \rightarrow e^+ e^-$ for the canonical A' model is used but is small
3382 compared to the other decay widths. Once again assuming $2m_e < m_{V_D} < 2m_\mu$, the decay width of
3383 V_D is:

$$\Gamma(V_D \rightarrow e^+ e^-) = \frac{16\pi\alpha_D\alpha\epsilon^2 f_{\pi_D}^2}{3m_{V_D}^2} \left(\frac{m_{V_D}^2}{m_{A'}^2 - m_{V_D}^2} \right)^2 \sqrt{1 - \frac{4m_e^2}{m_{V_D}^2}} \left(1 + \frac{2m_e^2}{m_{V_D}^2} \right) m_{V_D} \times x \quad (6.7)$$

3384 where $x = 2$ for a dark ρ and $x = 1$ for a dark ϕ (the only two dark mesons of interest). Decays
3385 into SM hadrons and muons are not explored in this work because the mass hierarchy kinematically
3386 forbids such decays.

3387 From the decay widths, the livetimes can be trivially computed and are shown in Fig. 6.18.
3388 Note that the additional parameters in the SIMP model decouple the livetime and production cross-
3389 section such that it is possible to have a high rate of long-lived particles. This is ideal for HPS and
3390 is opposed to the canonical A' model which have coupled lifetimes and cross-sections.

3391 For this study, to further reduce the number of parameters, a fixed ratio of the masses of the three
3392 new particles is fixed. The ratio of $m_{A'} : m_{V_D} : m_{\pi_D}$ is chosen to be $3.0 : 1.8 : 1.0$ which respects the
3393 constraints required for a visible signal at HPS and also kinematically forbids a $A' \rightarrow V_D V_D$ which
3394 complicates the search as previously described. This ratio also respects the relation described in Eq.
3395 6.1. In addition, the other observables are the lifetimes and cross-sections which can be trivially
3396 reweighted after MC reconstruction. Thus, with the fixed mass ratio and reweighting scheme, the
3397 model can effectively reduced to two parameters - $m_{A'}$ and livetime.

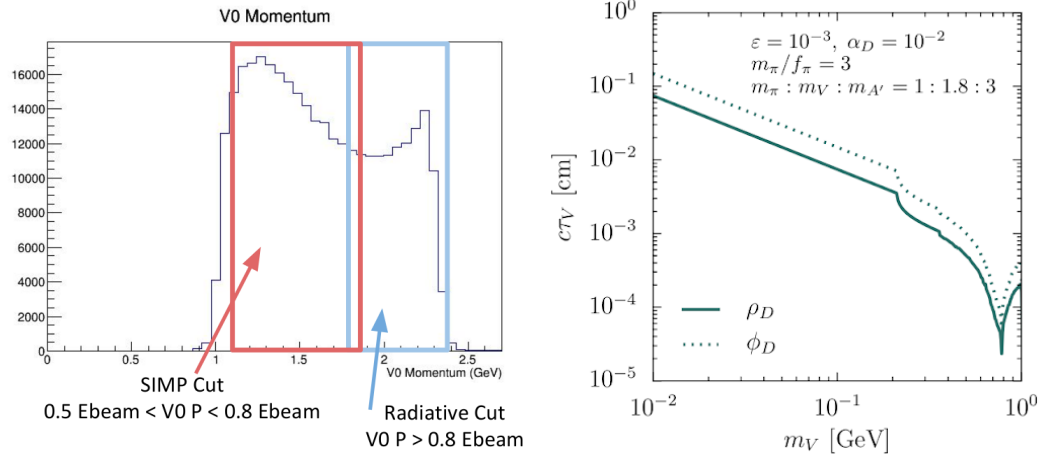


Figure 6.18: Left: The reconstructed V0 momentum that shows roughly the different parameter space for canonical A' 's and SIMPs. The lower momentum sum of the SIMP parameter space is due to missing energy from the dark pion. Replace this figure Right: The livetime ($c\tau$) of two dark mesons (ρ_D and ϕ_D) for a given set of parameters. The livetime $c\tau \sim 0.1 - 10$ mm is within HPS range.

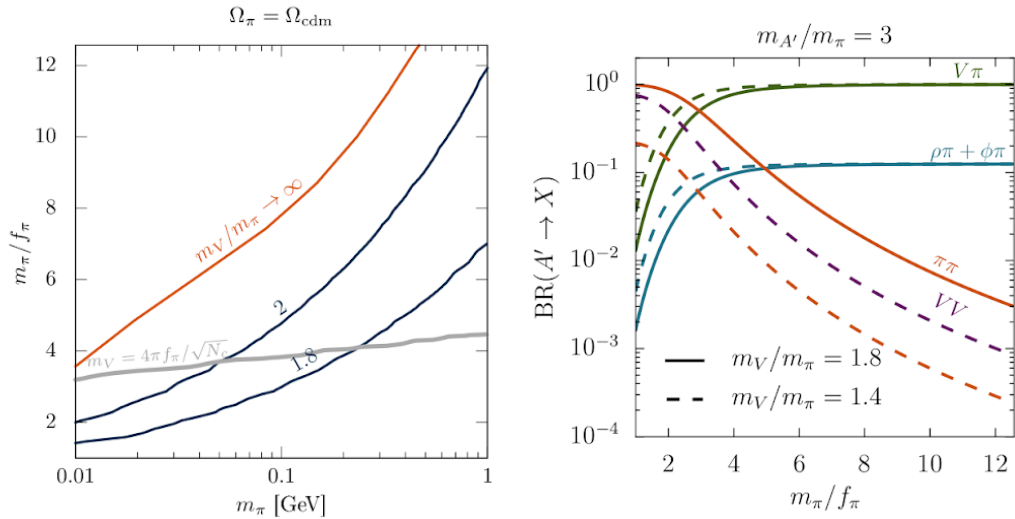


Figure 6.19: Contours in the $m_{\pi_D} - (m_{\pi_D}/f_{\pi_D})$ space for different choices of m_{V_D}/m_{π_D} assuming π_D makes up all the dark matter. Right: The branching ratio as a function of m_{π_D}/f_{π_D} . For HPS, the branching ratio in the parameter space of interest for the sum of ρ_D and ϕ_D is about $\sim 10\%$.

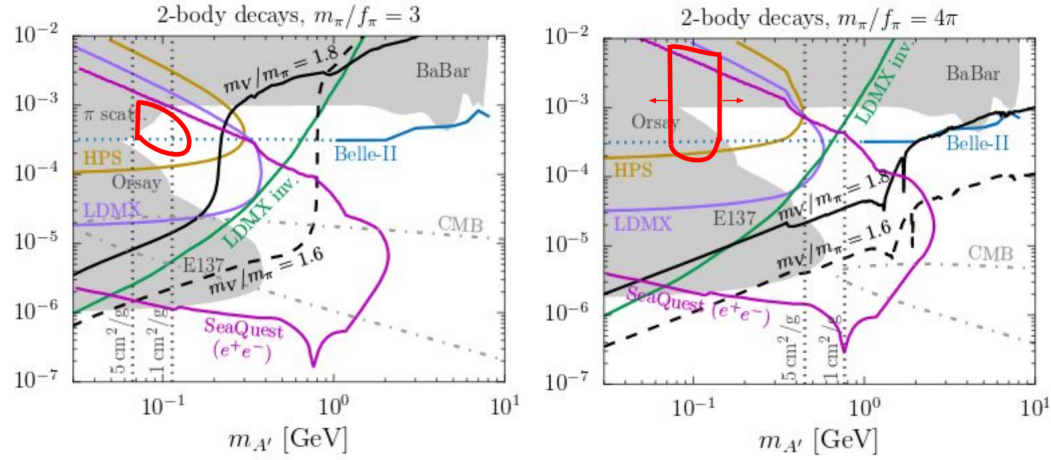


Figure 6.20: The SIMP reach estimate from the full 2016 Engineering Run dataset shown in e^2 - $m_{A'}$ space for $\alpha_{dark} = 0.01$ and for Left: $m_\pi/f_\pi = 3$ and Right: $m_\pi/f_\pi = 4\pi$. The ratio of the masses is kept constant at $m_{A'} : m_\rho : m_\pi = 3.0 : 1.8 : 1.0$ for simplicity. The contours are drawn at 2.3 expected events and the dataset is projected to set new limits in previously unprobed territory. These figures need to be replaced.

6.3.2 SIMP Projections

3398 Both the projections and the descriptions are out of date and need to be updated.

3399 Both the projections and the descriptions are out of date and need to be updated.

3400 **Chapter 7**

3401 **Conclusions**

3402 The Heavy Photon Search (HPS) is a fixed target experiment located in Hall B at Jefferson Lab-
3403 oratory dedicated to searching for heavy photons (dark photons or A' s). Heavy photons are an
3404 extension of the Standard Model, arise from an additional $U(1)$ abelian gauge symmetry, and are
3405 connected to several models of dark matter. Heavy photons are particularly appealing to sub-GeV
3406 dark matter models that require a new comparably light mediator to achieve the current observed
3407 relic abundance of dark matter.

3408 HPS utilizes a compact forward acceptance spectrometer to search for heavy photons in the mass
3409 range $\sim 10 - 300$ MeV and kinetic mixing strength $\epsilon^2 \sim 10^{-5} - 10^{-10}$ that decay to e^+e^- pairs. For
3410 relatively large ϵ^2 , HPS can utilize a bump hunt in which a sharp resonance peak at the A' mass
3411 appears over an invariant mass spectrum of QED tridents. For relatively small ϵ^2 , A' 's have a finite
3412 livetime and a search for displaced vertices can be performed.

3413 This dissertation focused on the results of the displaced vertex search for the 2016 Engineering
3414 Run. The luminosity from this dataset was, unfortunately, not enough to set a limit on the canonical
3415 A' model; however, the required background level to make this search possible was achieved on a
3416 blinded data sample. This provides confidence that such a search with upgrades and increased
3417 luminosity is feasible and projection with a dataset taken in 2019 show sensitivity in new territory.
3418 In addition, a search for A' 's that travel further downstream such that the daughter particles miss
3419 the full acceptance of the SVT was performed, and the feasibility of a displaced vertex search for
3420 models beyond the minimal A' model was shown.

Bibliography

- [1] Georges Aad et al. Observation of a new particle in the search for the Standard Model Higgs boson with the ATLAS detector at the LHC. *Phys. Lett.*, B716:1–29, 2012.
- [2] R. Aaij, B. Adeva, M. Adinolfi, Z. Ajaltouni, S. Akar, J. Albrecht, F. Alessio, M. Alexander, A. Alfonso Albero, S. Ali, G. Alkhazov, P. Alvarez Cartelle, A. A. Alves, S. Amato, S. Amerio, Y. Amhis, L. An, L. Anderlini, G. Andreassi, M. Andreotti, J. E. Andrews, R. B. Appleby, F. Archilli, P. d’Argent, J. Arnau Romeu, A. Artamonov, M. Artuso, E. Aslanides, M. Atzeni, G. Auriemma, M. Baalouch, I. Babuschkin, S. Bachmann, J. J. Back, A. Badalov, C. Baesso, S. Baker, V. Balagura, W. Baldini, A. Baranov, R. J. Barlow, C. Barschel, S. Barsuk, W. Barter, F. Baryshnikov, V. Batozskaya, V. Battista, A. Bay, L. Beaucourt, J. Beddow, F. Bedeschi, I. Bediaga, A. Beiter, L. J. Bel, N. Beliy, V. Bellee, N. Belloli, K. Belous, I. Belyaev, E. Ben-Haim, G. Bencivenni, S. Benson, S. Beranek, A. Berezhnoy, R. Bernet, D. Berninghoff, E. Bert-holet, A. Bertolin, C. Betancourt, F. Betti, M.-O. Bettler, M. van Beuzekom, Ia. Bezshyiko, S. Bifani, P. Billoir, A. Birnkraut, A. Bizzeti, M. Bjørn, T. Blake, F. Blanc, S. Blusk, V. Bocci, T. Boettcher, A. Bondar, N. Bondar, I. Bordyuzhin, S. Borghi, M. Borisjak, M. Borsato, F. Bossu, M. Boubdir, T. J. V. Bowcock, E. Bowen, C. Bozzi, S. Braun, T. Britton, J. Brodzicka, D. Brundu, E. Buchanan, C. Burr, A. Bursche, J. Buytaert, W. Byczynski, S. Cadeddu, H. Cai, R. Calabrese, R. Calladine, M. Calvi, M. Calvo Gomez, A. Camboni, P. Campana, D. H. Campora Perez, L. Capriotti, A. Carbone, G. Carboni, R. Cardinale, A. Cardini, P. Carniti, L. Carson, K. Carvalho Akiba, G. Casse, L. Cassina, M. Cattaneo, G. Cavallero, R. Cenci, D. Chambon, M. G. Chapman, M. Charles, Ph. Charpentier, G. Chatzikonstantinidis, M. Chefdeville, S. Chen, S. F. Cheung, S.-G. Chitic, V. Chobanova, M. Chrzaszcz, A. Chubykin, P. Ciambrone, X. Cid Vidal, G. Ciezarek, P. E. L. Clarke, M. Clemencic, H. V. Cliff, J. Closier, J. Co-gan, E. Cogneras, V. Cogoni, L. Cojocariu, P. Collins, T. Colombo, A. Comerma-Montells, A. Contu, A. Cook, G. Coombs, S. Coquereau, G. Corti, M. Corvo, C. M. Costa Sobral, B. Cou-turier, G. A. Cowan, D. C. Craik, A. Crocombe, M. Cruz Torres, R. Currie, C. D’Ambrosio, F. Da Cunha Marinho, E. Dall’Occo, J. Dalseno, A. Davis, O. De Aguiar Francisco, S. De Capua, M. De Cian, J. M. De Miranda, L. De Paula, M. De Serio, P. De Simone, C. T. Dean, D. Decamp,

- 3449 L. Del Buono, H.-P. Dembinski, M. Demmer, A. Dendek, D. Derkach, O. Deschamps, F. Det-
3450 tori, B. Dey, A. Di Canto, P. Di Nezza, H. Dijkstra, F. Dordei, M. Dorigo, A. Dosil Suárez,
3451 L. Douglas, A. Dovbnya, K. Dreimanis, L. Dufour, G. Dujany, P. Durante, R. Dzhelyadin,
3452 M. Dziewiecki, A. Dziurda, A. Dzyuba, S. Easo, M. Ebert, U. Egede, V. Egorychev, S. Ei-
3453 delman, S. Eisenhardt, U. Eitschberger, R. Ekelhof, L. Eklund, S. Ely, S. Esen, H. M. Evans,
3454 T. Evans, A. Falabella, N. Farley, S. Farry, D. Fazzini, L. Federici, D. Ferguson, G. Fernan-
3455 dez, P. Fernandez Declara, A. Fernandez Prieto, F. Ferrari, F. Ferreira Rodrigues, M. Ferro-
3456 Luzzi, S. Filippov, R. A. Fini, M. Fiorini, M. Firlej, C. Fitzpatrick, T. Fiutowski, F. Fleuret,
3457 K. Fohl, M. Fontana, F. Fontanelli, D. C. Forshaw, R. Forty, V. Franco Lima, M. Frank, C. Frei,
3458 J. Fu, W. Funk, E. Furfaro, C. Färber, E. Gabriel, A. Gallas Torreira, D. Galli, S. Gallorini,
3459 S. Gambetta, M. Gandelman, P. Gandini, Y. Gao, L. M. Garcia Martin, J. García Pardiñas,
3460 J. Garra Tico, L. Garrido, P. J. Garsed, D. Gascon, C. Gaspar, L. Gavardi, G. Gazzoni, D. Ger-
3461 ick, E. Gersabeck, M. Gersabeck, T. Gershon, Ph. Ghez, S. Gianì, V. Gibson, O. G. Girard,
3462 L. Giubega, K. Gizdov, V. V. Gligorov, D. Golubkov, A. Golutvin, A. Gomes, I. V. Gorelov,
3463 C. Gotti, E. Govorkova, J. P. Grabowski, R. Graciani Diaz, L. A. Granado Cardoso, E. Graugés,
3464 E. Graverini, G. Graziani, A. Grecu, R. Greim, P. Griffith, L. Grillo, L. Gruber, B. R. Gru-
3465 berg Cazon, O. Grünberg, E. Gushchin, Yu. Guz, T. Gys, C. Göbel, T. Hadavizadeh, C. Hadji-
3466 vasilious, G. Haefeli, C. Haen, S. C. Haines, B. Hamilton, X. Han, T. H. Hancock, S. Hansmann-
3467 Menzemer, N. Harnew, S. T. Harnew, C. Hasse, M. Hatch, J. He, M. Hecker, K. Heinicke,
3468 A. Heister, K. Hennessy, P. Henrard, L. Henry, E. van Herwijnen, M. Heß, A. Hicheur, D. Hill,
3469 C. Hombach, P. H. Hopchev, W. Hu, Z. C. Huard, W. Hulsbergen, T. Humair, M. Hushchyn,
3470 D. Hutchcroft, P. Ibis, M. Idzik, P. Ilten, R. Jacobsson, J. Jalocha, E. Jans, A. Jawahery,
3471 F. Jiang, M. John, D. Johnson, C. R. Jones, C. Joram, B. Jost, N. Jurik, S. Kandybei,
3472 M. Karacson, J. M. Kariuki, S. Karodia, N. Kazeev, M. Kecke, F. Keizer, M. Kelsey, M. Kenzie,
3473 T. Ketel, E. Khairullin, B. Khanji, C. Khurewathanakul, T. Kirn, S. Klaver, K. Klimaszewski,
3474 T. Klimkovich, S. Koliiev, M. Kolpin, R. Kopecna, P. Koppenburg, A. Kosmyntseva, S. Kotri-
3475 akhova, M. Kozeiha, L. Kravchuk, M. Kreps, F. Kress, P. Krokovny, F. Kruse, W. Krzemien,
3476 W. Kucewicz, M. Kucharczyk, V. Kudryavtsev, A. K. Kuonen, T. Kvaratskheliya, D. Lacar-
3477 rere, G. Lafferty, A. Lai, G. Lanfranchi, C. Langenbruch, T. Latham, C. Lazzeroni, R. Le Gac,
3478 A. Leflat, J. Lefrançois, R. Lefèvre, F. Lemaitre, E. Lemos Cid, O. Leroy, T. Lesiak, B. Lever-
3479 ington, P.-R. Li, T. Li, Y. Li, Z. Li, T. Likhomanenko, R. Lindner, F. Lionetto, V. Lisovskyi,
3480 X. Liu, D. Loh, A. Loi, I. Longstaff, J. H. Lopes, D. Lucchesi, M. Lucio Martinez, H. Luo, A. Lu-
3481 pato, E. Luppi, O. Lupton, A. Lusiani, X. Lyu, F. Machefert, F. Maciuc, V. Macko, P. Mack-
3482 owiak, S. Maddrell-Mander, O. Maev, K. Maguire, D. Maisuzenko, M. W. Majewski, S. Malde,
3483 B. Malecki, A. Malinin, T. Maltsev, G. Manca, G. Mancinelli, D. Marangotto, J. Maratas, J. F.
3484 Marchand, U. Marconi, C. Marin Benito, M. Marinangeli, P. Marino, J. Marks, G. Martellotti,

3485 M. Martin, M. Martinelli, D. Martinez Santos, F. Martinez Vidal, L. M. Massacrier, A. Mas-
3486 safferri, R. Matev, A. Mathad, Z. Mathe, C. Matteuzzi, A. Mauri, E. Maurice, B. Maurin,
3487 A. Mazurov, M. McCann, A. McNab, R. McNulty, J. V. Mead, B. Meadows, C. Meaux, F. Meier,
3488 N. Meinert, D. Melnychuk, M. Merk, A. Merli, E. Michielin, D. A. Milanes, E. Millard, M.-N.
3489 Minard, L. Minzoni, D. S. Mitzel, A. Mogini, J. Molina Rodriguez, T. Mombächer, I. A. Monroy,
3490 S. Monteil, M. Morandin, M. J. Morello, O. Morgunova, J. Moron, A. B. Morris, R. Mountain,
3491 F. Muheim, M. Mulder, D. Müller, J. Müller, K. Müller, V. Müller, P. Naik, T. Nakada,
3492 R. Nandakumar, A. Nandi, I. Nasteva, M. Needham, N. Neri, S. Neubert, N. Neufeld, M. Ne-
3493 uner, T. D. Nguyen, C. Nguyen-Mau, S. Nieswand, R. Niet, N. Nikitin, T. Nikodem, A. Nogay,
3494 D. P. O'Hanlon, A. Oblakowska-Mucha, V. Obraztsov, S. Ogilvy, R. Oldeman, C. J. G. Onder-
3495 water, A. Ossowska, J. M. Otalora Goicochea, P. Owen, A. Oyanguren, P. R. Pais, A. Palano,
3496 M. Palutan, A. Papanestis, M. Pappagallo, L. L. Pappalardo, W. Parker, C. Parkes, G. Passal-
3497 eva, A. Pastore, M. Patel, C. Patrignani, A. Pearce, A. Pellegrino, G. Penso, M. Pepe Altarelli,
3498 S. Perazzini, P. Perret, L. Pescatore, K. Petridis, A. Petrolini, A. Petrov, M. Petruzzo, E. Pi-
3499 catoste Olloqui, B. Pietrzky, M. Pikies, D. Pinci, F. Pisani, A. Pistone, A. Piucci, V. Placinta,
3500 S. Playfer, M. Plo Casasus, F. Polci, M. Poli Lener, A. Poluektov, I. Polyakov, E. Polycarpo,
3501 G. J. Pomery, S. Ponce, A. Popov, D. Popov, S. Poslavskii, C. Potterat, E. Price, J. Prisciandaro,
3502 C. Prouve, V. Pugatch, A. Puig Navarro, H. Pullen, G. Punzi, W. Qian, R. Quagliani, B. Quin-
3503 tana, B. Rachwal, J. H. Rademacker, M. Rama, M. Ramos Pernas, M. S. Rangel, I. Raniuk,
3504 F. Ratnikov, G. Raven, M. Ravonel Salzgeber, M. Reboud, F. Redi, S. Reichert, A. C. dos Reis,
3505 C. Remon Alepuz, V. Renaudin, S. Ricciardi, S. Richards, M. Rihl, K. Rinnert, V. Rives Molina,
3506 P. Robbe, A. Robert, A. B. Rodrigues, E. Rodrigues, J. A. Rodriguez Lopez, A. Rogozhnikov,
3507 S. Roiser, A. Rollings, V. Romanovskiy, A. Romero Vidal, J. W. Ronayne, M. Rotondo, M. S.
3508 Rudolph, T. Ruf, P. Ruiz Valls, J. Ruiz Vidal, J. J. Saborido Silva, E. Sadykhov, N. Sagidova,
3509 B. Saitta, V. Salustino Guimaraes, C. Sanchez Mayordomo, B. Sanmartin Sedes, R. Santace-
3510 saria, C. Santamarina Rios, M. Santimaria, E. Santovetti, G. Sarpis, A. Sarti, C. Satriano,
3511 A. Satta, D. M. Saunders, D. Savrina, S. Schael, M. Schellenberg, M. Schiller, H. Schindler,
3512 M. Schmelling, T. Schmelzer, B. Schmidt, O. Schneider, A. Schopper, H. F. Schreiner, M. Schu-
3513 biger, M.-H. Schune, R. Schwemmer, B. Sciascia, A. Sciubba, A. Semennikov, E. S. Sepulveda,
3514 A. Sergi, N. Serra, J. Serrano, L. Sestini, P. Seyfert, M. Shapkin, I. Shapoval, Y. Shcheglov,
3515 T. Shears, L. Shekhtman, V. Shevchenko, B. G. Siddi, R. Silva Coutinho, L. Silva de Oliveira,
3516 G. Simi, S. Simone, M. Sirendi, N. Skidmore, T. Skwarnicki, E. Smith, I. T. Smith, J. Smith,
3517 M. Smith, I. Soares Lavra, M. D. Sokoloff, F. J. P. Soler, B. Souza De Paula, B. Spaan,
3518 P. Spradlin, S. Sridharan, F. Stagni, M. Stahl, S. Stahl, P. Steffo, S. Stefkova, O. Steinkamp,
3519 S. Stemmle, O. Stenyakin, M. Stepanova, H. Stevens, S. Stone, B. Storaci, S. Stracka, M. E.

- 3520 Stramaglia, M. Straticiuc, U. Straumann, J. Sun, L. Sun, W. Sutcliffe, K. Swientek, V. Sy-
 3521 ropoulos, T. Szumlak, M. Szymanski, S. T'Jampens, A. Tayduganov, T. Tekampe, G. Tellarini,
 3522 F. Teubert, E. Thomas, J. van Tilburg, M. J. Tilley, V. Tisserand, M. Tobin, S. Tolk,
 3523 L. Tomassetti, D. Tonelli, F. Toriello, R. Tourinho Jadallah Aoude, E. Tournefier, M. Traill,
 3524 M. T. Tran, M. Tresch, A. Trisovic, A. Tsaregorodtsev, P. Tsopelas, A. Tully, N. Tuning,
 3525 A. Ukleja, A. Usachov, A. Ustyuzhanin, U. Uwer, C. Vacca, A. Vagner, V. Vagnoni, A. Valassi,
 3526 S. Valat, G. Valenti, R. Vazquez Gomez, P. Vazquez Regueiro, S. Vecchi, M. van Veghel, J. J.
 3527 Velthuis, M. Veltri, G. Veneziano, A. Venkateswaran, T. A. Verlage, M. Vernet, M. Vesterinen,
 3528 J. V. Viana Barbosa, B. Viaud, D. Vieira, M. Vieites Diaz, H. Viemann, X. Vilasis-Cardona,
 3529 M. Vitti, V. Volkov, A. Vollhardt, B. Voneki, A. Vorobyev, V. Vorobyev, C. Voß,
 3530 J. A. de Vries, C. Vázquez Sierra, R. Waldi, C. Wallace, R. Wallace, J. Walsh, J. Wang,
 3531 D. R. Ward, H. M. Wark, N. K. Watson, D. Websdale, A. Weiden, C. Weisser, M. Whitehead,
 3532 J. Wicht, G. Wilkinson, M. Wilkinson, M. Williams, M. P. Williams, M. Williams, T. Williams,
 3533 F. F. Wilson, J. Wimberley, M. Winn, J. Wishahi, W. Wislicki, M. Witek, G. Wormser, S. A.
 3534 Wotton, K. Wraight, K. Wyllie, Y. Xie, M. Xu, Z. Xu, Z. Yang, Z. Yang, Y. Yao, H. Yin, J. Yu,
 3535 X. Yuan, O. Yushchenko, K. A. Zarebski, M. Zavertyaev, L. Zhang, Y. Zhang, A. Zhelezov,
 3536 Y. Zheng, X. Zhu, V. Zhukov, J. B. Zonneveld, and S. Zucchelli. Search for dark photons
 3537 produced in 13 tev pp collisions. *Phys. Rev. Lett.*, 120:061801, Feb 2018.
- 3538 [3] S. Abrahamyan et al. Search for a New Gauge Boson in Electron-Nucleus Fixed-Target Scat-
 3539 tering by the APEX Experiment. *Phys. Rev. Lett.*, 107:191804, 2011.
- 3540 [4] R. Acciarri, C. Adams, R. An, C. Andreopoulos, A. M. Ankowski, M. Antonello, J. Asaadi,
 3541 W. Badgett, L. Bagby, B. Baibussinov, B. Baller, G. Barr, N. Barros, M. Bass, V. Bellini,
 3542 P. Benetti, S. Bertolucci, K. Biery, H. Bilokon, M. Bishai, A. Bitadze, A. Blake, F. Boffelli,
 3543 T. Bolton, M. Bonesini, J. Bremer, S. J. Brice, C. Bromberg, L. Bugel, E. Calligarich, L. Camil-
 3544 leri, D. Caratelli, B. Carls, F. Cavanna, S. Centro, H. Chen, C. Chi, E. Church, D. Cianci, A. G.
 3545 Cocco, G. H. Collin, J. M. Conrad, M. Convery, G. De Geronimo, A. Dermenev, R. Dharmapalan,
 3546 S. Dixon, Z. Djurcic, S. Dytmar, B. Eberly, A. Ereditato, J. Esquivel, J. Evans, A. Fal-
 3547 cone, C. Farnese, A. Fava, A. Ferrari, B. T. Fleming, W. M. Foreman, J. Freestone, T. Gamble,
 3548 G. Garvey, V. Genty, M. Geynisman, D. Gibin, S. Gninenko, D. Glodi, S. Gollapinni, N. Golubev,
 3549 M. Graham, E. Gramellini, H. Greenlee, R. Gross, R. Guenette, A. Guglielmi, A. Hackenburg,
 3550 R. Hnni, O. Hen, J. Hewes, J. Ho, G. Horton-Smith, J. Howell, A. Ivashkin, C. James, C. M. Jen,
 3551 R. A. Johnson, B. J. P. Jones, J. Joshi, H. Jostlein, D. Kaleko, L. N. Kalousis, G. Karagiorgi,
 3552 W. Ketchum, B. Kirby, M. Kirby, M. Kirsanov, J. Kisiel, J. Klein, J. Klinger, T. Kobilarcik,
 3553 U. Kose, I. Kreslo, V. A. Kudryavtsev, Y. Li, B. Littlejohn, D. Lissauer, P. Livesly, S. Lockwitz,
 3554 W. C. Louis, M. Lthi, B. Lundberg, F. Mammoliti, G. Mannocchi, A. Marchionni, C. Mari-
 3555 ani, J. Marshall, K. Mavrokordidis, N. McCauley, N. McConkey, K. McDonald, V. Meddage,
 3556 A. Menegolli, G. Meng, I. Mercer, T. Miao, T. Miceli, G. B. Mills, D. Mladenov, C. Montanari,

- 3557 D. Montanari, J. Moon, M. Mooney, C. Moore, Z. Moss, M. H. Mouhai, S. Mufson, R. Mur
 3558 rells, D. Naples, M. Nessi, M. Nicoletto, P. Nienaber, B. Norris, F. Noto, J. Nowak, S. Pal,
 3559 O. Palamara, V. Paolone, V. Papavassiliou, S. Pate, J. Pater, Z. Pavlovic, J. Perkin, P. Picchi,
 3560 F. Pietropaolo, P. Poski, S. Pordes, R. Potenza, G. Pulliam, X. Qian, L. Qiuguang, J. L. Raaf,
 3561 V. Radeka, R. Rameika, A. Rappoldi, G. L. Raselli, P. N. Ratoff, B. Rebel, M. Richardson,
 3562 L. Rochester, M. Rossella, C. Rubbia, C. Rudolf von Rohr, B. Russell, P. Sala, A. Scaramelli,
 3563 D. W. Schmitz, A. Schukraft, W. Seligman, M. H. Shaevitz, B. Sippach, E. Snider, J. Sobczyk,
 3564 M. Soderberg, S. Sldner-Rembold, M. Spanu, J. Spitz, N. Spooner, D. Stefan, J. St. John,
 3565 T. Strauss, R. Sulej, C. M. Sutera, A. M. Szczelc, N. Tagg, C. E. Taylor, K. Terao, M. Thiesse,
 3566 L. Thompson, M. Thomson, C. Thorn, M. Torti, F. Tortorici, M. Toups, C. Touramanis,
 3567 Y. Tsai, T. Usher, R. Van de Water, F. Varanini, S. Ventura, C. Vignoli, T. Wachala, M. We-
 3568 ber, D. Whittington, P. Wilson, S. Wolbers, T. Wongjirad, K. Woodruff, M. Xu, T. Yang, B. Yu,
 3569 A. Zani, G. P. Zeller, J. Zenanno, and C. Zhang. A proposal for a three detector short-baseline
 3570 neutrino oscillation program in the fermilab booster neutrino beam, 2015.
- 3571 [5] M. Ackermann et al. Measurement of separate cosmic-ray electron and positron spectra with
 3572 the fermi large area telescope. *Phys. Rev. Lett.*, 108:011103, 2012.
- 3573 [6] A. Adare et al. Search for dark photons from neutral meson decays in $p+p$ and $d + \text{Au}$ collisions
 3574 at $\sqrt{s_{NN}} = 200$ GeV. *Phys. Rev.*, C91(3):031901, 2015.
- 3575 [7] P. A. R. Ade et al. Planck 2015 results. XIII. Cosmological parameters. 2015.
- 3576 [8] P. H. Adrian, N. A. Baltzell, M. Battaglieri, M. Bond, S. Boyarinov, S. Bueltmann, V. D. Burk-
 3577 ert, D. Calvo, M. Carpinelli, A. Celentano, G. Charles, L. Colaneri, W. Cooper, C. Cuevas,
 3578 A. D'Angelo, N. Dashyan, M. De Napoli, R. De Vita, A. Deur, R. Dupre, H. Egriyan,
 3579 L. Elouadrhiri, R. Essig, V. Fadeyev, C. Field, A. Filippi, A. Freyberger, M. Garon, N. Gevor-
 3580 gyan, F. X. Girod, N. Graf, M. Graham, K. A. Griffioen, A. Grillo, M. Guidal, R. Herbst,
 3581 M. Holtrop, J. Jaros, G. Kalicy, M. Khandaker, V. Kubarovskiy, E. Leonora, K. Livingston,
 3582 T. Maruyama, K. McCarty, J. McCormick, B. McKinnon, K. Moffett, O. Moreno, C. Munoz
 3583 Camacho, T. Nelson, S. Niccolai, A. Odian, M. Oriunno, M. Osipenko, R. Paremuzyan, S. Paul,
 3584 N. Randazzo, B. Raydo, B. Reese, A. Rizzo, P. Schuster, Y. G. Sharabian, G. Simi, A. Simonyan,
 3585 V. Sipala, D. Sokhan, M. Solt, S. Stepanyan, H. Szumila-Vance, N. Toro, S. Uemura, M. Un-
 3586 garo, H. Voskanyan, L. B. Weinstein, B. Wojtsekowski, and B. Yale. Search for a dark photon
 3587 in electro-produced e^+e^- pairs with the heavy photon search experiment at jlab, 2018.
- 3588 [9] Per Adrian, Nathan Baltzell, M. Battaglieri, M. Bond, S. Boyarinov, S. Bueltmann, V.D Burk-
 3589 ert, D. Calvo, Massimo Carpinelli, A. Celentano, Gabriel Charles, L. Colaneri, W. Cooper,
 3590 Chris Cuevas, Annalisa D'Angelo, N. Dashyan, M. Napoli, Roberta Vita, A. Deur, and Brown

- 3591 Yale. Search for a dark photon in electroproduced e + e pairs with the heavy photon search
3592 experiment at jlab. *Physical Review D*, 98, 11 2018.
- 3593 [10] Oscar Adriani et al. An anomalous positron abundance in cosmic rays with energies 1.5-100
3594 GeV. *Nature*, 458:607–609, 2009.
- 3595 [11] G. Agakishiev et al. Searching a Dark Photon with HADES. *Phys. Lett.*, B731:265–271, 2014.
- 3596 [12] S. Agostinelli, J. Allison, K. Amako, J. Apostolakis, H. Araujo, P. Arce, M. Asai, D. Axen,
3597 S. Banerjee, G. Barrand, F. Behner, L. Bellagamba, J. Boudreau, L. Broglia, A. Brunengo,
3598 H. Burkhardt, S. Chauvie, J. Chuma, R. Chytracek, G. Cooperman, G. Cosmo, P. Degtyarenko,
3599 A. Dell’Acqua, G. Depaola, D. Dietrich, R. Enami, A. Feliciello, C. Ferguson, H. Fesefeldt,
3600 G. Folger, F. Foppiano, A. Forti, S. Garelli, S. Giani, R. Giannitrapani, D. Gibin, J.J. [Gmez
3601 Cadenas], I. Gonzlez, G. [Gracia Abril], G. Greeniaus, W. Greiner, V. Grichine, A. Grossheim,
3602 S. Guatelli, P. Gumplinger, R. Hamatsu, K. Hashimoto, H. Hasui, A. Heikkinen, A. Howard,
3603 V. Ivanchenko, A. Johnson, F.W. Jones, J. Kallenbach, N. Kanaya, M. Kawabata, Y. Kawa-
3604 bata, M. Kawaguti, S. Kelner, P. Kent, A. Kimura, T. Kodama, R. Kokoulin, M. Kossov,
3605 H. Kurashige, E. Lamanna, T. Lampn, V. Lara, V. Lefebure, F. Lei, M. Liendl, W. Lock-
3606 man, F. Longo, S. Magni, M. Maire, E. Medernach, K. Minamimoto, P. [Mora de Freitas],
3607 Y. Morita, K. Murakami, M. Nagamatu, R. Nartallo, P. Nieminen, T. Nishimura, K. Ohtsubo,
3608 M. Okamura, S. O’Neale, Y. Oohata, K. Paech, J. Perl, A. Pfeiffer, M.G. Pia, F. Ranjard,
3609 A. Rybin, S. Sadilov, E. [Di Salvo], G. Santin, T. Sasaki, N. Savvas, Y. Sawada, S. Scherer,
3610 S. Sei, V. Sirotenko, D. Smith, N. Starkov, H. Stoecker, J. Sulkimo, M. Takahata, S. Tanaka,
3611 E. Tcherniaev, E. [Safai Tehrani], M. Tropeano, P. Truscott, H. Uno, L. Urban, P. Urban,
3612 M. Verderi, A. Walkden, W. Wander, H. Weber, J.P. Wellisch, T. Wenaus, D.C. Williams,
3613 D. Wright, T. Yamada, H. Yoshida, and D. Zschiesche. Geant4a simulation toolkit. *Nuclear In-
3614 struments and Methods in Physics Research Section A: Accelerators, Spectrometers, Detectors
3615 and Associated Equipment*, 506(3):250 – 303, 2003.
- 3616 [13] M. Aguilar et al. First result from the Alpha Magnetic Spectrometer on the International Space
3617 Station: Precision measurement of the positron fraction in primary cosmic rays of 0.5-350 gev.
3618 *Phys. Rev. Lett.*, 110:141102, 2013.
- 3619 [14] A.A. Aguilar-Arevalo, M. Backfish, A. Bashyal, B. Batell, B.C. Brown, R. Carr, A. Chatterjee,
3620 R.L. Cooper, P. deNiverville, R. Dharmapalan, and et al. Dark matter search in a proton beam
3621 dump with miniboone. *Physical Review Letters*, 118(22), May 2017.
- 3622 [15] Sergey Alekhin et al. A facility to Search for Hidden Particles at the CERN SPS: the SHiP
3623 physics case. 2015.

- 3624 [16] J. Alexander. *Baltimore lectures on molecular dynamics and the wave theory of light*, 2016.
 3625 <https://indico.cern.ch/event/507783/contributions/2150181/attachments/1266367/1874844/SLAC->
 3626 MMAPS-alexander.pdf.
- 3627 [17] Johan Alwall, Pavel Demin, Simon de Visscher, Rikkert Frederix, Michel Herquet, Fabio Maltoni, Tilman Plehn, David L Rainwater, and Tim Stelzer. Madgraph/madevent v4: the new
 3628 web generation. *Journal of High Energy Physics*, 2007(09):028028, Sep 2007.
- 3630 [18] R. Amanullah, C. Lidman, D. Rubin, G. Aldering, P. Astier, K. Barbary, M. S. Burns, A. Conley,
 3631 K. S. Dawson, S. E. Deustua, and et al. Spectra and hubble space telescope light curves of six
 3632 type ia supernovae at $0.511 \leq z \leq 1.12$ and the union2 compilation. *The Astrophysical Journal*,
 3633 716(1):712738, May 2010.
- 3634 [19] Sarah Andreas, Carsten Niebuhr, and Andreas Ringwald. New limits on hidden photons from
 3635 past electron beam dumps. *Phys. Rev. D*, 86:095019, 2012.
- 3636 [20] F. Archilli et al. Search for a vector gauge boson in ϕ meson decays with the KLOE detector.
 3637 *Phys. Lett.*, B706:251–255, 2012.
- 3638 [21] Nima Arkani-Hamed, Douglas P. Finkbeiner, Tracy R. Slatyer, and Neal Weiner. A Theory of
 3639 Dark Matter. *Phys. Rev.*, D79:015014, 2009.
- 3640 [22] Nima Arkani-Hamed and Neal Weiner. LHC Signals for a SuperUnified Theory of Dark Matter.
 3641 *JHEP*, 12:104, 2008.
- 3642 [23] Bernard Aubert et al. Search for Dimuon Decays of a Light Scalar Boson in Radiative Transitions $\Upsilon \rightarrow \gamma A_0$. *Phys. Rev. Lett.*, 103:081803, 2009.
- 3644 [24] D. Babusci et al. Limit on the production of a light vector gauge boson in phi meson decays
 3645 with the KLOE detector. *Phys. Lett.*, B720:111–115, 2013.
- 3646 [25] I. Balossino, N. Baltzell, M. Battaglieri, M. Bond, E. Buchanan, D. Calvo, A. Celentano,
 3647 G. Charles, L. Colaneri, A. DAngelo, and et al. The hps electromagnetic calorimeter. *Nuclear
 3648 Instruments and Methods in Physics Research Section A: Accelerators, Spectrometers, Detectors
 3649 and Associated Equipment*, 854:8999, May 2017.
- 3650 [26] N. Baltzell, H. Egiyan, M. Ehrhart, C. Field, A. Freyberger, F.-X. Girod, M. Holtrop, J. Jaros,
 3651 G. Kalicy, T. Maruyama, B. McKinnon, K. Moffeit, T. Nelson, A. Odian, M. Oriunno, R. Pare-
 3652 muzyan, S. Stepanyan, M. Tiefenback, S. Uemura, M. Ungaro, and H. Vance. The heavy photon
 3653 search beamline and its performance. *Nuclear Instruments and Methods in Physics Research
 3654 Section A: Accelerators, Spectrometers, Detectors and Associated Equipment*, 859:69 – 75, 2017.

- 3655 [27] D. Banerjee, V.E. Burtsev, A.G. Chumakov, D. Cooke, P. Crivelli, E. Depero, A.V. Dermenev,
 3656 S.V. Donskov, R.R. Dusaev, T. Enik, and et al. Dark matter search in missing energy events
 3657 with na64. *Physical Review Letters*, 123(12), Sep 2019.
- 3658 [28] J. R. Batley et al. Search for the dark photon in π^0 decays. *Phys. Lett.*, B746:178–185, 2015.
- 3659 [29] M. Battaglieri, A. Bersani, B. Caiffi, A. Celentano, R. De Vita, E. Fanchini, L. Marsicano,
 3660 P. Musico, M. Osipenko, F. Panza, M. Ripani, E. Santopinto, M. Taiuti, V. Bellini, M. Bond,
 3661 M. De Napoli, F. Mammoliti, E. Leonora, N. Randazzo, G. Russo, M. Sperduto, C. Sutera,
 3662 F. Tortorici, N. Baltzell, M. Dalton, A. Freyberger, F. X. Girod, V. Kubarovský, E. Pasyuk,
 3663 E. S. Smith, S. Stepanyan, M. Ungaro, T. Whitlatch, E. Izaguirre, G. Krnjaic, D. Snowden-Ifft,
 3664 D. Loomba, M. Carpinelli, V. Sipala, P. Schuster, N. Toro, R. Essig, M. H. Wood, M. Holtrop,
 3665 R. Paremuyan, G. De Cataldo, R. De Leo, D. Di Bari, L. Lagamba, E. Nappi, R. Perrino,
 3666 I. Balossino, L. Barion, G. Ciullo, M. Contalbrigo, P. Lenisa, A. Movsisyan, F. Spizzo, M. Tur-
 3667 isini, F. De Persio, E. Cisbani, F. Garibaldi, F. Meddi, G. M. Urciuoli, D. Hasch, V. Lucherini,
 3668 M. Mirazita, S. Pisano, G. Simi, A. D'Angelo, L. Lanza, A. Rizzo, C. Schaerf, I. Zonta, A. Fil-
 3669 ippesi, S. Fegan, M. Kunkel, M. Bashkanov, P. Beltrame, A. Murphy, G. Smith, D. Watts,
 3670 N. Zachariou, L. Zana, D. Glazier, D. Ireland, B. McKinnon, D. Sokhan, L. Colaneri, S. Anefalos
 3671 Pereira, A. Afanasev, B. Briscoe, I. Strakovsky, N. Kalantarians, L. Weinstein, K. P. Adhikari,
 3672 J. A. Dunne, D. Dutta, L. El Fassi, L. Ye, K. Hicks, P. Cole, S. Dobbs, and C. Fanelli. Dark
 3673 matter search in a beam-dump experiment (bdx) at jefferson lab, 2016.
- 3674 [30] M. Battaglieri et al. The Heavy Photon Search Test Detector. *Nucl. Instrum. Meth.*, A777:91–
 3675 101, 2015.
- 3676 [31] T. Beranek, H. Merkel, and M. Vanderhaeghen. Theoretical framework to analyze searches
 3677 for hidden light gauge bosons in electron scattering fixed target experiments. *Phys. Rev.*,
 3678 D88:015032, 2013.
- 3679 [32] P. Billoir and S. Qian. Fast vertex fitting with a local parametrization of tracks. *Nuclear*
 3680 *Instruments and Methods in Physics Research Section A: Accelerators, Spectrometers, Detectors*
 3681 *and Associated Equipment*, 311(1):139 – 150, 1992.
- 3682 [33] J. D. Bjorken, S. Ecklund, W. R. Nelson, A. Abashian, C. Church, B. Lu, L. W. Mo, T. A.
 3683 Nunamaker, and P. Rassmann. Search for Neutral Metastable Penetrating Particles Produced
 3684 in the SLAC Beam Dump. *Phys. Rev.*, D38:3375, 1988.
- 3685 [34] James D. Bjorken, Rouven Essig, Philip Schuster, and Natalia Toro. New Fixed-Target Experi-
 3686 ments to Search for Dark Gauge Forces. *Phys. Rev.*, D80:075018, 2009.

- 3687 [35] V. Blobel. A new fast track-fit algorithm based on broken lines. *Nuclear Instruments and*
3688 *Methods in Physics Research Section A: Accelerators, Spectrometers, Detectors and Associated*
3689 *Equipment*, 566(1):14 – 17, 2006. TIME 2005.
- 3690 [36] V. Blobel. Software alignment for tracking detectors. *Nuclear Instruments and Methods in*
3691 *Physics Research Section A: Accelerators, Spectrometers, Detectors and Associated Equipment*,
3692 566(1):5 – 13, 2006. TIME 2005.
- 3693 [37] Volker Blobel, Claus Kleinwort, and Frank Meier. Fast alignment of a complex tracking detector
3694 using advanced track models. *Computer Physics Communications*, 182(9):1760 – 1763, 2011.
3695 Computer Physics Communications Special Edition for Conference on Computational Physics
3696 Trondheim, Norway, June 23-26, 2010.
- 3697 [38] A. Bross, M. Crisler, S. Pordes, J. Volk, S. Errede, and J. Wrbanek. Search for short-lived
3698 particles produced in an electron beam dump. *Phys. Rev. Lett.*, 67:2942–2945, 1991.
- 3699 [39] Volker D. Burkert. The JLab 12 GeV upgrade and the initial science program - Selected topics.
3700 *Proc. Int. Sch. Phys. Fermi*, 180:303–332, 2012.
- 3701 [40] Serguei Chatrchyan et al. Observation of a new boson at a mass of 125 GeV with the CMS
3702 experiment at the LHC. *Phys. Lett.*, B716:30–61, 2012.
- 3703 [41] Ilias Cholis and Dan Hooper. Dark Matter and Pulsar Origins of the Rising Cosmic Ray Positron
3704 Fraction in Light of New Data From AMS. *Phys. Rev.*, D88:023013, 2013.
- 3705 [42] Michele Cicoli, Mark Goodsell, Joerg Jaeckel, and Andreas Ringwald. Testing String Vacua in
3706 the Lab: From a Hidden CMB to Dark Forces in Flux Compactifications. *JHEP*, 07:114, 2011.
- 3707 [43] Douglas Clowe, Anthony Gonzalez, and Maxim Markevitch. Weak lensing mass reconstruction
3708 of the interacting cluster 1e 0657558: Direct evidence for the existence of dark matter. *The*
3709 *Astrophysical Journal*, 604(2):596603, Apr 2004.
- 3710 [44] D0 Collaboration. Layer 2-5 silicon sensor specifications for D0 SMTII. *Internal Note*, 2003.
- 3711 [45] S. Coutu. Positrons galore. *Phys. Online J.*, 6, 40:1-40:3, 2013.
- 3712 [46] Patrick deNiverville, Maxim Pospelov, and Adam Ritz. Light new physics in coherent neutrino-
3713 nucleus scattering experiments. *Phys. Rev. D*, 92:095005, Nov 2015.
- 3714 [47] Jozef Dudek et al. Physics Opportunities with the 12 GeV Upgrade at Jefferson Lab. *Eur.*
3715 *Phys. J.*, A48:187, 2012.
- 3716 [48] Rouven Essig, Philip Schuster, Natalia Toro, and Bogdan Wojtsekhowski. An Electron Fixed
3717 Target Experiment to Search for a New Vector Boson A' Decaying to e+e-. *JHEP*, 02:009,
3718 2011.

- 3719 [49] Jonathan L. Feng, Bartosz Fornal, Iftah Galon, Susan Gardner, Jordan Smolinsky, Tim M.P.
 3720 Tait, and Philip Tanedo. Particle physics models for the 17 mev anomaly in beryllium nuclear
 3721 decays. *Physical Review D*, 95(3), Feb 2017.
- 3722 [50] Sean Fraser, Andi Hektor, Gert Htsi, Kristjan Kannike, Carlo Marzo, Luca Marzola, Antonio
 3723 Racioppi, Martti Raidal, Christian Spethmann, Ville Vaskonen, and Hardi Veerme. The edges
 3724 21 cm anomaly and properties of dark matter. *Physics Letters B*, 785:159 – 164, 2018.
- 3725 [51] M. J. French et al. Design and results from the APV25, a deep sub-micron CMOS front-end
 3726 chip for the CMS tracker. *Nucl. Instrum. Meth.*, A466:359–365, 2001.
- 3727 [52] S. Gardner, R. J. Holt, and A. S. Tadepalli. New Prospects in Fixed Target Searches for Dark
 3728 Forces with the SeaQuest Experiment at Fermilab. 2015.
- 3729 [53] Mark Goodsell, Joerg Jaeckel, Javier Redondo, and Andreas Ringwald. Naturally Light Hidden
 3730 Photons in LARGE Volume String Compactifications. *JHEP*, 11:027, 2009.
- 3731 [54] Mark Goodsell and Andreas Ringwald. Light Hidden-Sector U(1)s in String Compactifications.
 3732 *Fortsch. Phys.*, 58:716–720, 2010.
- 3733 [55] Norman Graf and Jeremy McCormick. Simulator for the linear collider (slic): A tool for ilc
 3734 detector simulations. *AIP Conference Proceedings*, 867(1):503–512, 2006.
- 3735 [56] Norman A Graf. org.lcsim: Event reconstruction in java. *Journal of Physics: Conference Series*,
 3736 331(3):032012, dec 2011.
- 3737 [57] M. Graham. Track efficiency, wide-angle bremsstrahlung and trident rates in the 2016 hps
 3738 data. [https://confluence.slac.stanford.edu/display/hpsg/Physics+Analysis+Notes?
 3739 preview=/146715820/275087425/hps_trkeff_tridents_2016_v1.pdf](https://confluence.slac.stanford.edu/display/hpsg/Physics+Analysis+Notes?preview=/146715820/275087425/hps_trkeff_tridents_2016_v1.pdf).
- 3740 [58] H Hirayama, Y Namito, AF Bielajew, SJ Wilderman, and WR Nelson. The egs5 code system,
 3741 slac report 730. *United States Department of Energy*, 2005.
- 3742 [59] Kuflik Eric Murayama Hitoshi Hochberg, Yonit. Simp spectroscopy. *Journal of High Energy
 3743 Physics*, 90, May 2016.
- 3744 [60] Yonit Hochberg, Eric Kuflik, Hitoshi Murayama, Tomer Volansky, and Jay G. Wacker. Model for
 3745 thermal relic dark matter of strongly interacting massive particles. *Phys. Rev. Lett.*, 115:021301,
 3746 Jul 2015.
- 3747 [61] Bob Holdom. Two U(1)’s and Epsilon Charge Shifts. *Phys. Lett.*, B166:196–198, 1986.
- 3748 [62] Philip Ilten, Yotam Soreq, Jesse Thaler, Mike Williams, and Wei Xue. Inclusive Dark Photon
 3749 Search at LHCb. 2016.

- 3750 [63] Philip Ilten, Jesse Thaler, Mike Williams, and Wei Xue. Dark photons from charm mesons at
3751 LHCb. *Phys. Rev.*, D92(11):115017, 2015.
- 3752 [64] Joerg Jaeckel and Andreas Ringwald. The low-energy frontier of particle physics. *Annual
3753 Review of Nuclear and Particle Science*, 60(1):405437, Nov 2010.
- 3754 [65] Reza Kazimi, John Hansknecht, Michael Spata, and Haipeng Wang. Source and Extraction for
3755 Simultaneous Four-hall Beam Delivery System at CEBAF. In *Proceedings, 4th International
3756 Particle Accelerator Conference (IPAC 2013)*, page WEPFI085, 2013.
- 3757 [66] B. Kelvin. *Baltimore lectures on molecular dynamics and the wave theory of light*, 1904.
3758 <https://archive.org/details/baltimorelecture00kelviala>.
- 3759 [67] Claus Kleinwort. General broken lines as advanced track fitting method. *Nuclear Instruments
3760 and Methods in Physics Research Section A: Accelerators, Spectrometers, Detectors and Asso-
3761 ciated Equipment*, 673:107110, May 2012.
- 3762 [68] A. Konaka, K. Imai, H. Kobayashi, A. Masaike, K. Miyake, T. Nakamura, N. Nagamine,
3763 N. Sasao, A. Enomoto, Y. Fukushima, E. Kikutani, H. Koiso, H. Matsumoto, K. Nakahara,
3764 S. Ohsawa, T. Taniguchi, I. Sato, and J. Urakawa. Search for neutral particles in electron-
3765 beam-dump experiment. *Phys. Rev. Lett.*, 57:659–662, 1986.
- 3766 [69] T. Kraemer. Track Parameters in LCIO. *LC-Notes*, 2006.
- 3767 [70] A. J. Krasznahorkay, M. Csatlos, L. Csige, J. Gulyas, M. Koszta, B. Szihalmi, J. Timar, D. S.
3768 Firak, A. Nagy, N. J. Sas, and A. Krasznahorkay. New evidence supporting the existence of the
3769 hypothetic x17 particle. 2019.
- 3770 [71] A.J. Krasznahorkay, M. Csatls, L. Csige, Z. Gcsi, J. Guly, M. Hunyadi, I. Kuti, B.M. Nyak,
3771 L. Stuhl, J. Timr, and et al. Observation of anomalous internal pair creation inbe8: A possible
3772 indication of a light, neutral boson. *Physical Review Letters*, 116(4), Jan 2016.
- 3773 [72] J. P. Lees, V. Poireau, V. Tisserand, E. Grauges, A. Palano, G. Eigen, D. N. Brown, M. Derdzin-
3774 ski, A. Giuffrida, Yu. G. Kolomensky, M. Fritsch, H. Koch, T. Schroeder, C. Hearty, T. S.
3775 Mattison, J. A. McKenna, R. Y. So, V. E. Blinov, A. R. Buzykaev, V. P. Druzhinin, V. B.
3776 Golubev, E. A. Kravchenko, A. P. Onuchin, S. I. Serednyakov, Yu. I. Skovpen, E. P. Solodov,
3777 K. Yu. Todyshev, A. J. Lankford, J. W. Gary, O. Long, A. M. Eisner, W. S. Lockman, W. Pan-
3778 duro Vazquez, D. S. Chao, C. H. Cheng, B. Echenard, K. T. Flood, D. G. Hitlin, J. Kim,
3779 T. S. Miyashita, P. Ongmongkolkul, F. C. Porter, M. Röhrken, Z. Huard, B. T. Meadows,
3780 B. G. Pushpawela, M. D. Sokoloff, L. Sun, J. G. Smith, S. R. Wagner, D. Bernard, M. Verderi,
3781 D. Bettoni, C. Bozzi, R. Calabrese, G. Cibinetto, E. Fioravanti, I. Garzia, E. Luppi, V. Santoro,
3782 A. Calcaterra, R. de Sangro, G. Finocchiaro, S. Martellotti, P. Patteri, I. M. Peruzzi, M. Piccolo,

- 3783 M. Rotondo, A. Zallo, S. Passaggio, C. Patrignani, H. M. Lacker, B. Bhuyan, U. Mallik, C. Chen,
 3784 J. Cochran, S. Prell, H. Ahmed, A. V. Gritsan, N. Arnaud, M. Davier, F. Le Diberder, A. M.
 3785 Lutz, G. Wormser, D. J. Lange, D. M. Wright, J. P. Coleman, E. Gabathuler, D. E. Hutchcroft,
 3786 D. J. Payne, C. Touramanis, A. J. Bevan, F. Di Lodovico, R. Sacco, G. Cowan, Sw. Banerjee,
 3787 D. N. Brown, C. L. Davis, A. G. Denig, W. Gradl, K. Griessinger, A. Hafner, K. R. Schubert,
 3788 R. J. Barlow, G. D. Lafferty, R. Cenci, A. Jawahery, D. A. Roberts, R. Cowan, S. H. Robertson,
 3789 B. Dey, N. Neri, F. Palombo, R. Cheaib, L. Cremaldi, R. Godang, D. J. Summers, P. Taras,
 3790 G. De Nardo, C. Sciacca, G. Raven, C. P. Jessop, J. M. LoSecco, K. Honscheid, R. Kass, A. Gaz,
 3791 M. Margoni, M. Posocco, G. Simi, F. Simonetto, R. Stroili, S. Akar, E. Ben-Haim, M. Bomben,
 3792 G. R. Bonneauaud, G. Calderini, J. Chauveau, G. Marchiori, J. Ocariz, M. Biasini, E. Manoni,
 3793 A. Rossi, G. Batignani, S. Bettarini, M. Carpinelli, G. Casarosa, M. Chrzaszcz, F. Forti, M. A.
 3794 Giorgi, A. Lusiani, B. Oberhof, E. Paoloni, M. Rama, G. Rizzo, J. J. Walsh, A. J. S. Smith,
 3795 F. Anulli, R. Faccini, F. Ferrarotto, F. Ferroni, A. Pilloni, G. Piredda, C. Bünger, S. Dit-
 3796 trich, O. Grünberg, M. Heß, T. Leddig, C. Voß, R. Waldi, T. Adye, F. F. Wilson, S. Emery,
 3797 G. Vasseur, D. Aston, C. Cartaro, M. R. Convery, J. Dorfan, W. Dunwoodie, M. Ebert, R. C.
 3798 Field, B. G. Fulsom, M. T. Graham, C. Hast, W. R. Innes, P. Kim, D. W. G. S. Leith, S. Luitz,
 3799 D. B. MacFarlane, D. R. Muller, H. Neal, B. N. Ratcliff, A. Roodman, M. K. Sullivan, J. Va'vra,
 3800 W. J. Wisniewski, M. V. Purohit, J. R. Wilson, A. Randle-Conde, S. J. Sekula, M. Bellis, P. R.
 3801 Burchat, E. M. T. Puccio, M. S. Alam, J. A. Ernst, R. Gorodeisky, N. Guttman, D. R. Peimer,
 3802 A. Soffer, S. M. Spanier, J. L. Ritchie, R. F. Schwitters, J. M. Izen, X. C. Lou, F. Bianchi,
 3803 F. De Mori, A. Filippi, D. Gamba, L. Lanceri, L. Vitale, F. Martinez-Vidal, A. Oyanguren,
 3804 J. Albert, A. Beaulieu, F. U. Bernlochner, G. J. King, R. Kowalewski, T. Lueck, I. M. Nugent,
 3805 J. M. Roney, R. J. Sobie, N. Tasneem, T. J. Gershon, P. F. Harrison, T. E. Latham, R. Prepost,
 3806 and S. L. Wu. Search for invisible decays of a dark photon produced in e^+e^- collisions at babar.
 3807 *Phys. Rev. Lett.*, 119:131804, Sep 2017.
- 3808 [73] Giuseppe Mandaglio. KLOE/KLOE-2 results and perspectives on dark force search. *PoS*,
 3809 EPS-HEP2017:073, 2017.
- 3810 [74] M. Markevitch, A. H. Gonzalez, D. Clowe, A. Vikhlinin, W. Forman, C. Jones, S. Murray, and
 3811 W. Tucker. Direct constraints on the dark matter selfinteraction cross section from the merging
 3812 galaxy cluster 1e 065756. *The Astrophysical Journal*, 606(2):819824, May 2004.
- 3813 [75] T. Maruyama et al. A systematic study of polarized electron emission from strained gaas/gaasp
 3814 superlattice photocathodes. *Appl. Phys. Lett.*, 85:2640, 2004.
- 3815 [76] H. Merkel et al. Search at the Mainz Microtron for Light Massive Gauge Bosons Relevant for
 3816 the Muon g-2 Anomaly. *Phys. Rev. Lett.*, 112(22):221802, 2014.
- 3817 [77] Giacomo De Pietro. First data at belle ii and dark sector physics, 2018.

- 3818 [78] H. Poincaré. The Milky Way and the Theory of Gases. *Popular Astronomy*, 14:475–488, October
3819 1906.
- 3820 [79] M. Raymond et al. The CMS tracker APV25 0.25-mu-m CMOS readout chip. *Conf. Proc.*,
3821 C00091111:130–134, 2000. [,130(2000)].
- 3822 [80] V. C. Rubin, N. Thonnard, and W. K. Ford, Jr. Rotational properties of 21 SC galaxies with
3823 a large range of luminosities and radii, from NGC 4605 /R = 4kpc/ to UGC 2885 /R = 122
3824 kpc/. *Astrophys. J.*, 238:471, 1980.
- 3825 [81] David N. Schramm and Michael S. Turner. Big-bang nucleosynthesis enters the precision era.
3826 *Reviews of Modern Physics*, 70(1):303–318, January 1998.
- 3827 [82] Yung-Su Tsai. Pair Production and Bremsstrahlung of Charged Leptons. *Rev. Mod. Phys.*,
3828 46:815, 1974. [Erratum: Rev. Mod. Phys.49,521(1977)].
- 3829 [83] B. Wojtsekhowski, D. Nikolenko, and I. Racheck. Searching for a new force at VEPP-3. 2012.
- 3830 [84] S. Yellin. Finding an upper limit in the presence of an unknown background. *Phys. Rev. D*,
3831 66:032005, Aug 2002.
- 3832 [85] S. Yellin. Some ways of combining optimum interval upper limits, 2011.
- 3833 [86] F. Zwicky. Die Rotverschiebung von extragalaktischen Nebeln. *Helv. Phys. Acta*, 6:110–127,
3834 1933.
- 3835 [87] Torsten kesson, Asher Berlin, Nikita Blinov, Owen Colegrove, Giulia Collura, Valentina Dutta,
3836 Bertrand Echenard, Joshua Hiltbrand, David G. Hitlin, Joseph Incandela, John Jaros, Robert
3837 Johnson, Gordan Krnjaic, Jeremiah Mans, Takashi Maruyama, Jeremy McCormick, Omar
3838 Moreno, Timothy Nelson, Gavin Niendorf, Reese Petersen, Ruth Pttgen, Philip Schuster, Na-
3839 talia Toro, Nhan Tran, and Andrew Whitbeck. Light dark matter experiment (ldmx), 2018.